



Cite this: *Sens. Diagn.*, 2023, 2, 988

# An overview of Schiff base-based fluorescent turn-on probes: a potential candidate for tracking live cell imaging of biologically active metal ions

A. Afrin, Anjitha Jayaraj, M. S. Gayathri and Chinna Ayya Swamy P.  \*

The development of new fluorescent turn-on probes has attracted much attention due to the selective and sensitive detection of biologically important metal ions and their applicability in live cell imaging. Since it has been established that fluorescent probes work well in cellular media, many intriguing investigations are under progress. It is desirable to use quick and easy methods for detecting metal ions in biological and environmental systems, and the probes should provide enhanced photophysical properties with sensitivity, selectivity, a low detection threshold, a quick response time, operational simplicity, and real-time analysis, which are non-lethal to living cells, demanding extensive research. There are several novel fluorescent turn-on probes reported thus far; however, Schiff base-based probes have gained particular interest because of their intriguing optical characteristics, great thermal stability, and ease of synthesis. Moreover, they stand out in the bioactive domain as promising fluorescent chemosensors for biologically prominent metal cations and are well known for their low cytotoxicity. Schiff bases exhibit strong luminescence properties in synergistic systems with many ideal fluorophores such as quinoline, anthracene, coumarin, fluorescein, rhodamine, boron-dipyrromethene (BODIPY), dansyl, and naphthalimide. As a result, these synthetically flexible compounds with coordination sites such as N and O can rigidly bind to a wide range of transition metal ions with turn-on fluorescence properties. This review compiles the detailed sensing properties of numerous Schiff base-based probes for biologically important metal cations such as Fe(II), Zn(II), Cu(II), Ni(II), Co(II), Ag(I), Au(III), Hg(II), Cd(II) and Pd(II) via a fluorescence turn-on mechanism. Further, it covers the detection approaches elucidating the optoelectronic characteristics as well as their application in cellular imaging, which will provide a better understanding of the accumulation of metal ions in organelles.

Received 9th May 2023,  
Accepted 10th June 2023

DOI: 10.1039/d3sd00110e

rsc.li/sensors

## 1. Introduction

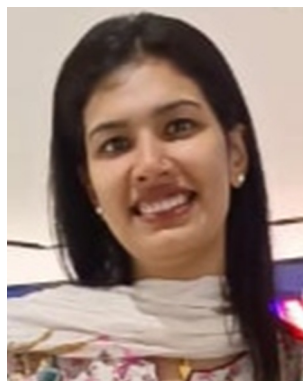
Bio-imaging probes have become an integral part in the determination of the activities of biomolecules in biomedical

Main group Organometallics Optoelectronic Materials and Catalysis lab,  
Department of Chemistry, National Institute of Technology, Calicut, India-673601.  
E-mail: swamy@nitc.ac.in



A. Afrin

Afrin A. currently works as a Junior Research Fellow (JRF) at the Department of Chemistry, National Institute of Technology Calicut. She had completed master's degree in chemistry from Cochin University of Science and Technology in the year 2020. Her current research areas include modulation of solid-state emissive properties of donor-acceptor conjugates.



Anjitha Jayaraj

Anjitha Jayaraj obtained her MSC degree from National Institute of Technology Calicut in 2020. She is currently pursuing her research carrier from the same institute, under the guidance of Dr Chinna Ayya Swamy P. Her present study focuses on designing N-heterocyclic carbene metal-based catalysts for hydrofunctionalisation reactions.



research, and therefore, the design of such non-invasive probes is a current requirement in the research field.<sup>1</sup> The metal ions present in biological systems regulate a variety of functions important including neurophysiology, protein cofactors, dioxygen binding, and transport for maintaining human health.<sup>2</sup> Excessiveness or deficiency, however, can be harmful and even fatal. Moreover, the urbanism unscrupulously contaminates the natural environment with metal ions, affecting people's health by denaturing biological processes. As a matter of fact, metal ion detection has always been a hot topic in the research community.<sup>3</sup> There are several spectrophotometric methods and electroanalytical techniques such as atomic absorption/emission spectroscopy (AAS/AES),<sup>4</sup> inductively coupled plasma mass spectroscopy (ICP-MS),<sup>5</sup> inductively coupled plasma atomic emission spectroscopy (ICP-AES),<sup>6</sup> and electrochemical<sup>7</sup> and colorimetric methods<sup>8</sup> available to detect various metal ions. However, the application of these techniques is limited because they require expensive instrumentation and complicated pre-treatments take time, resulting in low detection speed and the inability to detect and inspect cells and living tissues on site.<sup>9</sup> Fluorescent chemosensors have made notable progress to the meteoric rise of analytical chemistry notably in the cellular media due to their non-lethal nature in living cells with enhanced photophysical properties of sensitivity and selectivity, low detection limits, rapid response, operational simplicity, real-time analysis.<sup>10–15</sup> Furthermore, the visual validation aided by this technique, as well as the cost-effectiveness, made them serve for the past few decades.

Fluorescent chemosensors are probes that have a binding site and a fluorophore, as well as a possible communication mechanism between the two sites.<sup>16</sup> Noncovalent interactions including hydrogen bonding, electrostatic attractions, and

coordination events are used by most fluorescent probes to bind analytes. Active fluorescent probes are being developed for a wide range of applications with a focus on the detection of metal ions rather than anions or neutral molecules.<sup>17</sup> Furthermore, these novel fluorescent sensors based on simple organic compounds have the potential to be useful in monitoring biological events under both *in vitro* and *in vivo* conditions.<sup>18</sup> Subsequently, they became capable of monitoring the subcellular localization and dynamics of biological targets, possessing good biocompatibility, high spatiotemporal resolution, and ease of chemical modification. The common detection mechanisms altering the photophysical processes include aggregation-induced emission (AIE), excited-state intramolecular proton transfer (ESIPT), photoinduced electron transfer (PET), intramolecular charge transfer (ICT), chelation-induced enhanced fluorescence (CHEF), C=N isomerization, fluorescence resonance energy transfer (FRET) and spin-orbit coupling.<sup>19,20</sup>

In general, chemosensors are classified into two types based on optical signals: fluorescent off-on and on-off systems. The non-fluorescent free compound will recognize fluorescent analytes in off-on probes and *vice versa* in on-off probes.<sup>21–23</sup> Another method is the use of ratiometric sensors, which analyse the shift in emission and are useful for the quantification of ions.<sup>24–26</sup> Further, many novel designs with sensor systems such as chemodosimeters are being developed with the goal of improving the selectivity and sensitivity. Here, the probe on interaction with a specific analyte undergoes an irreversible chemical reaction and produces different optical properties, and the chemodosimeter function depends on these properties.<sup>27–29</sup> All of these have proven to be vital tools in subcellular habitats for clinical diagnostic, physiological, and pathological functions involving metal ions.<sup>30</sup>



M. S. Gayathri

*Gayathri M. S. completed her post-graduation in chemistry from National Institute of Technology Calicut. She was the project student under the guidance of Dr Chinna Ayya Swamy P. Her area of focus of study was synthesis of novel Schiff base complexes for the detection of metal ions.*



Chinna Ayya Swamy P.

*Dr Swamy obtained MSc in General chemistry from the University of Hyderabad in 2009 and PhD from the IISc, India, in the field of main group organometallics in 2014. After completion of the PhD, he has spent five years abroad as a post-doctoral fellow in the area of supramolecular chemistry and organometallics chemistry. Later, he joined as Assistant Professor in the Department of Chemistry, National Institute of Technology*

*Calicut in 2020. Currently, he works on the design and synthesis of supramolecular architecture for stabilizing low-valent main group compounds, metal-based asymmetric catalysis and chemosensors for biologically important ions.*



Reportedly, major research endeavors in the detection of ions with varying fluorophores are being made in order to study their intriguing luminescence properties. Quinoline,<sup>31</sup> anthracene,<sup>32</sup> coumarin,<sup>33</sup> fluorescein,<sup>34</sup> rhodamine<sup>35</sup> and bipyridine are among the commonly investigated probes. However, many of them have low solubility, poor recognition sensitivity, and complex synthesis under extreme conditions.<sup>36</sup> As a result, there is always room for improvement in designing probes to overcome these constraints. Schiff bases or imines are one type of compound that has been highlighted in many fields of chemistry due to its ease of synthesis and structural modification.<sup>37–39</sup> Furthermore, Schiff bases with coordination sites such as N and O enable them to rigidly bind to many transition metal ions with fluorescence turn-on response.<sup>40–43</sup> Hence, Schiff bases in synergistic systems with other ideal fluorophores act as fascinating turn-on probes exhibiting selective affinity for metal cations, and are employed in cellular imaging.<sup>44–46</sup>

Recently, we have reported on a simple acyclic salen Schiff base showing selective fluorescence turn-on response for the detection of Zn(II) ions in the nanomolar range, which is employed for confocal fluorescence microscopic imaging in HeLa cells.<sup>47</sup> Recognizing the importance of this hot research topic, many notable reviews have been published,<sup>48–50</sup> focusing on classifying fluorophore combinations rather than differentiating metal ion analytes. This review examines the recent advances in the development of Schiff base-based fluorescent turn-on chemosensors, including synthesis, design principle with photophysical properties, sensing mechanism, and analyte recognition studies with many parameters, primarily emphasizing on biological applications.

## 2. Schiff base-based fluorescent turn-on probes for Zn(II) ions

The second most prevalent transition-metal ion, zinc, plays a very important role in the biological system, including the transcription of genes, activity of metalloenzymes, transmission of brain signals, and DNA-binding proteins.<sup>51–54</sup> Moreover, the irregularity of Zn(II) ions causes numerous diseases such as neurodegenerative illness, including epilepsy, stroke, Alzheimer's, and Parkinson's.<sup>55</sup> In addition to its numerous other uses, the excess amount of Zn(II) ions are highly hazardous, and cause diabetes, skin conditions, and prostatic adenocarcinoma.<sup>56</sup> It also decreases soil microbial activity, which results in phytotoxic consequences.<sup>57</sup> Due to their high sensitivity, precise measurement, and spatiotemporal resolution compared to other detection methods, fluorescence techniques are employed for Zn(II) sensing.<sup>58,59</sup> Therefore, the creation of simple, widely available, and selective fluorescent Zn(II) probes is essential for both environmental and biological studies.<sup>60</sup>

In this regard, a ratiometric probe based on benzothiazole was synthesized by Shuang *et al.* in 2021,<sup>61</sup> which shows very

selective recognition of Zn(II) ions *via* the fluorescence turn-on mechanism. The **probe-1** was synthesized by reacting aminothiophenol with 4-bromosalicylaldehyde under acidic conditions, leading to the formation of substituted benzothiazole. Further, the Duff reaction of this benzothiazole was conducted followed by reacting with substituted urea, yielding the final probe (**probe-1**). The designed principle of **probe-1** is that 2-(2'-hydroxyphenyl) benzothiazole fluorophore acts as a signaling moiety and the Schiff base unit acts as a receptor site. When Zn(II) ions are added to **probe-1**, the maximum emission wavelength shifts by 82 nm from 570 to 488 nm, and the color changes from orange to green, with no change detected for the other competitive metal ions. This color change incorporated emission of **probe-1** upon binding to Zn(II) in 1 : 1, which can be explained on the basis of inhibition of ESIPT process and can result in a CHEF due to the engagement of the phenolic O atom in the coordination of **probe-1** with Zn(II) ions (Fig. 1). The detection limit of **probe-1** with Zn(II) ions determined *via* fluorescence spectra is 37.7 nM. Furthermore, **probe-1** has a low cytotoxicity, which qualifies its efficacy for tracing and visualizing Zn(II) ions *in vitro* in HeLa cells and live SH-SY5Y neuroblastoma cells.

Fluorescent **probe-2** was developed by combining *ortho*-vanillin with 1-(3-aminopropyl)imidazole *via* a simple condensation reaction<sup>62</sup> by Mobin and co-workers in 2019. **Probe-2** was structurally characterized by various spectroscopic techniques such as nuclear magnetic resonance (NMR), high-resolution mass spectrometry (HRMS), and infra-red (IR), and single-crystal X-ray diffraction (XRD) analysis to confirm its molecular entity. Synthesized **probe-2** is selective, sensitive and reversible towards the Zn(II) ions *via* the fluorescence turn-on mechanism and shows no or minimal response upon the addition of various metal ions. The restriction of the C=N imine bond isomerization on effective coordination by Zn(II) ions could be the cause of the fluorescence turn-on, and a new bathochromic band arises in the absorption spectrum. The detection limit was determined to be 31.044 nM using the equation  $LOD = 3\sigma/\text{slope}$ . Moreover, the single-crystal XRD identified formation of

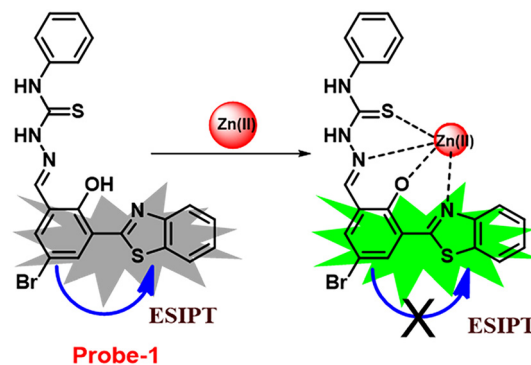
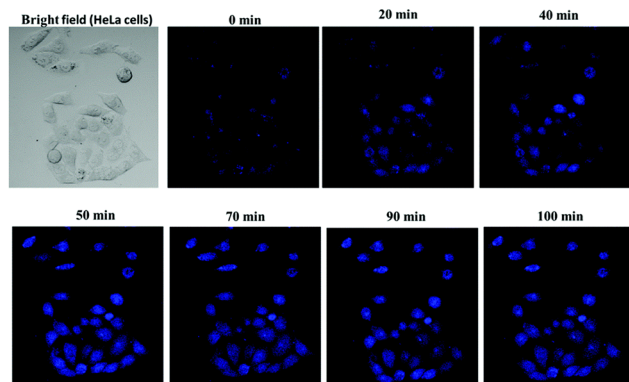
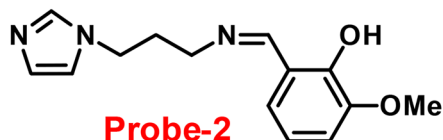


Fig. 1 Chemical structure and proposed sensing mechanism of **probe-1** with Zn(II) (redrawn the ChemDraw structure from ref. 61).







**Fig. 2** Chemical structure of **probe-2** (top) and confocal fluorescence images of **probe-2** (25  $\mu$ M, 2 h) with Zn(II) ions on HeLa cells with different time intervals (bottom) (redrawn and reprinted with permission from ref. 62, Copyright 2019 Royal Society of Chemistry).

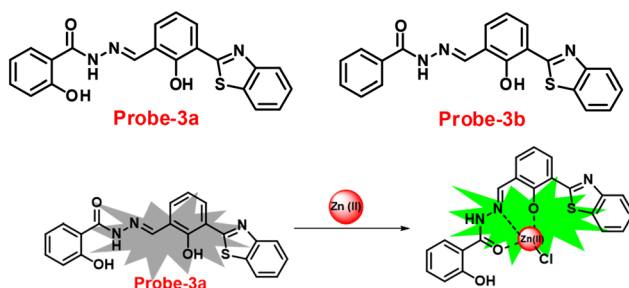


**Fig. 3** Chemical structures of **probe-(3a-3b)** and proposed sensing mechanism of **probe-3a** with Zn(II) (redrawn the ChemDraw structure from ref. 63).

dinuclear Zn(II) complexes indicates that **probe-2** strongly binds to the Zn(II) ions. The detection of Zn(II) ions by **probe-2** in biological media was investigated on HeLa and DU-145

cancer cell lines, since **probe-2** was proven to be non-toxic and highly biocompatible for cellular proliferation by the MTT cell viability assay, which is helpful for the detection or monitoring of Zn(II) ions in biological samples (Fig. 2).

A novel fluorescent chemosensor, **probe-3**, was synthesized *via* a simple condensation reaction of the aldehyde and amine, which leads to the formation of **probe-3a** and **probe-3b** by Mondal *et al.*<sup>63</sup> in 2019. The **probes** selectively exhibit strong ratiometric changes in the emission spectra, upon addition of Zn(II) ions, resulting in a blue shift from 550 nm to 478 nm, which occurs as a consequence of the ESIPT process in a successful (Fig. 3) stoichiometric ratio of 1 : 1 with a low detection limit value of 0.16  $\mu$ M for **probe-3a**. The binding constant of **probe-3a** with Zn(II) ions was estimated to be  $1.6 \times 10^5 \text{ M}^{-1}$  *via* fluorescence titration according to the Benesi-Hildebrand (B-H) plot, indicating that **probe-3a-Zn(II)** is an adequately stable complex. The binding mechanism of **probes** with Zn(II) was strongly supported by  $^1\text{H}$  NMR, density functional theory (DFT), time-dependent density-functional theory (TD-DFT), and electrospray ionisation mass spectrometry (ESI-MS). Consequently, dip-stick experimentation, which enabled real-time monitoring without the use of an instrument, resulted in an instant qualitative detection of Zn(II) with the **probes**, and was confirmed by the color change in the absorption and fluorescence. Further, the **probes** were subjected to the sensing of Zn(II) ions in biological media, and an experiment was carried out on human breast cancer cell lines (MCF-7) and tissues. These cells exhibited distinct fluorescence colors upon introducing Zn(II), which supports the recognition of Zn(II) ions in biological samples (Fig. 4).

The one-step condensation reaction of 5-phenylsalicylaldehyde and 2-aminobenzohydrazide yielded a Schiff base derivative **probe-4** by Lu *et al.* in 2018 (ref. 64) with remarkable selectivity and sensitivity towards Zn(II) ions. The addition of Zn(II) ions to the aqueous solution of **probe-4** caused an intense green fluorescence emission with a substantial red shift, even in the presence of other competing metal ions (Fig. 5). The three-atom cage containing Zn(II) narrowed **probe-4**'s free rotation and twisting, resulting in

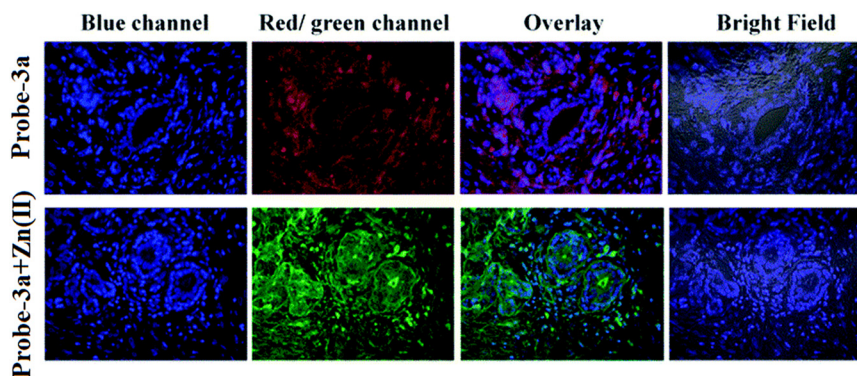


**Fig. 4** Confocal bio-imaging of human breast tissues on treatment with 15  $\mu$ M **probe-3a** with Zn(II) (reprinted with permission from ref. 63, Copyright 2019 Royal Society of Chemistry).





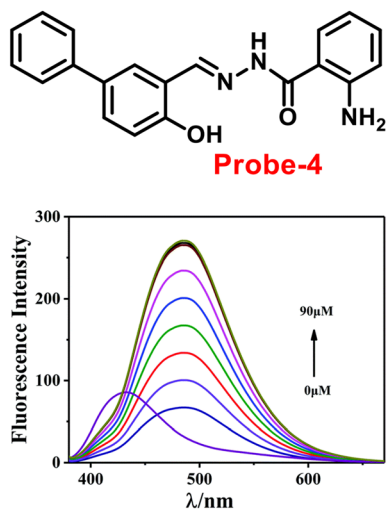


Fig. 5 Chemical structure of **probe-4** (top) and fluorescence spectra of **probe-4** (10 μM) in the presence of increasing concentrations of Zn(II) (bottom) (redrawn and reprinted with permission from ref. 64, Copyright 2018 Royal Society of Chemistry).

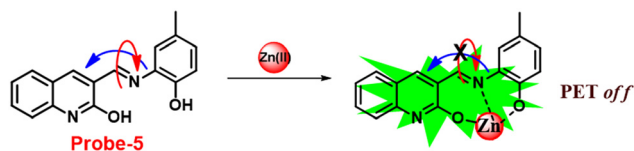


Fig. 6 Chemical structure and proposed sensing mechanism of **probe-5** with Zn(II) (redrawn the ChemDraw structure from ref. 65).

strong stiffness and high co-planarity of the molecular assembly, which led to the induction of ICT and CHEF upon complexation with Zn(II) ions. The detection limit value of **probe-4** with Zn(II) ions was determined to be 72 nM, which is much lower than that of WHO-recommended level (76 μM Zn(II) ions) in drinking water. The stoichiometry of **probe-4** with Zn(II) ions was determined *via* Job's plot and disclosed as 2:1 binding ratio. The reversibility of **probe-4** towards Zn(II) was confirmed *via* addition of EDTA to **probe-4**-Zn(II) in CH<sub>3</sub>CN-H<sub>2</sub>O, which leads to the regeneration of **probe-4** alone, these results strongly supported the reversibility of

**probe-4**. Finally, **probe-4** was demonstrated as a feasible fluorescent sensor for real-time monitoring of Zn(II) in biological systems *via* bio-imaging in living HeLa cells and zebrafish models, with minimal cellular damage.

In 2017, Annaraj and colleagues<sup>65</sup> developed quinoline-based **probe-5** by easily combining 2-hydroxyquinoline-3-carbaldehyde and 2-amino-4-methyl phenol, which exhibits very high sensitivity and selectivity towards Zn(II) ions *via* fluorescence turn-on behavior and no response to other competitive ions such as Cd(II), Pb(II), Hg(II), Co(II), Cu(II), Co(II), Pb(II), and Ni(II) ions. The effective anchoring of Zn(II) to **probe-5** *via* two -OH and imine nitrogen resulted in limited free rotation and enhanced the CHEF action by inhibiting PET, which were responsible for the fluorescence turn-on (Fig. 6). The fluorescence response of **probe-5** with Zn(II) ions was found to be linearly rising upon the incremental addition of Zn(II), and the LOD was determined to be 72 nM. The significant Stokes shift value and red emission favored this probe and indicated that it is a biocompatible probe for the bio-imaging of Zn(II) ions in A549 cells and zebrafish embryos.

Chattopadhyay and co-workers synthesized pyrazole-based Schiff base chemosensor **probe-6** in a good yield, *via* a simple condensation reaction between 3-amino-5-phenylpyrazole and 2,6-diformyl-4-methyl-phenol<sup>66</sup> in 2017. The pure nature of **probe-6** displayed very poor emission, which exhibits green luminescence turn-on towards Zn(II) ions *via* the generation of dinuclear Zn(II) complexes (Fig. 7). In the presence of other competing ions, there was no change in the fluorescence spectra, caused by the addition of Zn(II) ions, which was explained by the CHEF mechanism. According to Job's plot calculation, Zn(II) ions form a 2:1 binding ratio, and **probe-6** was found to detect Zn(II) ions at extremely low levels up to 27.80 nM.

It is essential to develop and synthesize a probe that can detect Zn(II) ions even in the presence of other competing metal ions. In this regard, Misra and co-workers focused on the synthesis of **probe-7** from 3-hydroxy-2-naphthoic hydrazide and *ortho*-vanillin under reflux conditions<sup>67</sup> in 2016, which was structurally confirmed by multinuclear NMR and HRMS. **Probe-7** can be utilised as an active fluorescent probe for Zn(II) ions with aggregation-induced emission enhancement

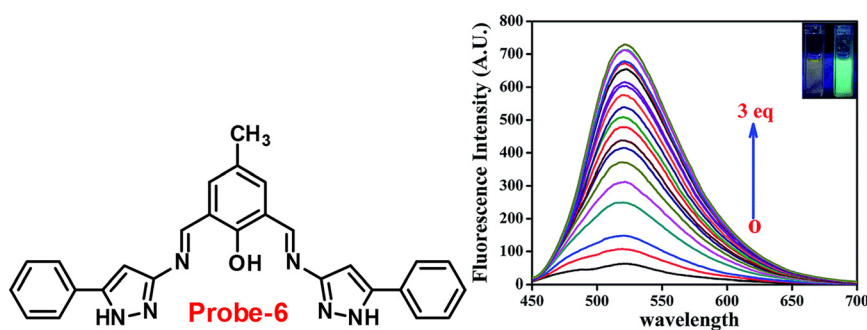


Fig. 7 Chemical structure of **probe-6** (left) and fluorescence spectra of **probe-6** with addition of Zn(II) ions (right) (redrawn and reprinted with permission from ref. 66, Copyright 2017 Royal Society of Chemistry).



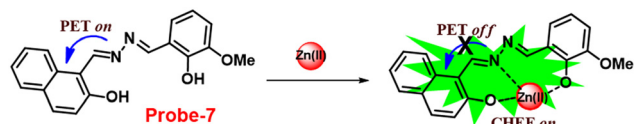


Fig. 8 Chemical structure and proposed sensing mechanism of **probe-7** with  $\text{Zn(II)}$  (redrawn the ChemDraw structure from ref. 67).

(AIEE). **Probe-7** could not only detect  $\text{Zn(II)}$  ions by acute chromogenic and selective fluorescence turn-on responses, but also differentiate among its substantial AIEE activity in a high water ratio, and  $\text{Zn(II)}$  induced AIEE activity through separate luminescence signals without interfering the competitive metal ions, which was explained by the CHECF and PET off mechanisms (Fig. 8). The limit of detection (LOD) of **probe-7** for  $\text{Zn(II)}$  ions was estimated from fluorescence spectra, which was found to be  $0.11 \mu\text{M}$ . The results strongly suggested that **probe-7** is highly biocompatible in biological media as well as detecting  $\text{Zn(II)}$  ions in physiological media.

Benzothiazole-based fluorescent **probes 8a–c** were designed and synthesized by Chen and co-workers in 2017 (ref. 68) for the detection of  $\text{Zn(II)}$  ions *via* the fluorescence turn-on mechanism. The **probes** were structurally characterized *via* various analytical techniques such as multinuclear NMR and HRMS. There was a considerable change in the emission of these **probes 8a–c** upon binding with  $\text{Zn(II)}$  ions from a very poor yellow color emission to a strong blue color emission, whereas no change was seen in fluorescence spectra upon addition of other competitive metal ions (Fig. 9). However, **probe-8a** displayed a very high sensitivity towards  $\text{Zn(II)}$  ions as compared with **probe-8b** and **8c**. The LOD value of **probe-8a** with  $\text{Zn(II)}$  ions was calculated from the equation  $3\sigma/\text{slope}$  and found to be as low as  $7 \text{ nM}$  with high sensitivity with respect to **probe-8b** and **8c**. Furthermore, confocal laser scanning micrographs of HeLa cells demonstrate that **probe-8a** has high cell permeability and can specifically recognize  $\text{Zn(II)}$  ions in living cells.

Wang and colleagues developed quinoline-conjugated fluorescent turn-on **probe-9** that is simple, quick to

respond, and highly selective for  $\text{Zn(II)}$  ions<sup>69</sup> in 2021. **Probe-9** was synthesized *via* condensation of 2-quinolinecarboxaldehyde and 2-picolinyl hydrazide. The native state of **probe-9** showed very low emission, whereas the rapid amplification of luminescence intensity was observed on complexation with  $\text{Zn(II)}$  ions, which could be explained by the effective suppression of PET. Thus, the CHEF effect improves the molecule's planarity and stiffness by limiting free rotation (Fig. 10). Further, **probe-9** was also utilized as a fluorescent probe for detecting  $\text{Zn(II)}$  ions across a wide pH range. The binding ability and mechanism was determined by Job's plot analysis, FT-IR spectrum, and  $^1\text{H}$  NMR titration. Furthermore, **probe-9** is being developed into test strips for quick, convenient, quantitative, and qualitative  $\text{Zn(II)}$  ion determination. On the basis of the IUPAC guideline for  $\text{Zn(II)}$  ions, the detection limit of the probe is particularly essential in the field of supramolecular chemistry, and the authors determined the limit of detection using the equation of  $3\sigma/\text{slope}$  to be  $72 \text{ nM}$ , which is much lesser than that of IUPAC recommendation. Further, the binding constant of **probe-9** with  $\text{Zn(II)}$  ions was calculated to be  $6.65 \times 10^3 \text{ M}^{-1}$  using the B–H equation.

Gorden and co-workers successfully synthesized and characterized a pentadentate Schiff base ligand (**probe-10**)<sup>70</sup> in 2019, which has the ability to act as a fluorescent turn-on probe for  $\text{Zn(II)}$  ions. **Probe-10** was synthesized *via* a simple condensation reaction between 3,5-di-*tert*-butyl-2-hydroxybenzaldehyde and pyridine-2,6-diylidimethanamine in EtOH under reflux conditions. The synthesized **probe-10** was very poorly emissive in nature, and upon adding  $\text{Zn(II)}$  ions, there was an enhancement in the emission and the quantum yields increased by 1.6% (Fig. 11). However, under similar conditions, no change or very minimal changes were perceived for other competitive metal ions. The titration of **probe-10** with competitive metal ions produced an unusual result in which the accumulation of heterometals such as  $\text{Ca(II)}$ ,  $\text{Mg(II)}$ ,  $\text{K(I)}$ , and  $\text{Cd(II)}$  causes an increase in emission as compared with other metal ions. The binding constant of **probe-10** with  $\text{Zn(II)}$  ions was estimated as  $1.8 \times 10^{-1} \text{ M}^{-1}$ . The

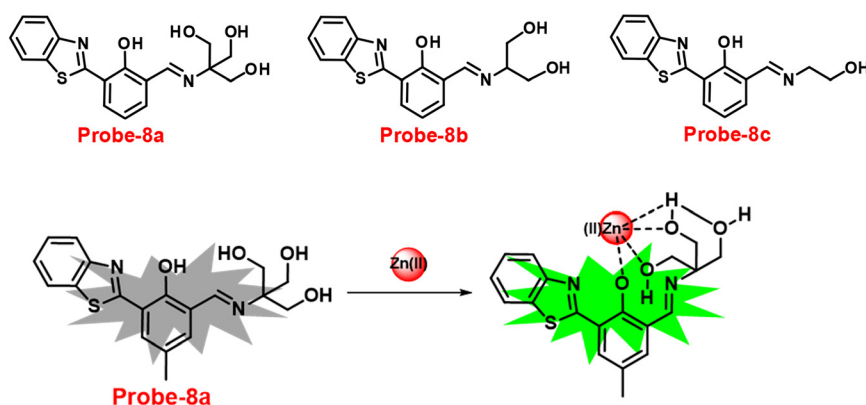


Fig. 9 Chemical structures of **probe-8(a–c)** and sensing mechanism of **probe-8a** with  $\text{Zn(II)}$  (redrawn the ChemDraw structure from ref. 68).



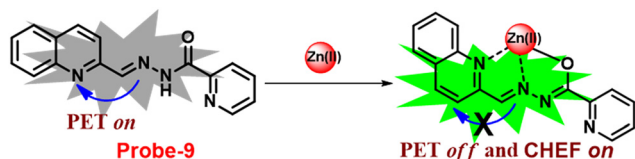


Fig. 10 Chemical structure and proposed sensing mechanism of **probe-9** with  $\text{Zn(II)}$  (redrawn the ChemDraw structure from ref. 69).

LOD of **probe-10** in the presence of  $\text{Zn(II)}$  was determined to be  $7.2 \mu\text{M}$ .

Sreekanth *et al.* developed a chemosensor with thiophene-appended carbohydrazide, which exhibits luminescence turn-on recognition for  $\text{Zn(II)}$  ions *via* the CHEF process<sup>71</sup> in 2021. **Probe-11** (Fig. 12) was produced *via* a simple condensation reaction of thiophene-2,5-dicarbohydrazide and 2-hydroxynaphthaldehyde in EtOH under reflux conditions, yielding a yellow colour solid. Fluorescence titration data revealed that in the presence of other metal ions, no changes in fluorescence spectra were observed even at very high concentrations, whereas upon addition of  $\text{Zn(II)}$  ions, the emission intensity was gradually increased. The LOD of **probe-11** with  $\text{Zn(II)}$  ions was estimated to be  $0.15 \mu\text{M}$  using the  $3\sigma/\text{slope}$  method from fluorescence spectra, and the association constant was calculated using the B-H equation to be  $1.15 \times 10^4 \text{ M}^{-1}$ . The stoichiometry of **probe-11** with  $\text{Zn(II)}$  was estimated to be 1:1 using Job's plot. Further, the binding interaction and fluorescence turn-on response of **probe-11** with  $\text{Zn(II)}$  ions were strongly held by the DFT calculations. The reversibility of **probe-11** +  $\text{Zn(II)}$  was studied using EDTA, producing a better output, which was then converted into a logic circuit. The remarkable properties of **probe-11** can be used to detect  $\text{Zn(II)}$  ions in both biological and environmental samples.

Roy *et al.* synthesized two Schiff base compounds named **Probe-12a** and **Probe-12b** *via* the condensation reaction of 2-hydrazinylquinoline with 2-hydroxy-5-methylbenzaldehyde and 2-hydroxy-benzaldehyde respectively<sup>72</sup> in 2019. **Probe-12a** and **probe-12b** are as very sensitive and selective towards  $\text{Zn(II)}$  ions; however, their sensing abilities vary from each other, for example, upon addition of one equivalent of  $\text{Zn(II)}$  ions, the emission intensity of **probe-12a** at 490 nm was enriched by 4.5-fold upon excitation at 410 nm, whereas **probe-12b** exhibited the increment of fluorescence intensity by 30 folds upon excitation at 515 nm due to the suppression

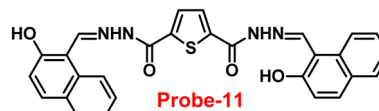


Fig. 12 Chemical structure of **probe-11** (redrawn the ChemDraw structure from ref. 71).

of PET process (Fig. 13). The more sensing ability of **probe-12b** might be attributed to the existence of the methyl group, and thus, **probe-12b** acts as better luminescent probe for  $\text{Zn(II)}$  ions. Further, the authors demonstrated the interaction of several competitive metal ions and the results suggest that there was no change observed in the fluorescence spectra. The binding constant and limit of detection of **probe-12b** with  $\text{Zn(II)}$  ions were estimated from the emission titration spectra *via* the B-H and  $3\sigma/\text{slope}$  equation respectively and found to be  $5.90 \times 10^4 \text{ M}^{-1}$  and  $220.6 \text{ nM}$  correspondingly. Furthermore, the authors tested **probe-12b** in a practical application, detecting  $\text{Zn(II)}$  in water using the dip strike method, and the results indicated that **probe-12b** could be a potential candidate for detecting  $\text{Zn(II)}$  ions in solid state as well. Finally,  $\text{Zn(II)}$  ions were detected in biological samples using **probe-12b**, which was incubated with C6 cells, and upon treatment with  $\text{Zn(II)}$  ions, the probe showed strong green colour fluorescence enhancement inside the cells. As a result, **probe-12b** was identified as a possible candidate for detecting  $\text{Zn(II)}$  ions in both environmental and biological samples.

It is critical to investigate the variations in  $\text{Zn(II)}$  ion levels in clinical, medical, and environmental circles. Taking this into account, Shen and his colleagues synthesized biocompatible and tissue permeable dual-channel fluorescent off-on Schiff base **probe-13** for  $\text{Zn(II)}$  ions<sup>73</sup> in 2021. When exposed to  $\text{Zn(II)}$ , **probe-13** produced a blue luminescence signal (455 nm) due to the suppression of PET process, and upon addition of various competitive metal ions, no change in fluorescence spectra was observed, which strongly demonstrated that **probe-13** is ideal for the detection of  $\text{Zn(II)}$  ions (Fig. 14). Further, authors evaluated the applications of **probe-13** for the detection of  $\text{Zn(II)}$  ions in biological samples *via* bio-imaging on live cells, larval zebrafish, and plants. **Probe-13** has a LOD of  $56 \text{ nM}$  for  $\text{Zn(II)}$ , which was calculated from the fluorescence spectra. Further, authors performed

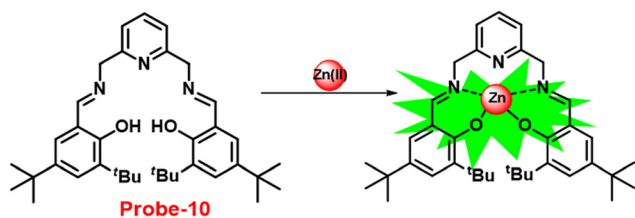


Fig. 11 Chemical structure and proposed sensing mechanism of **probe-10** with  $\text{Zn(II)}$  (redrawn the ChemDraw structure from ref. 70).

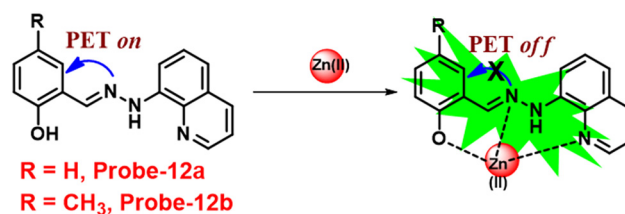


Fig. 13 Chemical structure and proposed sensing mechanism of **probe-12a-b** with  $\text{Zn(II)}$  (redrawn the ChemDraw structure from ref. 72).





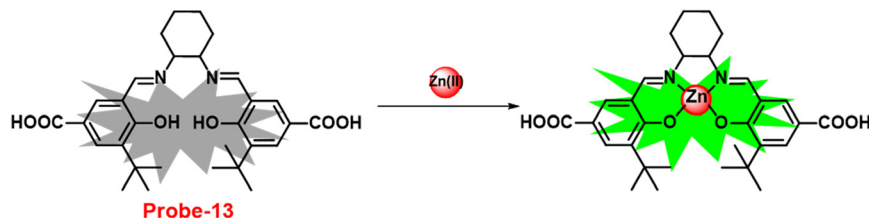


Fig. 14 Chemical structure and proposed sensing mechanism of **probe-13** with Zn(II) (redrawn the ChemDraw structure from ref. 73).

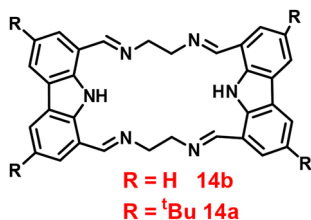


Fig. 15 Chemical structure of **probe-14a** and **probe-14b**.

the sensitive response characterization in the pH range of 7.0 to 9.4 ( $pK_a = 8.40$ ). Furthermore, **probe-13** is the best because of its great stability and reversibility, which may be used to detect Zn(II) ions in environmental and biological materials.

Brooker *et al.* reported the first excursion into the new generations of innovative macrocyclic-based Schiff bases in 2018 *via* a simple condensation reaction between carbazole-dialdehyde and ethylene diamine and created [2 + 2] Schiff base macrocycles.<sup>74</sup> Authors mainly focused on the synthesis of two **probes** (**14a** and **14b**) (Fig. 15), which show selectivity as well as sensitivity, and can also be utilized as powerful turn-on blue luminescent sensors for Zn(II) ions in DMF at 335 nm, which might be attributed to the enhancement of CHEF and suppression of PET. In the presence of other competitive metal ions, **probe-14a** as well as **14b** shows no change or very minimal change in the fluorescence spectra, which strongly suggested that the **probes** are potential for the recognition of Zn(II) ions, on addition of other metal ions. The detection limits of **probes** with Zn(II) ions were calculated to be in the nanomolar range *via* fluorescence titration spectra. Further, the binding ability of **probes** towards Zn(II) ions were validated *via* <sup>1</sup>H NMR, ESI and DFT calculations.

An ESIPT-based 2-(20-aminophenyl)benzothiazole derivative, **probe-15**, as the fluorescent turn-on probe, was synthesized by Thennaraasu and coworkers in 2016.<sup>75</sup> The effect of Zn(II) ions on ESIPT inhibition was examined by

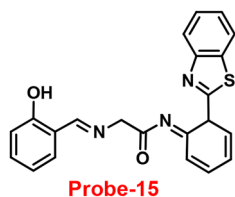


Fig. 16 Chemical structure of **probe-15**.

evaluating the absorbance and fluorescence spectra of **probe-15** (Fig. 16), and the results strongly suggested that the fluorescence band of **probe-15** changed from 556 nm to 459 nm with enhanced fluorescence signals. However, in the presence of competitive metal ions (10 eq.), **probe-15** displayed no or very little fluorescence changes. From the above-mentioned results, one can conclude that only Zn(II) ions caused a noteworthy change in the fluorescence profiles of **probe-15**, while no other metal ions caused significant variations and could be applied as potential candidates for Zn(II) ions with other competitive metal ions. Furthermore, in order to know the binding mode and fluorescence enhancement of **probe-15** with Zn(II) ions, authors conducted FT-IR, DFT, and <sup>1</sup>H-NMR studies, which strongly supported the contribution of -NH-, -CH=N-, and -OH groups in ESIPT and -C=N- isomerization processes, which were suppressed upon binding with Zn(II) ions, resulting in fluorescence improvement. In addition, the stoichiometric ratio of **probe-15** with Zn(II) ions was calculated *via* Job's plot to be 1:1, which was further confirmed by ESI-mass data. The LOD of **probe-15** with Zn(II) ions was estimated to be 4.5 nM by the 3 $\sigma$ /slope method. Further, the binding constant was estimated by the B-H method to be  $2.4 \times 10^4 \text{ M}^{-1}$ . **Probe-15** demonstrated very good thermal stability and the decomposition of the **probe-15**-Zn(II) complex was found to be very minimal (1.15%) at a temperature of 259.38 °C, which endows **probe-15** with the potential for the detection of environmental samples.

Coumarin is a phytochemical, and a majority of its conjugates have a diverse range of pharmacological effects, which make it useful in biology due to its less cytotoxicity. A Schiff base-based probe (**probe-16**) was obtained by condensation of 1,2-bis(2-aminophenylthio) ethane with 8-formyl-7-hydroxy-4-methylcoumarin by Sinha *et al.* in 2016.<sup>76</sup> In the presence of Zn(II) ions with **probe-16**, the emission intensity was increased at 514 nm, while it is

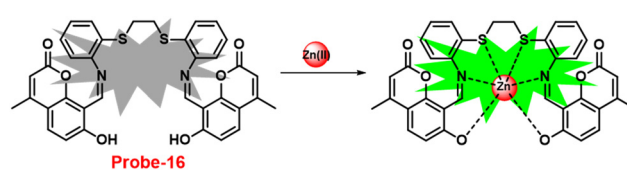


Fig. 17 Chemical structure and proposed sensing mechanism of **probe-16** with Zn(II) (redrawn the ChemDraw structure from ref. 76).

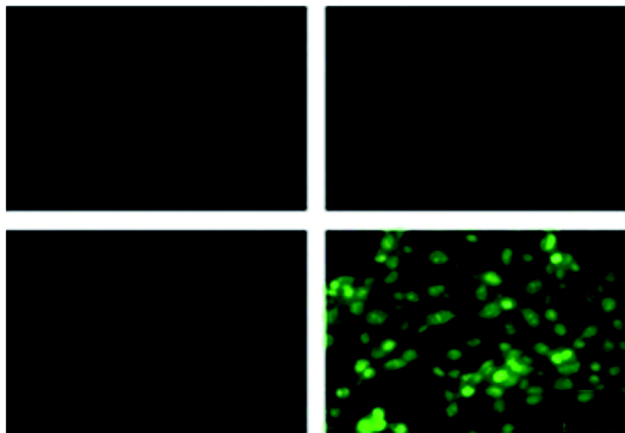


Fig. 18 Fluorescence microscopic images of SCC084 (human oral carcinoma) with **probe-16** and Zn(II) ions + **probe-16** (reprinted with permission from ref. 76, Copyright 2016 Royal Society of Chemistry).

unresponsive to other cations. The binding mechanism of **probe-16** with Zn(II) ions was explained by the restriction of ESIPT and CHEF (Fig. 17). The association constant of **probe-16** with Zn(II) is  $6.49 \times 10^4 \text{ M}^{-1}$  by the B-H method and the  $3\sigma/\text{slope}$  method was used to estimate the LOD of Zn(II) ions, which was found to be as minimal as  $0.068 \mu\text{M}$ . The **probe-16** showed lower cytotoxicity, which suggests that **probe-16** has a potential application for the *in vitro* and *in vivo* recognition of Zn(II) ions. The authors performed the bio-imaging on SCC084 (human oral carcinoma) cells for the sensing of Zn(II) ions and the whole cell line emission enhancement was obtained, which demonstrated the potential of **probe-16** for the recognition of Zn(II) ions in a cellular medium (Fig. 18).

A flexible ligand, *N*1,*N*3-bis(3-methoxysalicylidene) diethylenetriamine (**probe-17**),<sup>77</sup> was successfully synthesized by Goswami and coworkers in 2017, which gave various coordination modes to give trinuclear Zn complexes with  $\text{Zn}(\text{NO}_3)_2 \cdot 6\text{H}_2\text{O}$ ,  $\text{ZnBr}_2$ , and  $\text{ZnI}_2$ . All the synthesized compounds were structurally characterized by multinuclear NMR, FT-IR spectroscopy, elemental analysis (EA) and single-crystal XRD analysis. The authors performed the fluorescence spectroscopic techniques to understand the sensing potential of **probe-17** (Fig. 19), and the results established great sensitivity and selectivity towards Zn(II) ions in aqueous solutions at pH 7.4. The emission intensity was increased by 19-fold with maxima at 467 nm when different amounts of

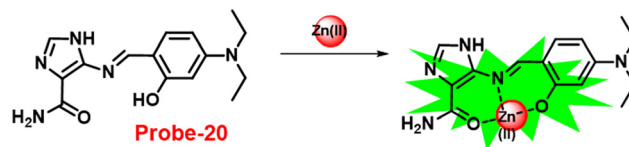


Fig. 20 Chemical structure and proposed sensing mechanism of **probe-20** with Zn(II) (redrawn the ChemDraw structure from ref. 80).

Zn(II) were added, whereas no or minimal difference was found for the other metal ions. The binding ability and fluorescence enhancement ability could be attributed to the CHEF, which occurs when **probe-17** binds to Zn(II) ions and forms intramolecular hydrogen bonds among phenolic OH and amine nitrogen, allowing for ESIPT. Further, **probe-17** serves as a dependable sensor with a LOD in the nanomolar range ( $6.72 \text{ nM}$ ), and it is utilized for imaging in HCT 116 cells for the real-time monitoring. The binding constant of **probe-17** with Zn(II) was estimated using the B-H equation and displayed as  $31.647 \times 10^4 \text{ M}^{-1}$ . The binding ratio of **probe-17** with Zn(II) ions was estimated with Job's plot and found out to be 1:1, which was strongly validated by ESI-MS and DFT calculations. In addition, the complex-Zn(II) turned out to detect pyrophosphate (PPi) with among all other phosphates in an aqueous medium with both chromogenic and fluorogenic response with a LOD of  $5.12 \text{ nM}$ .

Sahoo *et al.* designed Schiff base-based **probe-18** (Fig. 19) by the condensation of vitamin B6 cofactor pyridoxal with the 1-pyrenemethylamine, which functions as a three-in-one sensor for three bioactive analytes with the recognition unit being pyrene fluorophore and the vitamin B6 cofactor pyridoxal<sup>78</sup> in 2018. The structural characterization of target compound (**probe-18**) was established by  $^1\text{H-NMR}$ , attenuated total reflectance-Fourier transform infrared spectroscopy (ATR-FTIR), HRMS, and EA. When the fluorescence spectra were acquired, **probe-18** showed significant fluorescence amplification at 485 nm when Zn(II) ions were added. Furthermore, fluorescence titration experiments of **probe-18** with gradual incremental addition of Zn(II) caused in the **probe-18**'s luminescence was increased vertically and a new band arising at 485 nm. However, in the presence of other metal ions, **probe-18** resulted in very minimal or no response in fluorescence spectra. The suppression of the PET mechanism, in which the transfer of a lone pair of electrons from the nitrogen atom ( $-\text{C}=\text{N}-$ ) to the pyrene fluorophore in the excited state is hampered by binding with Zn(II), could

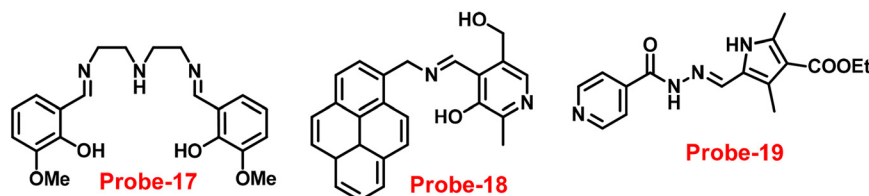


Fig. 19 Chemical structures of **probe-17-19** (redrawn the ChemDraw structure from ref. 77-79).



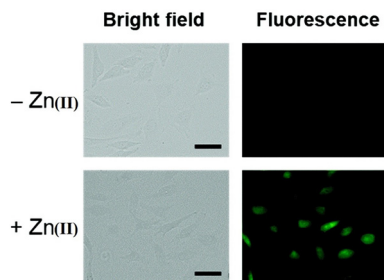


Fig. 21 Fluorescence imaging of HeLa cells incubated with **probe-20** followed by the addition of Zn(II) (reprinted with permission from ref. 80, Copyright 2019 Royal Society of Chemistry).

explain this vertical amplification of bands. Interestingly, **probe-18** detects three essential bioactive analytes Zn(II),  $\text{H}_2\text{PO}_4^-$ , and cysteine, with LOD values of 2.3  $\mu\text{M}$ , 0.21  $\mu\text{M}$ , and 0.16  $\mu\text{M}$ , respectively. *In vitro* cellular imaging was also used to detect intracellular Zn(II) ions using **probe-18**. Further, **probe-18** was utilized in recognition of Zn(II) ions in HeLa cells. Hence, based on the efficacy of **probe-18**, it can be applied for the recognition of Zn(II) ions in biological and environmental samples.

Schiff base with pyrrole units is a versatile chelating combination that has received a lot of attention, in this regard, Wang and colleagues designed and synthesized a hydrazone with a pyrrole unit, **probe-19**, (Fig. 19) for the selective and sensitive detection with the luminescence turn-on mechanism of Zn(II) ions in 2018.<sup>79</sup> The target compound was obtained upon condensation reaction with ethyl 5-formyl-2,4-dimethyl-pyrrole-3-carboxylate and isonicotinohydrazide in ethanol under reflux conditions. **Probe-19** was structurally characterised *via* multinuclear NMR, ESI-MS, and EA. **Probe-19** displayed poor emission in the native state and in the presence of Zn(II) ions, the emission intensity was enhanced at 550 nm with moderately high quantum yields due to the presence of CHEF process. **Probe-19** exhibited very low LOD for Zn(II) ions, for example, 0.18  $\mu\text{M}$ , which was calculated by the  $3\sigma/\text{slope}$  method. Job's plot was established using fluorescence spectra that showed a 1:1 stoichiometry for **probe-19** with Zn(II) ions and a binding constant ( $K_a$ ) of  $1.25 \times 10^4 \text{ M}^{-1}$ . Due to the presence of very low detection limit, **probe-19** was applied for the real-time monitoring of Zn(II) ions in imaging intracellular cells. Further, **probe-19** shows potential for application in the

detection of biological samples, which was performed on U251 cell lines. The cells were treated with **probe-19** and showed no fluorescence, whereas upon incorporation with the Zn(II) ions, the color changed into strong green color fluorescence inside the cell line.

Kim *et al.* synthesized highly potential **probe-20** based on the imidazole derivative in 2019,<sup>80</sup> which shows luminescence turn on-off detection of Zn(II) and  $\text{S}^{2-}$  ions with very low LOD values of 1.59  $\mu\text{M}$  and 8.03  $\mu\text{M}$ , correspondingly. The synthesis of the target compound was followed by a very simple condensation reaction between (4-amino-4(5)-(aminocarbonyl)imidazole hydrochloride and 4-diethylaminosalicylaldehyde in MeOH under reflux conditions. The native state of **probe-20** exhibited very poor emission as a result of PET and upon addition of Zn(II) ion fluorescence enrichment was observed, which was attributed to the suppression of PET and CHEF (Fig. 20). To find out the stoichiometry of **probe-20** with Zn(II) ions, authors performed Job's plot and results discovered the 1:1 binding ratio. The fluorescence changes of **probe-20** for Zn(II) were investigated further to rule out the interference of other cations, whereas the fluorescence quenching was caused by Fe(III), Cu(II), Cr(III), Fe(II), and Co(II) (78–100%), and competitive metal ion shows no change in the fluorescence spectra. The binding constant of **probe-20** with Zn(II) ions was calculated from the fluorescence spectra using B–H equation as  $2.0 \times 10^3 \text{ M}^{-1}$ . **Probe-20** displayed good reversibility with EDTA, which extends its real-time applicability and also in live cell imaging (Fig. 21).

Ghosh and his colleagues developed an iminophenol probe (**probe-21**)<sup>81</sup> with 1,2,3-triazole in the proximal position that exhibits a significant increase in emission upon interaction with Zn(II) ions as compared with other metal ions in 2021. The authors proposed the sensing mechanism responsible for fluorescence turn-on, which is the chelation of Zn(II) ions in the Schiff base core. From Job's plots, the binding ratio of **probe-21** (Fig. 22) and Zn(II) ions was estimated to be 1:1, which was established *via* ESI-MS and DFT studies. The binding constant was calculated from the equation of B–H to be  $9.06 \times 10^4 \text{ M}^{-1}$ . The LOD was determined using fluorescence titration as 1.8  $\mu\text{M}$ . Moreover, picric acid (PA) was successfully detected by a zinc-ensemble over a series of other nitroaromatics and was confirmed by DFT studies. Yang and co-workers synthesized a simple probe (**probe-22**)<sup>82</sup> from 4-diethylaminosalicylaldehyde and

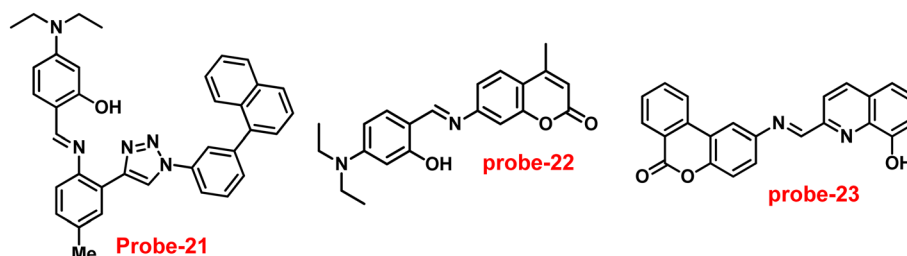


Fig. 22 Chemical structures of **probe-21–23** (redrawn the ChemDraw structure from ref. 81–83).





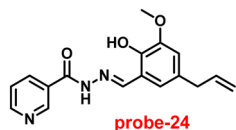


Fig. 23 Chemical structure of **probe-24** (redrawn the ChemDraw structure from ref. 84).

7-amino-4-methyl coumarin, which acts as a selective and sensitive probe for Zn(II) ions in 2016. **Probe-22** (Fig. 22) was found to be very poorly emissive in nature and an increase in emission was observed at 500 nm with Zn(II) ions, increasing the quantum yields ( $\phi = 0.1651$ ). Though, upon addition of other metal ions, there was no change in the fluorescence spectra specifying **probe-22** was very selective to Zn(II) ions. Further, the fluorescence enhancement might be attributed to the suppression of C=N isomerization and the inhibition of PET. The binding ratio among **probe-22** and Zn(II) ions was calculated using Job's plot as 2:1 and was strongly held by ESI-MS,  $^1\text{H}$  NMR, and DFT calculations. Furthermore, the LOD and the binding constant of **probe-22** with Zn(II) ions were found as  $\log K = 6.04$  and  $2.59 \mu\text{M}$ , respectively. Since, **probe-22** has a moderately high association constant with Zn(II) ions and a low detection limit, it could be applicable to biological and environmental samples.

Singh *et al.* focused on dual coumarin-based Schiff base **probe-23** (ref. 83) for the selective and sensitive detection of Zn(II) ions in 2016. **Probe-23** (Fig. 22) was synthesized *via* a simple condensation reaction between 6-amino-3,4-benzocoumarin and 8-hydroxy quinolone-2-carboxaldehyde in ethanol under reflux conditions. The titration of **probe-23** was conducted using a UV-visible and fluorescence spectrophotometer, and the results indicated a colorimetric response towards Fe(III) and a fluorescence turn-on behavior for Zn(II) ions. The emission turn-on mechanism might be due to the presence of strong complexation *via* O and N heteroatoms, which resulted in an increase in the radiative decay as well as suppression of PET and *cis-trans* isomerism. The B-H relation was used to calculate the binding constant as  $3.8 \times 10^3 \text{ M}^{-1}$ . The LOD of **probe-23** with Zn(II) ions was

calculated from the fluorescence titration spectra *via* the  $3\sigma$ /slope method and showed to be  $10 \mu\text{M}$ . The binding ratio of **probe-23** and Zn(II) was calculated from Job's plot as 1:1. The reversible studies of **probe-23** + Zn(II) were conducted with EDTA and the restored **probe-23**, which is again utilized for the detection of Zn(II) ions. Furthermore, **probe-23**'s fluorescence emission response can be examined as a binary logic function.

Kuwar and colleagues designed and synthesized nicotin-based Schiff base **probe-24**, which showed very selective and sensitive nature towards Zn(II) ions in 2018.<sup>84</sup> The pure form of **probe-24** (Fig. 23) displayed very poor emission due to the presence of *cis-trans* isomerism and PET, which was suppressed by CHEF effects upon addition of Zn(II) ions; as a result, a substantial enrichment of emission at 517 nm in a binary mixture of acetonitrile/water (50:50, v/v) was detected. However, in the presence of other metal ions, there was no or minimal fluorescence changes observed. Further, authors determined the detection limit *via* fluorescence titration spectra to be  $4.35 \text{ nM}$ . The binding constant of **probe-24** and Zn(II) was estimated by non-linear curve fitting of the fluorescence titration spectra and found to be  $\log K = 5.63$  (0.15). Further, stoichiometry was determined from Job's plot, and the results were exhibited to be 1:1. Finally, authors conducted the cytotoxicity of **probe-24** on A549 cells, and the results indicated very low toxicity, which strongly supported the use of **probe-24** to monitor Zn(II) ions in biological samples (Fig. 24).

A single molecular structure of imine was designed by Kim *et al.* from 5-methylisoxazole-3-amine and 2-hydroxy-1-naphthaldehyde, which contains an imine as a chromophore and a naphthol group as a fluorophore in 2019.<sup>85</sup> The native state of **probe-25** was poorly emissive in nature; on titrating with Zn(II) ions, the emission intensity was gradually increased, which attributed to the CHEF effect (Fig. 25). However, upon introduction of other competitive metal ions to **probe-25**, there was no change in fluorescence spectra, which strongly suggested the very selectivity towards Zn(II) ions. Job's plot supported the 1:1 binding of **probe-25** with Zn(II), which was strongly supported by the ESI-MS, DFT and

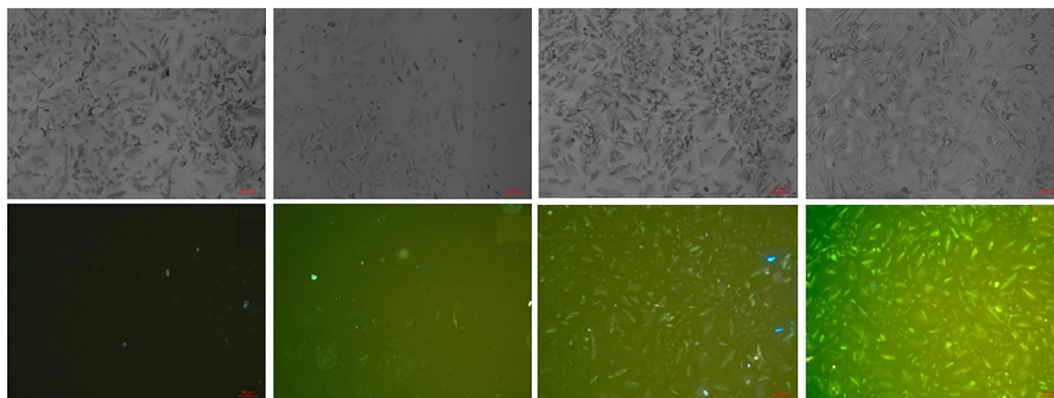


Fig. 24 Bioimaging study images of **probe-24** on A549 cells with Zn(II) ions (reprinted with permission from ref. 84, Copyright 2018 Elsevier).



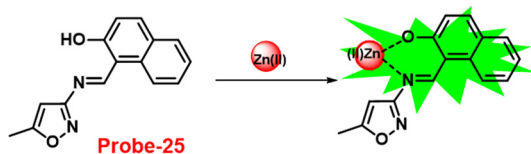


Fig. 25 Chemical structure and proposed sensing mechanism of probe-25 with Zn(II) (redrawn the ChemDraw structure from ref. 85).

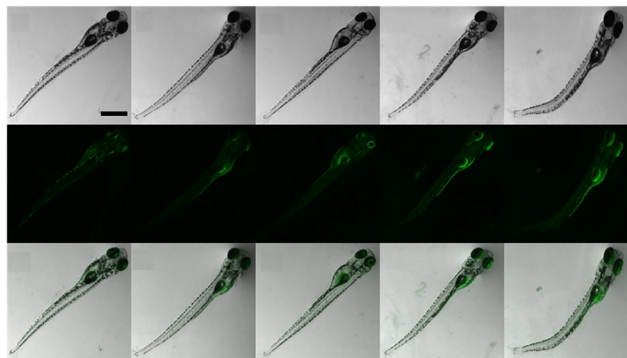


Fig. 26 Bioimaging study images of probe-25 on zebrafish with Zn(II) ions (reprinted with permission from ref. 85, Copyright 2019 Elsevier).

$^1\text{H}$  NMR data. The LOD and association constant of probe-25 with Zn(II) were evaluated from the fluorescence titration spectra as  $1.29\ \mu\text{M}$  and  $7.9 \times 10^4\ \text{M}^{-1}$  respectively. Further, authors performed the recognition of Zn(II) ions in biological applications; for this, Zebrafish was incubated with probe-25 and data supported that strong luminescence was generated inside the Zebrafish (Fig. 26).

In 2018, Yang and colleagues developed new fluorescent probe-26 with rhodamine and chromone moieties as a fluorescent “turn-on” probe for Zn(II) ions that works via inhibited PET<sup>86</sup> (Fig. 27). When Zn(II) is added to probe-26, the emission intensity at 490 nm increases in an ethanol/HEPES solution (7/3, pH = 7.2). Further, the authors determined the stoichiometry between probe-26 and Zn(II) ions to be 1:1 via Job's plot, which was supported by ESI-MS,  $^1\text{H}$  NMR and DFT data. The LOD and association constants were calculated using fluorescence titration data and reported as  $0.33\ \mu\text{M}$  and  $9.98 \times 10^4\ \text{M}^{-1}$  correspondingly. Finally, the authors used probe-26 in a practical application, such as test strips, and developed a practical, efficient, and low-cost Zn(II) ion testing tool.

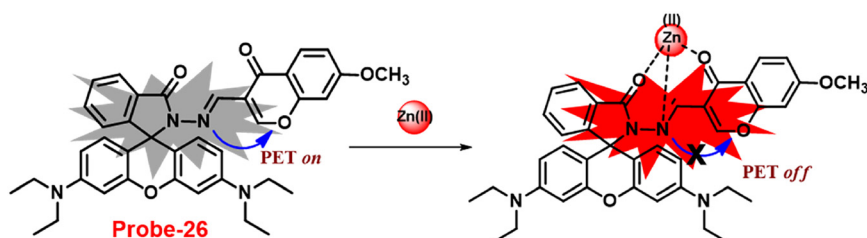


Fig. 27 Chemical structure and proposed sensing mechanism of probe-26 with Zn(II) (redrawn the ChemDraw structure from ref. 86).

In 2018, Viswanthamurthi *et al.* established a powerful tracker for Zn(II) and PPI ions in biological systems by appending benzoxazole to dipodal Schiff base (probe-27).<sup>87</sup> Probe-27 was synthesized from benzoxazole, which underwent a double Duff reaction followed by the reaction with isonicotinic hydrazide in a methanol solution at room temperature and gave the final product as a yellow coloured solid. When probe-27 was titrated with Zn(II) ions, the emission intensity progressively increased and attained maxima upon addition of one eq. via the ICT mechanism (Fig. 28). However, upon addition of competitive metal ions, there was no difference in the fluorescence profile, which strongly supports the selectivity of probe-27 towards Zn(II) ions. Fluorescence titrations were used to determine the LOD and binding value ( $K_a$ ) of the probe-27-Zn(II) complex, which were  $0.52\ \mu\text{M}$  and  $4.53 \times 10^4\ \text{M}^{-1}$  respectively. Further, authors determined the complexation ratio between probe-27 and Zn(II) ions to be 1:1 via Job's plot, which was further supported by ESI-MS,  $^1\text{H}$  NMR and DFT results. Furthermore, the emission intensity at 525 nm of the probe-27-Zn(II) ensemble was reduced dramatically upon addition of a  $100\ \mu\text{M}$  solution of PPI anions, but remained stable for other anions, which showed the potential of probe-27 to detect both the biologically important metal ions (Zn(II)) and anion (PPI) (Fig. 29).

Pu and co-workers reported a fast response diarylethene derivative containing phenoxyaniline and Schiff base (probe-28),<sup>88</sup> which exhibited the fluorescence “turn-on” mechanism for the recognition of Zn(II) ions in 2019. Probe-28 was titrated with several metal ions including Zn(II) ions and upon addition of Zn(II) ions, the emission intensity was gradually increased to 105 times at 582 nm and the fluorescence color has changed from non-fluorescence to bright yellow due to the suppression of C=N isomerization and CHEF (Fig. 30). However, no difference was detected in fluorescence spectra of probe-28 in the presence of other metal ions. Job's plot analysis and HRMS revealed a 1:1 binding stoichiometry for probe-28 and Zn(II) ions. Furthermore, probe-28 was successfully demonstrated for the analysis of real-time applications due to the presence of very low detection limits such as  $13.4\ \text{nM}$ . The fluorescence titration data yields a binding constant of  $3.49 \times 10^4\ \text{M}^{-1}$  from the B-H equation and gratifyingly, it could be applied to design a logic gate.



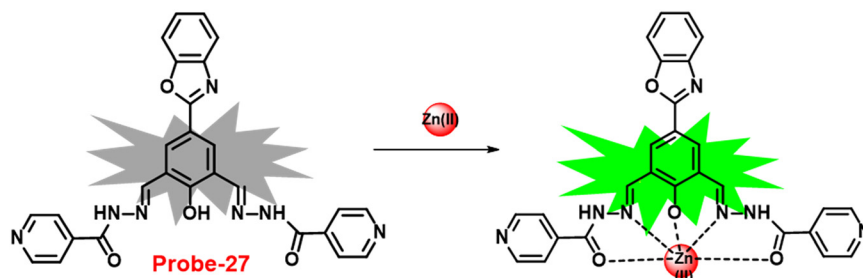


Fig. 28 Chemical structure and proposed sensing mechanism of **probe-27** with Zn(II) (redrawn the ChemDraw structure from ref. 87).

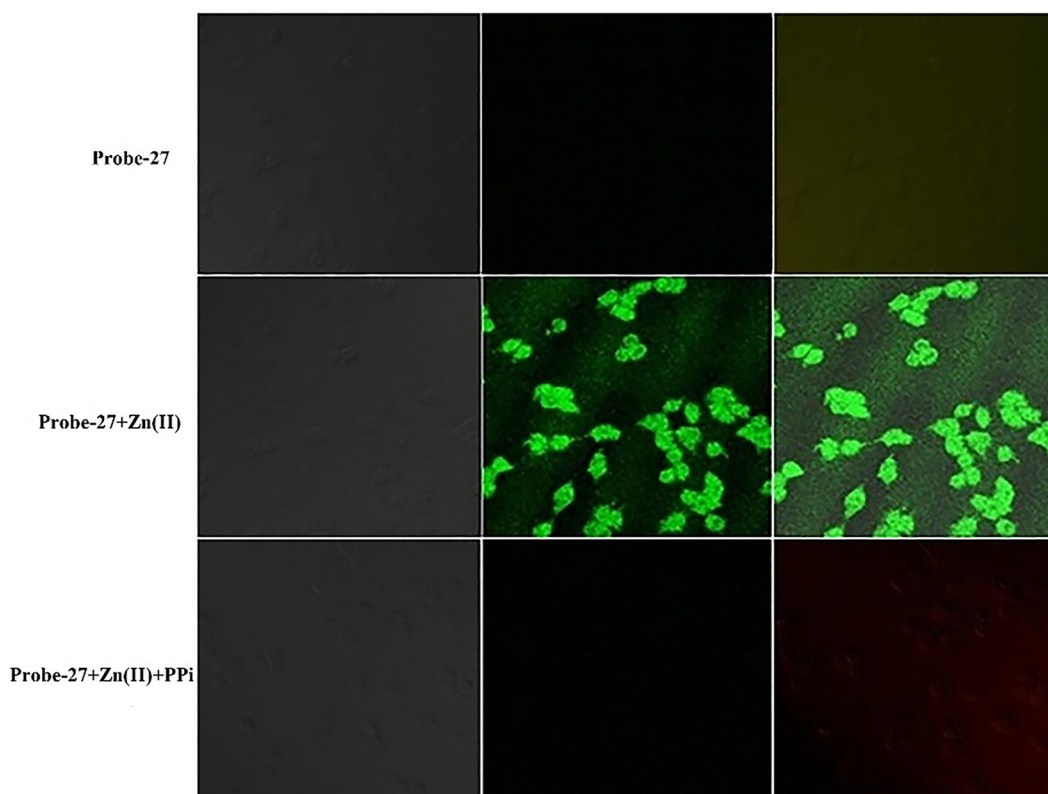


Fig. 29 Fluorescence images of cells (HeLa) treated with **probe-27**, **probe-27** + Zn(II) and **probe-27** + Zn(II) + PPI (reprinted with permission from ref. 87, Copyright 2019 Elsevier).

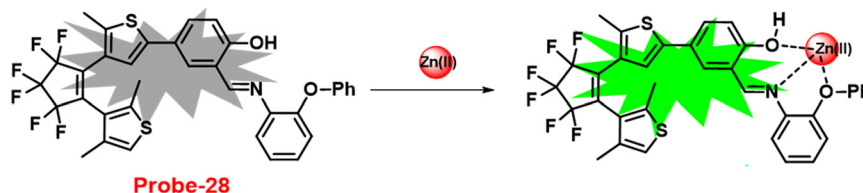


Fig. 30 Chemical structure and proposed sensing mechanism of **probe-28** with Zn(II) (redrawn the ChemDraw structure from ref. 88).

In 2019, Yang and colleagues designed an imine probe (**probe-29**)<sup>89</sup> from a 4-methyl-7-acetamide-1,8-naphthyridyl moiety and a trihydroxybenzoyl hydrazine unit that acts as a sensitive probe for Zn(II) ions *via* the fluorescence turn-on mechanism. **Probe-29** alone demonstrated weak emission, but the addition of Zn(II) resulted in the formation of a new

band centred at 504 nm with increased intensity, which attributed to the suppression of PET and CHEF process (Fig. 31). On the basis of nonlinear B-H equation from emission titration values, Job's plot method yielded a coordinative stoichiometry ratio of 2:1 with a binding constant ( $K_a$ ) of  $1.14 \times 10^5 \text{ M}^{-1}$ . The LOD of **probe-29** with





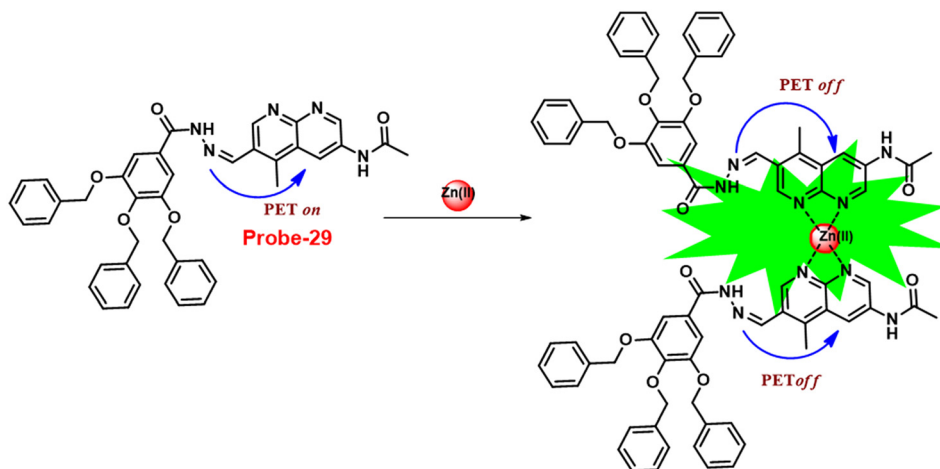


Fig. 31 Chemical structure and proposed sensing mechanism of **probe-29** with  $\text{Zn(II)}$  (redrawn the ChemDraw structure from ref. 89).

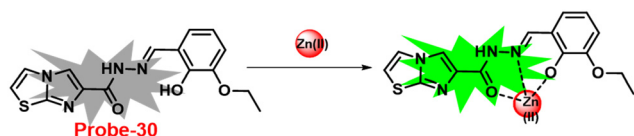


Fig. 32 Chemical structure and proposed sensing mechanism of **probe-30** with  $\text{Zn(II)}$  (redrawn the ChemDraw structure from ref. 90).

$\text{Zn(II)}$  ions was determined to be 7.52 nM. The perfect reversibility and renewability of **probe-29** for the recognition of  $\text{Zn(II)}$  was confirmed using  $\text{Na}_2\text{EDTA}$ , a chelating agent, in which the fluorescence emission of complex **probe-29**– $\text{Zn(II)}$  was significantly quenched with the addition of  $\text{Na}_2\text{EDTA}$  and can be utilized for various practical applications.

Lin and colleagues developed a Schiff base, **probe-30**, from imidazo[2,1-*b*]thiazole-6-carboxylic acid and 3-ethoxy-2-hydroxybenzaldehyde for the selective and sensitive sensing of  $\text{Zn(II)}$  *via* the fluorescence turn-on mechanism<sup>90</sup> in 2019.

**Probe-30** showed very poor emission with low emission intensity ( $\phi = 0.016$ ). However, the addition of  $\text{Zn(II)}$  ions to **probe-30** could cause a significant change in the emission intensity ( $\phi = 0.3$ ) at 511 nm, resulting in a 42-fold increase in intensity, due to the presence of CHEF process and the absence of PET (Fig. 32 and 33). **Probe-30** binds to  $\text{Zn(II)}$  in a ratio of 1:1, as confirmed by  $^1\text{H}$  NMR, DFT/TD-DFT, mass spectral analysis and Job's plot. The association constant of **probe-30** with  $\text{Zn(II)}$  ions was estimated with a nonlinear B–H as  $2.2 \times 10^5 \text{ M}^{-1}$ . The LOD was estimated using emission titration data to be 1.2 nM by the  $3\sigma/\text{slope}$  method. In contrast, this recognition process was reversible, as the fluorescence titration experiment of **probe-30**– $[\text{Zn(II)}]$  to PPI results in lower emission, which results strongly supported by regeneration of **probe-30**. Finally, authors claims that the fluorescence signals of **probe-30** were used to build a molecular INHIBIT logic gate.

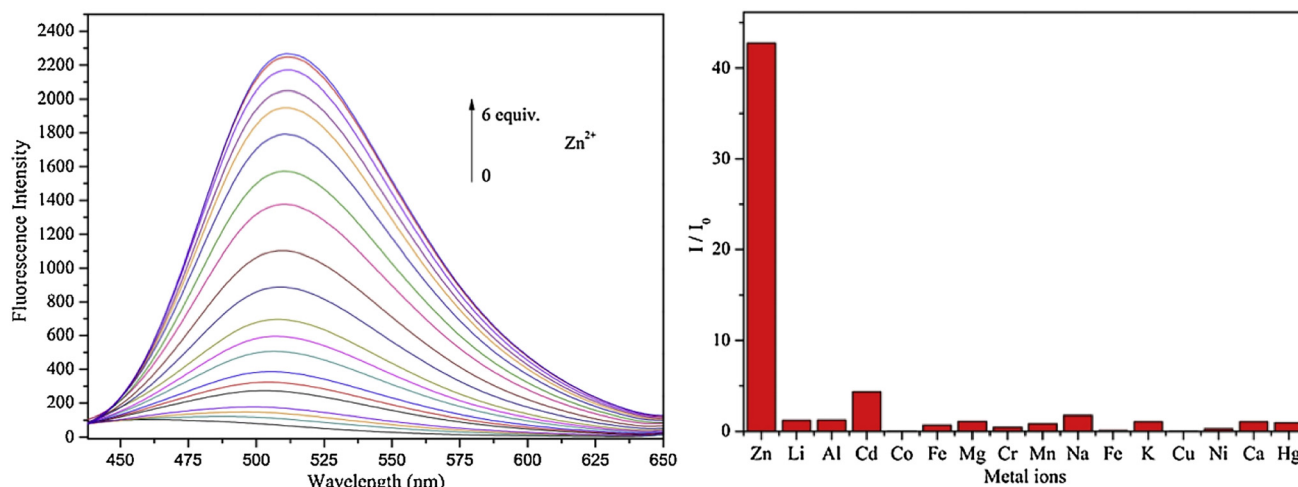


Fig. 33 Fluorescence spectra of **probe-30** with  $\text{Zn(II)}$  ions (left) and competitive binding study of **probe-30** with different metal ions (right) (reprinted with permission from ref. 90, Copyright 2019 Elsevier).



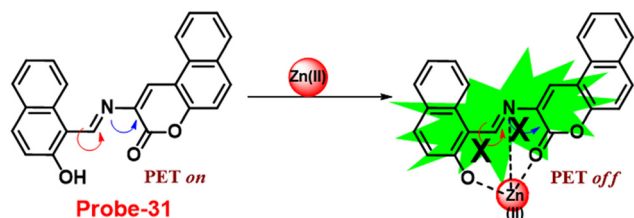


Fig. 34 Chemical structure and proposed sensing mechanism of **probe-31** with  $\text{Zn(II)}$  (redrawn the ChemDraw structure from ref. 91).

Yang and his coworkers demonstrated benzocoumarin-based single **probe-31**, which was synthesized from the 3-amino-5,6-benzocoumarin and 2-hydroxy-1-naphthaldehyde in ethanol under reflux conditions<sup>91</sup> in 2019. The native state of **probe-31** was poorly emissive in nature and showed enhancement in fluorescence emission upon addition of  $\text{Zn(II)}$  ions (Fig. 35). The LOD of **probe-31** towards  $\text{Zn(II)}$  was established as  $3.6 \mu\text{M}$  via fluorescence titration data, and the binding constant as  $3.21 \times 10^4 \text{ M}^{-1}$  using B-H equation. According to Job's plot, the stoichiometric ratio between **probe-31** and  $\text{Zn(II)}$  was 1 : 1, which was strongly supported by ESI-MS and  $^1\text{H}$  NMR. Finally, authors proposed the mechanism of fluorescence turn-on due to the complexation and simultaneous blocking of two processes, *i.e.*, PET and  $\text{C}=\text{N}$  isomerization (Fig. 34).

A Schiff-base ligand (**probe-32**) based on 2-hydroxy-5-methylisophthalaldehyde was synthesized by Saha *et al.* for the sensing of  $\text{Zn(II)}$  ions via the fluorescence turn-on mechanism in 2019.<sup>92</sup> The **probe-32** displayed very poor emission, upon addition of  $\text{Zn(II)}$  ions, the gradual increase in emission intensity and reached 16-fold after saturation (Fig. 36). The **probe-32** showed colorimetric response towards  $\text{Zn(II)}$  ions, in which color changed from light yellow to green, whereas in the presence of  $\text{Cu(II)}$  ions, it turned from light yellow to colorless. Further, authors calculated detection limits via emission titration data and found as  $1.059 \text{ nM}$  for  $\text{Zn(II)}$  ions. Further, fluorescence titration experiments, ESI-MS analysis, and DFT studies demonstrated **probe-32-Zn(II)**

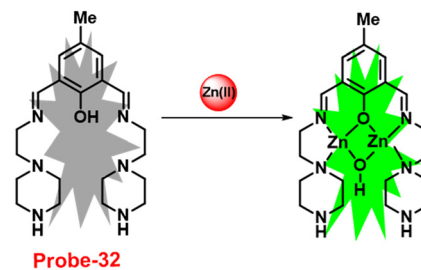


Fig. 36 Chemical structure and proposed sensing mechanism of **probe-32** with  $\text{Zn(II)}$  (redrawn the ChemDraw structure from ref. 92).

complex have 1 : 2 binding. Furthermore, the use of  $\text{Na}_2\text{EDTA}$  solution allows the **probe-32** to be fully regenerate from **probe-32** +  $\text{Zn(II)}$  complex. Finally, the authors utilized the **probe-32** for the real-time quantitative detection of  $\text{Zn(II)}$  in water samples and biological systems by a quick change in emission intensity of **probe-32** in the pH range 6–8 against  $\text{Zn(II)}$  ions. Further, the **probe-32** was subjected for the recognition of  $\text{Zn(II)}$  ions in biological samples, the authors incubated MDA-MB-468 cells which exhibited no fluorescence and upon addition of  $\text{Zn(II)}$  to cells, which generated strong green color fluorescence around cells and results strongly suggested that the **probe-32** was potential for the sensing of  $\text{Zn(II)}$  ions in biological samples (Fig. 37).

The Schiff base (**probe-33**) was synthesized by Mondal *et al.* via the condensation reaction of 3,5-dichlorosalicylaldehyde and 2,2'-(butane-1,4-diylbis(sulfanediyl))dianiline in methanol under reflux conditions in 2021.<sup>93</sup> The native state of **probe-33** (Fig. 38) exhibited very poor emission and, upon addition of  $\text{Zn(II)}$  ions, displayed fluorescence turn-on response and no difference was detected with other competitive metal ions. Fluorescence spectral titration results indicated that the LOD for  $\text{Zn(II)}$  is  $1.73 \text{ nM}$ , which is much lesser as compared with the WHO recommended level. Further, the authors, calculated the association constant of **probe-33** with  $\text{Zn(II)}$  ions from the titration data and found as  $6.91 \times 10^4 \text{ M}^{-1}$ . The reversibility of **probe-33** was performed using the EDTA as

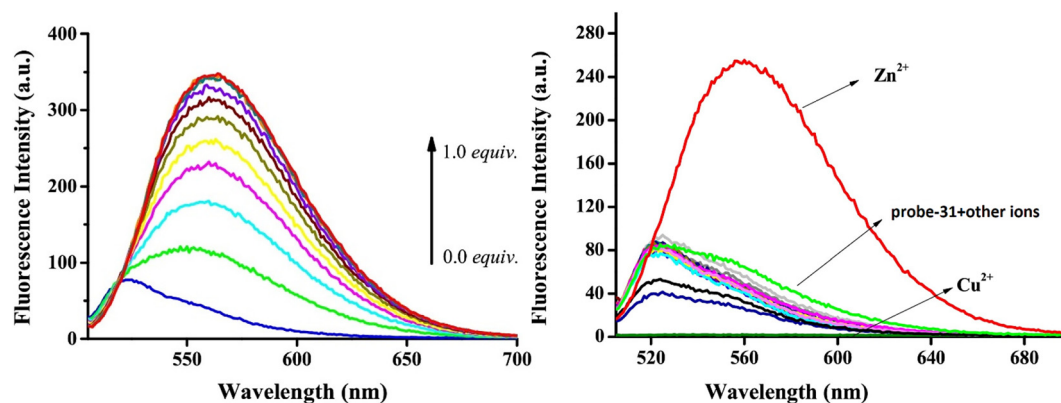


Fig. 35 Fluorescence spectra of **probe-31** with incremental addition of  $\text{Zn(II)}$  ions (left) and fluorescence spectra of **probe-31** in the presence of different metal ions (right) (reprinted with permission from ref. 91, Copyright 2019 Elsevier).



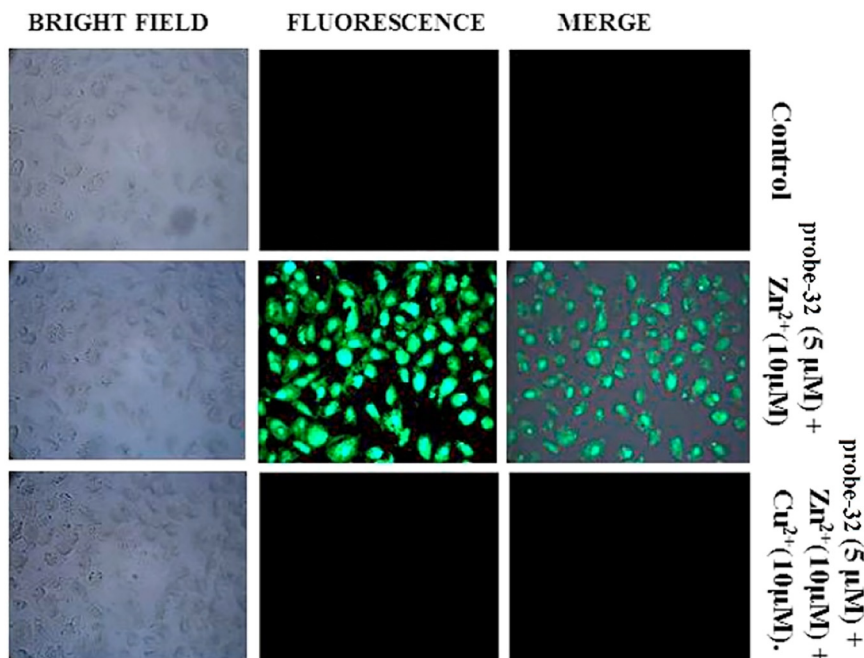


Fig. 37 Bio-imaging images of untreated MDA-MB-468 (control), cells treated with **probe-32** (5  $\mu\text{M}$ ) +  $\text{Zn}(\text{II})$  (10  $\mu\text{M}$ ) and with **probe-32** (5  $\mu\text{M}$ ) +  $\text{Zn}(\text{II})$  (10  $\mu\text{M}$ ) +  $\text{Cu}(\text{II})$  (10  $\mu\text{M}$ ) (reprinted with permission from ref. 92, Copyright 2019 Elsevier).

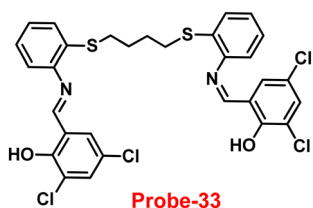


Fig. 38 Chemical structure of **probe-33** (redrawn the ChemDraw structure from ref. 93).

chemical inputs, an INHIBIT logic gate was built and regeneration of **probe-33** was observed. Job's plot suggested 1:1 complexation of **probe-33** with  $\text{Zn}(\text{II})$  ions, which was

further confirmed by single crystal XRD analysis. Finally, the authors utilized **probe-33** for the detection of  $\text{Zn}(\text{II})$  in the intracellular region of human breast cancer cells (MCF-7) (Fig. 39).

A series of 'naked-eye' bis-Schiff base fluorescent chemosensors (**probe-34a**, **probe-34b** and **probe-34c**)<sup>94</sup> were synthesized based on ESIPT by Wang *et al.* in 2020. The **probes** were synthesized *via* a simple condensation reaction between aldehyde and amines and were structurally characterized by multinuclear NMR, ESI-MS and other analytical techniques. The native state of **probes** showed very poor emission; upon addition of  $\text{Zn}(\text{II})$  ions, emission intensity was increased and color changes from colorless to

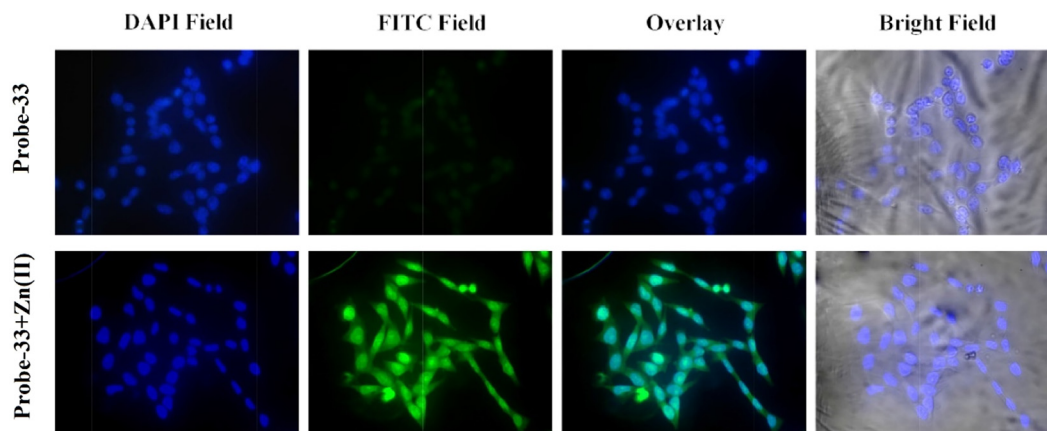


Fig. 39 Fluorescence images of MCF-7 cells after incubation with **probe-33** (top) and the **probe-33**- $\text{Zn}(\text{II})$  complex (bottom) (reprinted with permission from ref. 93, Copyright 2021 Elsevier).





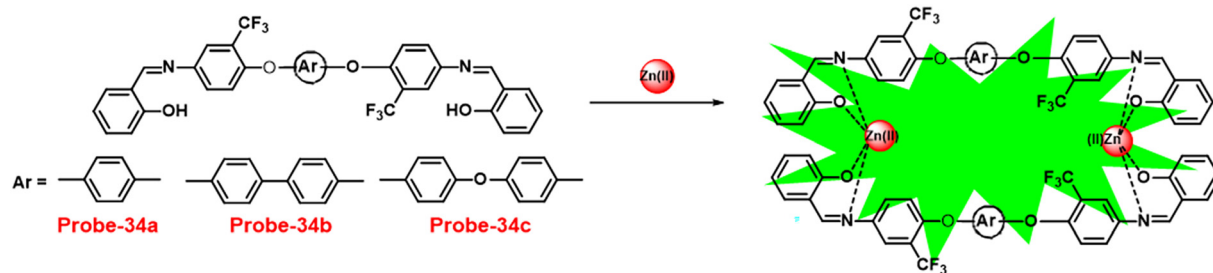


Fig. 40 Chemical structures of probe-(34a–c) and proposed sensing mechanism of probe-34a with Zn(II) (redrawn the ChemDraw structure from ref. 94).

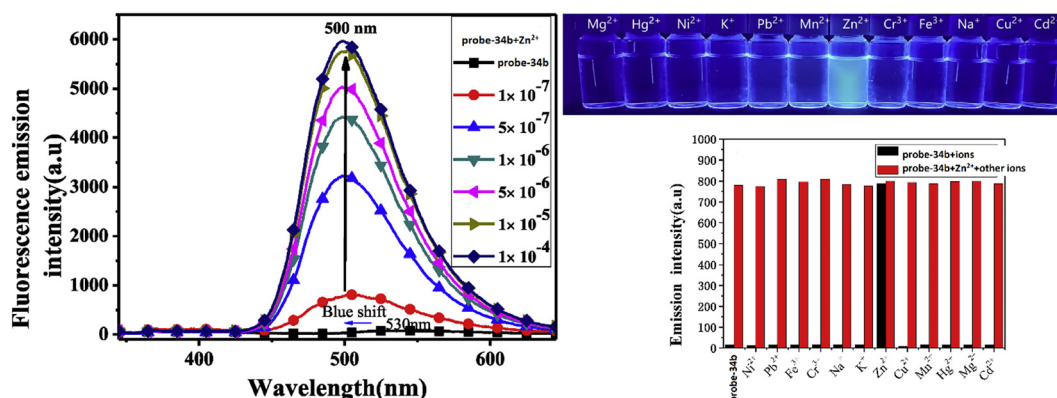


Fig. 41 Fluorescence spectra changes of probe-34b on adding Zn(II) ions (left), fluorescence colour change of probe-34b with different metal ions under a UV lamp (right top) and metal ion competitive studies of probe-34b (right bottom) (reprinted with permission from ref. 94, Copyright 2020 Elsevier).

bluish green, which may be the result of Zn(II) chelating with the target probes and limiting C=N isomerization (Fig. 40 and 41). However, there were no such observations noticed upon addition of other competitive metal ions. For the detection of probe-34a, probe-34b and probe-34c, with Zn(II) ions showed very less LOD (67.2 nM) with good anti-interference capabilities and quick response. A binding ratio of 1:1 was determined for the three probes with Zn(II) ions based on Job's plot analysis of the fluorescence data, which was further supported by the  $^1H$  NMR data. An inverted fluorescence microscopy imaging experiment was conducted and the findings showed that the probes exhibit good cell membrane permeability and hypotoxicity. Probe-34a was used for the detection of Zn(II) ions in SW620 cancer cells, and the results showed that the probe-34a alone exhibited no fluorescence; upon addition of Zn(II) ions, strong luminescence was observed inside the cells. From the above-mentioned results, authors claimed that probe-34a is potential for the recognition of Zn(II) ions in both biological and environmental samples.

Gudasi and colleagues developed a simple and inexpensive optical sensor (probe-35)<sup>95</sup> via a condensation reaction between 2-hydroxy-1-naphthaldehyde and 5-di-*tert*-butyl-2-hydroxybenzohydrazide in MeOH in 2020. The pure form of probe-35 exhibited very poor emission, and with the increase in the concentration of Zn(II) ions, the fluorescence

intensity was increased by 17-fold and a 60 nm blue shift in the emission maxima was observed, which turned the colorless solution into a vivid yellow solution in 20% aqueous acetonitrile. However, under similar conditions, upon addition of various competitive metal ions to probe-35, there were no observable changes present in the fluorescence spectra, which indicate that probe-35 was very selective towards Zn(II) ions. The authors proposed the mechanism for fluorescence turn-on response, which might be attributed to the ESIPT and ICT processes (Fig. 42). The stoichiometry ratio between probe-35 and Zn(II) ions was determined to be 1:1 via Job's plot, which was strongly supported by B–H plots,  $^1H$  NMR and ESI-MS analyses. The binding constant and LOD value of probe-35 with Zn(II) ions were estimated from titration data and displayed as  $7.79 \times 10^6 M^{-1}$  and 0.31

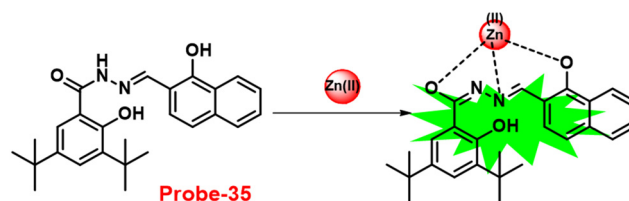


Fig. 42 Chemical structure and proposed sensing mechanism of probe-35 with Zn(II) (redrawn the ChemDraw structure from ref. 95).



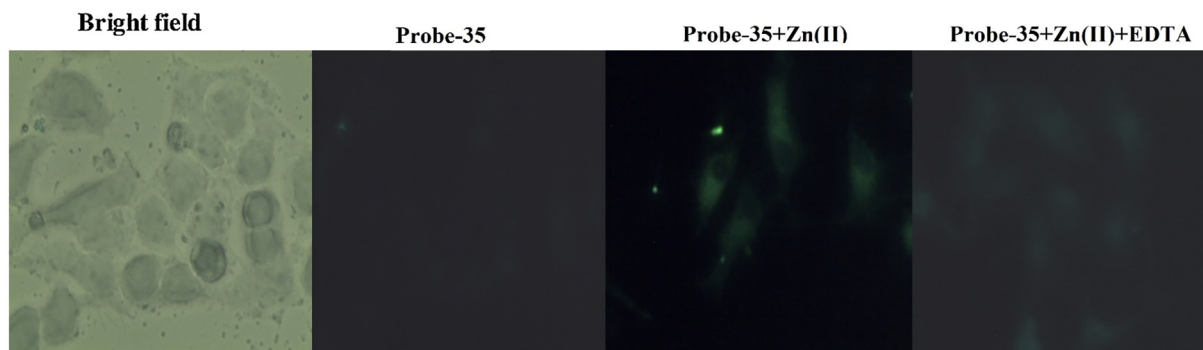


Fig. 43 Bio-imaging images of HeLa cells with **probe-35** with the addition of Zn(II) (reprinted with permission from ref. 95, Copyright 2020 Elsevier).

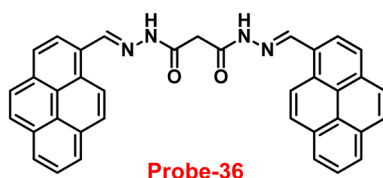


Fig. 44 Chemical structure of **probe-36** (redrawn the ChemDraw structure from ref. 96).

$\mu\text{M}$  respectively. Finally, authors decided to apply **probe-35** to sense Zn(II) ions from the biological samples, in which cytotoxicity experiments revealed that **probe-35** showed very less cytotoxicity. **Probe-35** was incubated with HeLa cells, which showed no emission, and upon treatment with Zn(II) ions, the fluorescence intensity was seen inside the cells. From the above-mentioned results, authors concluded that **probe-35** shows potential to sense Zn(II) ions in environmental and biological samples (Fig. 43).

In 2021, Rani *et al.* developed a pyrene-based Schiff base **probe-36** (ref. 96) for sensitive and selective detection of Zn(II) ions. The synthesis of **probe-36** (Fig. 44) involves two steps: first, the synthesis of malonohydrazide, which was treated

with 2 eq. of pyrene carboxyaldehyde, as a result of which the product has two pyrene units on either side of the molecule. The native state of **probe-36** was poorly emissive in nature due to the presence of PET and was suppressed with the Zn(II) ions and caused fluorescence “turn-on”, whereas **probe-36** did not respond significantly to other competitive ions. Further, **probe-36** and Zn(II) ion interaction produced an effective fluorescence enhancement that was observable with the naked eye as a blue color emission under a UV lamp (Fig. 45). The LOD of **probe-36** with Zn(II) was estimated to be  $5.1 \text{ nM}$  *via* fluorescence titration spectra ( $3\sigma/\text{slope}$ ), this is significantly lower than the WHO-recommended standard of  $76 \mu\text{M}$  for safe drinking water. The association constant of **probe-36** with Zn(II) ions was estimated from the fluorescence titration spectra and displayed as  $3 \times 10^5 \text{ M}^{-1}$ . Job's plot suggested a 1:1 stoichiometric ratio for the **probe-36**–Zn(II) complex. Finally, the authors concentrated on the identification of Zn(II) ions in biological samples, and a cytotoxicity experiment using **probe-36** was carried out and the results strongly indicated the poor cytotoxicity of **probe-36** under biological conditions. The results encouraged to further investigate in this regard. Therefore, **probe-36** was

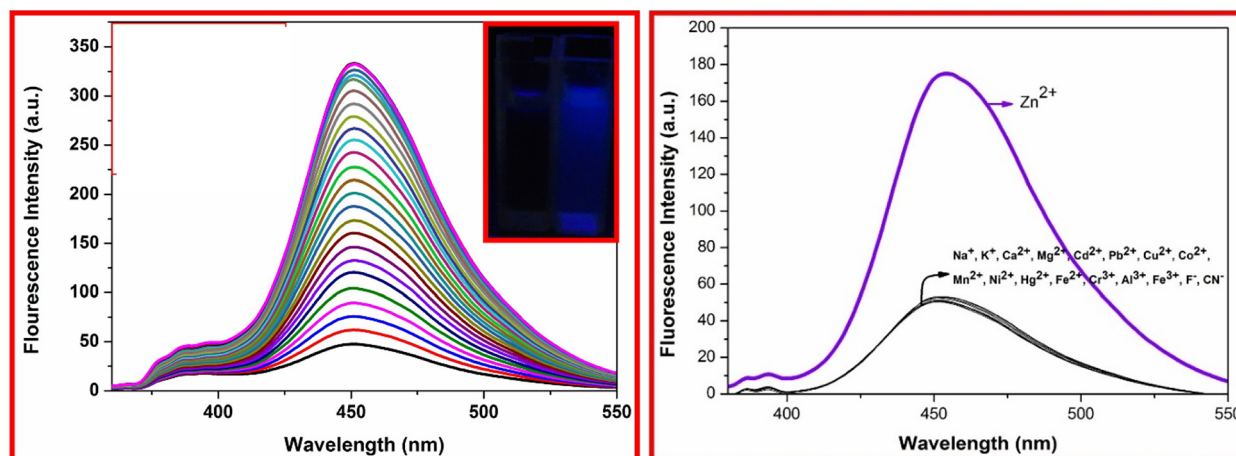


Fig. 45 Emission spectra of **probe-36** upon addition of Zn(II) ions (left) and competitive binding study of **probe-36** with different metal ions (reprinted with permission from ref. 96, Copyright 2021 Elsevier).



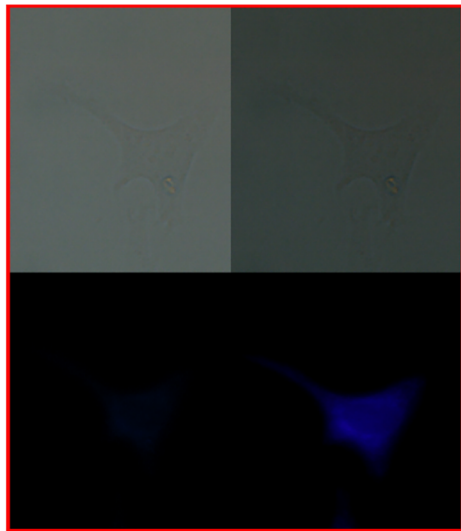


Fig. 46 Fluorescence images of live HeLa cells with **probe-36** with  $\text{Zn(II)}$  ions (reprinted with permission from ref. 96, Copyright 2021 Elsevier).

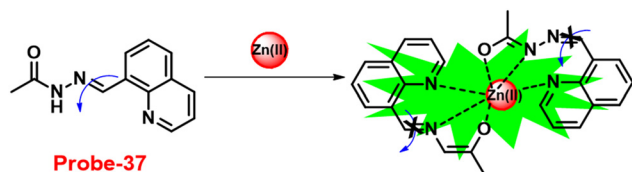


Fig. 47 Chemical structure and proposed sensing mechanism of **probe-37** with  $\text{Zn(II)}$  (redrawn the ChemDraw structure from ref. 97).

incubated in HeLa cells and no emission was observed, and the incorporation of  $\text{Zn(II)}$  ions to the cells produced a strong

blue color emission inside the cells (Fig. 46), which strongly supported the potential of **probe-36** for the recognition of  $\text{Zn(II)}$  ions in biological samples.

Xue and co-workers obtained quinolone-based Schiff base (**probe-37**)<sup>97</sup> for the recognition of  $\text{Zn(II)}$  ions *via* the fluorescence turn-on mechanism in 2018. The pure form of **probe-37** displayed poor emission, and upon addition of  $\text{Zn(II)}$  ions, the increase in emission intensity was noticed with good quantum yields and exhibited a significant large Stokes shift  $>200$  nm due to the absence of  $\text{C=N}$  isomerization (Fig. 47). The LOD of **probe-37** with  $\text{Zn(II)}$  ions calculated from fluorescence spectra and was found to be 89.3 nM. A 2:1 stoichiometry was found for **probe-37** with  $\text{Zn(II)}$  ions, which was validated by fluorescence measurements, UV-vis, ESI-MS, absorption analysis,  $^1\text{H}$  NMR spectra and DFT studies. The reversibility of **probe-37** was tested using  $\text{Na}_2\text{EDTA}$ . Finally, the authors tested the sensing of  $\text{Zn(II)}$  ions in cellular media, in which a cytotoxicity experiment was conducted with **probe-37** that was found to exhibit very poor cytotoxicity on HeLa cells. The results encouraged the authors to recognize  $\text{Zn(II)}$  ions in biological samples. **Probe-37** incubated with  $\text{Zn(II)}$  ions exhibited very bright luminescence inside the cells, which strongly suggested the potential of **probe-37** for the sensing of biological  $\text{Zn(II)}$  samples (Fig. 48).

Following the above-mentioned report, Xu and co-workers focused on the synthesis of bis-quinoline based **probe-38**,<sup>98</sup> which showed selective fluorescence turn-on for  $\text{Zn(II)}$  ions and chromogenic response for  $\text{Co(II)}$  ions in 2020. The synthesized **probe-38** showed very poor emission, and upon incorporation of  $\text{Zn(II)}$  ions, the fluorescence intensity increased, whereas other competitive metal ions showed no change in fluorescence spectra and

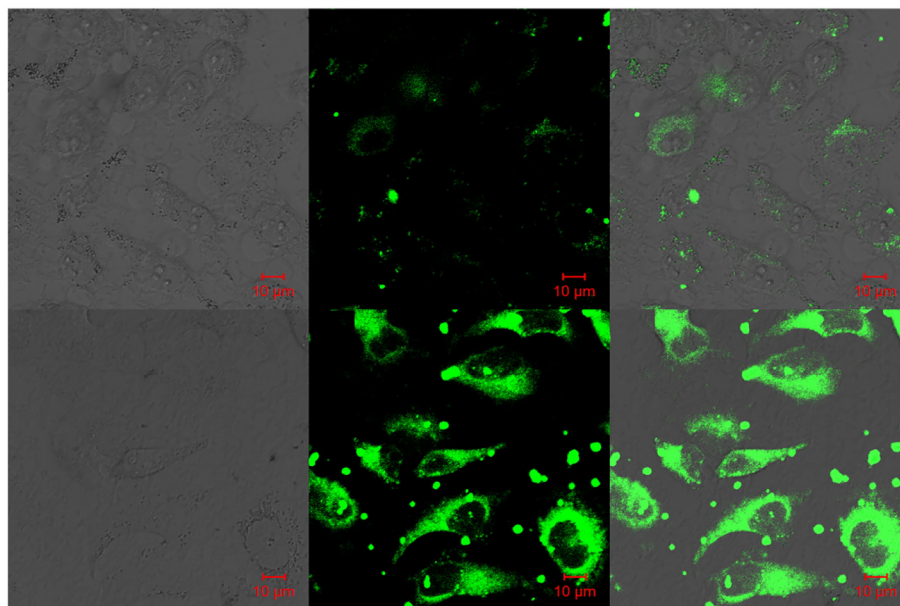


Fig. 48 Confocal fluorescence images of HeLa cells incubated with **probe-37** in the presence of  $\text{Zn(II)}$  ions (reprinted with permission from ref. 97, Copyright 2018 Elsevier).





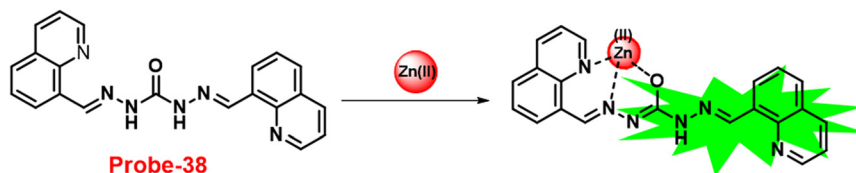


Fig. 49 Chemical structure and proposed sensing mechanism of **probe-38** with Zn(II) (redrawn the ChemDraw structure from ref. 98).

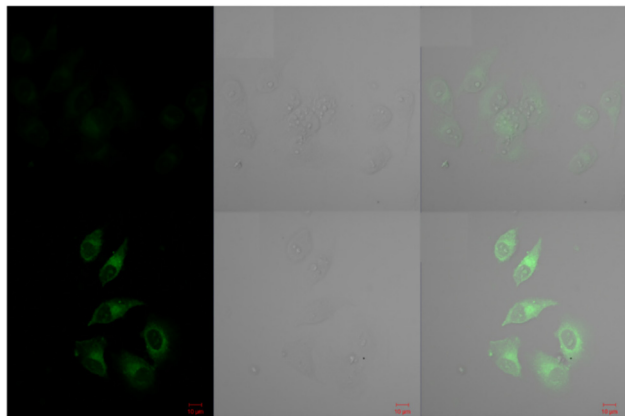


Fig. 50 Confocal fluorescence images of HeLa cells of **probe-38** with Zn(II) ions (reprinted with permission from ref. 98, Copyright 2020 Elsevier).

the results strongly supported that **probe-38** is very selective towards Zn(II) ions *via* fluorescence turn-on, which was caused by metal chelation effects (CHEF) (Fig. 49). Further, **probe-38** can also function as a chromogenic probe for Zn(II) ion recognition with least interference from other competitive metal ions, which demonstrates a long wavelength emission (570 nm) with a substantial large Stokes shift over 170 nm. The limit of detection of **probe-38** was estimated to be 0.66  $\mu\text{M}$  from the fluorescence spectra for Zn(II). Further, the association constant calculated for **probe-38** with Zn(II) from the absorption titration data was  $1.03 \times 10^4 \text{ M}^{-1}$ . The stoichiometric ratio of **probe-38** with Zn(II) ions was calculated to be 1:1 by Job's plot, which was confirmed *via*  $^1\text{H}$  NMR and ESI-MS data. Finally, the authors established the potential of **probe-38** for the sensing of Zn(II) ions in biological samples and outcomes strongly supported that **probe-38** was capable for the recognition of Zn(II) ions in biological samples and was confirmed by intracellular imaging of Zn(II) ions (Fig. 50).

In 2021, Wang *et al.* designed a luminous probe with great selectivity, sensitivity and significant Stokes shift for the sensing of Zn(II) ions using a triphenylamine Schiff base (**probe-39**).<sup>99</sup> The target compound was synthesized *via* a Schiff base condensation reaction between 2-hydroxy-1-naphthaldehyde and an amine derivative of triphenylamine in ethanol under reflux conditions. The native state of **probe-39** was poorly emissive in nature; upon addition of Zn(II) ions, the turn-on response was observed with greater fluorescence intensity in DMF-H<sub>2</sub>O. **Probe-39** has shown strong anti-interference performance even when several other metal ions or anions were present, which strongly supported the selectivity of **probe-39**. The LOD value of **probe-39** with Zn(II) ions was determined from the fluorescence titration values as 19.134 nM in DMF-H<sub>2</sub>O, and **probe-39** accomplished the detection of Zn(II) ions with remarkable linear correlation. Additionally, **probe-39**-Zn(II) complex has a stoichiometric ratio of 1:1 with an association constant of  $3.24 \times 10^4 \text{ M}^{-1}$ . Further, the fluorescence studies of **probe-39** were carried out at various pH values and found to show better results in the range of 5–8. Furthermore, the binding mechanism (Fig. 51) and fluorescence turn-on mechanism were confirmed *via* DFT calculations,  $^1\text{H}$  NMR titration, FT-IR, and ESI-MS and were used to demonstrate the interaction properties. The authors utilized **probe-39** for the recognition of Zn(II) ions in living cells along with environmental areas (Fig. 52). Consequently, **probe-39** has potential applications for sensing Zn(II) ions in the environment and biological systems.

Venkatesan *et al.* developed a novel fluorescent turn-on probe for the detection of Zn(II) ions using both cyclic (**probe-40a**) and noncyclic (**probe-40b**) Schiff's bases in 2019. Under two distinct catalytic conditions, the condensation of 4-(diethylamino)salicylaldehyde and 2 aminobenzenethiol in sulphuric acid produces the product **probe-40a**, while with acetic acid yields **probe-40b**.<sup>100</sup> The native state of **probes** displayed very poor emissive properties due to the presence of ESIPT in CH<sub>3</sub>OH/H<sub>2</sub>O, while upon addition of Zn(II) ions,

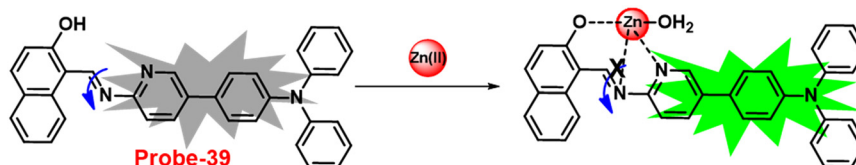


Fig. 51 Chemical structure and proposed sensing mechanism of **probe-39** with Zn(II) (redrawn the ChemDraw structure from ref. 99).





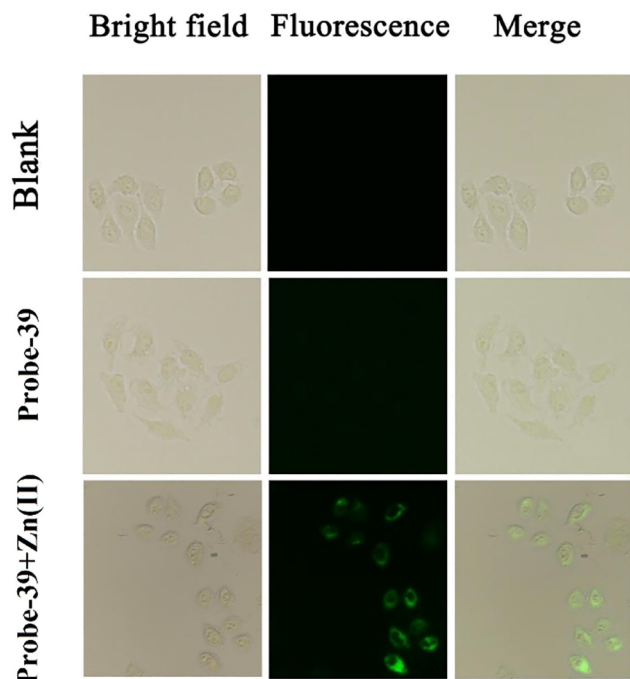


Fig. 52 Fluorescence microscopic images of HeLa cells treated with **probe-39** and **probe-39**-Zn(II) ions (reprinted with permission from ref. 99, Copyright 2021 Elsevier).

there is increase in the intensity of emission due to the CHEF process (Fig. 53). However, on titrating with other metal ions, no change was observed in the fluorescence spectra. The results of Job's plot and B-H plot analysis showed the development of 2:1 and 1:1 stoichiometry, with association constants ( $K_a$ ) of  $4.9 \times 10^4 \text{ M}^{-1}$  and  $2.1 \times 10^4 \text{ M}^{-1}$  with **probe-40a** and **probe-40b**, respectively. The reversibility of **probes** was tested using EDTA and data showed very good results. **Probe-40a** and **probe-40b** were found to have detection limits of 67 nM and 0.36  $\mu\text{M}$ , respectively, which were calculated from the fluorescence titration data. The detection of Zn(II) ions in various water samples and pharmaceutical

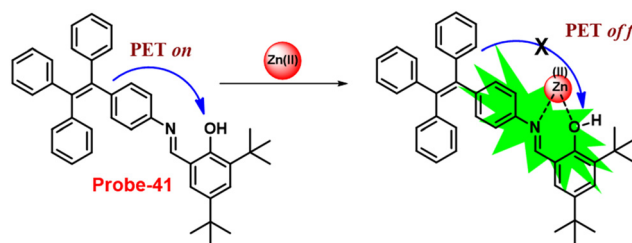


Fig. 54 Chemical structure and proposed sensing mechanism of **probe-41** with Zn(II) (redrawn the ChemDraw structure from ref. 101).

multivitamin tablets was accomplished with **probe-40a** and **probe-40b**.

Jia and co-workers synthesized a multi-responsive tetraphenylethylene-functionalised salicylaldehyde-based Schiff base (**probe-41**),<sup>101</sup> which displayed AIE-activity and could be utilized for the detection of Zn(II) ions *via* the fluorescence turn-on mechanism. **Probe-41** displayed reversible mechanofluorochromism (MFC), as shown by the color change of emission from yellowish green to orange-yellow following grinding. The solution state of **probe-41** showed very poor emission, and upon addition of Zn(II) ions, the fluorescence intensity drastically increased as a result of suppression of ESIPT (Fig. 54), and other metal ions do not affect the fluorescence spectra, which strongly suggested the selectivity and sensitivity towards Zn(II). The complexation ratio between **probe-41** and Zn(II) were determined to be 1:1, which was validated by Job's plot, ESI-MS and  $^1\text{H}$  NMR. Further, authors observed a large Stokes shift of emission spectra during the titration process, which showed clearly visible changes in the fluorescence (from blue to bright orange). The sensing mechanism was proposed, based on the inhibition of PET and ESIPT. Further, the LOD value of **probe-41** and Zn(II) was estimated to be as low as 80.5 nM.

In 2021, Sun *et al.* reported the synthesis of a novel pyrene-incorporated Schiff base (**probe-42**) with an AIEE property that was used for the OTFT and solution-state detection of Zn(II) ions.<sup>102</sup> **Probe-42** was synthesized using an

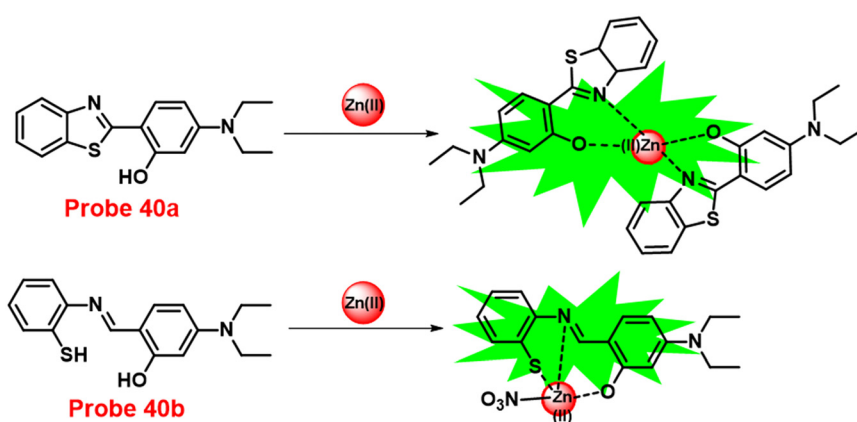


Fig. 53 Chemical structure and proposed sensing mechanism of **probe-40a** and **probe-40b** with Zn(II) (redrawn the ChemDraw structure from ref. 100).



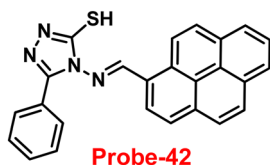


Fig. 55 Chemical structure of **probe-42** (redrawn the ChemDraw structure from ref. 102).

one-pot reflux reaction of pyrene-1-carboxaldehyde and 4-amino-5-phenyl-4H-1,2,4-triazole-3-thiol. The presence of *J*-aggregation, crystalline changes, and nanofiber formation in the AIEE studies of **probe-42** (Fig. 55) (in CH<sub>3</sub>CN) at various water fractions (*f<sub>w</sub>*: 0–97.5%) was validated by UV-vis absorption/photoluminescence (UV/PL), powder X-ray diffraction (PXRD), scanning electron microscopy (SEM), transmission electron microscopy (TEM), atomic force microscopy (AFM), and dynamic light scattering (DLS). The pure form of **probe-42** displayed poor emission and upon addition of Zn(II) ions, a gradual increment in the fluorescence spectra with enhanced quantum yields was observed, which attributed to the suppression of PET. However, in the presence of other competitive metal ions, no change in fluorescence spectra was found. The LOD value of Zn(II) with **probe-42** was calculated to be 0.79 nM, from the standard deviation and linear fittings of fluorescence titration spectra. The stoichiometry of **probe-42** with Zn(II) ions was estimated with Job's plot and found to be 2:1, which was confirmed by HRMS and <sup>1</sup>H NMR data. The MTT assay and IC<sub>50</sub> studies, as well as *in vitro/in vivo* imaging for **probe-42** with Zn(II) ions, were conducted on B16F10 cell lines and in zebrafish, to determine the **probe's** biocompatibility and it demonstrated applications of **probe-42** in biological samples (Fig. 56). The OTFT devices was created upon incorporation of **probe-42** with pentacene, which validated the reversibility discovered to be more than 90% change in drain-source current in response to Zn(II) with

a LOD of 5.46 μM. The OTFT devices additionally exhibited Zn(II) ion detection in samples of tap water and lake water.

In 2019, Upadhyay and colleagues synthesized a novel coumarin-based Schiff-base sensor, **probe-43**, for the selective and sensitive fluorescence turn-on recognition of Zn(II) ions.<sup>103</sup> A “turn-on” green emissive response was produced by **probe-43** (Fig. 57) after selective Zn(II)-triggered hydrolysis in ethanol, which was then reconstructed into fragments. This response was verified by a number of physicochemical tests, and single-crystal XRD studies. The idea of hydrolysis and restructuring was supported by spectroscopic data combined with ESI-MS, which suggests that the **probe-43**-Zn(II) ensemble assumed the form of dimer in solutions. XRD examinations revealed more evidence for the **probe-43**-Zn(II) ensemble, demonstrating that this Schiff base represents another unique Schiff base created *in situ* during the growth of single crystals. However, upon addition of other competitive metal ions to **probe-43**, there was no change in the fluorescence spectra, which strongly supports the selectivity of **probe-43** towards Zn(II) ions. The authors proposed that upon binding, **probe-43** and Zn(II) ions cause the reduction of intramolecular interactions (π–π interactions), which results in a blue-shift emission band, and the suppression of PET is responsible for the increase in quantum yields. The detection limits of **probe-43** with Zn(II) ions were calculated to be in the sub-nanomolar range from the fluorescence titration spectra. Further, **probe-43** was effectively utilized for the detection of Zn(II) optically and also *via* live cell imaging by selective hydrolytic fluorogenic events in SiHa cells (Fig. 58).

Das and co-workers obtained a macrocyclic Schiff base (**probe-44**)<sup>104</sup> for the selective and sensitive sensing of Zn(II) ions *via* the fluorescence turn-on mechanism in 2016. The macrocyclic ligand **probe-44** (Fig. 59) was synthesized by treating Zn(NO<sub>3</sub>)<sub>2</sub> with an acyclic side-off compartmental ligand, which forms a dinuclear macrocyclic zinc(II) complex, which further undergoes hydrolysis of the starting ligand *via*

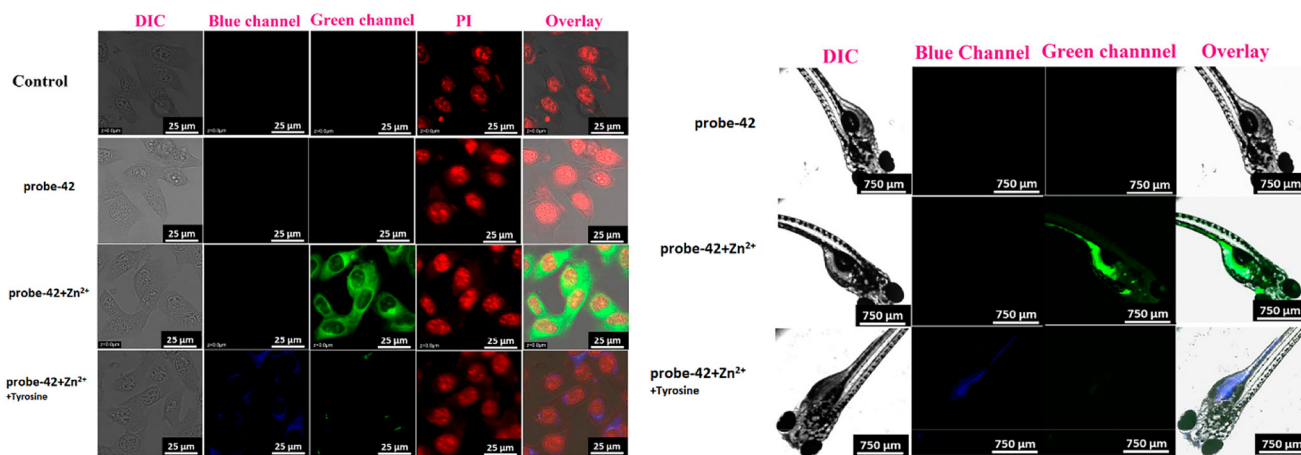


Fig. 56 Cellular images of **probe-42** Zn(II) and **probe-42** Zn(II) + tyrosine and zebrafish imaging of **probe-42** Zn(II) and **probe-42** Zn(II) + tyrosine (reprinted with permission from ref. 102, Copyright 2021 American Chemical Society).



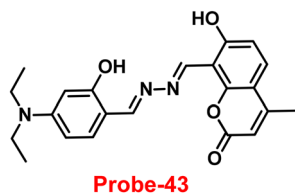


Fig. 57 Chemical structure of **probe-43** (redrawn the ChemDraw structure from ref. 103).

Zn(II)-catalyzed processes. The authors used various analytical and spectroscopic techniques to confirm the formation of macrocyclic ligand **probe-44** in the solution. The pure form of **probe-44** displayed a strong green color emission, and addition of Zn(II) ions causes the appearance of a new fluorescence emission band at 481 nm, whose strength gradually increases. As a result, ligand **probe-44** functions as a ratiometric fluorescence chemodosimeter for the targeted recognition of Zn(II) ions, even in the presence of other competitive metal ions.

In 2019, Kim *et al.* synthesized a new Schiff base chemosensor **probe-45** using 1-aminohydantoin hydrochloride and 3-methoxysalicylaldehyde in ethanol with stirring under room temperature conditions.<sup>105</sup> The native form of **probe-45** was weak emissive in nature; upon incorporation of Zn(II) ions, the emission intensity was gradually improved in aqueous solutions due to the CHEF effect (Fig. 60). However, in the presence of other competitive metal ions, there was no or minimal change in the fluorescence spectra, which demonstrated the selectivity towards Zn(II) ions. The LOD value of **probe-45** with Zn(II) ions was calculated to be 11.9  $\mu\text{M}$  from the fluorescence titration spectra using the  $3\sigma/\text{slope}$ , which was much less than WHO-recommended levels (76.0  $\mu\text{M}$ ). The reversibility of **probe-45** was demonstrated using EDTA, and it was found that Zn(II) binding could be reversible. Finally, authors applied **probe-45** for the sensing of Zn(II) ions in biological media and showed a very significant role in the detection of Zn(II) in live cells (Fig. 61). Additionally, **probe-45** could be used for the

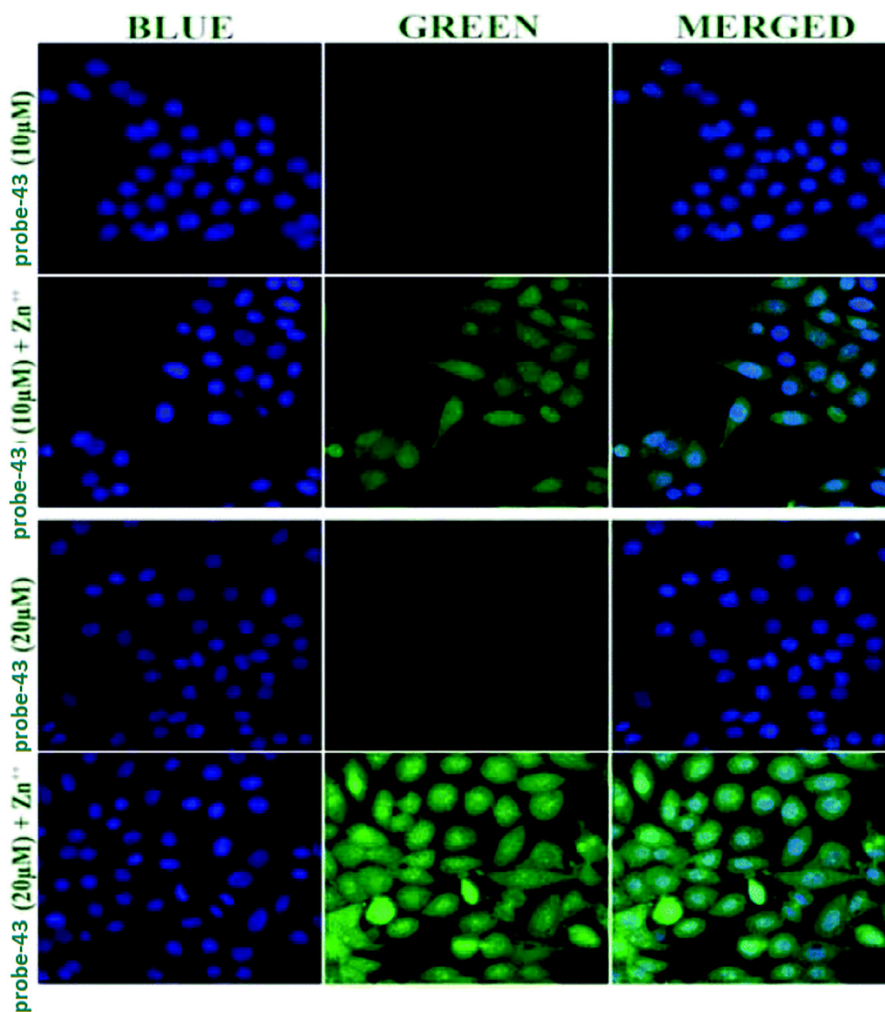


Fig. 58 Fluorescence microscopic images of SiHa cells treated with **probe-43** in the presence of Zn(II) ions (reprinted with permission from ref. 103, Copyright 2019 Royal Society of Chemistry).



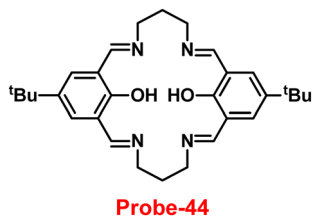


Fig. 59 Chemical structure of **probe-44** (redrawn the ChemDraw structure from ref. 104).

detection of Cu(II) colorimetrically, which changes the color from colorless to pink.

A novel bis(salamo)-type fluorescent probe (**probe-46**)<sup>106</sup> based on naphthalenediol was synthesized by Dong and colleagues for the selective recognition of Zn(II) *via* the fluorescence turn-on mechanism in 2019. The native form of **probe-46** displayed poor emissive properties, and upon incorporation of Zn(II) ions, the emission intensity was enhanced gradually, because of the inhibition of PET (Fig. 62), whereas under similar conditions in the presence of other competitive metal ions, no change was observed in the emission spectra. The LOD and association constant of **probe-46** with Zn(II) ions were estimated to be 0.52  $\mu\text{M}$  and  $2.71 \times 10^4 \text{ M}^{-1}$  respectively from the fluorescence titration spectra. A 1:3 stoichiometry was estimated by Job's plot for the complex between **probe-46** and Zn(II) ions and was supported by fluorescence and UV-vis titrations; ESI-MS, single crystal as well as theoretical calculations were used to understand their detection mechanisms. Further, the binding mode of **probe-46** with Zn(II) ions was confirmed *via* Hirshfeld surface analysis, EA, IR, UV-Vis spectroscopy, and fluorescence spectroscopy.

In 2018, Pu *et al.* developed a potential chromogenic and fluorogenic chemosensor of Cu(II) and Zn(II) ions established on diarylethene conjugated with 2-(methylthio)benzenamine Schiff's moiety (**probe-47**).<sup>107</sup> **Probe-47** (Fig. 63) showed discrimination of two metal ions such as Zn(II) and Cu(II) *via* fluorescence turn-on and colorimetric studies respectively. **Probe-47** displayed poor emission; upon incorporation of Zn(II) ions, the fluorescence was gradually increased up to 53.8-fold as well as a shift in luminous color from light red to bright yellow. However, in the presence of other competitive metal ions, no change was observed in the fluorescence spectra of **probe-47** and Cu(II) ions were found to be fluorescence quenched up to 98%, resulting in a color change from light red to non-fluorescent. The coordination

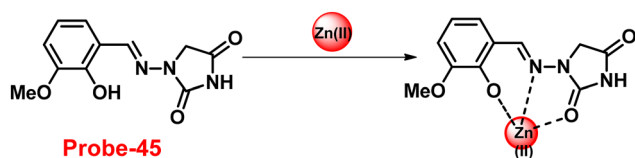


Fig. 60 Chemical structure and proposed sensing mechanism of **probe-45** with Zn(II) (redrawn the ChemDraw structure from ref. 63).

stoichiometry between **probe-47** and Cu(II)/Zn(II) was found to be 1:1 in both cases. With the help of these discoveries, a different input switch and an embedded logic circuit were effectively built.

In 2018, Wang and co-workers obtained novel coumarin-based fluorescent **probe-48** (Fig. 64),<sup>108</sup> which could be useful for the sensing of Zn(II) ions *via* the fluorescence turn-on mechanism. The target compound was synthesized *via* a simple condensation reaction between thiosemicarbazide and 8-formyl-7-hydroxy-4-methylcoumarin. **Probe-48** showed a colorimetric response towards Fe(III) ions and color variations from colorless to brown but fluorescence turn-on behavior towards the Zn(II) ions (Fig. 65). In the presence of other metal ions, **probe-48** only showed a high ability to coordinate toward Zn(II) and Fe(III) ions, with the LOD values as low as 6 nM and 5.38  $\mu\text{M}$ , correspondingly. The stoichiometry between **probe-48** and Zn(II)/Fe(III) was found to be 1:1, which was confirmed by Job's plot. Moreover, **probe-48** could quickly, easily, and practically monitor Zn(II) and Fe(III) ions using conventional test strips. Fluorescence cell images also identified the potential of **probe-48** to be used as a bio-imaging fluorescent sensor to identify Zn(II) ions in human cancer cells (Fig. 66).

Swamy *et al.* synthesized two acyclic Schiff base probes,<sup>47</sup> **probe-49a** and **probe-49b**, that could be used for the detection of Zn(II) *via* fluorescence turn-on and as colorimetric chemosensors for Zn(II), Cu(II), and Co(II) ions by altering from colorless to yellow, and no change was observed in the emission spectra in the presence of other competitive metal ions in 2022. The fluorescence turn-on mechanism proposed for these **probes** was the conquest of  $-\text{C}=\text{N}-$  isomerization, PET blocking, and the ESIPT process (Fig. 67). The recognition mechanism of Zn(II) ions with **probe-49a**/**probe-49b** was further supported by  $^1\text{H}$  NMR titrations. Furthermore, Job's plot analysis displayed 1:1 binding for **probes** with Zn(II) ions, which was established by DFT,  $^1\text{H}$  NMR, UV-vis, and fluorescence spectroscopy studies. In

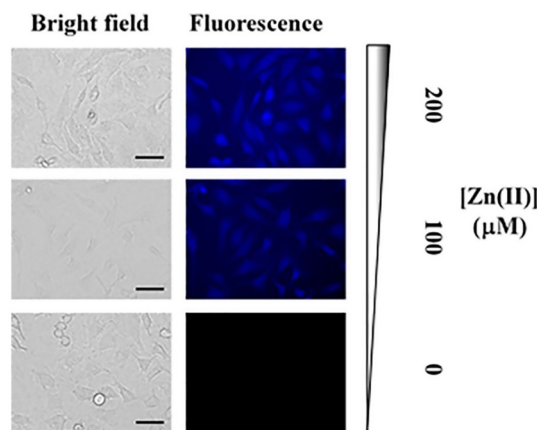


Fig. 61 Fluorescence microscopic images of HeLa cells in **probe-45** in the presence of Zn(II) ions (reprinted with permission from ref. 105, Copyright 2019 Elsevier).





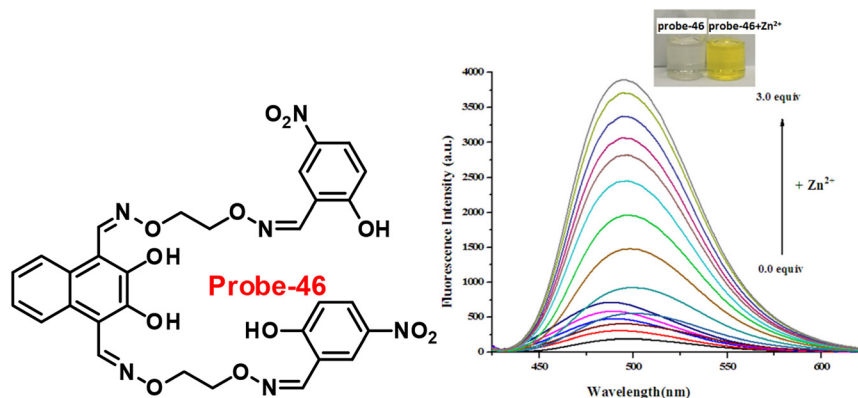


Fig. 62 Chemical structure of **probe-46** (left) and changes in the fluorescence spectra of **probe-46** upon increasing the Zn(II) ion concentration (right) (reprinted with permission from ref. 106, Copyright 2019 Elsevier).

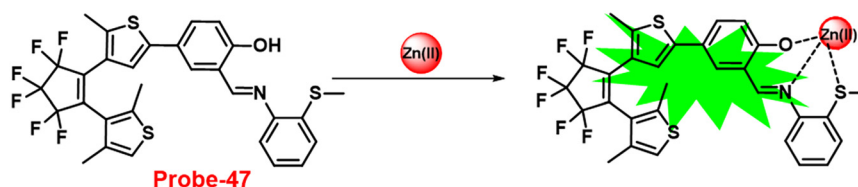


Fig. 63 Chemical structure and proposed sensing mechanism of **probe-47** with Zn(II) (redrawn the ChemDraw structure from ref. 107).

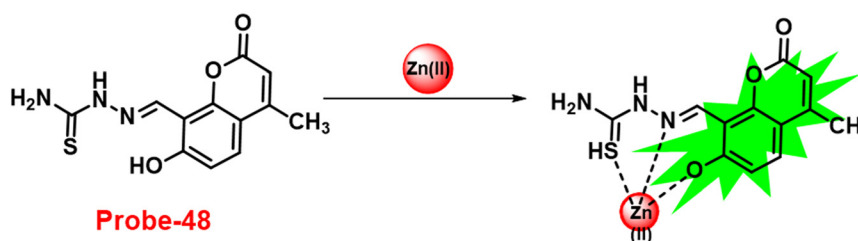


Fig. 64 Chemical structure and proposed sensing mechanism of **probe-48** with Zn(II) (redrawn the ChemDraw structure from ref. 108).

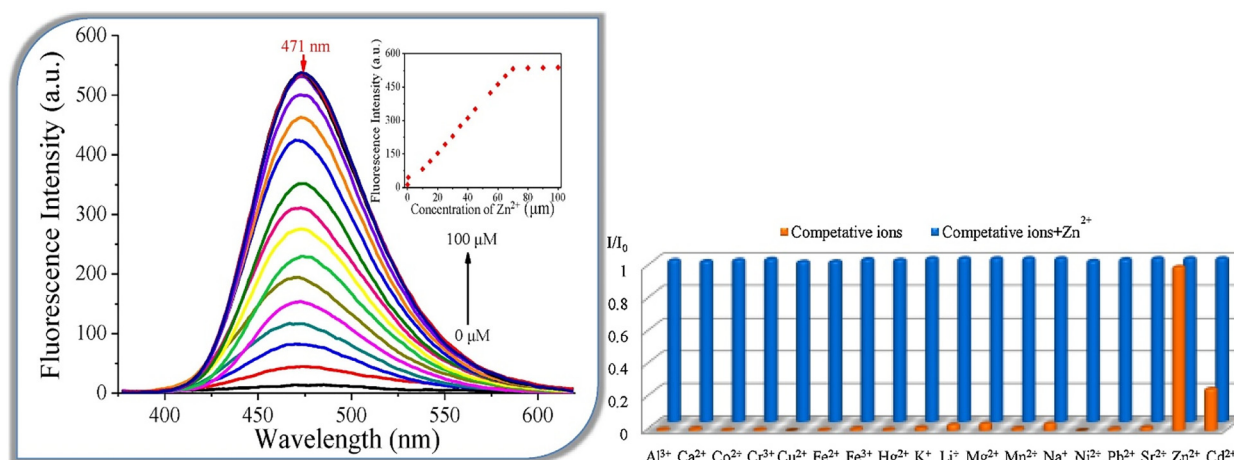


Fig. 65 Changes in the fluorescence spectra of **probe-48** upon incremental addition of Zn(II) ions (left) and competitive binding study of **probe-48** with different metal ions (right) (reprinted with permission from ref. 108, Copyright 2018 Elsevier).



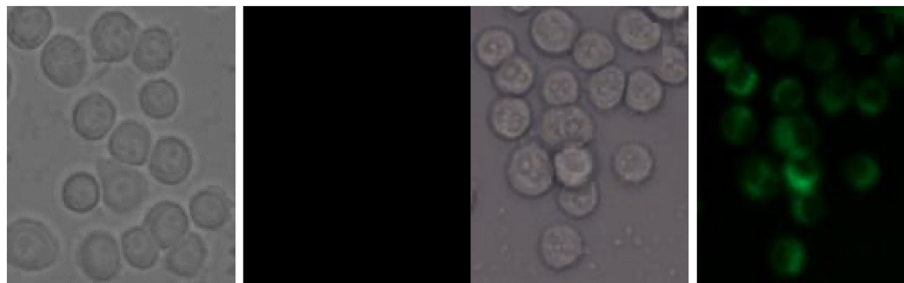


Fig. 66 Bioimaging images of cancer cells treated with **probe-48** followed by the addition of  $\text{Zn(II)}$  ions (reprinted with permission from ref. 108, Copyright 2018 Elsevier).

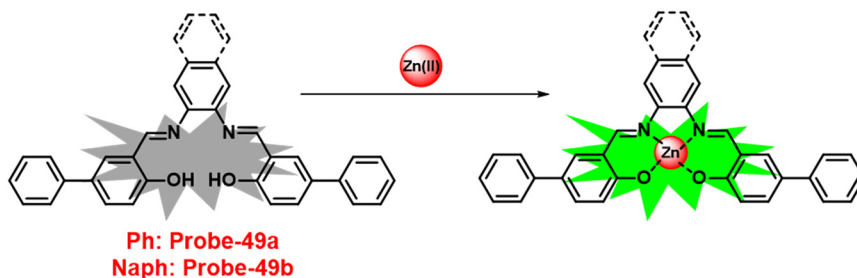


Fig. 67 Chemical structure and proposed sensing mechanism of **probe-49a** and **probe-49b** with  $\text{Zn(II)}$  (redrawn the ChemDraw structure from ref. 47).

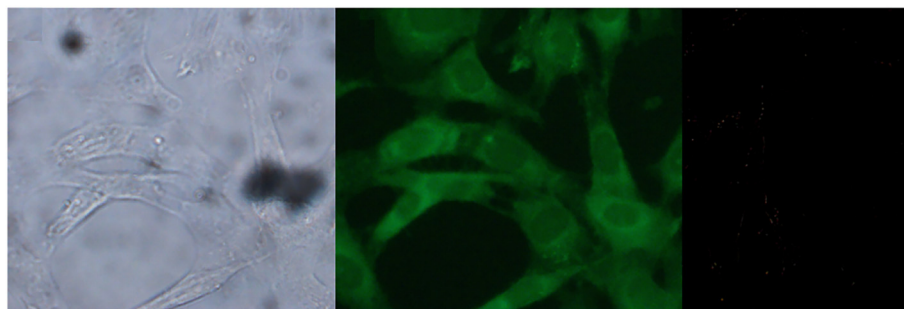


Fig. 68 Bio-imaging images of HeLa cells treated with **probe-49a** followed by addition of  $\text{Zn(II)}$  ions (reprinted with permission from ref. 47, Copyright 2022 Elsevier).

addition, the LOD values of **probe-49a** and **probe-49b** for  $\text{Zn(II)}$  ions were found to be 7.69 and 5.35 nM, correspondingly, which were much lesser than permitted by the U.S. Environmental Protection Agency (US-EPA). The **probes** could be used as an efficient luminescent probe for the recognition of  $\text{Zn(II)}$  ions in living cells, based on the fluorescence microscopic imaging in HeLa cells, which strongly demonstrates the immense potential of this simple chemosensor in cellular imaging (Fig. 68).

### 3. Schiff base-based fluorescent turn-on probes for $\text{Hg(II)}$ ions

As we know, heavy metals have lethal effects on human life, in this regard mercury, which has attracted special attention due to its extreme toxicity.<sup>109,110</sup> Even at extremely low

concentrations, it can have significant negative impacts on human body, such as impairing the ability of proteins and enzymes to function, movement disorders, cognitive dysfunction, brain damage, and kidney failure.<sup>111–113</sup> There are several conventional methods such as ICP-MS and AES/AAS for the recognition of  $\text{Hg(II)}$  ions in waste water.<sup>114</sup> Recently, researchers focused on selective and sensitive probes for the recognition of  $\text{Hg(II)}$  ions, which can be utilized for both in environmental waste samples and in living cells.<sup>115–119</sup>

In 2021, Jiao and co-workers constructed a rhodamine-based Schiff base (**probe-50**)<sup>120</sup> fluorescent turn-on probe for  $\text{Hg(II)}$  ions, which was obtained from rhodamine B and acenaphtho[1,2-*b*]quinoxaline-9-amine. The target compound was structurally characterized by several analytical techniques such as  $^1\text{H}$  NMR,  $^{13}\text{C}$  NMR, HRMS, and single-crystal XRD.



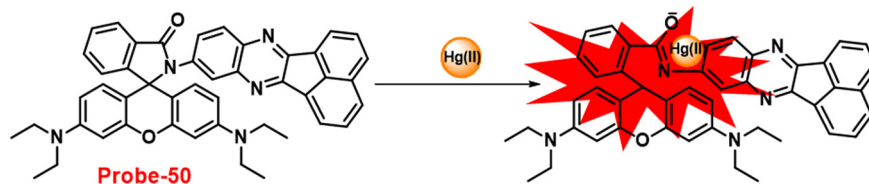


Fig. 69 Chemical structure and proposed sensing mechanism of probe-50 with Hg(II) (redrawn the ChemDraw structure from ref. 120).

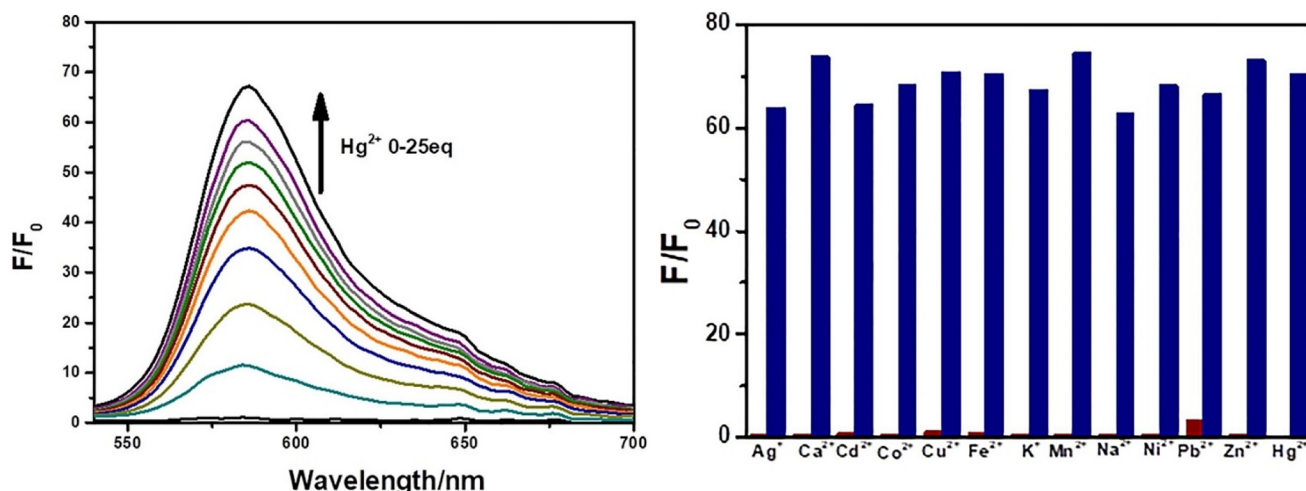


Fig. 70 Emission spectra of probe-50 upon incremental addition of Hg(II) ions (left) and changes in the emission spectra of probe-50 with different metal ions (right) (reprinted with permission from ref. 120, Copyright 2021 Elsevier).

The native state of **probe-50** displayed poor emission, whereas upon incorporation of Hg(II) ions, the spirocyclic ring undergoes a ring-opening process (Fig. 69), and the fluorescence intensity at 586 nm is considerably enhanced 70-fold in C<sub>2</sub>H<sub>5</sub>OH/HEPES (1:1, v/v) (Fig. 70). However, on titrating with other competitive metal ions, there was no change in the emission spectra, these results strongly suggested that **probe-50** is very selective towards Hg(II) ions

(Fig. 70). The LOD of **probe-50** with Hg(II) ions was estimated as 10 nM from the emission titration spectra. Furthermore, **probe-50** finds a method for monitoring variations in Hg(II) ion content in biological systems by confocal laser microscopy, such as fluorescence imaging of HeLa live cells and zebra fish (Fig. 71).

Niu *et al.* developed an effective Schiff-base fluorescent chemosensor, **probe-51**,<sup>121</sup> made from low-cost starting

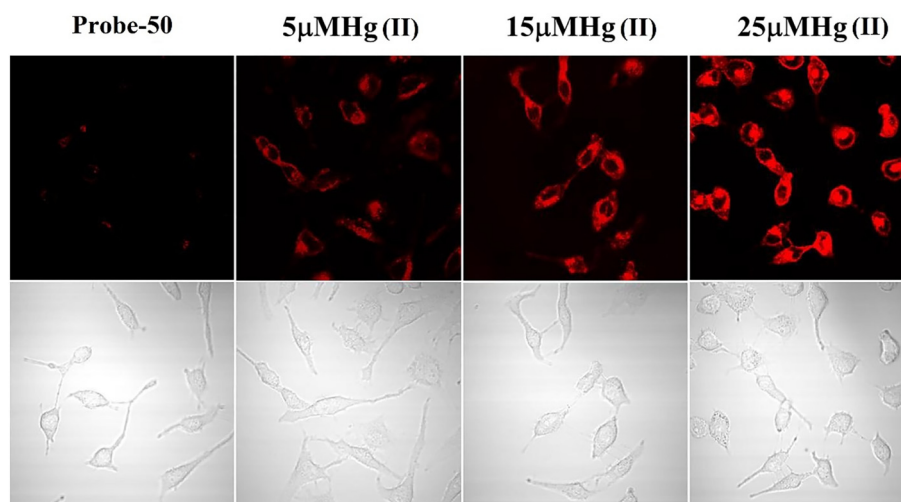


Fig. 71 Confocal fluorescence images of HeLa cells treated with probe-50 and incubated with different concentrations of Hg(II) ions (reprinted with permission from ref. 120, Copyright 2021 Elsevier).



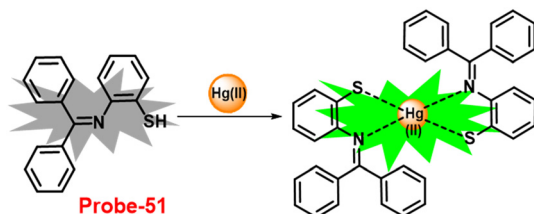


Fig. 72 Chemical structure and proposed sensing mechanism of **probe-51** with  $\text{Hg(II)}$  (redrawn the ChemDraw structure from ref. 63).

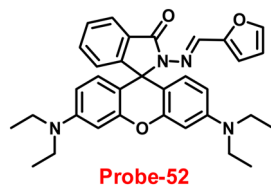


Fig. 73 Chemical structure of **probe-52** (redrawn the ChemDraw structure from ref. 122).

materials such as benzophenone and 2-aminobenzenethiol, which was characterised by IR,  $^1\text{H}$  NMR, and  $^{13}\text{C}$  NMR, revealing highly selective and sensitive sensing of  $\text{Hg(II)}$  ions. Due to the precise binding of  $\text{Hg(II)}$  with imine N and thiol S atoms, **probe-51** shows a distinct turn-on emission behavior for  $\text{Hg(II)}$  ions throughout a wide range of pH values, whereas in the presence of other metal ions, there was no change in the fluorescence spectra. The suppression of  $\text{C=N}$  isomerization and ESIPT could be attributed to the fluorescence turn-on response of **probe-51** (Fig. 72). Further, **probe-51**– $\text{Hg(II)}$  was also regenerated back to **probe-51** when EDTA was added, which provided the potentiality of **probe-51**. The 2:1 binding for **probe-51**– $\text{Hg(II)}$  was determined by utilizing the method of continuous variations and Job's plot, which was further validated by the B–H method. The binding constant was found to be  $4.484 \times 10^5 \text{ M}^{-1}$ , and the fluorescence titration profile shows that **probe-51** has a detection limit of 22 nM for  $\text{Hg(II)}$ , which is as low as to

detect submillimolar concentrations of  $\text{Hg(II)}$  ions seen in practice.

In 2016, Yang *et al.* conducted a study aimed to synthesise a rhodamine based chemosensor (**probe-52**) for the selective and sensitive recognition of  $\text{Hg(II)}$  ions in ethanol/HEPES (pH 7.3, 3:7, v/v, ex = 480 nm) via the fluorescence turn-on mechanism.<sup>122</sup> **Probe-52** (Fig. 73) was synthesized from rhodamine hydrazide and furfural in ethanol. **Probe-52** was structurally characterized by ESI-MS,  $^1\text{H}$ ,  $^{13}\text{C}$  NMR, FT-IR (KBr) and EA. The native state of **probe-52** exhibited very weak emission, on titrating with  $\text{Hg(II)}$  ions, and the fluorescence intensity gradually increased as “green” luminescence enhanced by 320-fold. However, the authors tested other metal ions, which showed no change in the fluorescence spectra. Further, the association constant of **probe-52** with  $\text{Hg(II)}$  was computed to be  $1.01 \times 10^4 \text{ M}^{-1}$  and the solution color changed from colorless to green fluorescence when exposed to a UV lamp. Meanwhile, Cys can significantly reduce the green fluorescence of **probe-52**– $\text{Hg(II)}$ ; however, no change in fluorescence spectra was observed for  $\text{GSH}$ ,  $\text{SO}_4^{2-}$ ,  $\text{SO}_3^{2-}$ ,  $\text{CN}^-$ ,  $\text{CO}_3^{2-}$ , or  $\text{HCY}$ . The LOD values for  $\text{Hg(II)}$  and Cys were calculated to be 0.09  $\mu\text{M}$  and 0.08  $\mu\text{M}$ , respectively, and they could be applied as dual fluorescent probes that can distinguish  $\text{Hg(II)}$  ions from other metal ions as well as Cys from other biothiols, and thus, are highly utilizable in aqueous media and bio-imaging studies (Fig. 74).

In 2016, Yang reported a facile synthesis method of a novel  $\pi$ -conjugated linear bis-Schiff base (**probe-53**) containing an  $\alpha$ -cyanostilbene unit.<sup>123</sup> The structural characterization of **probe-53** was carried out by several analytical techniques. **Probe-53** (Fig. 75) possesses very interesting AIE effects and is utilized for the sensing of  $\text{Hg(II)}$  ions with strong affinities, as evidenced by a visible color change or fluorescence emission of the sample in THF and THF/water solutions. The authors proposed that the sensing mechanism of fluorescence turn-on could be explained by the suppression of the restricted intramolecular rotations (RIR) of aromatic rotors and inhibition of the  $\text{C=N}$

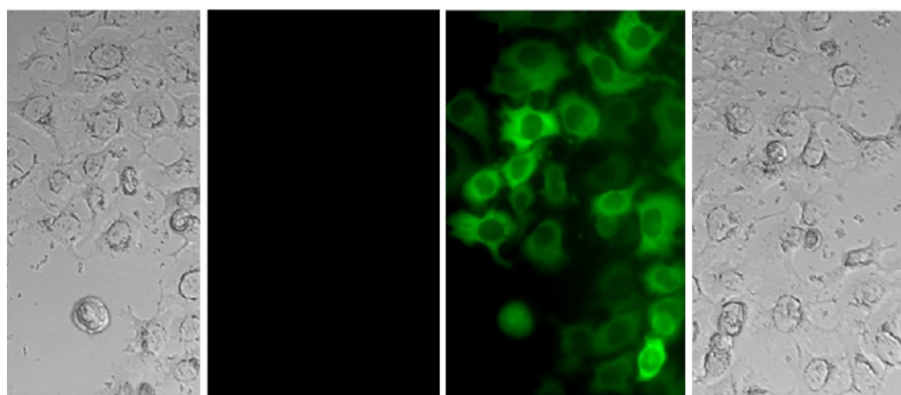


Fig. 74 Fluorescence microscopic images of SW480 cells with **probe-52** in the presence of  $\text{Hg(II)}$  ions and Cys (reprinted with permission from ref. 122, Copyright 2016 Elsevier).





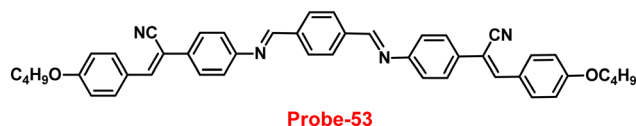


Fig. 75 Chemical structure of **probe-53** (redrawn the ChemDraw structure from ref. 123).

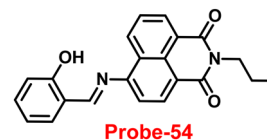


Fig. 77 Chemical structure of **probe-54** (redrawn the ChemDraw structure from ref. 124).

isomerization, which block the non-fluorescence pathway of **probe-53**. The competitive studies of **probe-53** revealed high selectivity towards  $\text{Hg(II)}$  ions even with other metal ions. Further, to find out the recognition of  $\text{Hg(II)}$  ions in biological media, authors performed the sensing studies on HeLa cells, which strongly suggested that **probe-53** could be able to sense  $\text{Hg(II)}$  ions in biological samples (Fig. 76). Due to the very high sensitivity and selectivity of **probe-53** towards  $\text{Hg(II)}$  ions *via* the fluorescence turn-on behavior with a low LOD (3.4 nM in THF, 0.24  $\mu\text{M}$  in THF/water), it became a compatible sensor in both environmental and biological samples.

Luxami and co-workers obtained a novel naphthalimide-based Schiff base, **probe-54**,<sup>124</sup> which exhibited high selectivity and sensitivity towards  $\text{Hg(II)}$  ions *via* the fluorescence turn-on mechanism in 2017. The target compound was synthesized *via* a reaction between aminonaphthamide and salicylaldehyde in ethanol under reflux conditions, which was confirmed by multinuclear NMR and HRMS spectrometry. **Probe-54** (Fig. 77) demonstrated a spectacular ratiometric absorbance response as well as a turn-on emission behavior towards nanomolar concentrations of  $\text{Hg(II)}$  ions without interference from other metal ions. A B-H equation was utilized to calculate the binding constant for **probe-54** with  $\text{Hg(II)}$  in  $\text{CH}_3\text{OH}$  to be  $6.89 \times 10^6 \text{ M}^{-1}$ . It was found that **Probe-54** had the lowest LOD value of 0.5 nM for  $\text{Hg(II)}$  based on the titration results. Further, **probe-54** showed good DNA intercalator abilities by fluorescence enhancement when bound to Ct-DNA and had a higher binding constant than amonafide, indicating that it might be used as a therapeutic candidate.

In 2017, Yao *et al.* synthesized two sulfur-rich Schiff base-based chemosensors, namely, **probe-55a** and **probe-55b**, with thiooxo-rhodamine and bithiophene units under sulfur-rich conditions, which provided better selectivity and highly

sensitive detection of  $\text{Hg(II)}$  *via* colorimetric and fluorometric responses.<sup>125</sup> The two **probes** were synthesized *via* a simple condensation reaction between thiooxo-rhodamine B hydrazone and [2,2-bithiophene]-5-carboxaldehyde in an ethanol solution under reflux conditions and characterized by several analytical techniques. The pure state of **probes** (Fig. 78) was found to be poorly emissive in nature, but upon addition of  $\text{Hg(II)}$  ions, the emission intensity gradually increased, whereas in the presence of other metal ions, no change in the emission spectra strongly supported the selectivity of **probes**. The determined LOD values for **probe-55a** and **probe-55b** were 0.62 ppb and 0.59 ppb, respectively with a high binding constant attributed to the sulphur environment. The fluorescence signal changing behavior of **probe-55a** was found to follow the FRET and **probe-55b** only demonstrated the traditional 'Off-On' response to  $\text{Hg(II)}$  addition. By comparing the bithiophene and rhodamine B-normalised spectra, **probe-55a**'s FRET process was established. The overlap region between the bithiophene and rhodamine B absorption and emission spectra suggested that FRET between the donor bithiophene and the recipient rhodamine (acceptor) could occur in this region. Both chemosensors demonstrated rapid response, high selectivity, and excellent sensitivity to  $\text{Hg(II)}$ , with visible color changes recognizable with the naked eye. In addition, the detection of trace  $\text{Hg(II)}$  ions in tap water and actual lake water with good recovery efficiency is a practical application of **probe-55a** and **probe-55b**. Additionally, the **probes** could be employed with low cytotoxicity by confocal fluorescence microscopy to see  $\text{Hg(II)}$  in live HeLa cells (Fig. 79).

In 2018, Singh and colleagues demonstrated a fluorescence turn-on signal for  $\text{Hg(II)}$  facilitated by a sensibly developed new Schiff base probe (**probe-56**).<sup>126</sup> The pure state of **probe-56** exhibited poor emission and dramatic rise in fluorescence intensity on titrating with  $\text{Hg(II)}$  ions, which could be explained by the conventional CHEF mechanism (Fig. 80), whereas in the presence of other competitive metal ions, no change in the emission intensity was observed. The binding constant and LOD of **probe-56** with  $\text{Hg(II)}$  ions were estimated as  $2.5 \times 10^4 \text{ M}^{-1}$  and 2  $\mu\text{M}$  respectively from the fluorescence titration spectra. Furthermore, **probe-56** displayed very intriguing features that discriminate two heavy metal ions such as  $\text{Hg(II)}$  ions with fluorescence turn-on and  $\text{Ag(I)}$  ions *via* the fluorescence turn-off mechanism. Due to the potentiality of **probe-56**, it could be applied for the recognition of both heavy metal ions simultaneously.

A facile fluorescent "turn-on" **probe** for  $\text{Hg(II)}$  ions was prepared *via* single-step condensation reactions between

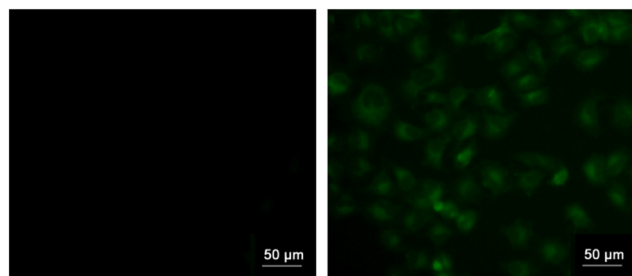


Fig. 76 Fluorescence microscopic images of HeLa cells incubated with **probe-53** (left) and **probe-53** +  $\text{Hg(II)}$  ions (right) (reprinted with permission from ref. 123, Copyright 2016 Elsevier).



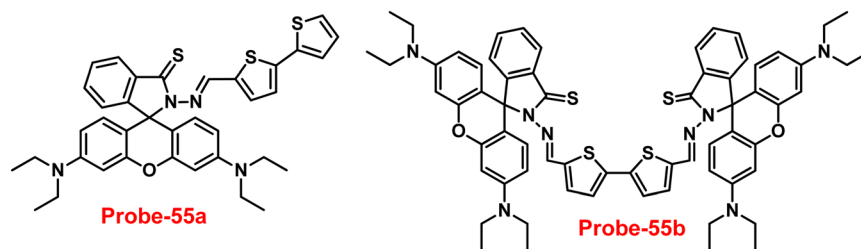


Fig. 78 Chemical structures of probe-55a and probe-55b (redrawn the ChemDraw structure from ref. 125).

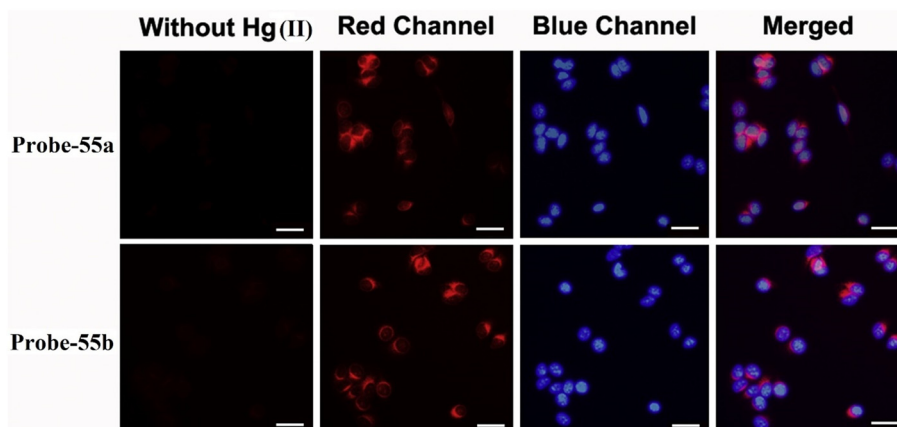


Fig. 79 Confocal fluorescence images of probe-55a and probe-55b in HeLa cells in the presence of Hg(II) ions (reprinted with permission from ref. 125, Copyright 2018 Elsevier).

2,3-diamino naphthalene and *o*-salicylaldehyde, and *m*, or *p*-hydroxybenzaldehyde, as demonstrated by Shen and co-workers in 2019.<sup>127</sup> The emission response of the **probes** towards Hg(II) ions can be explained by the geometry of **probes** that match the size of Hg(II) ions, and these results indicate that the **probe** containing a salicylaldehyde group is having more affinity towards Hg(II) with a binding ratio of 1 : 1. Increases in Hg(II) ion concentration were found to significantly increase the fluorescence intensity at the maximum emission peak of **probes** in an aqueous solution of ACN and water. This finding was interpreted as the result of an ESIPT-coupled AIEE process that was made possible by the coordination of the **probes** with Hg(II) ions (Fig. 81). The **probes** exhibit high sensitivity and selectivity over other interfering metal ions with a LOD value over 12.5 ppb.

In 2020, Lee *et al.* designed a rhodamine-based Schiff base (**probe-58**),<sup>128</sup> which was utilized for the synthesis of

fluorescent organic nanoparticles by a simple re-precipitation method. The optical properties of nanoparticles including UV-vis, emission and TCS-PC measurements are remarkably different from that of the parent organic moiety. According to the sensing studies, titrating with Hg(II) ions significantly enhance the emission of nanoparticles by nearly 7-fold more than its initial value among the series of heavy metal ions. The increased emission can be due to the CHEF, on better

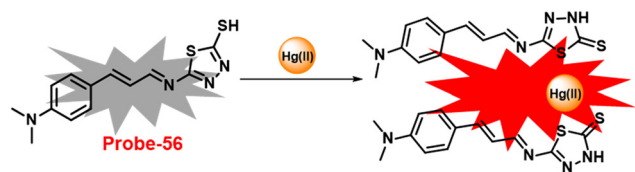


Fig. 80 Chemical structure and proposed sensing mechanism of probe-59 with Hg(II) (redrawn the ChemDraw structure from ref. 126).

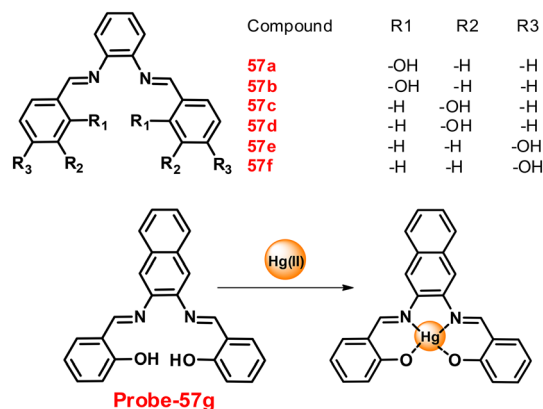


Fig. 81 Chemical structures of probe-57(a-f) and proposed sensing mechanism of probe-57g with Hg(II) (redrawn the ChemDraw structure from ref. 127).

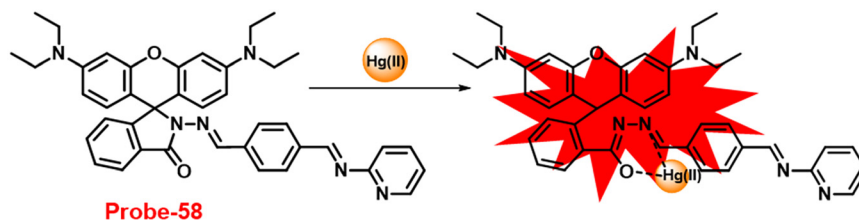


Fig. 82 Chemical structure and proposed sensing mechanism of **probe-58** with  $\text{Hg(II)}$  (redrawn the ChemDraw structure from ref. 128).

interactions of **probe-58** and  $\text{Hg(II)}$  ions with more reactive imine ( $\text{C=N}$ ) groups and oxygen (O) of carbonyl groups when the spirolactone ring of the rhodamine core is opened (Fig. 82). The LOD value of  $\text{Hg(II)}$  ions was estimated to be  $1.729 \text{ ng mL}^{-1}$  and the binding ratio of **probe-58** with  $\text{Hg(II)}$  ions to be 1:1. Moreover, the addition of a  $0\text{--}2 \text{ g mL}^{-1}$   $\text{Hg(II)}$  ion solution increases the lifetime value from  $5.63 \text{ ns}$  to  $6.12 \text{ ns}$ , indicating the formation of complexes in the excited state. The intracellular recognition of  $\text{Hg(II)}$  ions using **probe-58** is another advantage of prepared nanoparticles that will be probed for potential applications in the biomedical field (Fig. 83).

In 2021, Sekar and colleagues created a novel carbazole-hydrazinobenzothiazole sensor (**probe-59**)<sup>129</sup> that detects  $\text{Hg(II)}$  ions by emitting green fluorescence emission from a pool of other metal ions with the lowest LOD value of about

$0.14 \text{ }\mu\text{M}$ . **Probe-59** was synthesized from 9-ethyl-9H-carbazolyl-3-carbaldehyde and hydrazine benzothiazole in methanol under reflux conditions and was structurally characterized *via* various analytical techniques. The synthesized pure **probe-59** displayed poor emission upon coordination with  $\text{Hg(II)}$  ions *via* nitrogen atoms of the hydrazine unit with the sulphur atom of the benzothiazole unit resulting in the fluorescence enhancement and was determined by using  $^1\text{H}$  NMR, ESI-MS, and IR titration studies. Upon complexation with  $\text{Hg(II)}$  ions, the switch on the ICT between the benzothiazole moiety and the carbazole unit could be related to its sensing behavior (Fig. 84). Using one- and three-dimensional fluorescence spectral analysis, it was also determined whether **probe-59** could be used to target metal ions in proteins and subcellular organelles in cells and other organisms. The

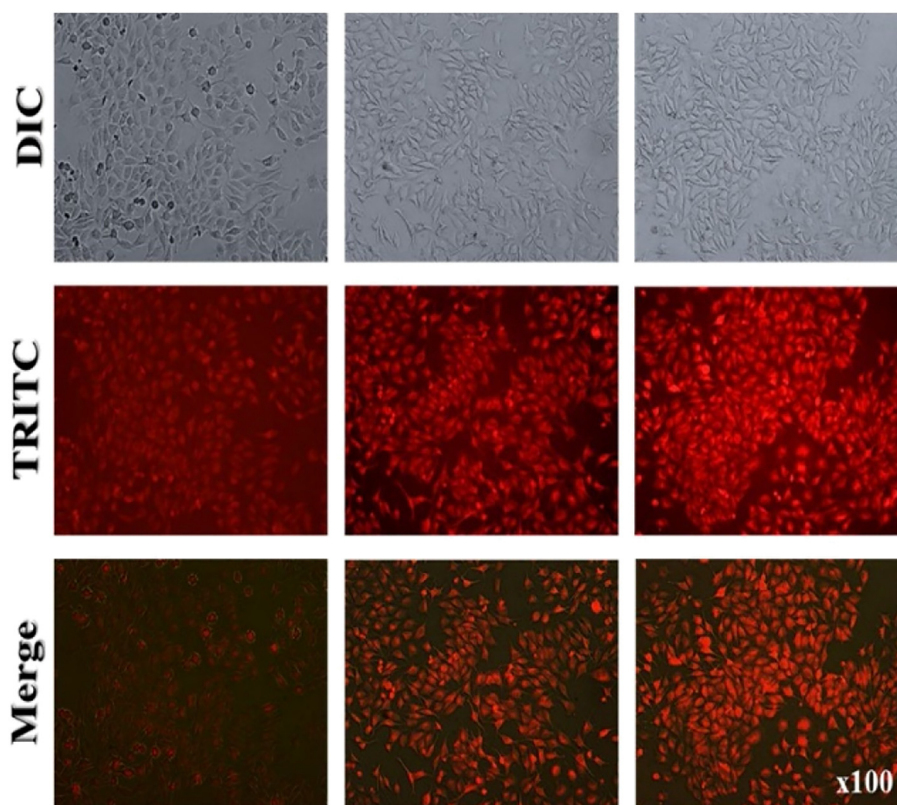


Fig. 83 Fluorescence microscopic images of **probe-58** in living A375 cells with  $\text{Hg(II)}$  ions. (reprinted with permission from ref. 128, Copyright 2020 Elsevier).



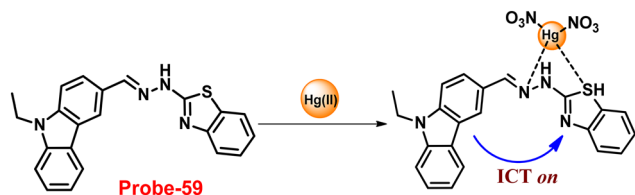


Fig. 84 Chemical structure and proposed sensing mechanism of **probe-59** with  $\text{Hg(II)}$  (redrawn the ChemDraw structure from ref. 129).

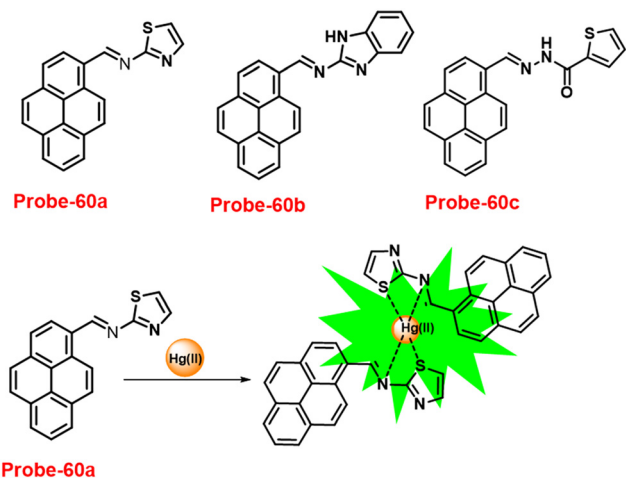


Fig. 85 Chemical structures of **probe-60a–c** (top) and sensing mechanism of **probe-60a** with  $\text{Hg(II)}$  (bottom) (redrawn the ChemDraw structure from ref. 130).

potential ability in electrochemical sensing of  $\text{Hg(II)}$  ions was investigated by CV analysis of **probe-59** with different metal ions. The results indicated that **probe-59** exhibits a shift to a higher oxidation potential in the presence of  $\text{Hg(II)}$ , demonstrating the possibility of an electrochemical process caused by the CHEF effect and showing no effect for the other metal ions.

In 2019, Trivedi and colleagues prepared simple pyrene-based probes **60a–c** from pyrene-1-carboxaldehyde and different types of amines, and characterized by FT-IR, ESI-Mass, UV-vis,  $^1\text{H}$  NMR, and  $^{13}\text{C}$  NMR.<sup>130</sup> The synthesized compounds are very weak emissive in nature; upon addition of  $\text{Hg(II)}$  ions, the emission was gradually increased in which **probe-60a** showed better efficiency. Conversely, with other metal ions, there was no change in fluorescence spectra. The authors proposed the binding ability of **probes** with  $\text{Hg(II)}$

ions; first, the  $\text{C=N}$  (imine) link of the thiazole moiety is hydrolyzed by  $\text{Hg(II)}$ , whereas pyrene-carboxaldehyde molecules operate as 'turn-on' chemodosimeters for  $\text{Hg(II)}$  ions (Fig. 85). The detection limit of **probe-60a** with  $\text{Hg(II)}$  ions was found to be  $0.270\ \mu\text{M}$ . Additionally, the **probe-60a**'s chemodosimetric irreversible hydrolysis was investigated by FT-IR spectroscopy, UV/Vis, liquid chromatography with tandem mass spectrometry (LC-MS), fluorescence,  $^1\text{H}$  NMR, and DFT analysis.

Duan *et al.* fabricated novel Schiff-based luminescent probes (**probe-61a** and **probe-61b**) (Fig. 86), with triazolyl and rhodamine hydrazide conjugates<sup>131</sup> that selectively recognize  $\text{Hg(II)}$  ions, exhibiting major color change from colorless to pink and emission turn-on mechanism, while upon titration with other competitive metal ions, there was no change in the fluorescence spectra in 2020. The addition of 1.0 eq. of  $\text{Hg(II)}$  ions caused 600-fold and 350-fold enhancement in the emission intensity of **probe-61a** and **probe-61b**, respectively, which could be attributed to a reduction in the PET process and  $\text{C=N}$  isomerization on  $\text{Hg(II)}$  ion coordination. The LOD value was measured to be  $13.4\ \text{nM}$  and  $15.6\ \text{nM}$  respectively for both **probe-61a** and **probe-61b** toward  $\text{Hg(II)}$  ions using the equation  $\text{DL} = 3\sigma/\text{slope}$ . Due to their potentiality, these **probes** can be utilized in future applications for the recognition of  $\text{Hg(II)}$  in various media. The DFT studies predicted the equivalent molecular geometric arrangement, orbital electron distribution, and orbital energy of both **probes** with their metal complexes. Job's plot analysis gave a binding ratio of 1:1, and further, the **probes** were fruitfully used for imaging  $\text{Hg(II)}$  ions in live breast cancer cells and MCF-7 cells, illustrating the **probe's** applications for biological- $\text{Hg(II)}$  ion detection (Fig. 87).

In 2016, Lee *et al.* developed **probe-62** (ref. 132) by combining quinolone-hydrazino-1,8-naphthalimide conjugates for sensitive and selective sensing of  $\text{Hg(II)}$  ions. The target compound was synthesized with 2-(2-(dimethylamino)ethyl)-6-hydrazinyl-1H-benzo[d,e]isoquinoline-1,3(2H)-dione and 8-hydroxy-2-quinolinecarboxaldehyde in ethanol under reflux conditions and was structurally characterized by various analytical techniques. The native state of **probe-62** displayed poor emission, upon incorporation of  $\text{Hg(II)}$  ions due to the absence of PET; the emission intensity progressively enhanced 6-fold at  $535\ \text{nm}$  (Fig. 88) and no change was observed with other metal ions. The LOD value of **probe-62** for  $\text{Hg(II)}$  ions was observed to be  $0.24\ \mu\text{M}$ , and Job's plot analysis discovered a complex ratio of 1:1 with a binding constant of  $4.12 \times 10^5\ \text{M}^{-1}$ . In addition, **probe-62**

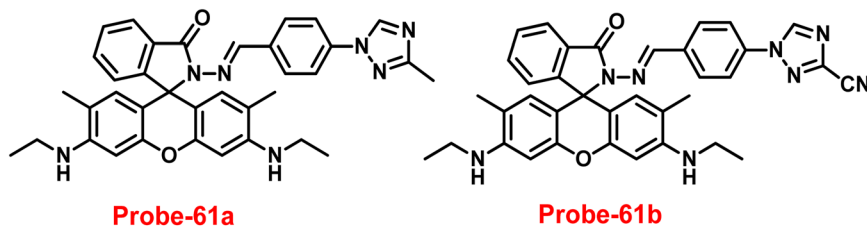


Fig. 86 Chemical structures of **probe-61a** and **probe-61b** (redrawn the ChemDraw structure from ref. 131).





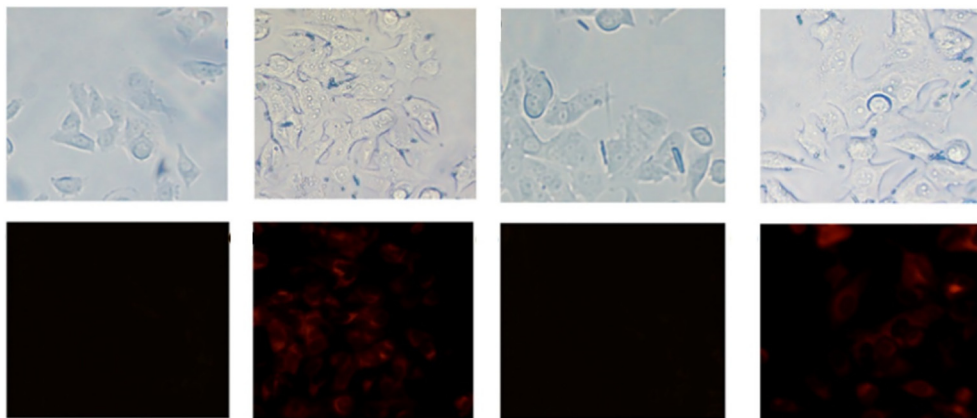


Fig. 87 Fluorescence images of MCF-7 cells treated with **probe-61a** (left) and **probe-61b** (right) with  $\text{Hg(II)}$  ions. (reprinted with permission from ref. 131, Copyright 2020 American Chemical Society).

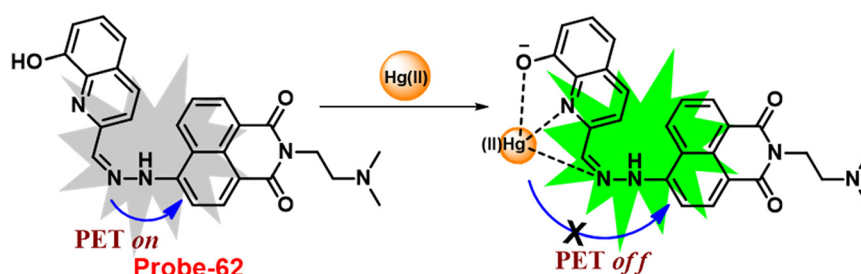


Fig. 88 Chemical structure and proposed sensing mechanism of **probe-62** with  $\text{Hg(II)}$  (redrawn the ChemDraw structure from ref. 132).

changes color in response to the anions  $\text{CN}^-$  and  $\text{F}^-$ , agreeing for dual mode detection of several analytes.

In 2017, Wu *et al.* synthesized a Schiff base sensor (**probe-63**)<sup>133</sup> by the combination of rhodamine B hydrazide and 2-(phenylselanyl)benzaldehyde, and it was structurally characterized by  $^1\text{H}$  NMR,  $^{13}\text{C}$  NMR, and HRMS data. In  $\text{CH}_3\text{-OH}/\text{H}_2\text{O}$  (v/v 9:1) solutions, **probe-63** demonstrates high selectivity and sensitivity towards  $\text{Hg(II)}$  ions and the color changed to pink with 48-fold fluorescence amplification, which is caused by the ring opening of the rhodamine unit (Fig. 89), whereas no change was observed in the absorption and emission spectra with other competitive metal ions. In addition, the molecule binds to  $\text{Hg(II)}$  in a 1:1, which was validated by Job's plot and was supported by the ESI-MS and DFT calculations. The LOD value of **probe-63** from the

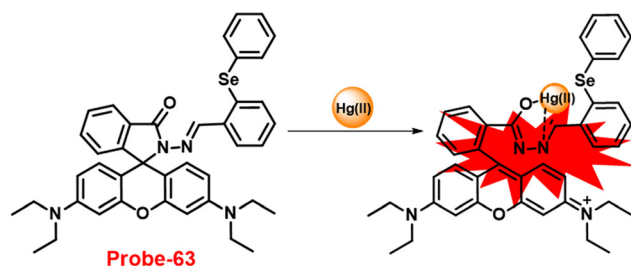


Fig. 89 Chemical structure and proposed sensing mechanism of **probe-63** with  $\text{Hg(II)}$  (redrawn the ChemDraw structure from ref. 133).

fluorescence titration spectra was calculated to be 12 nM and could be utilized effectively for  $\text{Hg(II)}$  sensing over a wide pH range of 4.0–10.0. Finally, the authors applied **probe-63** for sensing  $\text{Hg(II)}$  ions in *in vitro* and *in vivo* studies, including test strips, bio imaging in HeLa cells and zebrafish with the help of confocal fluorescence microscopy (Fig. 90).

In 2019, Wang *et al.* developed a novel chemosensor, **probe-64**,<sup>134</sup> using a commercially accessible pyrazole derivative and rhodamine 6G as the precursors and structurally described it *via* various analytical and spectroscopic analysis. **Probe-64** showed high fluorescence “turn-on” behavior towards  $\text{Hg(II)}$  ions in an aqueous DMSO solution *via* a complexation reaction, and the color changed from colorless to pink even in the presence of other interfering metal ions, which strongly suggested that **probe-64** was very selective towards  $\text{Hg(II)}$  ions. **Probe-64** exhibits good fluorescence amplification on introducing  $\text{Hg(II)}$  ions, because of the extended conjugated structure, which may be related to the hindered PET process and CHEF behavior (Fig. 91). The LOD value was as low as 0.2 nM, making them appropriate for the quantitative determination of  $\text{Hg(II)}$  ions in aqueous media. Job's plot revealed a binding ratio of 1:1 for the **probe-64**– $\text{Hg(II)}$  complex. It was further demonstrated that it was a straightforward and efficient solid-state probe because the color of the sensor substantially changed when it was impregnated on filter paper and submerged in a  $\text{Hg(II)}$  solution.



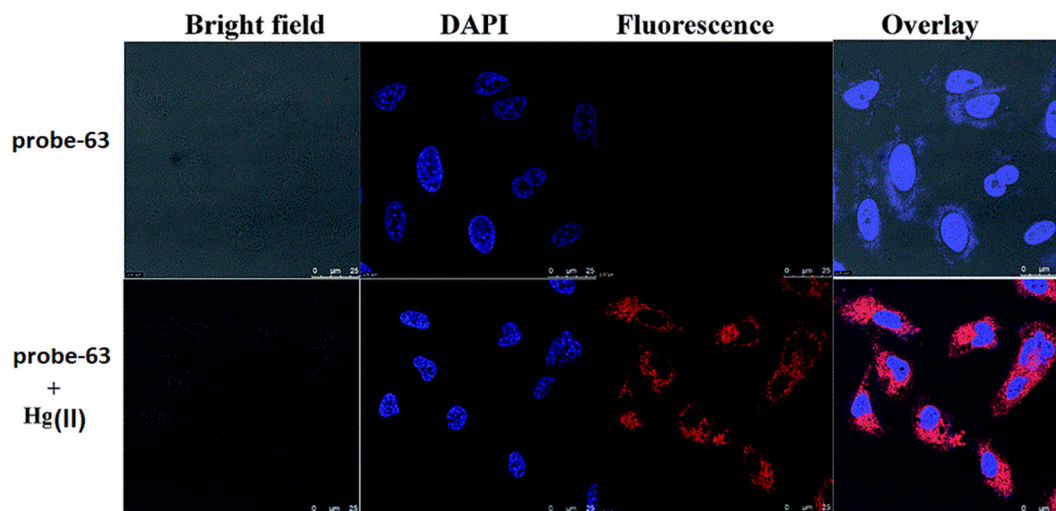


Fig. 90 Confocal microscopic images of **probe-63** treated with  $\text{Hg(II)}$  ions in HeLa cells. (reprinted with permission from ref. 133, Copyright 2017 Royal Society of Chemistry).

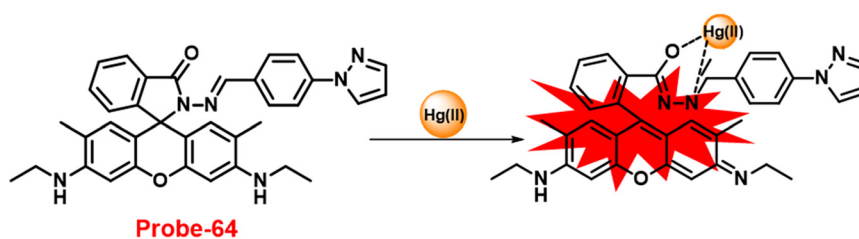


Fig. 91 Chemical structure and proposed sensing mechanism of **probe-64** with  $\text{Hg(II)}$  (redrawn the ChemDraw structure from ref. 134).

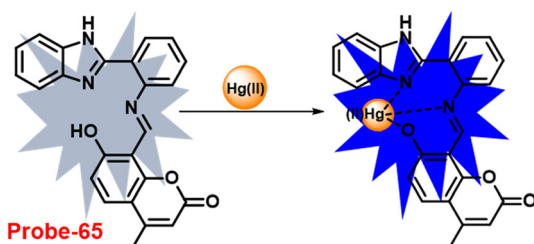


Fig. 92 Chemical structure and proposed sensing mechanism of **probe-65** with  $\text{Hg(II)}$  (redrawn the ChemDraw structure from ref. 135).

In 2017, Chen *et al.* focused on the synthesis of a unique Schiff base probe (**probe-65**)<sup>135</sup> via a simple condensation reaction of 7-hydroxy-4-methyl-2-oxo-2H-chromene-8-

carbaldehyde and 2-(2-aminophenyl)benzimidazole in ethanol under reflux conditions, which was characterized by multinuclear ESI-MS, IR, and NMR. The pure form of **probe-65** displayed poor emission, upon addition of  $\text{Hg(II)}$  ions the sudden increment in fluorescence, implies that  $\text{Hg(II)}$  ions stimulated hydrolysis of a  $\text{Hg(II)}$ -**probe-65** complex transforms the imine group to the aldehyde group (Fig. 92). A Job's plot reveals 1:1 binding, and the **probe-65**- $\text{Hg(II)}$  binding constant was calculated as  $8.75 \times 10^4 \text{ M}^{-1}$ . Furthermore, the **probe-65** was successfully used in cell imaging, indicating that it has a potential application for sensing  $\text{Hg(II)}$  ions in living cells (Fig. 93).

Chatterjee *et al.* synthesized a 1,1'-unsymmetrical substituted ferrocene-based chemosensor (**66a-c**),<sup>136</sup> which shows a sensitive and selective fluorescence turn-on behavior towards  $\text{Hg(II)}$  ions via selective functionalization of

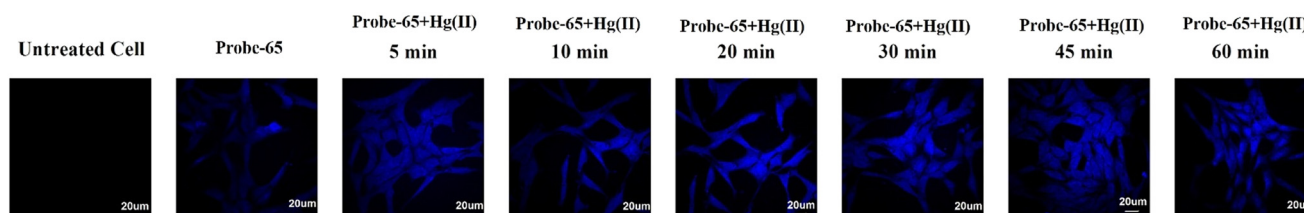


Fig. 93 Bio-imaging of **probe-65** treated with  $\text{Hg(II)}$  ions in HeLa cells. (reprinted with permission from ref. 135, Copyright 2017 Elsevier).

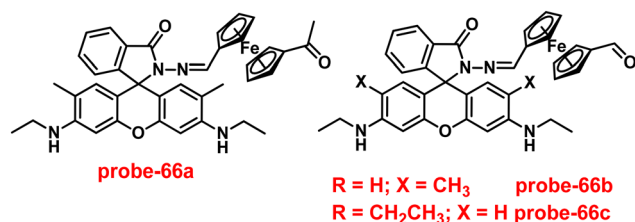


Fig. 94 Chemical structures of **probe-66a–c** (redrawn the ChemDraw structure from ref. 136).

ferrocenyl species with a fluorescent active rhodamine moiety in 2021. The **probes** (Fig. 94) possess active organometallic complexes with rhodamine moieties, demonstrating the exceptional recognition ability of metal ions in solutions and at the subcellular level. The native state of the **probes** was found to be very poorly emissive in nature, and upon incorporation of Hg(II) ions, the emission properties drastically change with quantum yields, while with other competitive metal ions, there was no change in the emission spectra. The DFT studies and spectroscopic analysis have been used to establish the binding nature of the unsymmetrical ferrocene-based rhodamine organometallic **probes** with Hg(II) ions. The study also showed the significant intracellular metal identification and imaging properties, which can be used in applications related to the bio-imaging of heavy metal ions. The bio-imaging investigation of the

THP-1 cancer cell line revealed significant chemical bioaccumulation and interactions with heavy metal ions (Fig. 95). The unsymmetrical ferrocenyl-rhodamine derivatives showing turn-on response were also used to monitor various molecular logic operations.

In 2016, Zang and colleagues developed a rhodamine B conjugate with a NS<sub>2</sub>-containing sensor (**probe-67**),<sup>137</sup> which could be used as a dual probe for Cu(II) colorimetrically and Hg(II) ions fluorogenically. The target compound was structurally characterized *via* various analytical and spectroscopic techniques. The native mode of **probe-67** displayed poor fluorescence intensity; upon titration with Hg(II) ions, the emission intensity drastically enhanced under aqueous conditions, while Cu(II) ions showed an exceptional colorimetric response. The interference of other examined environmentally relevant species did not affect **probe-67**, which strongly suggested that **probe-67** has a potential ability to detect Hg(II) ions *via* the fluorescence turn-on mechanism (Fig. 96) and Cu(II) *via* colorimetric response. **Probe-67** showed very good selectivity towards Cu(II) and Hg(II) in aqueous solutions at a physiological pH, with very low LOD values of 1.63 μM and 2.36 μM, correspondingly. The authors proposed the sensing mechanism of **probe-67**; when spirolactam was opening upon metal binding, the coordination mechanism results in ring opening, which causes a high UV-vis absorption and fluorescence amplification in both recognition processes. A

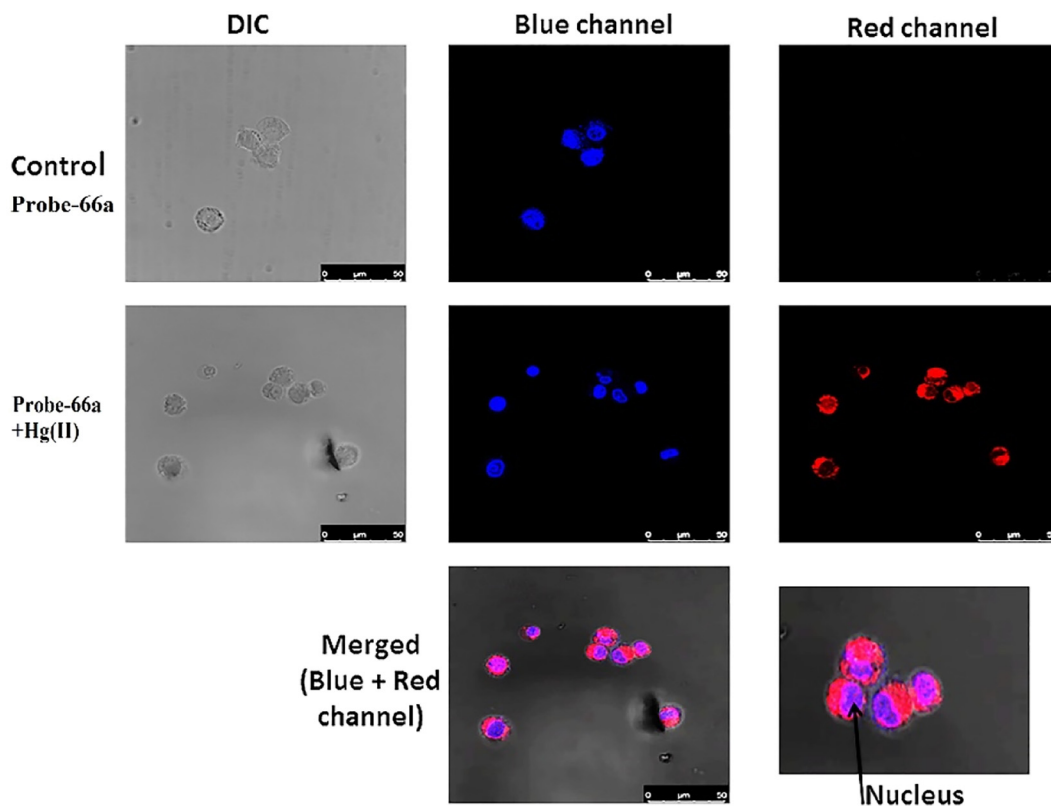


Fig. 95 Confocal fluorescence images of THP-1 cells of **probe-66a** with Hg(II) ions. (reprinted with permission from ref. 136, Copyright 2021 Elsevier).



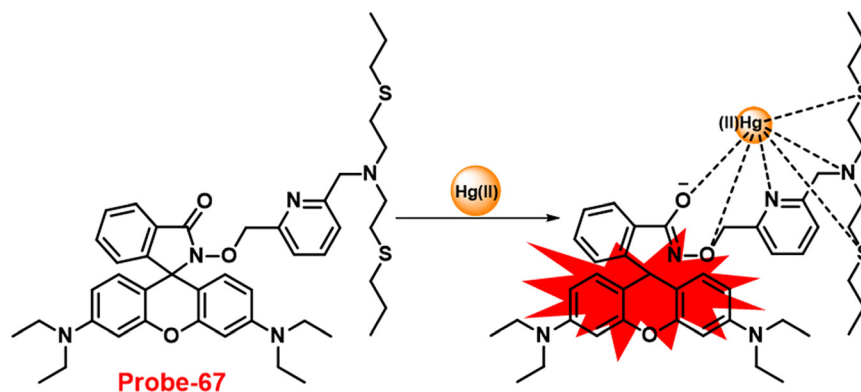


Fig. 96 Chemical structure and proposed sensing mechanism of probe-67 with Hg(II) (redrawn the ChemDraw structure from ref. 137).

proof-of-concept test illustrates the possible use of **probe-67** for the recognition of trace Hg(II) and Cu(II) in challenging environment water samples. Furthermore, **probe-67**, which has good membrane permeability, is successfully used in microscopic imaging to detect Hg(II) ions in PC3 cells (Fig. 97).

In 2021, Lee *et al.* synthesized a new fluorescent chemosensor, **probe-68**, based on rhodamine 6G for the selective sensing of Hg(II) ions.<sup>138</sup> The sensing studies were carried out with Hg(II) ions and other metal ions in the combined organic aqueous phase, and the fluorescent chemosensor (**probe-68**) (Fig. 98) exhibits exceptional sensitivity and selectivity for Hg(II) ions. The sensing mechanism of **probe-68** demonstrated enhanced fluorescence with the Hg(II) ions, which caused the spirocyclic form (spirolactum) to change into an open-ring form. According to Job's plot and <sup>1</sup>H NMR experiment, the stoichiometric ratio of the **probe-68**-Hg(II) complex was

found to be 1:1. For **probe-68**-Hg(II) complexation, the calculated association constant and LOD were  $6 \times 10^4 \text{ M}^{-1}$  and 30.37 nM, respectively. The Hg(II) metal ion was successfully detected by a spike and recovery method from actual water samples in practical use. **Probe-68** was also utilized for the sensing of Hg(II) ions in biological media, which was carried out by the MTT assay for the cytotoxicity and the data showed very low cytotoxicity, providing valuable information for the identification of intracellular Hg(II) ions in MDA-MB-231 and A375 breast cancer cells (Fig. 99).

In 2017, Li *et al.* developed a rhodamine-based sensor, **probe-69**, for detecting Hg(II) ions<sup>139</sup> by the reflux reaction of rhodamine 6G hydrazide and 7-diethylamino-3-(1-hydroxy-3-oxobut-1-enyl)-2H-chromen-2-one and structurally characterized it by various analytical and spectroscopic techniques. **Probe-69** (Fig. 100) demonstrated remarkable selectivity towards Hg(II) under neutral aqueous conditions as a colorimetric and ratiometric fluorescent sensor. More remarkably, **probe-69** could sense Hg(II) with emission amplification at moderately high pH values. Under such conditions, **probe-69** showed colorimetric response towards Cu(II) ions, whereas upon titrating with other metal ions, there was no change in emission spectra as well as absorption spectra. Job's plot analysis revealed that the binding of **probe-69** to Hg(II) is of 1:1 stoichiometry from the absorption spectra. **Probe-69** could find use as a Hg(II) detector in living cells (Fig. 101) or water samples.

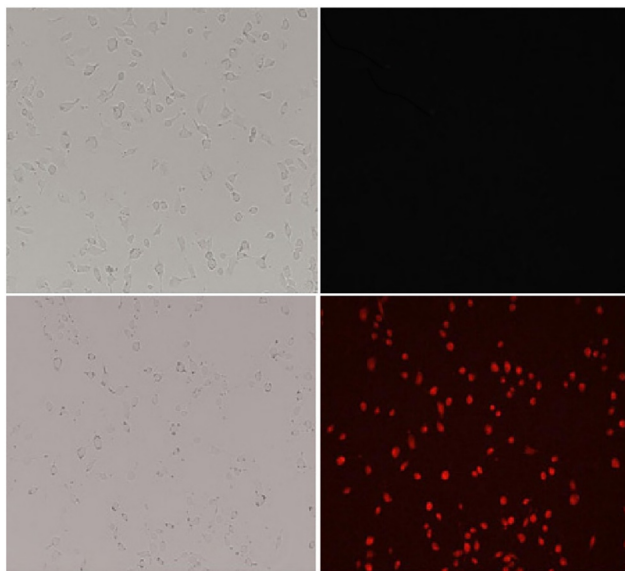


Fig. 97 Confocal fluorescence images of PC3 cells of probe-67 with Hg(II) ions. (reprinted with permission from ref. 137, Copyright 2016 Elsevier).

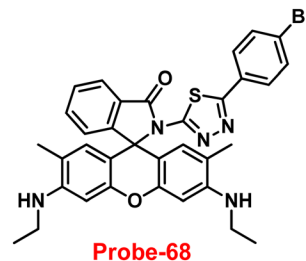


Fig. 98 Chemical structure of probe-68 (redrawn the ChemDraw structure from ref. 138).





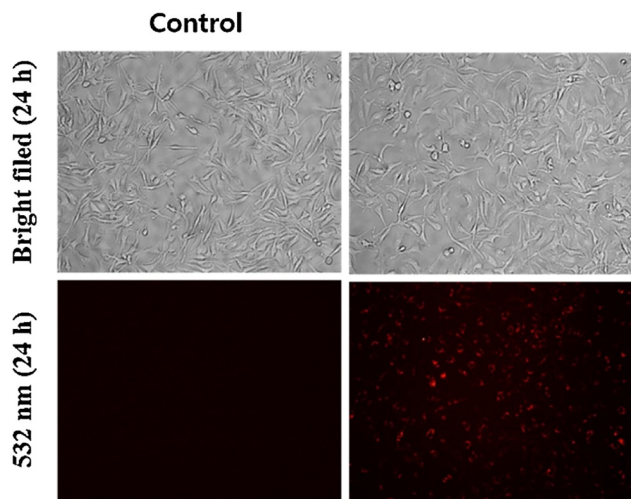


Fig. 99 Bio-imaging images of living MDA-MB-231 cells with **probe-68** and **probe-68** + 5  $\mu\text{M}$   $\text{Hg(II)}$  ions (reprinted with permission from ref. 138, Copyright 2021 Elsevier).

#### 4. Schiff base-based fluorescent turn-on probes for $\text{Cd(II)}$ ions

Despite their toxicity, heavy metals have potential uses. For instance, cadmium is used in pigments, electroplating, metallurgy, batteries, and agriculture.<sup>140–143</sup> In contrast, it has been discovered that cadmium metal is extremely hazardous and dangerous to people health even at very low levels.<sup>144–146</sup> As a result, it is imperative to design and synthesize probes that respond to  $\text{Cd(II)}$  ions for quantitative and qualitative examination in both biological and environmental samples due to the presence of its benefits and drawbacks.<sup>147–149</sup>

In 2019, the widespread health hazardous effects of  $\text{Cd(II)}$  influenced Wan *et al.* to develop a quinoline-containing Schiff base (**probe-70**) (Fig. 102),<sup>150</sup> which showed very high selectivity and sensitivity for the on-site recognition of  $\text{Cd(II)}$  ions. The target compound was obtained *via* a simple condensation reaction between ethylenediamine and quinoline aldehyde in an ethanol solution under reflux conditions, which was structurally characterized by various analytical and spectroscopic techniques. The native state of **probe-70** showed poor emission, and on titrating with  $\text{Cd(II)}$  ions, the emission

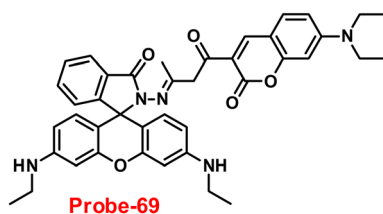


Fig. 100 Chemical structure of **probe-69** (redrawn the ChemDraw structure from ref. 139).

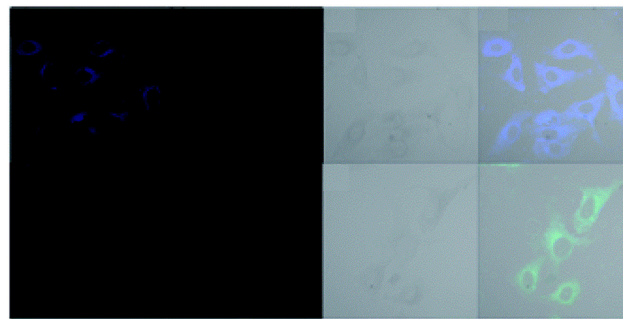


Fig. 101 Bio-imaging images of HeLa cells with **probe-69** (reprinted with permission from ref. 139, Copyright 2017 Royal Society of Chemistry).

intensity gradually increased and reached maxima after addition of 1 eq., whereas in the presence of other competitive metal ions, evident changes cannot be observed in the fluorescence spectra, which strongly suggested the potential of **probe-70** for the selective detection of  $\text{Cd(II)}$  ions (Fig. 103). **Probe-70** was sparklingly soluble in water and titration was conducted in methanol water combination at pH 7. Job's plot measurement indicated 1:1 stoichiometric complexation among **probe-70** and  $\text{Cd(II)}$  ions, which was strongly supported by  $^1\text{H}$  NMR and ESI-MS analysis. The LOD value of **probe-70** was calculated from emission titration spectra to be 2.4 nM.

In order to overcome the limitation of previously synthesized  $\text{Cd(II)}$  probes for the recognition of  $\text{Cd(II)}$  over  $\text{Zn(II)}$  in aqueous solutions, Rajesh *et al.* developed a quinoline-based Schiff base (**probe-71**)<sup>151</sup> in 2021, which detected  $\text{Cd(II)}$  in a semi aqueous medium and was synthesized by the reaction between 2-hydroxy-1-naphthalene carboxaldehyde and 2-hydrazino quinolone. The absorption data of **probe-71** with  $\text{Cd(II)}$  showed colorimetric response and changes from colorless to yellow-orange in  $\text{ACN-H}_2\text{O}$  (8:2, v/v). However, the fluorescence intensity of **probe-71** displayed poor emission, and upon addition of  $\text{Cd(II)}$  ions, the emission intensity was gradually increased 37-fold its original intensity at 510 nm. Under similar conditions, with other competitive metal ions, there was no change in the fluorescence spectra. The sensing mechanism of **probe-71** with  $\text{Cd(II)}$  was explained by the restriction of  $\text{C=N}$  isomerization and CHEF effects (Fig. 104). The LOD value of **probe-71** with  $\text{Cd(II)}$  ions was estimated to be 49.5 nM from the titration spectra using

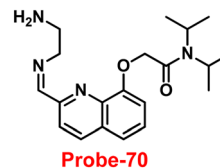


Fig. 102 Chemical structure of **probe-70** (redrawn the ChemDraw structure from ref. 150).



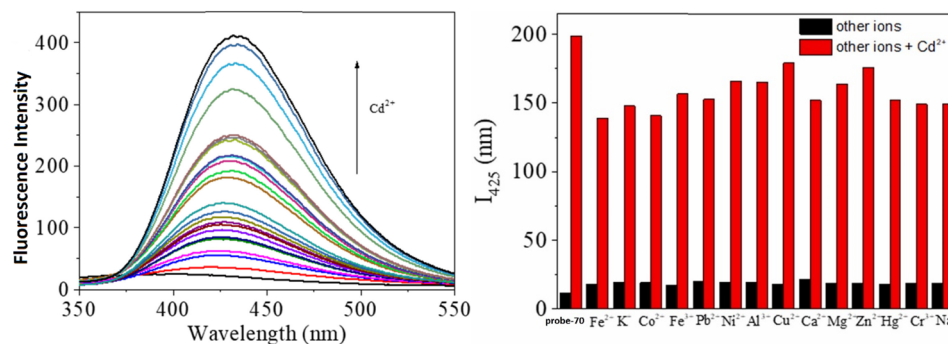


Fig. 103 Change in the emission spectra of **probe-70** upon increasing the concentration of Cd(II) ions (left) and with different metal ions (right) (reprinted with permission from ref. 150, Copyright 2019 Elsevier).

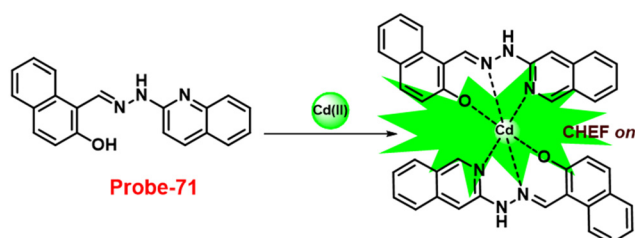


Fig. 104 Chemical structure and proposed sensing mechanism of **probe-71** with Cd(II) (redrawn the ChemDraw structure from ref. 151).

the  $3\sigma/\text{slope}$  equation. The binding constant was estimated to be  $1.77 \times 10^5 \text{ M}^{-1}$ . The stoichiometry of **probe-71** with Cd(II) ions was estimated to be 2:1 via Job's plot, which was confirmed by DFT, <sup>1</sup>H NMR and ESI-MS data.

In 2021, Lu *et al.* concentrated on the synthesis of a purine-constructed Schiff base-based fluorescent turn-on probe (**probe-72**)<sup>152</sup> for the recognition of Cd(II) ions in an EtOH-H<sub>2</sub>O solution. **Probe-72** was synthesized via a simple condensation reaction between 6-hydrazinyl-8-methyl-9-(naphthalen-1-yl)-9H-purine and quinoline-2-carbaldehyde in an ethanol solution under reflux conditions and structurally characterized by various analytical techniques. The pure form of **probe-72** showed very poor emission due to the presence of PET and C=N isomerism; upon incorporation of Cd(II) ions, the luminescence intensity was drastically increased and on titrating with other competitive metal ions, no change was observed in the emission spectra (Fig. 105). From the emission spectra, it was observed that the intensity of the peak at 530 nm increased with the gradual addition of Cd(II) and the detection limit was found to be 41 nM. Job's plot

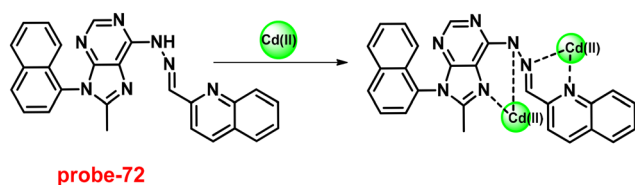


Fig. 105 Chemical structure and proposed sensing mechanism of **probe-72** with Cd(II) (redrawn the ChemDraw structure from ref. 152).

revealed the 1:2 stoichiometric complexations between **probe-72** and Cd(II) ions, which was strongly supported by <sup>1</sup>H NMR, IR and ESI-MS data. Further, the authors focused on the effect of pH on **probe-72** and showed that they did not produce any fluorescence change within the pH range of 6–11, whereas upon adding Cd(II), the fluorescence intensity exclusively amplified at pH 2–11, indicating that the detection of Cd(II) ions with **probe-72** was suitable for physiological pH. Apart from acting as a fluorescent probe, inoculating **probe-72** in HeLa cells in *in vivo* cell imaging was achieved by sensing Cd(II) ions by fluorescence microscopy without causing any harm to the cell line (Fig. 106).

In 2021, Khan and his colleagues created a novel Schiff base using a benzothiazole unit, which was obtained from the condensation reaction between 2-hydrazinobenzothiazole and 2-hydroxy-1-naphthaldehyde in ethanol under reflux conditions and was described by various spectroscopic and analytical techniques.<sup>153</sup> **Probe-73** exhibited poor emission; however, on adding Cd(II) ions, the emission intensity drastically increased and attained maxima after addition of one eq., which is due to the combined effect of ICT and CHEF (Fig. 107). However, with other metal ions, there was no change in fluorescence spectra, which strongly suggested

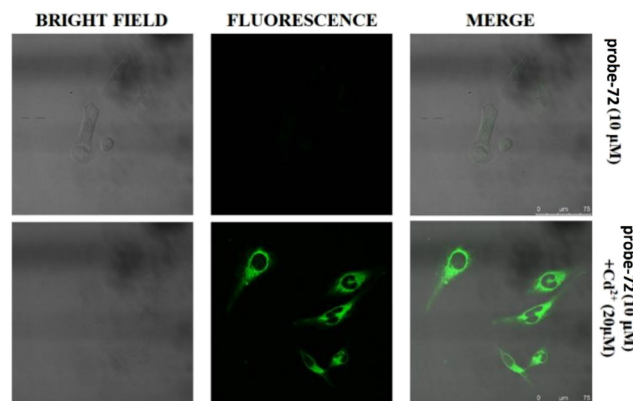


Fig. 106 Fluorescence microscopic imaging of **probe-72** in HeLa cells (top) in the presence of Cd(II) (bottom) (reprinted with permission from ref. 152, Copyright 2021 Elsevier).



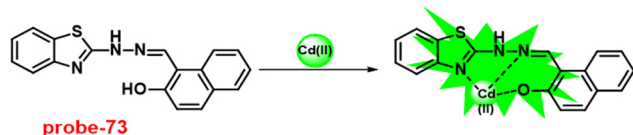


Fig. 107 Chemical structure and proposed sensing mechanism of **probe-73** with Cd(II) (redrawn the ChemDraw structure from ref. 63).

**probe-73** selective towards Cd(II) ions. B-H and the Job's plot approach both confirm that the binding ratio between **probe-73** and Cd(II) is 1:1. A binding constant of  $1.17 \times 10^4 \text{ M}^{-1}$  and detection limits in the micromolar range were calculated for **probe-73** with Cd(II) ions from the fluorescence titration spectra. Furthermore, the authors utilized **probe-73** for the sensing of Cd(II) ions in biological media; the HeLa cells were incubated with **probe-73** and showed no fluorescence, and in the presence of Cd(II) ions, the emission was generated inside the cells (Fig. 108), which strongly suggested that **probe-73** shows potential for the recognition of Cd(II) ions in biological media.

In 2020, a Schiff base fluorescent chemosensor (**probe-74**)<sup>154</sup> for the sensing of Cd(II) ions was prepared by Shuang *et al.* via a one-pot and one-step condensation reaction between 2,3-naphthalene diamine and imidazole-2-carboxaldehyde in MeOH under reflux conditions. The native state of **probe-74** showed poor emission and showed response towards Cd(II) ratiometrically over Zn(II) ions, whereas no response was observed for the other metals. The emission maxima were shifted towards the blue region for 74 nm with the consequently enhanced emission by the complexation of Cd(II) ions with **probe-74**, because of the suppression of the ICT process (Fig. 109). Some changes were observed in the ratio of fluorescence intensities ( $F_{398}/F_{472}$ ), on adding 1 eq. of metal ions and the 1:1 binding of **probe-74** with Cd(II), enabling the ratiometric sensing of Cd(II) ions

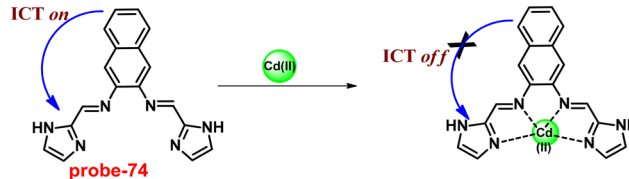


Fig. 109 Chemical structure and proposed sensing mechanism of **probe-74** with Cd(II) (redrawn the ChemDraw structure from ref. 154).

with a LOD value of  $0.38 \mu\text{M}$ . Additionally, confocal fluorescence microscopy was used to examine the use of **probe-74** to sense Cd(II) ions in human liver cancer cells (SMMC-7721), zebrafish, and live tissues of *Arabidopsis thaliana*, revealing that it can be used to monitor Cd(II) ions in various biological contexts with low toxicity (Fig. 110).

## 5. Schiff base-based fluorescent turn-on probes for Au(III) ions

Due to the relevance of gold in the fields of chemistry, biology, environmental protection, and medicine, it has gained a great deal of research interest.<sup>155–158</sup> Gold complexes are also used in biological systems and for the treatment of diseases such as tuberculosis, AIDS, cancer, asthma, brain lesions, rheumatoid arthritis, malaria, and asthma because of their catalytic activity, which is especially useful in chemical synthesis.<sup>159–164</sup> Therefore, it is crucial to recognize gold metal ions, and researchers concentrated on developing probes to find Au(I) and Au(III) ions.

The widespread use of Au(III) as a catalyst in numerous organic reactions, as well as the health risks associated with Au(III), prompted the researchers to develop a selective sensitive approach for detecting Au(III) ions. In this regard, Mondal *et al.* synthesized a rhodamine-appended naphthalene-based Schiff base (**probe-75**) in 2020 (Fig. 111),<sup>165</sup> which acts as a sensitive, selective fluorescence turn-on sensor for the detection of Au(III) ions. **Probe-75** was prepared by the condensation reaction of rhodamine B hydrazide and 4-hydroxy-1-naphthaldehyde followed by treatment with 1-fluoro-2,4-dinitrobenzene in

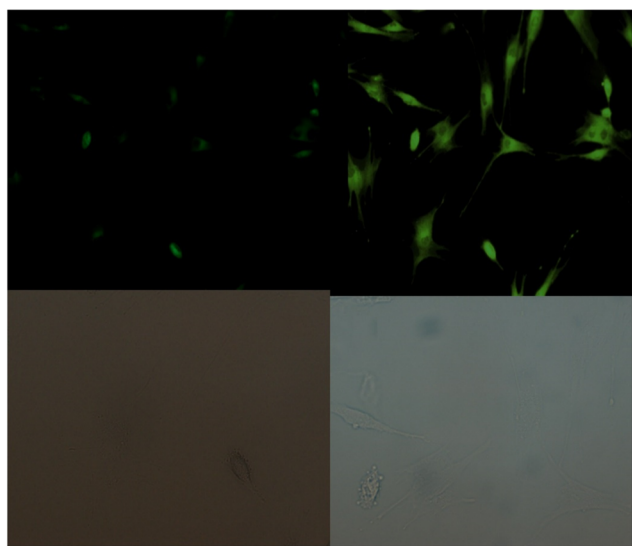


Fig. 108 Fluorescence microscopic imaging of **probe-73** in HeLa cells (reprinted with permission from ref. 153, Copyright 2021 Elsevier).

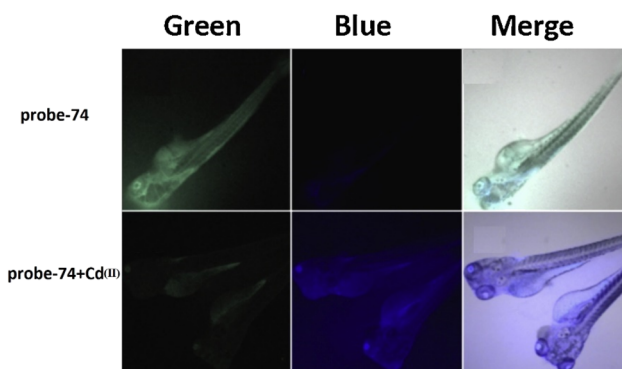


Fig. 110 Fluorescence microscopic imaging of **probe-74** in zebra fish (reprinted with permission from ref. 154, Copyright 2020 Elsevier).





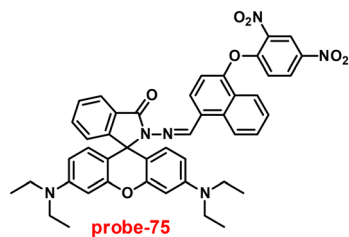


Fig. 111 Chemical structure of **probe-75** (redrawn the ChemDraw structure from ref. 165).

acetonitrile under reflux conditions, which was confirmed by several spectroscopic and analytical techniques. The native state of **probe-75** was poorly emissive in nature; on titrating with Au(III) ions, the emission intensity was drastically enhanced and attained saturation after addition of one eq. with a shift in the color of the solution from colorless to orange, while with other competitive metal ions, there was no influence on the fluorescence spectra. Furthermore, **probe-75** showed a colorimetric response towards Au(III) ions and the color shifts from colorless to pink color in CH<sub>3</sub>CN–H<sub>2</sub>O (1:1, v/v), which could be utilized for real-time monitoring. A further binding mechanism of **probe-75** was proposed by the authors and ring opening of spirolactum and suppression of PET process, which was supported by the ESI-MS, FT-IR and DFT calculations. The LOD value of **probe-75** with Au(III) was calculated to be 1.51 μM from the fluorescence titration data using the equation  $3\sigma/\text{slope}$ . Considering the ability of **probe-75** to act as a selective and sensitive fluorescent turn-on probe, *in vivo* cell imaging was achieved by inoculating **probe-75** in MC3T3 cells with very low cytotoxicity (determined by the MTT assay) (Fig. 112).

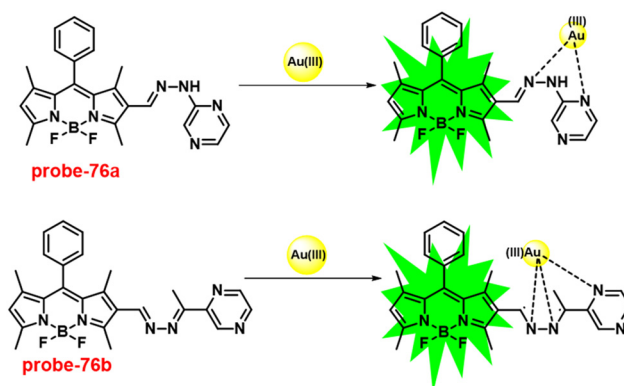


Fig. 113 Chemical structures and proposed sensing mechanism of **probe-76a** and **probe-76b** with Au(III) (redrawn the ChemDraw structure from ref. 166).

In order to develop a selective fluorescent probe for the detection of Au(III) ions, BODIPY dye was chosen as a fluorophore core considering its high photo stability and quantum yield, which results in intense absorption and emission bands. In 2016, the authors focused on the synthesis of BODIPY-appended 2-hydrazinopyrazine (**probe-76a**) and 2-acetylpyrazine group (**probe-76b**) for the selective recognition of Au(III) ions.<sup>166</sup> First, **probe-76** was used to test the sensing studies with Au(III) at different pH values and the results indicated distinguishable photophysical properties at pH 7. The **probes** showed poor emission, and upon addition of Au(III) ions, it showed enhanced fluorescence intensity, whereas other competitive metal ions do not show any noticeable changes in the fluorescence spectra. In the case of

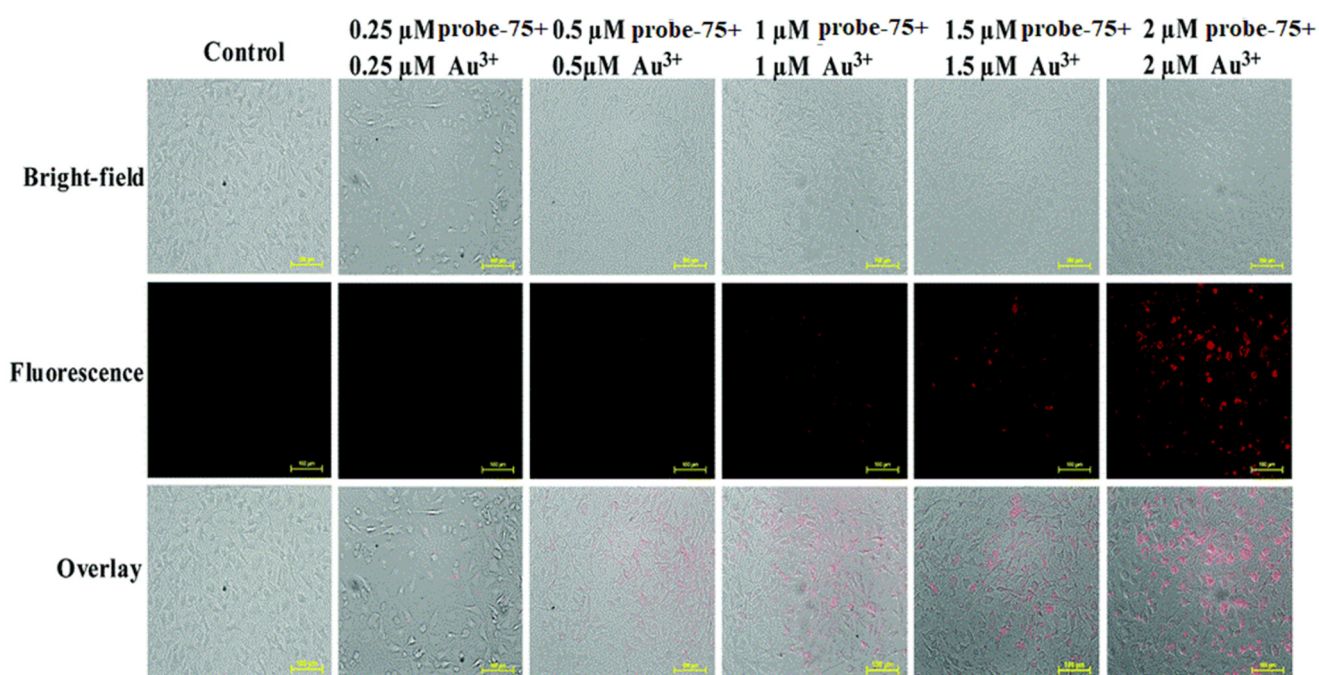


Fig. 112 Fluorescence microscopic imaging of MC3T3 cells with **probe-75** and Au(III) ions. (reprinted with permission from ref. 165, Copyright 2020 Royal Society of Chemistry).





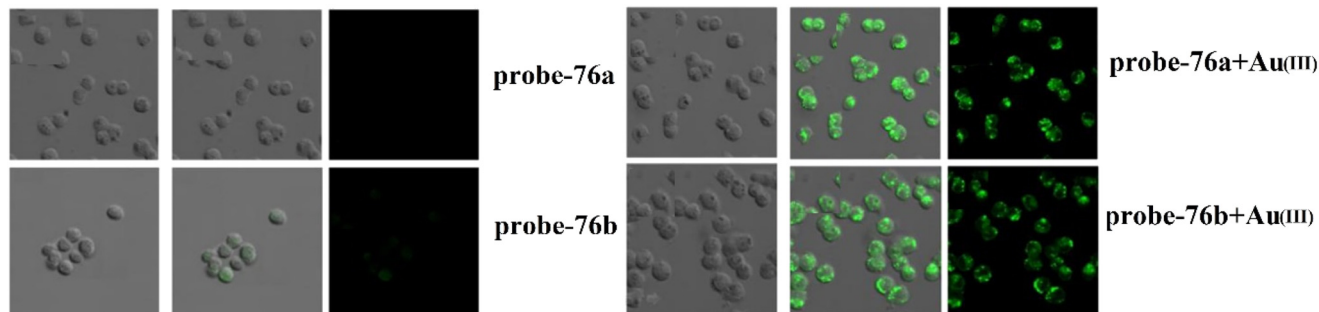


Fig. 114 Fluorescence microscopic imaging of PC12 cells with **probe-76a** and **probe-76b** treated with Au(III) ions. (reprinted with permission from ref. 166, Copyright 2016 Elsevier).

absorption spectra, color changes were observed from purple to light orange on adding Au(III) ions to **probe-76**. Furthermore, **probe-76b** showed potentiality towards Au(III) ions under strong acidic conditions and slow response time in comparison to **probe-76a**, which could be explained by the C=N bond's sensitivity to acidic pH, while **probe-76b** with a greater number of C=N bonds exhibited lower extent of hydrolysis by Au(III) than that of **probe-76a** (Fig. 113). The  $^1\text{H}$ -NMR data also suggested the formation of aldehyde groups by hydrolysis of the C=N group in the presence of Au(III) ions. Furthermore, the authors demonstrated the use of **probe-76a** in PC12 cells and zebrafish (with very low cytotoxicity determined by the MTT assay); *in vivo* cell imaging was obtained *via* Au(III) monitoring using laser confocal fluorescence microscopy (Fig. 114).

Although there are lot of gold ion probes developed so far, most of them were unable to distinguish between Au(III) and Au(I) ions. Initially, Feng *et al.* designed a two-photon fluorescent probe for the detection of gold ions, which was used for targeting mitochondria, but this probe was found to have similar issues due to coordination sites (N^N). In order to overcome the inability of previously reported probes to distinguish between Au(III) and Au(I), Feng *et al.* synthesized **probe-77** in 2017 (Fig. 115),<sup>167</sup> which replaced the coordination site N^N with N^O sites. The target compound was prepared by the reaction of a carbazole-containing aldehyde derivative with benzenesulfonylhydrazide in methanol and the structure was supported by  $^1\text{H}$  and  $^{13}\text{C}$ -NMR. **Probe-77** showed very weak fluorescence, and upon incorporation of Au(III) ions, a peak was acquired at 547 nm

along with 16-fold enhancement of intensity, whereas other competitive metal ions including Au(I) were unable to impart any changes in the fluorescence intensity, which indicate that **probe-77** was highly selective towards Au(III) ions. From the absorption spectra, it was noticed that an intense peak at 436 nm was obtained and titration of Au(III) ions with **probe-77** resulted in a blue-shift. Additionally, the binding nature of **probe-77** with Au(III) ions was supported by MALDI-TOF mass,  $^1\text{H}$ -NMR and DFT calculations. Further, inoculating **probe-77** into zebrafish, *in vivo* live cell imaging of Au(III) ions was achieved by two-photon microscopy, and very low cytotoxicity of **probe-77** was found against MCF-7 and HeLa cells (Fig. 116).

## 6. Schiff base-based fluorescent turn-on probes for Ag(I) ions

One of the precious metals, silver, is used in a variety of industries, including chemistry, electrical engineering, photography, and pharmaceuticals.<sup>168,169</sup> Due to the potentiality of silver, researchers devoted much effort to the synthesis of various probes for selective detection.<sup>170</sup> There are several analytical methods such as AAS,<sup>171</sup> surface-enhanced Raman scattering,<sup>172</sup> ion-selective electrodes,<sup>173</sup> voltammetry,<sup>174–176</sup> ICP-AES,<sup>177</sup> ICP-MS,<sup>178</sup> and potentiometry<sup>179</sup> available for the identification of silver ions.

In 2018, Kim and co-workers designed and synthesized an octopamine-appended cinnamaldehyde derivative (**probe-78**)<sup>180</sup> *via* a reaction between octopamine and 4-dimethylaminocinnamaldehyde in MeOH under reflux conditions and structurally characterized it by ESI-MS,  $^1\text{H}$  and  $^{13}\text{C}$ -NMR. Fluorescence emission spectra of **probe-78** displayed poor emission, and in the presence of Ag(I) ions, the emission intensity was gradually increased, whereas the other competitive metal ions Ga(III), Cd(II), Fe(II), Al(III), In(III), Cu(II), Mg(II), Pd(II), Au(III), Hg(II), Ni(II), Co(II), Fe(II) and Al(III) do not change the fluorescence intensity, which indicate the selective nature of **probe-78**. Job's plot revealed 1:1 stoichiometric complexation between **probe-78** and Ag(I) ions, which was further validated by ESI-MS,  $^1\text{H}$  NMR and DFT data. The DFT calculation indicated the lowering of band gap of **probe-78** upon binding with Ag(I), which ascertained that

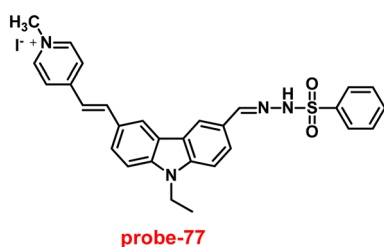


Fig. 115 Chemical structure of **probe-77** (redrawn the ChemDraw structure from ref. 167).



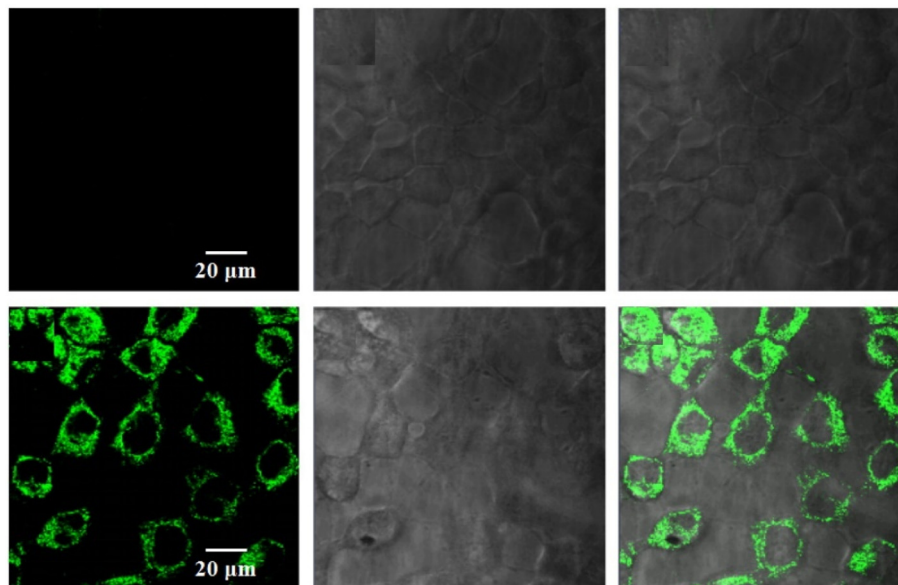


Fig. 116 Fluorescence microscopic imaging of MCF-7 cells with **probe-77** treated with Au(III) ions (reprinted with permission from ref. 167, Copyright 2017 Elsevier).

**probe-78** + Ag(I) complex formation causes a bathochromic shift. The sensing mechanism (Fig. 117) of **probe-78** with Ag(I) was confirmed by  $^1\text{H}$  NMR and the binding ratio was estimated to be 1:1 by Job's plot. Further, the authors demonstrated the influence of the pH detecting ability of **probe-78** with Ag(I), and at pH 7, it showed higher fluorescence intensity than that at other pH values, which strongly suggested that **probe-78** was potential for the detection in physiological media. The LOD value of **probe-78** with Ag(I) ions from the fluorescence titration spectra using the equation  $3\sigma/\text{slope}$  was found to be  $1.49\ \mu\text{M}$ .

In order to develop a fluorescent probe for the selective and sensitive recognition of Ag(I) in an aqueous medium, Nandhakumar *et al.* synthesized an oxygen-, sulphur- and nitrogen-containing heterocyclic chemosensor, **probe-79**,<sup>181</sup> in 2018 *via* a condensation reaction between methyl carbazate and 5-nitro-2-thiophenecarboxaldehyde in ethanol-acetic acid, and the structure was established by  $^1\text{H}$  and  $^{13}\text{C}$ -NMR. To establish the sensing ability of **probe-79**, the emission spectra displayed poor emission, the fluorescence intensity was gradually increased and the emission band shifted to 405 nm on titration with Ag(I) ions. However, **probe-79** does not alter the fluorescence spectra when other metal ions are present, which strongly confirms the selectivity. On varying the pH of the solution, it was found that **probe-79** effectively detects Ag(I) *via* showing spectral

changes within the pH range of 4–9. Therefore, **probe-79** could be applied for the sensing of Ag(I) ions at physiological pH (7.4). Fluorescence titration of **probe-79** with Ag(I) in MeOH:H<sub>2</sub>O (1:1, v/v), revealed 1:1 stoichiometric complexation, which was confirmed by Job's plot analysis, IR studies and ESI-MS. The proposed mechanism of **probe-79** with Ag(I) might be attributed to ICT (Fig. 118). Finally, the authors aimed to detect Ag(I) ions in biological samples, by inoculation of **probe-79** in *E. coli* cells followed by insertion of Ag(I); live cell imaging was obtained by laser confocal scanning microscopy (Fig. 119).

Considering the benefits of using the fluorescent probe rather than intensity-based probes to detect heavy metal ions, Nandhakumar *et al.* developed a quinolone-based Schiff base (**probe-80**)<sup>182</sup> in 2018 for ratiometric fluorescence turn-on for the Ag(I) ions, which can be utilized for the quantification of metal ions. **Probe-80** was prepared by the reaction between 2-hydroxyquinoline-3-carbaldehyde and 2-aminophenol in a methanol-triethylamine medium, and the structure was supported by several analytical and spectroscopic techniques. From the fluorescence emission spectra of **probe-80** in a MeOH:H<sub>2</sub>O (1:1, v/v) solution, it was found that dual emission bands appeared at 410 and 500 nm with very low

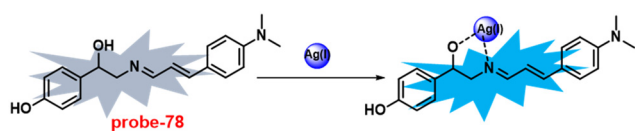


Fig. 117 Chemical structure and proposed sensing mechanism of **probe-78** with Ag(I) (redrawn the ChemDraw structure from ref. 180).

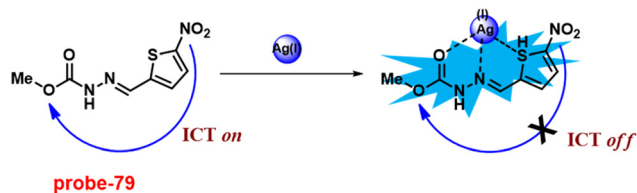


Fig. 118 Chemical structure and proposed sensing mechanism of **probe-79** with Ag(I) (redrawn the ChemDraw structure from ref. 181).

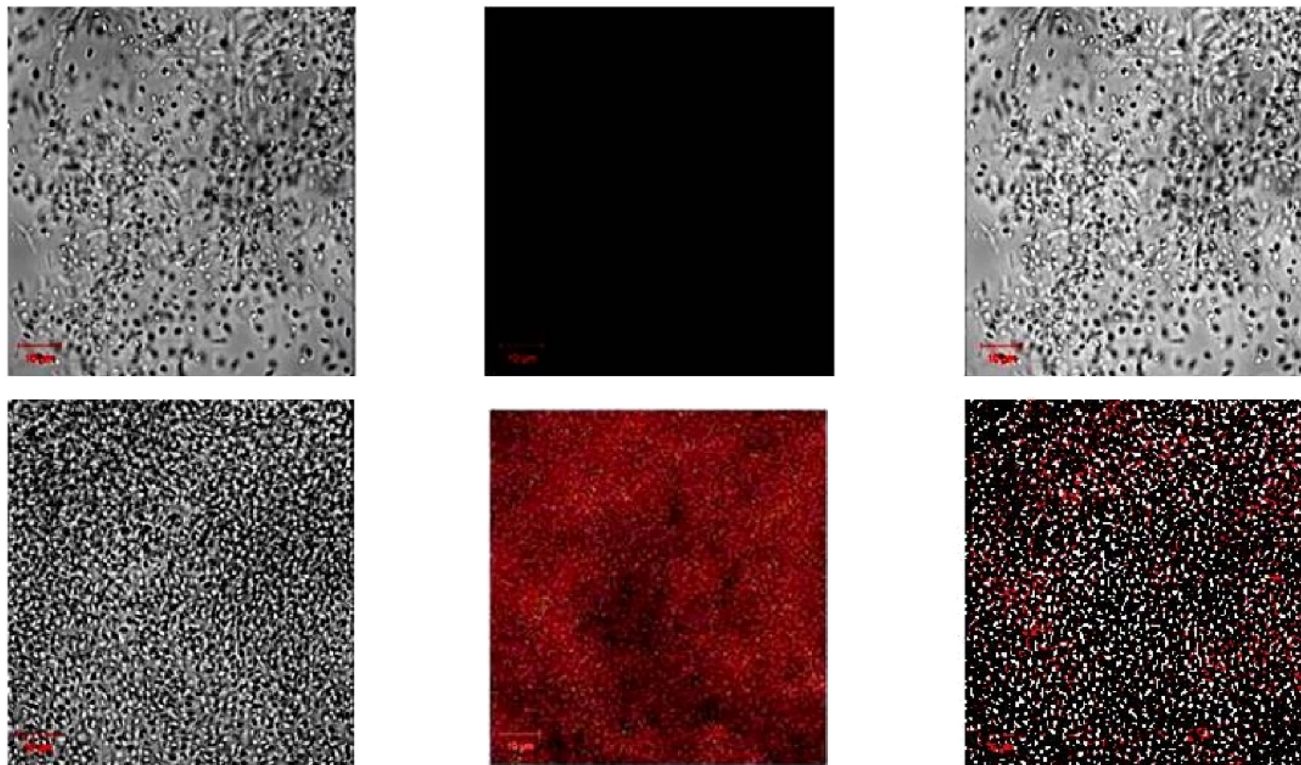


Fig. 119 Cellular images of **probe-79** in *E. coli* cells by laser confocal scanning microscopy (reprinted with permission from ref. 181, Copyright 2018 Elsevier).

intensity, while on titration with  $\text{Ag(I)}$  ions, the emission was progressively increased and saturated after addition of 1 eq., whereas no considerable change was observed in the fluorescence emission of **probe-80** in the presence of other competitive ions, which strongly supported the selectivity of probe. The fluorescence titration data showed the ratiometric response, in which the intensity of the peak at 410 nm increased and the peak at 500 nm decreased simultaneously. Moreover, authors focused on the titration experiments on varying pH, and it was noticed that **probe-80** and **probe-80** +  $\text{Ag(I)}$  remained stable in the pH range of 4 to 9, which indicated that **probe-80** could be utilised for the detection of  $\text{Ag(I)}$  under physiological pH (7.4). Fluorescence titration data revealed the 1 : 2 stoichiometric complexation between **probe-80** and  $\text{Ag(I)}$ , which was also supported by Job's plot and ESI-MS. The authors also proposed the sensing mechanism of

**probe-80**, where the  $\text{Ag(I)}$  ions coordinated through the lone pair of N-atoms and O-atoms, which leads to enhanced fluorescence as a result of inhibition of PET (Fig. 120). The association and LOD values of **probe-80** were found from the fluorescence titration spectra as  $2.41 \times 10^4 \text{ M}^{-2}$  and  $14 \mu\text{M}$  respectively. Further, for the practical application, fluorescence cell imaging of **probe-80** incubated with *E. coli* cells was obtained in the presence of  $\text{Ag(I)}$  ions using a laser scanning microscope as red fluorescence (Fig. 121).

In 2020, a fluorometric turn-on probe for the selective recognition of  $\text{Ag(I)}$  ions was synthesized by Patra and colleagues and characterized by XRD analysis, multinuclear NMR, ESI-MS, UV-vis spectra, and EA.<sup>183</sup> The native state of **probe-81** exhibited poor emission; on adding  $\text{Ag(I)}$  ions, the emission intensity was drastically enhanced, whereas with other competitive metal ions, there is no influence on the fluorescence spectra, which strongly suggested that **probe-81** showed very selective fluorescence turn-on towards  $\text{Ag(I)}$  ions (Fig. 122). Further, **probe-81** displayed a chromogenic response towards  $\text{Cu(II)}$  ions. The absorption titration data, Job's plot analysis, and ESI-MS analysis supported the 1 : 1 binding between **probe-81** and  $\text{Ag(I)}$  ions. The colorimetric detection of **probe-81** with  $\text{Cu(II)}$  and  $\text{Ag(I)}$  ions was estimated to be 1.7 and 2.2  $\mu\text{M}$ , respectively, and the  $\text{Ag(I)}$  fluorometric detection limit was up to 1.6  $\mu\text{M}$ . **Probe-81**, which works over a wide pH range, can be used to measure and identify the ions  $\text{Cu(II)}$  and  $\text{Ag(I)}$  in environmental samples as well as water samples.

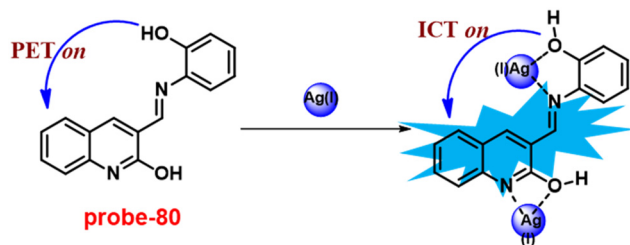


Fig. 120 Chemical structure and proposed sensing mechanism of **probe-80** with  $\text{Ag(I)}$  ions (redrawn the ChemDraw structure from ref. 182).





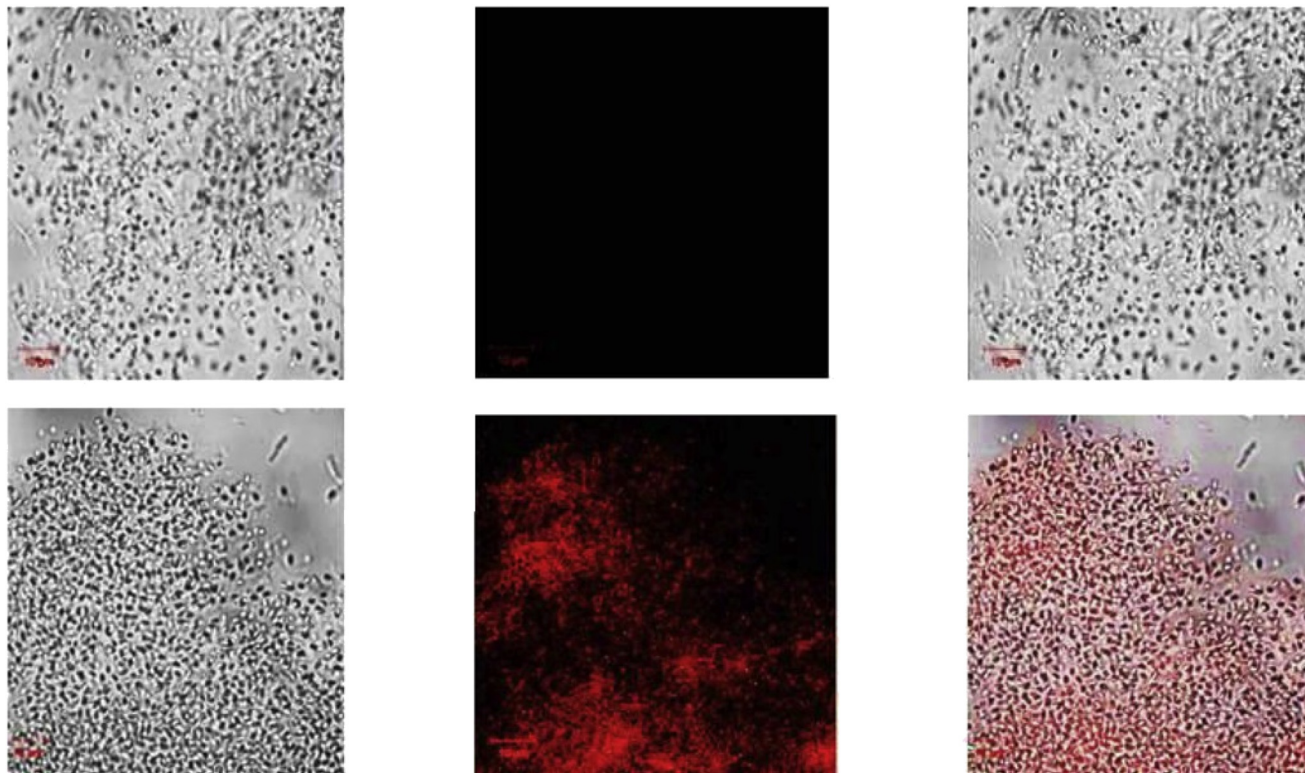


Fig. 121 Laser confocal scanning microscopic images of **probe-80** in *E. coli* cells in the presence of  $\text{Ag}^+$  ions. (reprinted with permission from ref. 182, Copyright 2018 Elsevier).

## 7. Schiff base-based fluorescent turn-on probes for $\text{Cu(II)}$ ions

Transition metal ions play crucial roles in biological systems, in which  $\text{Cu(II)}$  ions receive particular attention because they are used in numerous essential physiological functions in living things.<sup>184–190</sup> However, excessive copper levels that accumulate in organelles can cause Menkes disease,<sup>191</sup> Wilson's disease,<sup>192</sup> familial amyotrophic lateral sclerosis, Alzheimer's disease, Parkinson's disease, and prion disorders.<sup>193,194</sup> For the real-time response tool to analyze the level of  $\text{Cu(II)}$  ions for *in vitro* and *in vivo* research, a vital probe is therefore needed.

In 2018, Xu *et al.* designed and synthesized coumarin-based monocarbazone Schiff bases for selective fluorescent turn-on probes for  $\text{Cu(II)}$  ions.<sup>195</sup> The target **probe-82** was synthesized by mixing 1:1 proportion of 3*H*-benzo[*h*]

chromene-3-carbaldehyde and carbazide in ethyl alcohol, and the reaction mixture was stirred under reflux conditions to give a final product in good yields and was confirmed by various analytical techniques. **Probe-82** displayed very good aggregate induce ratiometric emission in methanol and water mixtures. The sensing studies were carried out in MeOH and water mixtures, where **probe-82** showed very poor emission ( $\phi = 0.061$ ) with a peak at 450 nm, and upon addition of  $\text{Cu(II)}$  ion, a very bright emission was generated at 511 nm with enhanced quantum yields ( $\phi = 0.25$ ), simultaneously decreasing the emission intensity at 450 nm. To find out better selectivity and sensitivity of **probe-82**, it was tested with several interfering metal ions and no difference in fluorescence spectra was observed. The binding mechanism of  $\text{Cu(II)}$  ions and **probe-82** was examined and found to be ICT combined with metal-induced association (Fig. 123). The detection limit of **probe-82** with  $\text{Cu(II)}$  was determined to be 10.4 nM using the formula  $3\sigma/\text{slope}$ . Moreover, for the practical application, bio-imaging of **probe-82** was carried out and the results suggested that **probe-82** successfully detects  $\text{Cu(II)}$  ions in biological media, which was confirmed by fluorescence microscopy (Fig. 124).

In 2019, Wang *et al.* focused on the synthesis of a Congo red-conjugated Schiff base derivative and characterized it using several analytical techniques.<sup>196</sup> **Probe-83** was exhibited to be very selective and sensitive towards  $\text{Cu(II)}$  ions *via* colorimetric and fluorescence turn-on responses, which was

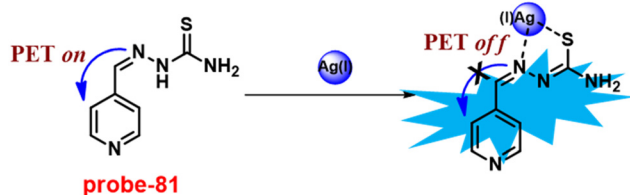


Fig. 122 Chemical structure and proposed sensing mechanism of **probe-81** with  $\text{Ag(I)}$  (redrawn the ChemDraw structure from ref. 183).





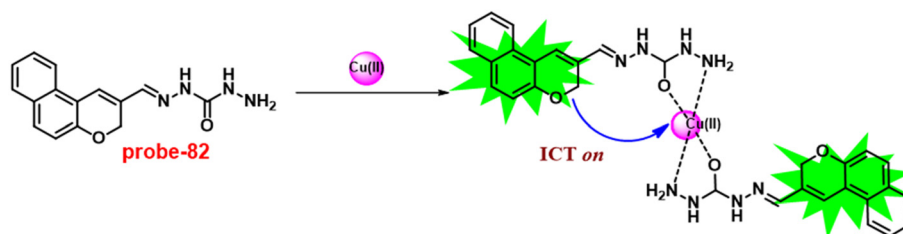


Fig. 123 Chemical structure and proposed sensing mechanism of **probe-82** with  $\text{Cu(II)}$  (redrawn the ChemDraw structure from ref. 195).

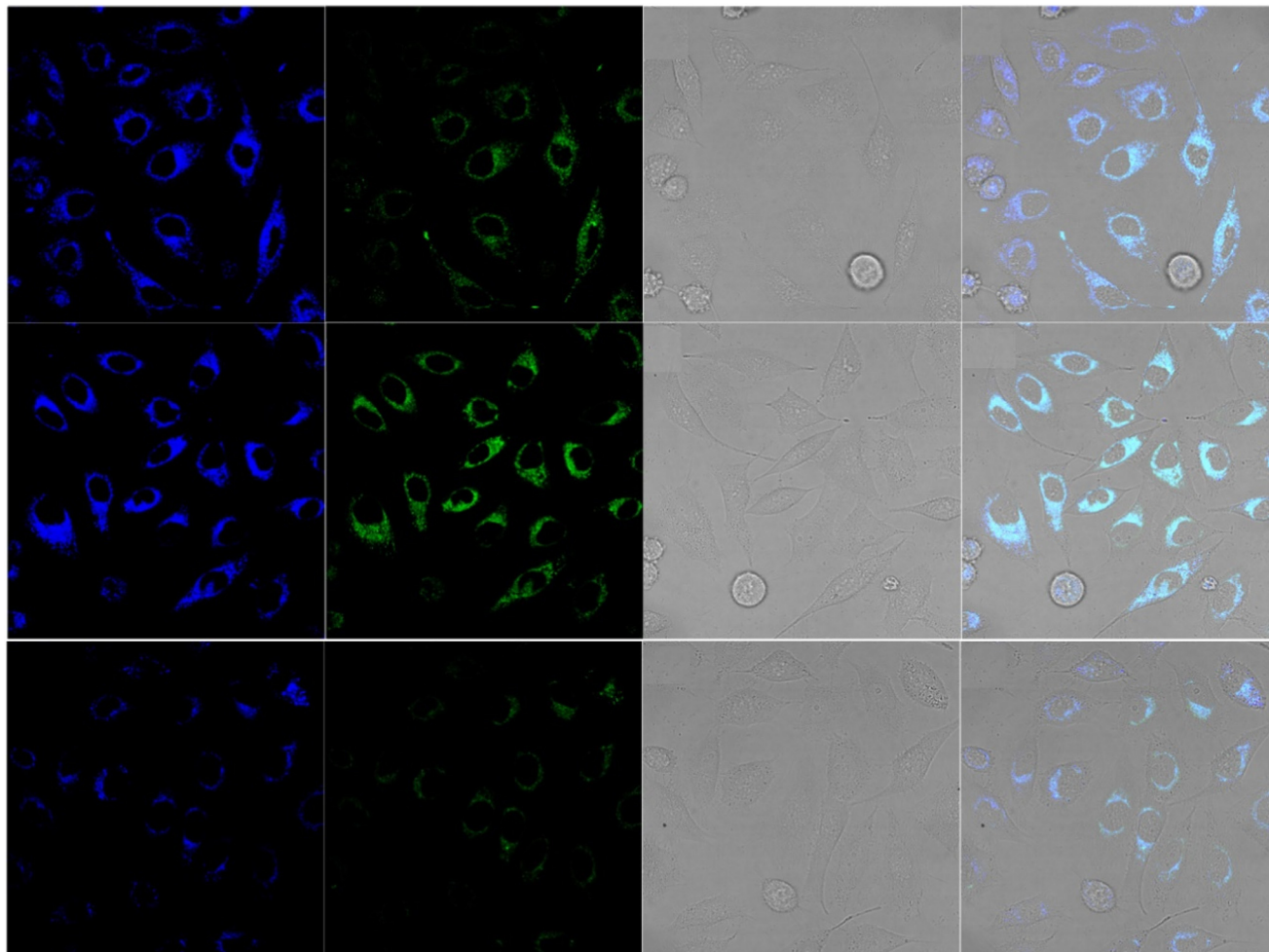


Fig. 124 Bio-imaging of **probe-82** on HeLa cells by laser confocal scanning microscopy (reprinted with permission from ref. 195, Copyright 2018 Elsevier).

based on the CHEF mechanisms in water and ethanol. **Probe-83** (Fig. 125) displayed a change in color from brown to colorless upon addition of  $\text{Cu(II)}$  ions, which was confirmed by changes in UV-vis absorption spectra. However, in the presence of other competitive metal ions, no response was observed in either fluorescence turn-on or colorimetry, which indicates that **probe-83** was very selective towards  $\text{Cu(II)}$  ions. The binding stoichiometry was obtained as 1:1 and confirmed by Job's plot and ESI-MS. **Probe-83** exhibited very good detection limit as well as association constants of 0.1

nM and  $1.03 \times 10^6 \text{ M}^{-1}$  correspondingly. As noted, detection limit values are much lower than that of WHO approved. The reversibility of **probe-83** was observed upon addition of a sodium sulfide solution to **probe-83** +  $\text{Cu(II)}$ . Further, cellular imaging of **probe-83** was performed on HepG2 cells, and it was found to have negligible cytotoxicity with very high cell permeability. The HepG2 cells were incubated with **probe-83** for 30 min, which did not show visible fluorescence, whereas upon treatment with  $\text{Cu(II)}$  ions, strong fluorescence images were observed using a fluorescence microscope (Fig. 126).



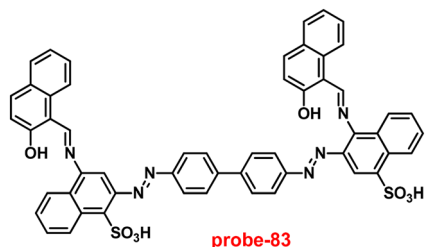


Fig. 125 Chemical structure of **probe-83** (redrawn the ChemDraw structure from ref. 196).

Thus, **probe-83** found to be a potential candidate for the recognition of Cu(II) ions in biological media.

A novel bithiophene-conjugated Schiff base was designed and synthesised *via* a simple condensation reaction of diamino malononitrile and 2-formyl thiophene in ethanol, and **probe-84** was structurally characterized *via* analytical techniques by Kumar and co-workers in 2019.<sup>197</sup> The sensing studies of **probe-84** were conducted in MeOH:H<sub>2</sub>O (8:2, v/v) media, which exhibited a chromogenic behavior towards Cu(II) ions, and the color changed from yellow to colorless, even though in the presence of other competitive metal ions, it does not show any changes in absorption spectra. The fluorescence studies of **probe-84** displayed fluorescence enhancement upon incremental addition of Cu(II) ions, which was explained by the CHEF mechanism (Fig. 127) and no change in emission intensity with other metal ions. The

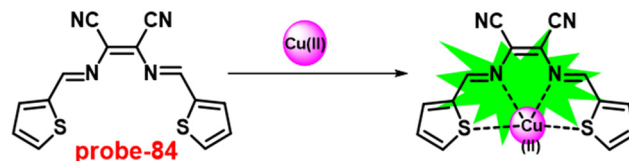


Fig. 127 Chemical structure and proposed sensing mechanism of **probe-84** with Cu(II) (redrawn the ChemDraw structure from ref. 63).

LOD value was calculated *via* fluorescence spectra as 14.5 nM, which was much lower than that of WHO guidelines (0.02  $\mu$ M) in drinking water. The stoichiometry of **probe-84** with Cu(II) ions was determined by Job's plot as 1:1. The association constant was assessed by the B-H method as  $7.31 \times 10^4 \text{ M}^{-1}$ . The nature of binding mode of **probe-84** with Cu(II) ions was strongly supported by FTIR, NMR, ESI-mass, as well as DFT data.

Mohan and co-workers designed and synthesized a very simple and efficient fluorescent chemosensor for Cu(II) ions *via* pyrene-conjugated Schiff base derivatives in 2018.<sup>198</sup> The target **probe-85** was synthesized upon a reaction between 1-pyrenecarboxaldehyde and 3-hydroxy-2-naphthoic hydrazide. The sensing studies of **probe-85** (Fig. 128) were conducted in DMSO:H<sub>2</sub>O, towards several metal ions by fluorescence spectroscopic methods. There was a gradual increase in fluorescence intensity at 450 nm on addition of Cu(II) ions to **probe-85** due to the absence of PET process, whereas in the presence of above-mentioned cations, no changes were

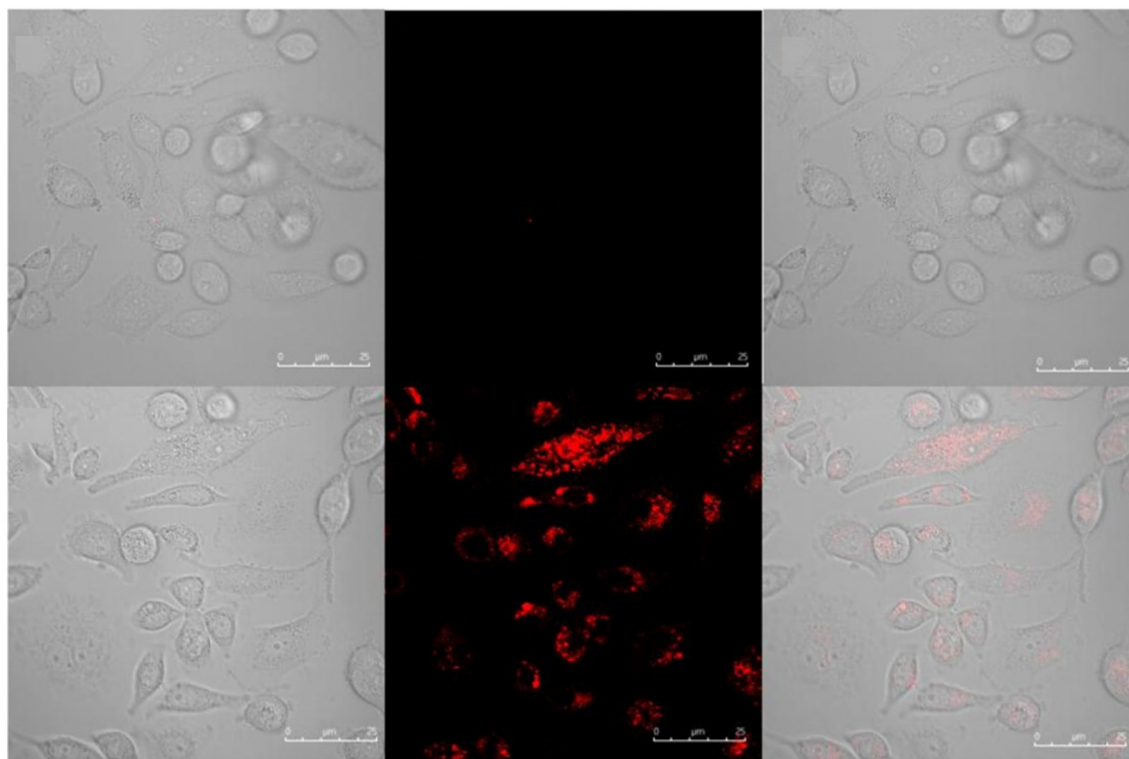


Fig. 126 Fluorescence microscopic images of HepG2 cells treated with **probe-83** and in the presence of Cu(II) ions (reprinted with permission from ref. 196, Copyright 2019 Elsevier).



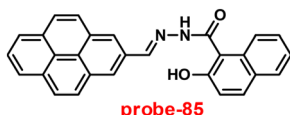


Fig. 128 Chemical structure of **probe-85** (redrawn the ChemDraw structure from ref. 198).

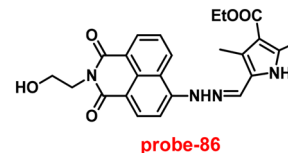


Fig. 130 Chemical structure of **probe-86** (redrawn the ChemDraw structure from ref. 199).

observed in the emission spectra. The results strongly suggested that **probe-85** showed selective response to Cu(II) ions with other interfering metal ions. The sensing studies were conducted in a wide range of pH (5–9), which does not affect the sensing ability of **probe-85** with Cu(II) ions. The binding constant and LOD values were found to be  $1.16 \times 10^4 \text{ M}^{-1}$  and  $0.26 \text{ }\mu\text{M}$  respectively. The reversibility studies of **probe-85** were performed using EDTA, which showed the emission quenching on titration with EDTA to **probe-85** + Cu(II). The cellular imaging experiments of **probe-85** were conducted on living RAW 264.7 cells in the presence of Cu(II) ions by fluorescence microscopy. **Probe-85** was incubated with cells, which showed insignificant fluorescence emission, whereas upon treatment with Cu(II) ions, it produced a very strong fluorescence emission under GFP (Fig. 129). Thus, **probe-85** was demonstrated as a potential candidate for the recognition of Cu(II) ions in biological media.

In 2017, a 1,8-naphthalimide hydrazine-conjugated pyrrole-based Schiff base, **probe-86**, was synthesised by Wang *et al.* via a simple condensation reaction, which exhibited very selective ratiometric fluorescence response towards Cu(II) ions in acetonitrile and water mixtures.<sup>199</sup> The absorption studies of **probe-86** (Fig. 130) changed color from colorless to

orange color on adding Cu(II) ions and resulted in drastic changes in absorption bands and no response for other metal ions. The binding mode of **probe-86** was determined by ESI-MS, IR, single-crystal XRD and DFT studies. The proposed sensing mechanism of **probe-86** was identified *via* a hydrolysis manner, which is a vigorous approach to design potential candidates for efficient ratiometric fluorescent sensors for Cu(II) ions. The LOD value of **probe-86** was estimated to be  $1.50 \text{ }\mu\text{M}$  from the linear response range covering 3–10  $\mu\text{M}$ . Finally, the authors established the efficacy of **probe-86** for the recognition of Cu(II) ions in biological media. The outcomes disclosed a strong emission in the presence of Cu(II) ions, which was observed by fluorescence microscopy (Fig. 131).

Kong and co-workers synthesized a coumarin-naphthol-based Schiff base unit for selective fluorescence turn-on for sensing Cu(II) ions in 1:99 proportion of DMSO and HEPES buffer. The target compound **probe-87** (ref. 200) was synthesized upon treatment of 7-diethylaminocoumarin-3-aldehyde with 3-amino-2-naphthol in EtOH, and the reaction was refluxed for 6 h. The sensing studies of **probe-87** obtained better sensitivity and selectivity towards particular

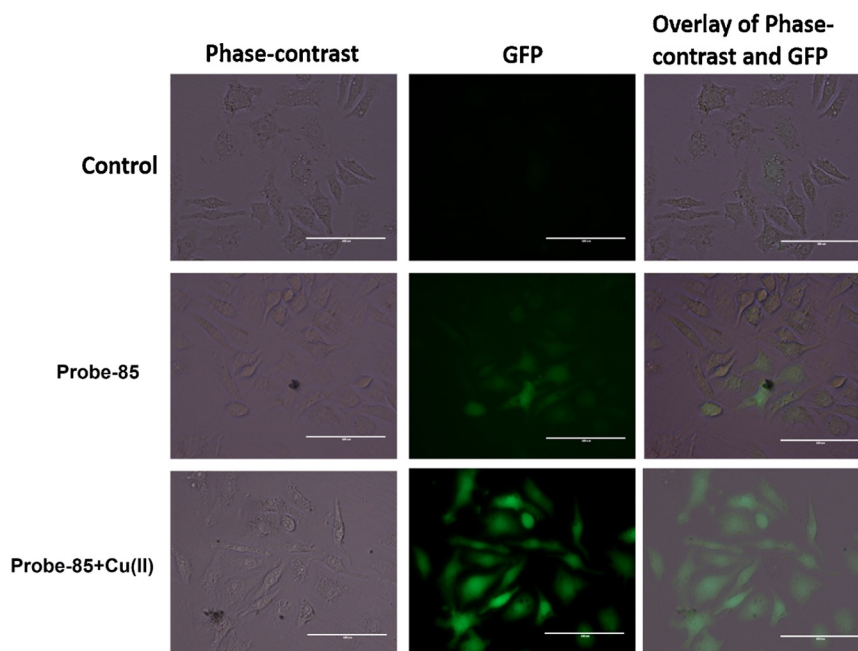


Fig. 129 Fluorescence microscopic images of RAW 264.7 cells treated with **probe-85** and in the presence of Cu(II) ions (reprinted with permission from ref. 198, Copyright 2018 Elsevier).





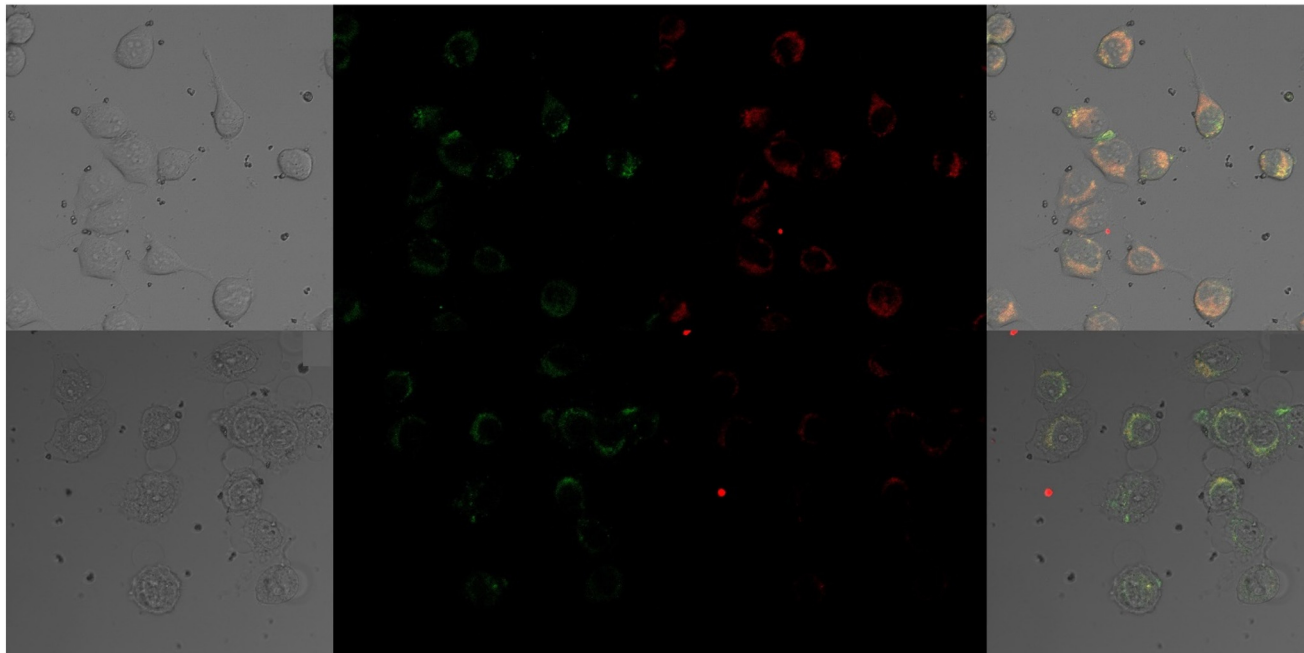


Fig. 131 Fluorescence microscopic images of HeLa cells treated with **probe-86** and in the presence of  $\text{Cu(II)}$  ions (reprinted with permission from ref. 199, Copyright 2017 Elsevier).

metal ions. Upon incremental addition of  $\text{Cu(II)}$  ions to **probe-87**, the absorption band at 345 nm progressively falls, whereas the adsorption band at 452 nm increased regularly. However, fluorescence titration data revealed that in the presence of  $\text{Cu(II)}$  ions, the emission peak at 520 nm gradually increased and reached maximum at 0.5 eq. with 60-fold enhancement, which detected that  $\text{Cu(II)}$  ions encouraged the decomposition of imines to discharge the fluorescence compound 7-diethylaminocoumarin-3-aldehyde (Fig. 132). The LOD value of **probe-87** was estimated to be  $0.82 \mu\text{g L}^{-1}$  (12.7 nM) using the equation  $3\sigma/\text{slope}$ , which is much lesser as recommended by WHO ( $2.0 \text{ mg L}^{-1}$ ) in drinking water. Job's plot revealed that the stoichiometry of **probe-87** with  $\text{Cu(II)}$  was 1:2 and the binding constant was estimated to be  $1.74 \times 10^5 \text{ M}^{-1}$ . The binding mechanism was analysed from the  $^1\text{H}$  NMR studies. The low cytotoxicity of **probe-87** was confirmed by the MTT assay and could be applied as the potential candidate for the recognition of  $\text{Cu(II)}$  ions in biological media, which was confirmed by

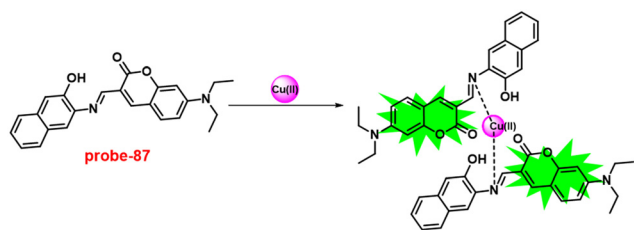


Fig. 132 Chemical structure and proposed sensing mechanism of **probe-87** with  $\text{Cu(II)}$  (redrawn the ChemDraw structure from ref. 200).

fluorescence microscopy (Fig. 133). Thus, **probe-87** will work as an excellent material in the field of biomedical research and bioimaging of  $\text{Cu(II)}$ -related syndromes.

A photochromic diarylethene-conjugated Schiff base entity was synthesised by Pu *et al.* in 2018.<sup>201</sup> **Probe-88** was extensively studied for the photochromic properties and fluorescence sensing of various metal ions, acids and bases in ACN. Upon addition of  $\text{Cu(II)}$  ions to **probe-88**, the fluorescence band gradually enhanced with 90-fold intensity and shifted to a blue region for 56 nm, and emission color alterations from dark red to brick red, due to the restriction of  $\text{C}=\text{N}$  isomerisation and enhancement of the CHEF process (Fig. 134). However, no change was perceived with excess amounts of other interfering metal ions. As a consequence, this **probe-88** was a very highly selective fluorescent chemosensor for the recognition of  $\text{Cu(II)}$  ions. Job's plot of **probe-88** exhibited maximum absorption at 0.3 of molar fraction, and the ratio of **probe-88**- $\text{Cu(II)}$  was found to be 2:1. The binding constant was calculated as  $4 \times 10^4 \text{ M}^{-1}$  from the B-H equation. The LOD value of **probe-88** was measured as  $1.49 \mu\text{M}$  using the equation  $3\sigma/\text{slope}$ . Further, for practical applications, **probe-88** was utilised for the sensing of  $\text{Cu(II)}$  in drinking water with high precision.

In 2018, Wang *et al.* designed and synthesized a new carbazole-based Schiff base moiety for the ultrasensitive recognition of  $\text{Cu(II)}$  ions in  $\text{CH}_3\text{CN}$ .<sup>202</sup> The sensing studies of **probe-89** were performed in acetonitrile as a solvent using the UV-vis and fluorescence spectroscopic studies. In the UV-vis spectra, upon addition of  $\text{Cu(II)}$  to **probe-89**, the absorption band at 400 nm completely diminished and the





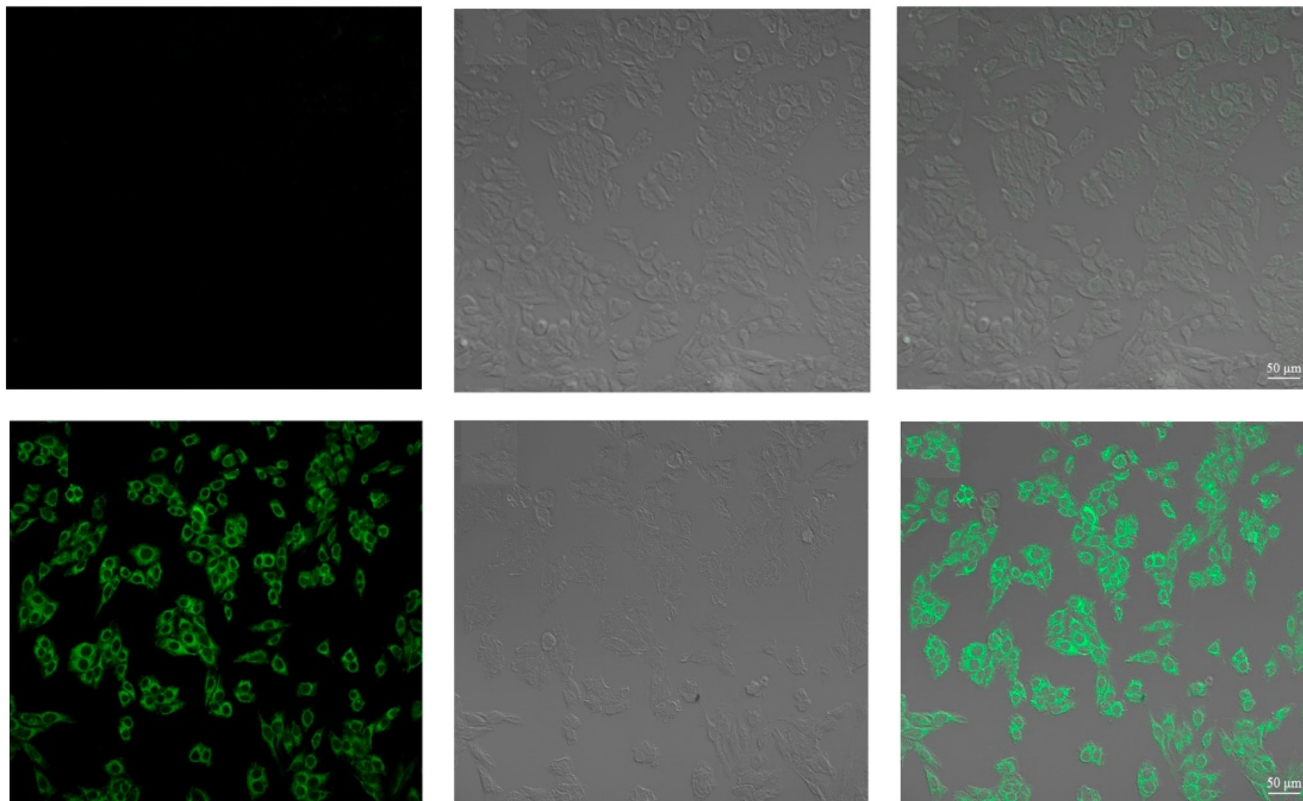


Fig. 133 Fluorescence microscopic images of HepG2 cells treated with **probe-87** and in the presence of Cu(II) ions (reprinted with permission from ref. 200, Copyright 2017 Elsevier).

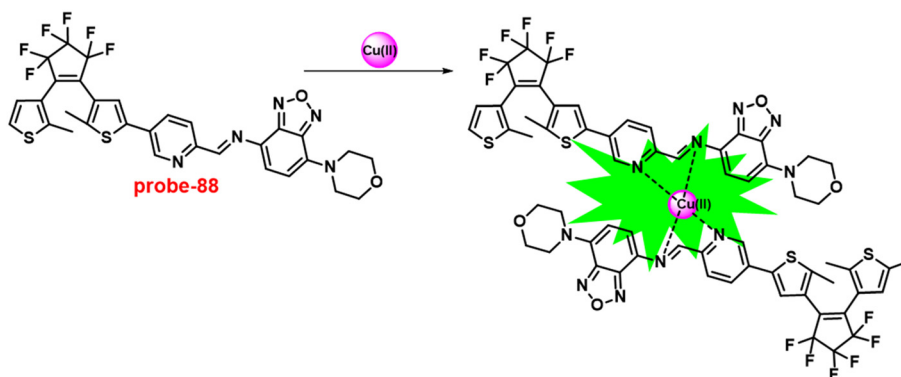


Fig. 134 Chemical structure and proposed sensing mechanism of **probe-88** with Cu(II) (redrawn the ChemDraw structure from ref. 201).

color changed from yellow to colorless. The emission studies revealed that the fluorescence enhanced up to 160-fold with 10 eq. Cu(II) ions added to **probe-89** over other competitive metal ions due to the ICT process (Fig. 135). The LOD value was obtained as 27.4 nM from the equation  $\text{LOD} = 3\sigma/\text{slope}$ , which is a much lower value as recommended by the US-EPA. The association constant was determined to be  $1.26 \times 10^{-6} \text{ M}^{-1}$  for **probe-89** and Cu(II) ions through the B-H plot. Job's plot determined a stoichiometry of 1:1 for **probe-89** and Cu(II) ions. Due to the very fast detection ability, **probe-89** has potential applications in biomedical and environmental monitoring applications.

In 2018, Wang and co-workers focused on the synthesis of a benzimidazole-based Schiff base for selective and sensitive

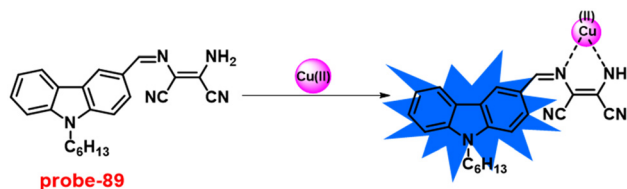


Fig. 135 Chemical structure and proposed sensing mechanism of **probe-89** with Cu(II) (redrawn the ChemDraw structure from ref. 202).



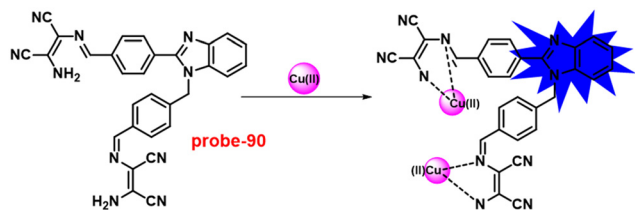


Fig. 136 Chemical structure and proposed sensing mechanism of **probe-90** with  $\text{Cu(II)}$  (redrawn the ChemDraw structure from ref. 203).

fluorescent turn-on probes for  $\text{Cu(II)}$  ions in  $\text{CH}_3\text{CN}$ -Tris solutions.<sup>203</sup> The UV-vis and fluorescence analysis confirmed that with  $\text{Cu(II)}$  ions, **probe-90** showed fluorescence enrichment by about 50-fold, due to the suppression of  $\text{C=N}$  isomerisation (Fig. 136) and ratiometric absorption in aqueous solutions over a varied pH array in the presence of other interfering metal ions with a very low detection limit of  $0.49 \mu\text{M}$ . Job's plot established the binding ratios of **probe-90** with  $\text{Cu(II)}$  as 1:2, as supported by ESI-MS and DFT calculations. Further, the binding value was calculated from the B-H plot to be  $2.5 \times 10^8 \text{ M}^{-2}$ , which revealed that **probe-90** had great attraction for  $\text{Cu(II)}$  ions. Further, for the practical applications of **probe-90**, cellular imaging investigations were carried out for the detection of  $\text{Cu(II)}$  ions in biological media. Thus, authors choose HepG2 cell lines, in which they found no fluorescence in the absence of  $\text{Cu(II)}$  ions, but a bright green colour emission in the presence of  $\text{Cu(II)}$ . This results suggested that **probe-90** have good permeability into cells for the detection of  $\text{Cu(II)}$  ions (Fig. 137).

In 2018, Wu and coworkers aimed to synthesise a dimethylamino-imidazole conjugate-based Schiff base for the

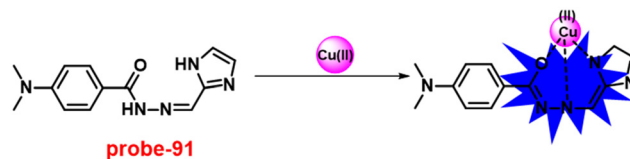


Fig. 138 Chemical structure and proposed sensing mechanism of **probe-91** with  $\text{Cu(II)}$  (redrawn the ChemDraw structure from ref. 204).

selective fluorescence turn-on detection of  $\text{Cu(II)}$  ions in acetonitrile/water ( $v/v = 3:2$ ) in a Tris-HCl solution at pH 7.4.<sup>204</sup> The sensing studies of **probe-91** demonstrated colorimetric response, color changes from colorless to yellow colour and fluorescence turn-on response towards  $\text{Cu(II)}$  ions over other competitive metal ions, due to the suppression of PET (Fig. 138). The LOD values of **probe-91** were calculated from the absorption and fluorescence spectra to be  $0.46 \mu\text{M}$  and  $15 \text{ nM}$ , which were much lesser as approved by WHO for drinking water ( $31.5 \mu\text{M}$ ). Job's plot data provided strong information regarding the binding stoichiometry such as 1:1 and the association constant was found to be  $4.3 \times 10^7 \text{ M}^{-1}$ . The reversibility experiment was performed using  $\text{S}^{2-}$  as the external source for the regeneration of **probe-91**, and the results indicated that **probe-91** has good reversible properties. Further, the mode of binding was supported by  $^1\text{H}$  NMR, ESI-MS and DFT calculations.

In 2019, a novel fluorene-conjugated Schiff base moiety was designed, synthesized and structurally characterised using several analytical techniques.<sup>205</sup> **Probe-92** was found to have very high selectivity towards  $\text{Cu(II)}$  ions with a very low LOD of  $1.54 \text{ nM}$  over other interfering metal ions. The absorption titration of **probe-92** towards  $\text{Cu(II)}$  ions displayed

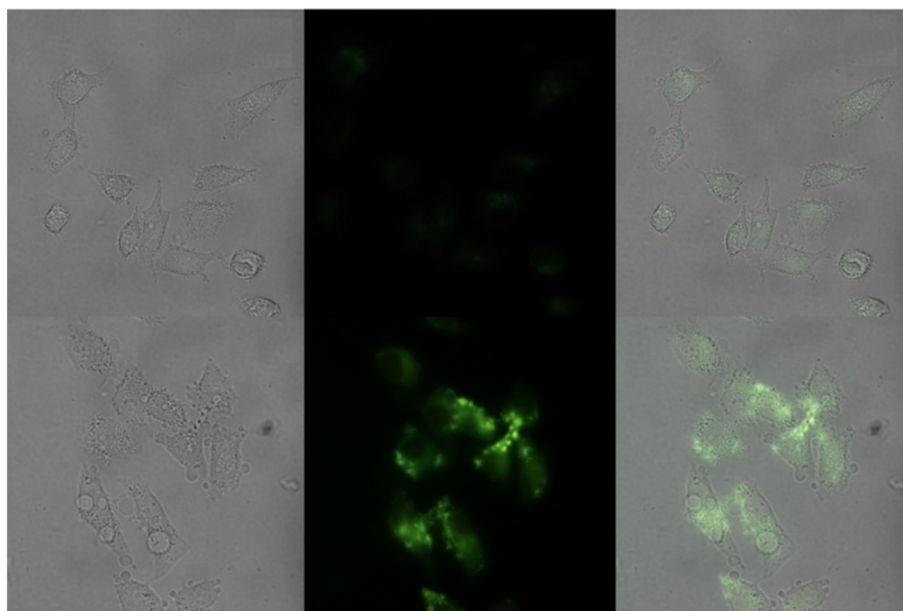


Fig. 137 Fluorescence microscopic images of HepG2 cells treated with **probe-90** and in the presence of  $\text{Cu(II)}$  ions (reprinted with permission from ref. 203, Copyright 2018 Elsevier).



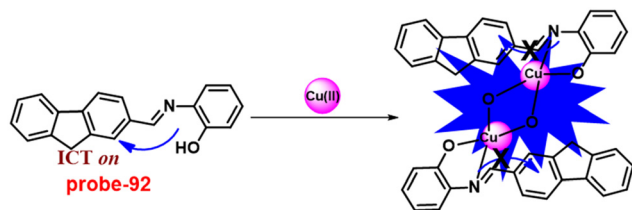


Fig. 139 Chemical structure and proposed sensing mechanism of **probe-92** with Cu(II) (redrawn the ChemDraw structure from ref. 205).

colorimetric response and color shifts from pale yellow to colorless, which gave visual detection. Upon addition of Cu(II) ions, **probe-92** showed fluorescence turn-on ascribed to the suppression of the isomerisation of imines and blocking of the ICT quenching process (Fig. 139) and no change was observed towards other metal ions. The stoichiometry ratio was determined *via* Job's plot as well as ESI-MS and displayed to be 1:1. Authors successfully demonstrated the practical applicability of **probe-92** by the recognition of Cu(II) ions in real samples of copper in electroplating wastewater. Additionally, **probe-92** was displayed as a very good chromogenic and fluorescent turn-on probe for CN<sup>−</sup> with a very low LOD of 0.18 μM.

In 2019, Amine *et al.* aimed at the synthesis of an azo group-conjugated Schiff base scaffold for sensitive and selective fluorescence turn-on for Cu(II) ions in methanol and H<sub>2</sub>O mixtures (7/3, v/v). **Probe-93** was obtained *via* a simple condensation reaction between 2-hydroxy-5-(p-tolyldiazenyl) benzaldehyde and *N*-(3-aminopropyl)imidazole in ethanol under reflux conditions.<sup>206</sup> The sensing studies of **probe-93** were conducted and enhanced emission was observed upon addition of Cu(II) ions (Fig. 141) without any interference with other metal ions, which is due to the collective consequence of the CHEF and suppression of C=N isomerization (Fig. 140). Thus, the results indicate very high selectivity towards Cu(II) ions. Job's plot gave strong information regarding the stoichiometric ratio of **probe-93** with Cu(II) ions, which was found to be 2:1, as confirmed by ESI-MS and <sup>1</sup>H NMR. Finally, the LOD value was estimated to be 1.8 μM that is much lesser than the WHO endorsement level (20 μM) for drinking water.

Xie *et al.* designed and synthesized a triphenylamine-based Schiff base conjugate for the selective fluorescence

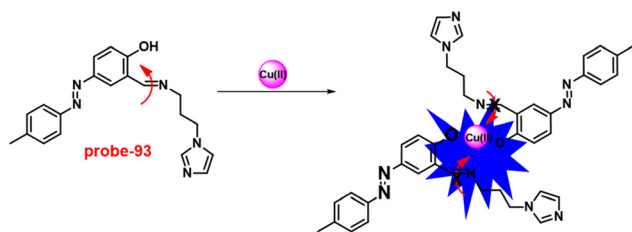


Fig. 140 Chemical structure and proposed sensing mechanism of **probe-93** with Cu(II) (redrawn the ChemDraw structure from ref. 206).

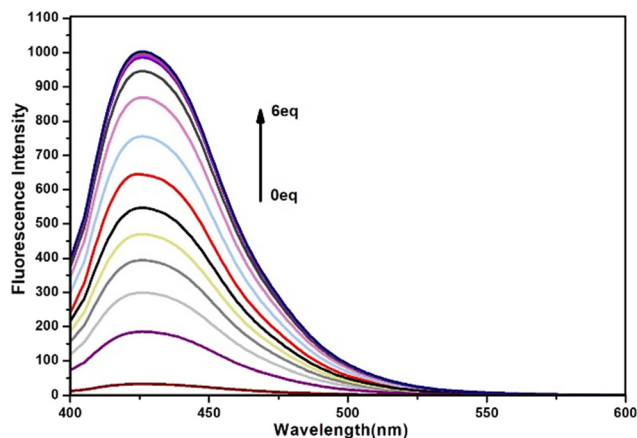


Fig. 141 Change in the emission spectra of **probe-93** on increasing the concentration of Cu(II) ions (left) and with different metal ions (right) (reprinted with permission from ref. 206, Copyright 2019 Elsevier).

turn-on detection of Cu(II) ions in 2017.<sup>207</sup> **Probe-94** was synthesised *via* a simple condensation reaction between triphenylamine aldehyde and 2-aminophenol in EtOH under reflux conditions. The emission of **probe-94** was very poor, whereas upon addition of Cu(II) ions to it a very bright emission at 450 nm was observed in acetonitrile/water, which results in the suppression of C=N isomerisation (Fig. 142). Further, the presence of excess amounts of different metal ions does not show any variation in the fluorescence spectra, which indicate that **probe-94** was very selective towards Cu(II) ions. The association constant of the complex in CH<sub>3</sub>CN and CH<sub>3</sub>CN/H<sub>2</sub>O (v/v = 4/6, pH = 7.4) HEPES buffer was calculated from the B-H plot as  $1.96 \times 10^7 \text{ M}^{-1}$  and  $5.43 \times 10^7 \text{ M}^{-1}$  respectively. Job's plot revealed that the binding ratio of **probe-94** and Cu(II) ions was found to be 1:1 and further confirmed by <sup>1</sup>H NMR and ESI-mass. The LOD value was estimated from the fluorescence spectra and displayed as 0.18 μM and 0.85 μM in CH<sub>3</sub>CN and CH<sub>3</sub>CN/H<sub>2</sub>O (v/v = 4/6, pH = 7.4) HEPES buffer correspondingly. Finally, authors demonstrated the practical applicability of **probe-94**, which could be employed for the sensing of Cu(II) ions in diverse water samples.

In 2019, Xiao and co-workers aimed to synthesise a naphthalene and pyridine-comprehending Schiff base conjugate that works as a very selective probe for Cu(II) ions in aqueous media.<sup>208</sup> The sensing studies of **probe-95** demonstrated selective fluorescence turn-on towards Cu(II)

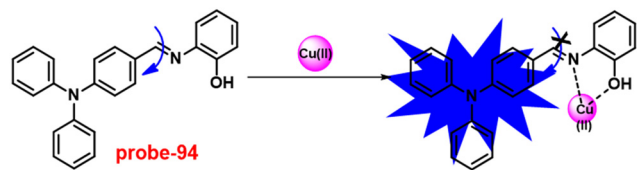


Fig. 142 Chemical structure and proposed sensing mechanism of **probe-94** with Cu(II) (redrawn the ChemDraw structure from ref. 207).





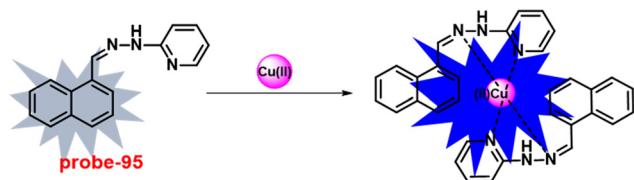


Fig. 143 Chemical structure and proposed sensing mechanism of **probe-95** with Cu(II) (redrawn the ChemDraw structure from ref. 208).

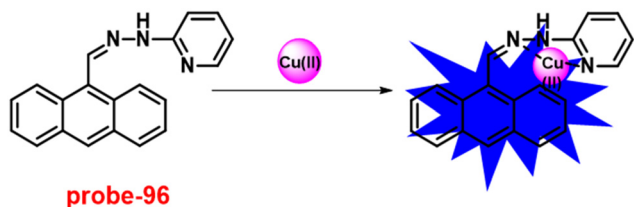


Fig. 144 Chemical structure and proposed sensing mechanism of **probe-96** with Cu(II) (redrawn the ChemDraw structure from ref. 209).

ions, which is ascribed to the PET process (Fig. 143), and there was no alteration in fluorescence emission with other competitive metal ions. The nature of binding mode of **probe-95** was estimated *via* Job's plot to be 2:1 of **probe-95** and Cu(II) ions, which was further supported by ESI-MS studies. The LOD and association constant of **probe-95** were found to be 3.90 nM and  $1.38 \times 10^5 \text{ M}^{-2}$  towards Cu(II) ions. The reversibility of **probe-95** was performed using the  $\text{S}^{2-}$  anion and the results strongly supported that upon addition of  $\text{S}^{2-}$  anion, **probe-95** + Cu(II) reproduced the probe and the results indicate that **probe-95** has very good reversible properties.

In 2016, Ko *et al.* designed an anthracene-pyridine-conjugated Schiff base moiety *via* a facile process for the fluorogenic turn-on behavior of Cu(II) ions.<sup>209</sup> The sensing

data demonstrated that upon addition of Cu(II) ions to **probe-96**, gradual fluorescence enhancement was observed 23-fold times as a result of suppression in PET process (Fig. 144). There was no change in fluorescence spectra with excess amounts of other competitive metal ions that indicate very high selectivity towards Cu(II) ions. Further, the absorption spectra also show changes in the presence of Cu(II) ions, *i.e.* a band at 405 nm was progressively decreased, whereas a band at 325 nm was increased simultaneously. The binding stoichiometry was calculated from Job's plot to be 1:1, which was supported by  $^1\text{H}$  NMR, and a binding constant was displayed as  $2.12 \times 10^6 \text{ M}^{-2}$ . The LOD value was calculated from the fluorescence spectra as 0.1 nM. Further, the formation of a **probe-96** complex was well characterized by quantum yield enhancement, SEM, and theoretical calculations. For the practical relevance of **probe-96**, the detection of Cu(II) ions in biological media (Raw 264.7 cells) was performed by fluorescence microscopy. The results strongly indicated that there was no fluorescence emission when **probe-96** was used alone, but upon its treatment with Cu(II) ions bright fluorescence emission was observed inside the cell (Fig. 145). Moreover, **probe-96** was found to have very low cytotoxicity as well as great permeability, which opened up the possibility for its use in drug delivery into cells.

Guchhait *et al.* obtained a pyrene-based Schiff base conjugate for the selective chromogenic and fluorometric sensing of Cu(II) ions. In 2016, **probe-97** (Fig. 146) was synthesized upon reaction between pyrene-1-carboxaldehyde hydrazone and 2-hydroxy-1-naphthaldehyde in MeOH at room temperature.<sup>210</sup> Target **probe-97** was structurally characterised by several NMR and analytical techniques. **Probe-97** was found to have very interesting solid structures such as a 3D polymeric network with several different type of interactions such as  $\text{CH}\cdots\pi$ ,  $\pi\cdots\pi$  (pyrene and pyrene) and intermolecular H-bonding, which influence the photophysical

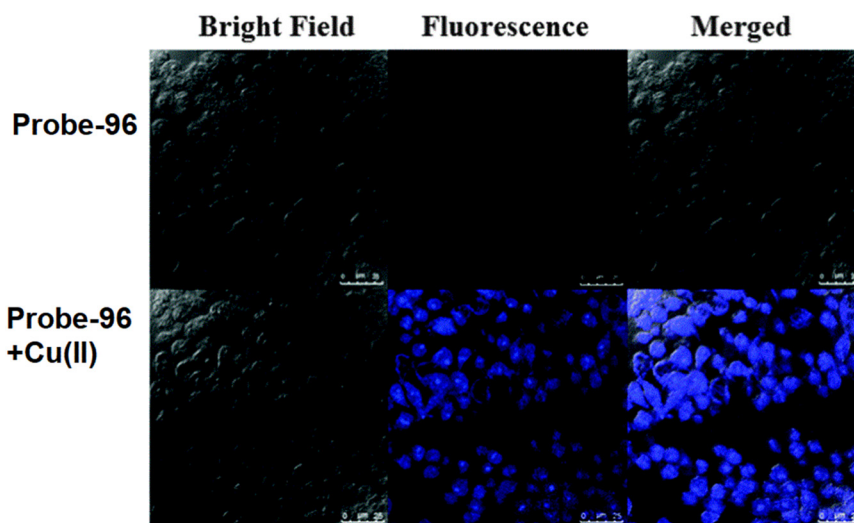


Fig. 145 Fluorescence microscopic images of Raw 264.7 cells treated with **probe-96** (top) and in the presence of Cu(II) ions (bottom) (reprinted with permission from ref. 209, Copyright 2016 Royal Society of Chemistry).



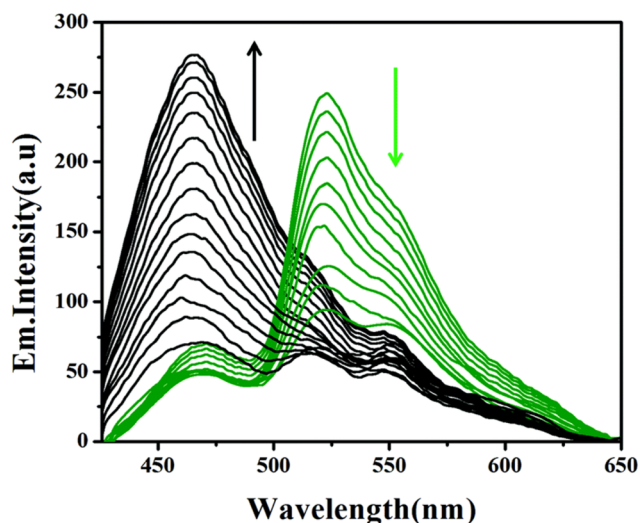
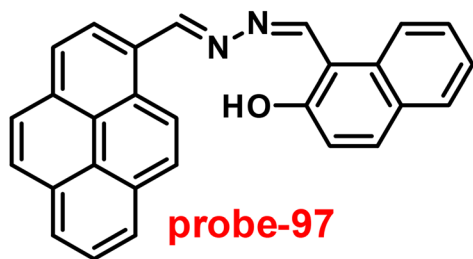


Fig. 146 Chemical structure of **probe-97** (top) and change in the emission spectra of **probe-97** on increasing the concentration of  $\text{Cu(II)}$  ions (bottom) (redrawn and reprinted with permission from ref. 210, Copyright 2016 Royal Society of Chemistry).

properties and sensing mechanism. The UV-vis spectra of **probe-97** showed drastic differences, and the color changes from colorless to yellow color, and hence, this **probe-97** could be applied for potential colorimetric detection of  $\text{Cu(II)}$  ions. However, upon addition of  $\text{Cu(II)}$  ions to **probe-97**, the broad emission band from 520 nm to 560 nm was significantly decreased to a assured point and became saturated. On titrating with  $\text{Cu(II)}$  ions, the fluorescence band at 466 nm progressively enhanced (Fig. 146). The observed findings are elucidated as follows: in the presence of  $\text{Cu(II)}$  ions, the excimer break down and once complexation between  $\text{Cu(II)}$  ions with **probe-97** gave rise to an enhancement emission band at 466 nm. Further, **probe-97** demonstrated the efficient sensing of  $\text{Cu(II)}$  ions in biological media, which was confirmed by confocal fluorescence microscopy.

In 2017, Kuwar synthesized a new terephthalaldehyde-based Schiff base, **probe-98**, and characterized it using several analytical techniques.<sup>211</sup> **Probe-98** was found to show very sensitive and selective fluorescence turn-on response to  $\text{Cu(II)}$  ions, even with the interfering metal ions. The absorption titration exhibited a colorimetric response to **probe-98**, and the color changes from colorless to red color with  $\text{Cu(II)}$  ions. The binding stoichiometry was determined by Job's plot as 1:2, which was confirmed *via* fluorescence enhancement at

386 nm. The LOD and association value ( $K_a$ ) of **probe-98** with  $\text{Cu(II)}$  ions were estimated to be  $0.62 \mu\text{M}$  and  $6.67 \times 10^4 \text{ M}^{-1}$ , correspondingly. The fluorescence turn-on mechanism was proposed, which might be due to the suppression of  $\text{C=N}$  isomerisation and PET process along with the CHEF (Fig. 147). Further, **probe-98** was found to show excellent performance towards the recognition of  $\text{Cu(II)}$  ions in biological media in live L929 cells (Fig. 148).

In 2019, Kang and co-workers obtained rhodamine and Schiff base conjugates for sensitive and selective fluorescence turn-on towards  $\text{Cu(II)}$  ions.<sup>212</sup> The sensing studies of **probe-99** demonstrated that the absorption band at 552 nm was gradually increased with the  $\text{Cu(II)}$  ions, whereas emission spectra fluorescence enhancement was observed with the increase in quantum yields, due to the ring opening of rhodamine (Fig. 149). However, the competitive binding studies of **probe-99** with metal ions showed no changes in the absorption and emission spectra, which indicates the selective and sensitive response towards  $\text{Cu(II)}$  ions. Finally, **probe-99** was tested for the recognition of  $\text{Cu(II)}$  ions in biological media, and the outcomes revealed that **probe-99** was found to have very high potential for cellular imaging in living cells as well as in live mice.

A new luminous **probe-100(a-c)** (Fig. 150) was created by Yamato and his coworkers in 2016. It is a pyrene with a long-chain Schiff base derivative at position 1.<sup>213</sup> **Probe-100b** and **probe-100c** were also developed to compare their binding efficiency for the sensing of  $\text{Cu(II)}$  ions. **Probe-100a** contained a methoxy group instead of the diethylaminocarbonylmethoxy group, and **probe-100c** contained a simply phenylimino moiety instead of the hydrazido carbonyl group. By forming a coordination connection with the hydrazidocarbonyl group, the ligands **probe-100a** and **probe-100b** can bind and detect  $\text{Cu(II)}$  in a 1:1 ligand-to-metal binding mode. In the  $\text{CH}_3\text{CN}/\text{CH}_2\text{Cl}_2$  solvent system, on adding 10 eq. of  $\text{Cu(II)}$  the emission intensity of ligands **probe-100a** and **probe-100b** increases by 65-fold and 25-fold, respectively. By inhibiting the PET while bound to  $\text{Cu(II)}$ , **probe-100a** causes a blue emission. Additionally, due to the significant suppression of PET and the distinct binding method of the ligand/metal complex formation, **probe-100a** is highly sensitive for the detection of  $\text{Cu(II)}$  compared to **probe-100b** and **probe-100c**.

In 2016, Jiang *et al.* synthesized novel **probe-101**, which could be applied for the selective recognition of  $\text{Cu(II)}$  ions and cysteine.<sup>214</sup> On titrating with  $\text{Cu(II)}$  ions, the Schiff base

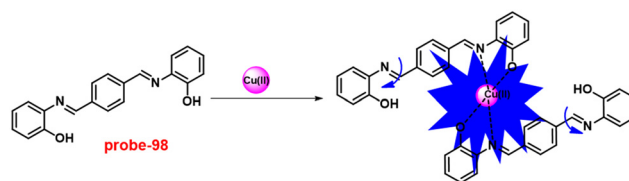
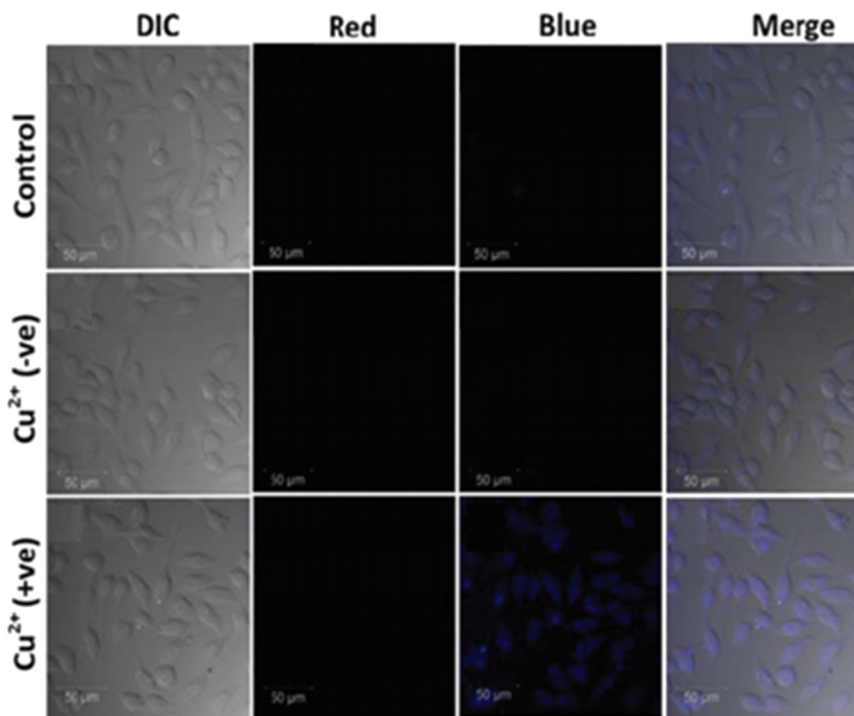


Fig. 147 Chemical structure and proposed sensing mechanism of **probe-98** with  $\text{Cu(II)}$  (redrawn the ChemDraw structure from ref. 211).





**Fig. 148** Fluorescence microscopic images of L929 cells treated with **probe-98** and in the presence of Cu(II) ions (reprinted with permission from ref. 211, Copyright 2017 Royal Society of Chemistry).

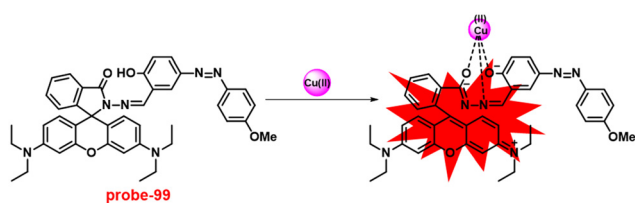
unit of **probe-101** (Fig. 151) can coordinate with Cu(II) and cause a highly selective fluorescence “turn-on” process. The terminal olefin of **probe-101** could interact with Cys and cause fluorescence quenching. The reversible nature of the produced **probe-101**-Cys exhibited improved Cu(II) binding properties and regained **probe-101** fluorescence. The detection limits of **probe-101** with Cu(II) and Cys were 25 nM and 11 nM respectively. Fluorescence imaging tests were performed in HeLa cells to further highlight **probe-101**'s usefulness in biological systems.

## 8. Schiff base-based fluorescent turn-on probes for Ni(II) ions

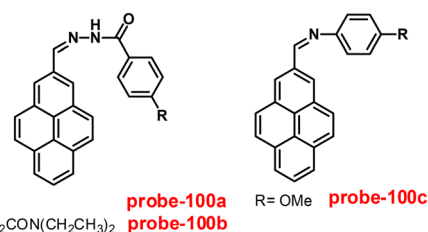
One of the transition metals, Ni(II) ions, is essential for many metallo-enzymes including carbon monoxide dehydrogenases, acireductone dioxygenases and hydrogenases. It also plays a role in respiration, biosynthesis, and metabolism in living things.<sup>215–219</sup> Apart from the

biological applications of Ni(II) ions, it has potential utility in the field of battery industry, such as electroplating, Ni–Cd batteries, and electroforming.<sup>220,221</sup> However, the excess amount of Ni(II) accumulation in organelles causes several health issues such as respiratory problems, allergies, pneumonitis, lung cancer, and central nervous disorders in humans.<sup>222–224</sup> Consequently, there is a necessity of selective and sensitive probe for the recognition and monitoring of Ni(II) ions in environmental and biological samples.

In 2019, Patra and co-workers aimed to synthesize novel **probe-102** for the sensitive and selective fluorescence turn-on behavior towards Ni(II) ions.<sup>225</sup> **Probe-102** in its original form was observed to be poorly emissive in nature, while upon addition of Ni(II) ions, the luminescence was gradually increased by 3-fold and was saturated after addition of one eq., due to suppression of PET, ESIPT and C=N isomerization (Fig. 152), while the emission spectra showed fluorescence quenching in the presence of Cu(II) ions. UV-vis



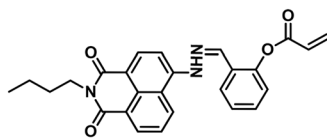
**Fig. 149** Chemical structure and proposed sensing mechanism of **probe-99** with Cu(II) (redrawn the ChemDraw structure from ref. 212).



**Fig. 150** Chemical structures of **probe-100a–c** (redrawn the ChemDraw structure from ref. 213).

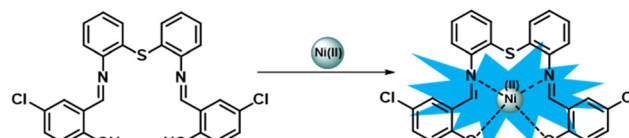






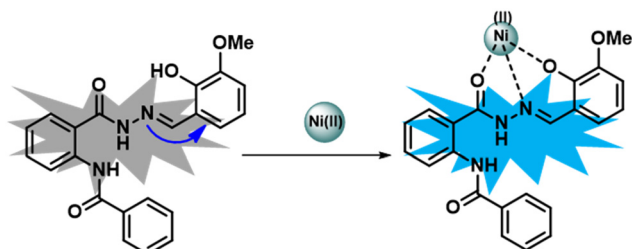
probe-101

Fig. 151 Chemical structure of **probe-101** (redrawn the ChemDraw structure from ref. 214).



probe-103

Fig. 154 Chemical structure and proposed sensing mechanism of **probe-103** with Ni(II) (redrawn the ChemDraw structure from ref. 226).



probe-102

Fig. 152 Chemical structure and proposed sensing mechanism of **probe-102** with Ni(II) (redrawn the ChemDraw structure from ref. 225).

studies show that in the presence of Ni(II) and Cu(II), a color change was observed from colorless to yellow, which is evidently observed from the rise of a new band towards the long wavelength region. Job's plot gave strong information regarding the complexation ratio of **probe-102** with Ni(II) ions, which was found to be 1:1, as supported by ESI-MS analysis and DFT studies. The detection limit of **probe-102** was analyzed from the fluorescence spectrum and found to be 1.71  $\mu\text{M}$  for Ni(II) ions, and much lesser than that approved by the WHO rules for drinking water. The reversibility of **probe-102** with Ni(II) and Cu(II) ions was obtained from the addition of Na<sub>2</sub>EDTA experiments. Further, the authors demonstrated the applicability of **probe-102** for the recognition of Ni(II) ions in biological samples and its excellent detection ability towards Ni(II) in cellular media, which was supported by fluorescence microscopy (Fig. 153).

In 2018, Sivaraman and his colleagues developed a new probe (**probe-103**)<sup>226</sup> with readily accessible "off-on-off" colorimetric and fluorescence responses *via* a condensation

reaction between 2-aminophenylsulphide and 5-chlorosalicylaldehyde and structurally characterized it *via* various analytical and spectroscopic techniques. The pure form of **probe-103** was very weak emissive in nature; on titrating with Ni(II) ions, the emission intensity was gradually enhanced because of CHEF (Fig. 154) and revealed no influence on emission spectra with other competitive metal ions. However, the UV-vis titration data of **probe-103** showed dramatic color change from colorless to dark yellow upon addition of Ni(II) ions. By using Job's plot analysis, the binding ratio was determined to be 1:1 between **probe-103** and Ni(II) ions. In addition, the LOD value for **probe-103** was calculated to be as low as 8.67 nM by the fluorescence approach and 0.361  $\mu\text{M}$  by the UV-vis method, which suggests a potential use for **probe-103** in detecting Ni(II) in the environment. The collected spectroscopic data of **probe-103** with Ni(II) were also used to demonstrate the molecular logic gates. **Probe-103** was also effectively used for Ni(II) fluorescence imaging in HeLa cells (Fig. 155). In order to show the practical applications of **probe-103** for the detection of Ni(II) ions, test kits were also created by dip-coating the **probe-103** solution onto filter paper and allowing it to dry in the air.

Patra and co-workers synthesized selective and sensitive fluorescent turn-on **probe-104**, which gave response towards Ni(II) ions, from 3-amino-2-phenyl-4(3H)-quinazolinone and 2-pyridine carboxaldehyde in methanol under reflux conditions and structurally characterized it by various analytical and spectroscopic techniques.<sup>227</sup> The purest form of **probe-104** showed very poor emission, and upon introduction of Ni(II) ions, the fluorescence intensity was gradually increased, whereas other competitive metal ions showed no effect on the fluorescence spectra. Further, **probe-**



Fig. 153 Fluorescence microscopic images of HeLa cells treated with **probe-102** and in the presence of Ni(II) ions (reprinted with permission from ref. 225, Copyright 2019 Royal Society of Chemistry).



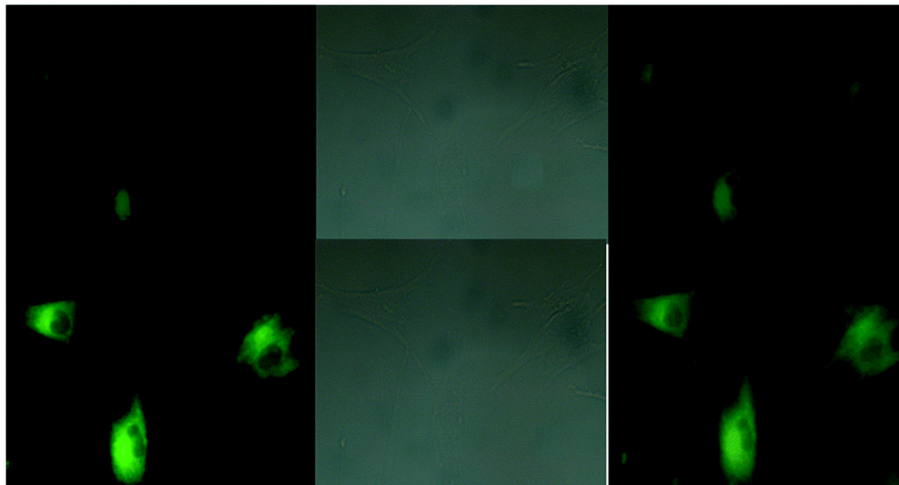


Fig. 155 Fluorescence microscopic images of HeLa cells treated with **probe-103** and in the presence of Ni(II) ions (reprinted with permission from ref. 226, Copyright 2018 Royal Society of Chemistry).

**104** displayed a colorimetric response towards Ni(II) ions. The DFT analyses and isolation of a single crystal of the metal complex gave additional confirmation of the recognition mechanism (Fig. 156). The binding stoichiometry of **probe-104** and Ni(II) was calculated to be 2:1 based on Job's plot calculation. The detection limit was substantially lower than that indicated by the WHO rules for drinking water, reaching up to 1.8  $\mu\text{M}$  and 1.18  $\mu\text{M}$  for colorimetric and fluorometric analyses respectively. The chemosensor has also been successfully used to make molecular logic gates, image living cells, and analyze real samples using a smartphone. HeLa cells were used in cell imaging studies to confirm **probe-104**'s affinity for Ni(II) ions present in an intracellular medium.

## 9. Schiff base-based fluorescent turn-on probes for Pd(II) ions

Palladium can bind to proteins (including casein, silk fibroin, and many enzymes), amino acids that contain thiols, vitamin B6, DNA, and other macromolecules due to its thiophilic

nature.<sup>228–232</sup> This can disrupt a number of cellular processes including DNA degradation, harm to cell mitochondria, and inhibition of enzyme activity.<sup>233,234</sup> The Pd(II) complexes are enormously used as catalysts in various cross-coupling reactions, and the byproducts containing trace amounts of Pd(II) are extremely toxic as well as carcinogenic,<sup>235,236</sup> which is very mandatory to sense the trace amount of Pd(II) in environmental and biological samples.

In 2017, Sinha *et al.* designed and synthesized rhodamine-appended allylic iminephenol (**probe-105**) for the sensitive and selective detection of Pd(II) at a very low LOD value *via* the fluorescence turn-on mechanism.<sup>237</sup> The native form of **probe-105** displayed poor emission, and on adding Pd(II) ions, the emission intensity increased by 22 times and reached a maximum after addition of one eq. (Fig. 157), and with other metal ions, no changes were observed in the fluorescence spectra, which strongly suggested that **probe-105** was very selective towards Pd(II) ions. The absorption spectral data were found to show colorimetric response, and the color changes from colorless to maroon due to the presence of LMCT in  $\text{CH}_3\text{CN}-\text{H}_2\text{O}$  (v/v = 1/4). The LOD value of **probe-105** with Pd(II) ions was estimated from the fluorescence titration spectra to be 50 nM, which was much lesser than the WHO recommended level. Job's plot suggested 1:1 stoichiometry between **probe-105** and Pd(II), which was supported by  $^1\text{H}$  NMR, ESI-MS and DFT calculations. Furthermore, DFT calculations also supported

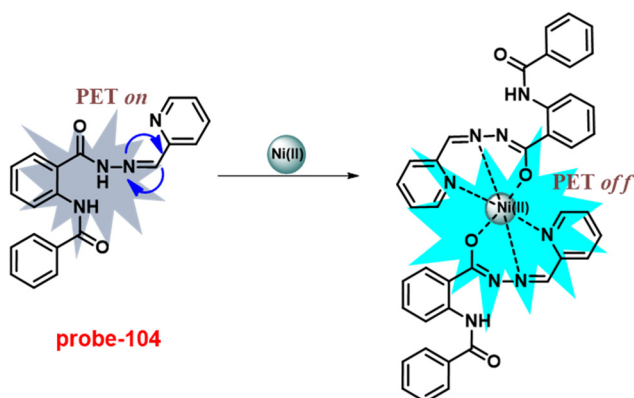


Fig. 156 Chemical structure and proposed sensing mechanism of **probe-104** with Ni(II) (redrawn the ChemDraw structure from ref. 227).

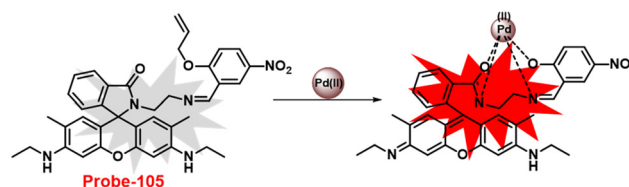


Fig. 157 Chemical structure and proposed sensing mechanism of **probe-105** with Pd(II) (redrawn the ChemDraw structure from ref. 237).



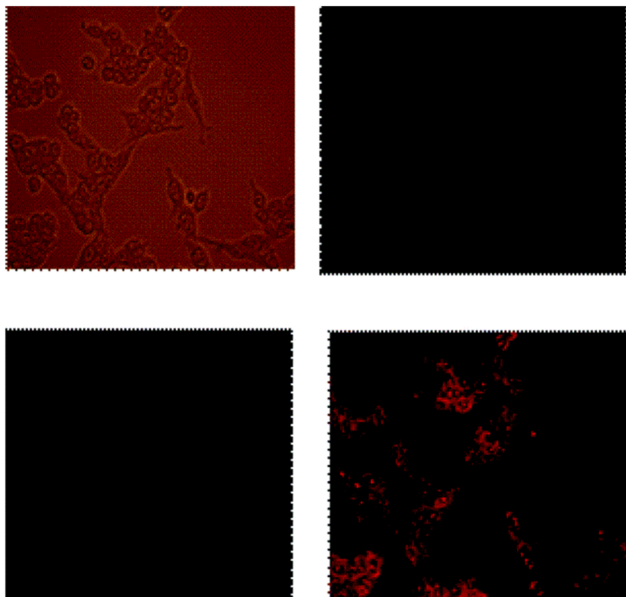


Fig. 158 Fluorescence microscopic images of HCT 116 cells treated with **probe-105** and in the presence of Pd(II) ions (reprinted with permission from ref. 237, Copyright 2017 Royal Society of Chemistry).

experimental data including the lengthening of the C=O bond causing a red shift of the absorption peak. In addition, by incubating **probe-105** with a Pd(II) ion solution in HCT116 cells, *in vivo* fluorescence cell imaging could be obtained (Fig. 158).

In view of the previous success of rhodamine derivatives as a fluorescent sensing probe of Pd(II) ions, Sinha *et al.* were influenced to synthesize a coumarinyl-rhodamine Schiff base (**probe-106**),<sup>238</sup> which was obtained from the condensation reaction of 4-methyl-7-hydroxy-8-formyl-coumarin and *N*-(rhodamine-B)lactam-1,2-ethylenediamine in ethanol under reflux conditions, and it was structurally characterized *via* several analytical and spectroscopic techniques in 2019. The native state of **probe-106** (Fig. 159) displayed poor emission; on adding Pd(II) ions, the luminescence intensity gradually enhanced, whereas in the presence of competitive ions, no considerable change was observed in the fluorescence spectra. Under similar conditions, the absorption spectra of **probe-106** with Pd(II) ions displayed colorimetric responses and the color changes from pink to pale yellow. The LOD value of **probe-106** with Pd(II) ions was estimated from the fluorescence titration data as 18.8 nM. Job's plot ascertained the 1:1 stoichiometry between **probe-106** and Pd(II) ions, which was validated by FTIR, <sup>1</sup>H NMR, DFT and ESI-MS data. The authors proposed the sensing mechanism of **probe-106**, which involved the formation of [CR-Pd(II)] + complex using hydroxy-O and imine-N of a coumarinyl-rhodamine moiety involving the opening of a spirolactam ring. The DFT calculations suggested the reduction in band gap of **probe-106** upon binding with Pd(II) ions, which was indicative of the increase in conjugation on ring opening and subsequent enhancement of fluorescence intensity as well as color

change. Furthermore, after incubating **probe-106** in MCF7 cells, the live imaging of Pd(II) ions was performed using a fluorescence microscopic technique. Moreover, **probe-106** provided *in vivo* cell imaging (Fig. 159) along with selective and sensitive sensing of Pd(II) ions at such low detection limits.

Pathak *et al.* developed **probe-107**, a Schiff base based on rhodamine-aminopyrone, *via* the reaction of 4-amino antipyrine and glyoxal, which was then followed by condensation with hydrazinated rhodamine B in ethanol under reflux conditions, and the structure was verified using a variety of analytical and spectroscopic techniques in 2019.<sup>239</sup> The pure state of **probe-107** (Fig. 160) found to be very poorly emissive in nature, on titrating with Pd(II) ions, the luminescence intensity gradually enhanced, whereas with other competitive metal ions, it failed to impart any considerable effect on fluorescence spectra (Fig. 161). Conversely, in the presence of Pd(II) ions, **probe-107** exhibited a colorimetric response, in which the color changes from colorless to pink. The LOD value was found to be 11.9  $\mu$ M which was determined by a fluorescence titration experiment. Job's plot revealed 1:1 stoichiometric complexation between **probe-107** and Pd(II), which was further supported by <sup>1</sup>H NMR, DFT and ESI-MS data. The DFT calculation also strongly supported the experimental data such as the reduction in the band gap of **probe-107** with Pd(II) ions, which was due to the formation of complex *via* hydroxy-O and enamine-N of a rhodamine moiety and carbonyl-O and imine-N of aminopyrone. The fluorescence-enhanced mechanism was proposed by authors, which was spirolactum ring opening upon metal binding. Furthermore, apart from acting as a sensitive and selective fluorescent turn-on sensor, incubating **probe-107** in MDA-MB-468 cells, *in vivo* cell imaging of Pd(II) was obtained without causing any harm (determined by the MTT assay) (Fig. 162).

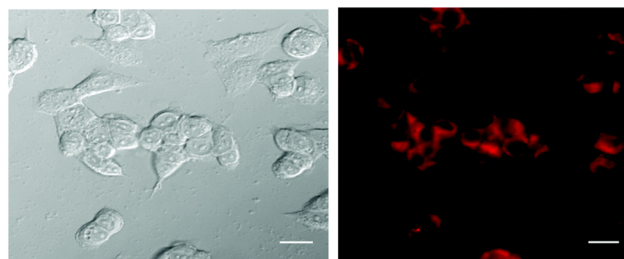
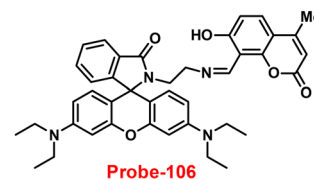


Fig. 159 Chemical structure of **probe-106** (top) and fluorescence microscopic images of MCF7 cells treated with **probe-106** and in the presence of Pd(II) ions (bottom) (redrawn and reprinted with permission from ref. 238, Copyright 2019 Royal Society of Chemistry).





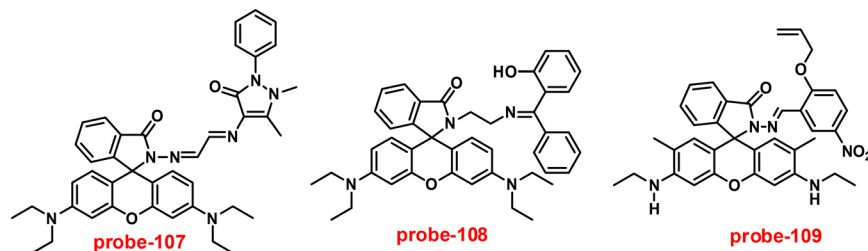


Fig. 160 Chemical structures of **probe-107–109** (redrawn the ChemDraw structure from ref. 239–241).

Sinha *et al.* designed and synthesized ethylenediamine-bridged 2-hydroxy benzophenone-rhodamine-B (**probe-108**)<sup>240</sup> by the reaction between ethylenediamine derivatives of rhodamine B and 2-hydroxy benzophenone and structurally characterised it by several analytical and spectroscopic techniques in 2019. The native state of **probe-108** (Fig. 160) was poorly emissive in nature and showed strong luminescence intensity in the presence of Pd(II) ions, whereas upon addition of other competitive metal ions, no intervening effect was seen in the fluorescence spectra. However, **probe-108** with Pd(II) ions showed colorimetric responses, showing changes from colorless to pink color. The ESI-MS and <sup>1</sup>H NMR data revealed 1:1 stoichiometric complexation between **probe-108** and Pd(II) ions, which was further supported by Job's plot analysis. Further, the effect of the pH on the detection capability of **probe-108** with Pd(II) ions was evaluated, and the results indicated no effect on the fluorescence spectra in the pH range of 8–12, which shows the potential of **probe-108** for the detection of Pd(II) ions in physiological media. The detection limit of **probe-108** with Pd(II) ions was calculated from the fluorescence titration experiment to be as low as 34 nM. Considering the selective and sensitive fluorescence turn-on response of **probe-108** towards Pd(II) ions, the authors applied for the detection of Pd(II) ions in biological media; firstly, **probe-108** was incubated in MDA-MB-231 cell lines and red fluorescence

image was obtained upon addition of Pd(II) ions using a microscope providing intracellular imaging (Fig. 163). The DFT calculation suggested a reduction in the band gap of **probe-108** upon binding with Pd(II), which signified the formation of [BR-Pd(II)] + complex *via* four coordination sites (hydroxy-O, imine-N of rhodamine moiety and hydroxy-O of benzophenone and imine-N which bridged these two moieties).

With the aim to overcome the oxidation state specificity of chemosensors in the detection of Pd(II) ions, in 2018, Sinha and coworkers developed an allyl-functionalized rhodamine Schiff base (**probe-109**) (Fig. 160)<sup>241</sup> *via* the reaction of 2-allyloxy-5-nitrobenzaldehyde and *N*-(rhodamine-6G) lactam hydrazine, which could show selective and sensitive detection for the Pd(II) ions *via* colorimetric as well as fluorescence turn-on response under physiological conditions (stable at pH 5–10), which was confirmed by analytical and spectroscopic methods. The fluorescence data of **probe-109** demonstrated that the emission intensity increases with high quantum yields on gradual addition of Pd(II) and the saturation point was reached after adding 1.1 eq., whereas upon addition of different competitive metal ions, it failed to impart any considerable changes in fluorescence spectra. The detection of Pd in all oxidation states (0, II, and IV) by **probe-109** was possible, as it was able to bind Pd(0) and Pd(II) through an allyl group and could bind Pd(IV) through O, N,

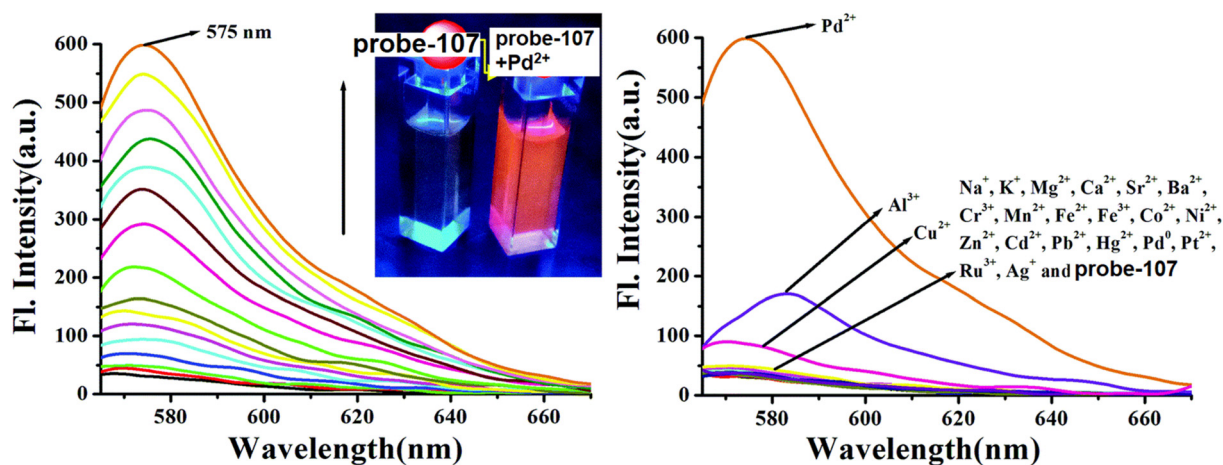


Fig. 161 Change in the emission spectra of **probe-107** on increasing the concentration of Pd(II) ions (left) and with different metal ions (right) (reprinted with permission from ref. 239, Copyright 2019 Royal Society of Chemistry).





Fig. 162 Fluorescence microscopic images of MDA-MB-468 cells treated with **probe-107** and in the presence of Pd(II) ions (reprinted with permission from ref. 239, Copyright 2019 Royal Society of Chemistry).

and O donor sites of lactones, imines and ethers respectively. The LOD value of Pd(II) was established to be 95 nM, which was calculated from the fluorescence titration spectra. Finally, the live cell imaging of detection of Pd(II) by **probe-109** was carried out in RAW 264.7 cells. The incubation of cells with **probe-109** followed by incubation with Pd(II) resulted in an enhancement in the fluorescence intensity, as observed by confocal microscopy, without causing any harm. The potency of **probe-109** in both *in vitro* and *in vivo* recognition of Pd(II) ions and fluorescence cell imaging was well established (Fig. 164).

## 10. Schiff base-based fluorescent turn-on probes for Fe(II)/Fe(III) ions

Since it actively participates in numerous metabolic processes including oxygen transport in haemoglobin and myoglobin, electron transfer from nutrients to oxygen, and DNA repair and synthesis in the living system, iron is a key metal ion in

all organisms.<sup>242–245</sup> In addition, iron plays a critical part in the manufacture of haemoglobin, wound healing, and healthy muscle function. However, the body's higher iron levels harm tissues and encourage the production of dangerous hydroxyl radicals, which can result in a variety of degenerative illnesses such as atherosclerosis, cancer, and neurological disorders.<sup>246–250</sup> Additionally, anemia can result from an iron shortage. An adult human must ingest 1.5 g of iron through their meals each day if they are menstruating due to the possibility of loss of iron, and in accordance with WHO guidelines, 1–3 mg L<sup>-1</sup> of iron is acceptable in drinking water.<sup>251</sup>

Nadakumar *et al.* synthesized a naphthalene-based Schiff base derivative for specific fluorescence turn-on recognition of Fe(II) ions in a mixture of acetonitrile and water in 2016.<sup>252</sup>

**Probe-110** was obtained from the reaction of 1-naphthaldehyde and 2-aminopyridine in ethanol at room temperature for 5 h. The target compound was structurally characterized *via* various NMR and other analytical techniques. The fluorescence sensing studies established that with Fe(II) ions, the emission intensity of **probe-110** increased with a 16 nm red shift in the emission band, and the LOD value as low as 0.15 μM, which was calculated from the 3σ/slope equation. However, no change was seen upon addition of several metal ions to **probe-110**, which strongly validate the selectivity towards Fe(II) ions. The proposed mechanism for turn-on response was due to the diminution of C=N isomerisation and the increase in the ICT process (Fig. 165). The binding constant of **probe-110** with Fe(II) ions was estimated from the absorption spectra to be 5.02 × 10<sup>4</sup> M<sup>-2</sup>. Further, stoichiometry determined *via* Job's plot and the ratio of **probe-110** to Fe(II) ions was displayed as 2:1. Finally the practical ability of **probe-110** was tested for the recognition of Fe(II) ions in tomato juice, tablets, dark chocolate and tap water and the results strongly suggested that **probe-110** is efficient for detecting and monitoring Fe(II) ions.

Simple **probe-111** for the sensing of Fe(II) based on pyrene conjugated with a Schiff base was synthesised by Wu *et al.* in 2016.<sup>253</sup> **Probe-111** (Fig. 166) was synthesized *via* a reaction between 2-aminobenzenethiol and pyrene-1-carbaldehyde in MeOH under reflux conditions for 12 h, which was confirmed *via* NMR and HRMS. The sensing studies of **probe-111** were conducted in acetonitrile by several heavy metal ions and

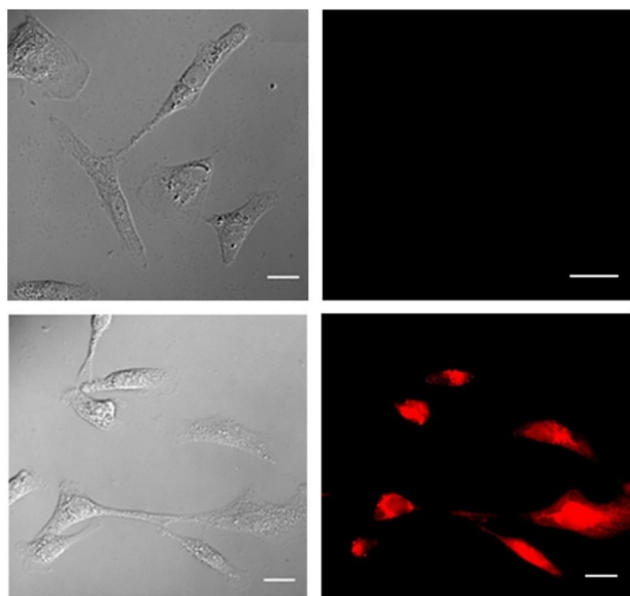


Fig. 163 Bio-imaging of MDA-MB-231 cells incubated with **probe-108** and in the presence of Pd(II) ions (reprinted with permission from ref. 240, Copyright 2019 American Chemical Society).



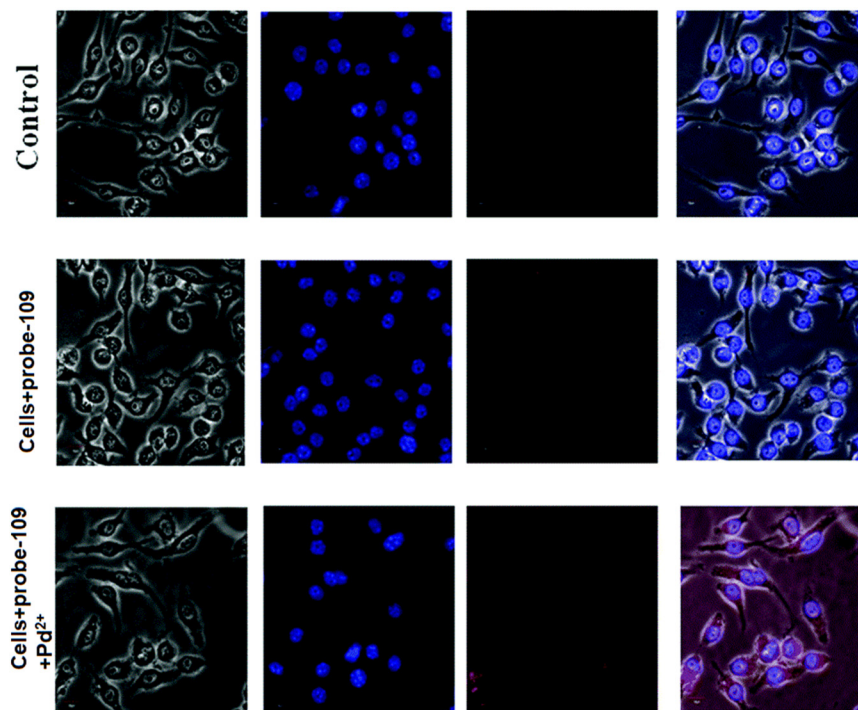


Fig. 164 Fluorescence microscopic images of RAW 264.7 cells treated with **probe-109** and in the presence of Pd(II) ions (reprinted with permission from ref. 241, Copyright 2018 Royal Society of Chemistry).

biologically important metals. The fluorescence emission of **probe-111** was found to be very weak at 448 nm and upon addition of Fe(II) and Fe(III) ions, the emission intensity was spontaneously increased by 16 times. However, in the case of Fe(III) ions, the luminescence band was moved towards red region with 115 nm; as a result, it shows bright green emission, whereas Fe(II) ions show only blue color emission under UV conditions. Thus, the emission enhancement was attributed to the establishment of rigid system and the CHEF effect was controlled. Further, the UV-vis titration data of **probe-111** displayed a colorimetric response towards Fe(III) ions and the color changes from colorless to yellow color, which could be used as a simple way for recognition through the naked eye. Thus, **probe-111** exhibited discrimination of Fe(II) and Fe(III) ions. The binding constant of **probe-111** for Fe(II), Fe(III) was calculated from the Hill equation and was estimated to be  $3.04 \times 10^9 \text{ M}^{-1}$  and  $3.97 \times 10^6 \text{ M}^{-1}$  correspondingly. Job's plots revealed binding ratios of **probe-**

**111** and Fe(II) and Fe(III) as 1 : 1, which was validated by ESI-MS and  $^1\text{H}$  NMR. The LOD value of **probe-111** with Fe(II) and  $\text{F}^-$  was determined from the fluorescence spectra to be 0.3 ppm and 25.7 ppb, respectively, which is much lesser as recommended by WHO. Further, the reversibility of **probe-111** + Fe(II) was monitored upon addition of TMEDA, whereas in the case of a fluoride complex, reversibility was established using calcium nitrate. Finally, **probe-111** was subjected to real-time monitoring Fe(II) ions in lake and drinking water and the results indicated that **probe-111** was able to show response towards Fe(II) ions. Thus, **probe-111** was found to be an efficient and potential candidate for the detection of Fe(II) ions in biological and environmental samples.

A novel rhodamine-based Schiff base (**probe-112**) was synthesized, characterized and investigated for its sensing capabilities by Gupta *et al.* in 2016.<sup>254</sup> **Probe-112** (Fig. 166) was found to exhibit a colorimetric response upon exposure to Cu(II) and Al(III) ions and on-off emission behavior upon

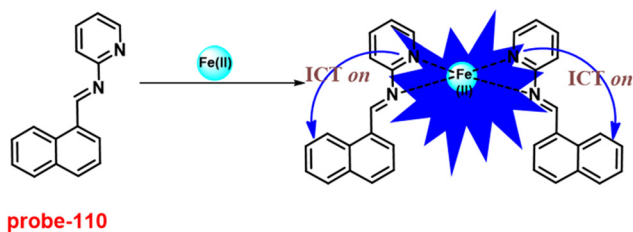


Fig. 165 Chemical structure and proposed sensing mechanism of **probe-110** with Fe(II) (redrawn the ChemDraw structure from ref. 252).

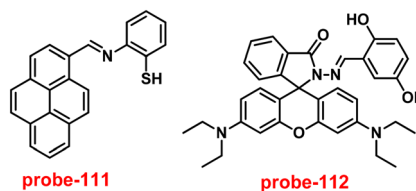


Fig. 166 Chemical structures of **probe-111** and **probe-112** (redrawn the ChemDraw structure from ref. 253 and 254).





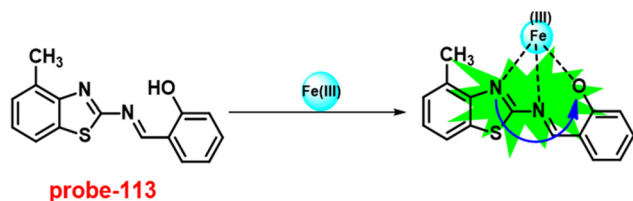


Fig. 167 Chemical structure and proposed sensing mechanism of **probe-113** with  $\text{Fe(III)}$  (redrawn the ChemDraw structure from ref. 255).

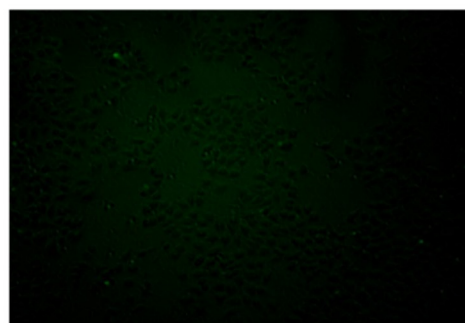
addition of  $\text{Fe(III)}$  ions. **Probe-112** was characterized by FT-IR, NMR and ESI mass spectra. The absorption spectra demonstrated significant spectral changes with  $\text{Al(III)}$  and  $\text{Cu(II)}$  and resulted in the corresponding color changes, which make **probe-112** as a colorimetric sensor. The selectivity studies were done by visual inspection, absorption and emission spectral analysis and ESI-MS and DFT experiments. Emission spectrum of **probe-112** was analyzed, which exhibited very weak luminescence upon excitation at 520 nm. Upon adding  $\text{Fe(III)}$  ions, a substantial change in emission profile was noted with the appearance of a strong emission band at 587 nm with 43-fold increment, which could be due to the formation of a ring-opened **probe-112-Fe(III)** complex. However, no spectral changes were observed in the presence of other metal ions. The binding stoichiometry was found to be 1 : 1 by Job's plot analysis with an association constant of  $5 \times 10^4 \text{ M}^{-1}$  from the absorption spectra. For investigating

the practical utility of **probe-112**, paper strips carrying the alcoholic solutions of **probe-112** were constructed and it was found that the paper strips were also giving positive responses in sensing. The red-shift in the fluorescence spectra of the **probe-112-Fe(III)** complex was verified by the DFT calculations, which revealed that the binding of  $\text{Fe(III)}$  to **probe-112** lowered the band gap.

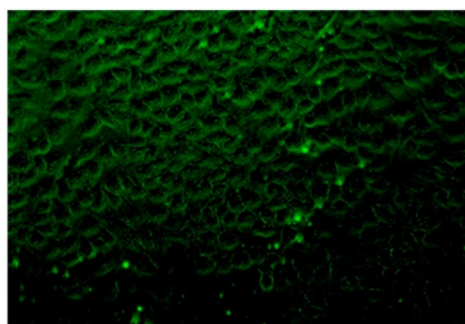
A simple chemo sensor (**probe-113**)<sup>255</sup> based on a benzothiazole and Schiff base derivative was synthesised by Pitchumani and co-workers in 2016. **Probe-113** was synthesized from 2-amino-4-methylbenzothiazole and salicylaldehyde in ethanol at room temperature and a target compound was characterised by NMR and several analytical techniques. The sensing studies of **probe-113** showed that titration with  $\text{Fe(III)}$  ions resulted in fluorescence intensity enhancement, whereas other metal ions imparted no significant response, which shows the selectivity of **probe-113** with a very low LOD value of 0.89 nM towards  $\text{Fe(III)}$  ions. The proposed mechanism for fluorescence enhancement was recognized for the generation of a new ICT process upon metal binding (Fig. 167) to **probe-113**, which was supported by TD-DFT calculations. The complexation ratio of **probe-113** with  $\text{Fe(III)}$  was determined *via* absorption spectra to be 1 : 1, which was proved by ESI-MS and TD-DFT studies. The association constant was calculated from the absorption spectra as  $3.6 \times 10^6 \text{ M}^{-1}$ , the value established the strong binding nature among **probe-113** and  $\text{Fe(III)}$  ions. Further,



Bright field image of HeLa cells



Fluorescence image of probe-113 with HeLa cells



Fluorescence images of probe-113+ $\text{Fe}^{3+}$  with HeLa cells

Fig. 168 Fluorescence microscopic images of HeLa cells treated with **probe-113** and in the presence of  $\text{Fe(III)}$  ions (reprinted with permission from ref. 255, Copyright 2016 Elsevier).



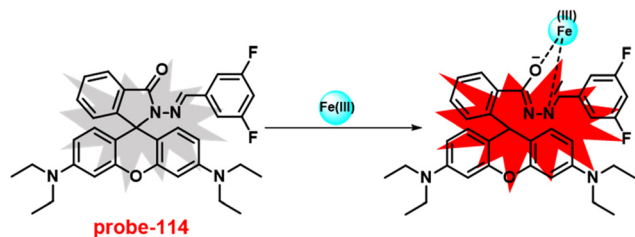


Fig. 169 Chemical structure and proposed sensing mechanism of probe-114 with Fe(III) (redrawn the ChemDraw structure from ref. 256).

**probe-113** was subjected for the sensing of Fe(III) ions in biological samples in cellular media, which was confirmed by fluorescence microscopy. The results demonstrated that the presence of Fe(III) ions in cells, which was already incubated with **probe-113**, gave a bright emission inside the cells that indicate that **probe-113** was a potential candidate for the detection of Fe(III) ions in biological samples (Fig. 168).

Rhodamine conjugated with a Schiff base was developed by Nayab *et al.* in 2017,<sup>256</sup> which displayed very sensitive and selective fluorescence turn-on behavior towards Fe(III) ions. **Probe-114** was synthesized from 3,5-difluorobenzaldehyde and rhodamine-B in methanol and refluxed for 12 h to give the target compound as a white color solid and analyzed it by various NMR and ESI-MS. The sensing studies of **probe-114** were conducted by UV-vis, fluorescence, <sup>1</sup>H NMR, and ESI-MS spectral studies. On titration with Fe(III) ions, **probe-114** exhibited color alterations from colorless to red color, which was confirmed by spectral changes observed in the UV-vis spectra, whereas other metal ions found no change. These results were strongly supported by the DFT data and reduction in the band gap after addition of Fe(III) ions. In the fluorescence spectra, on adding Fe(III) ions, the intensity was enhanced by 53-fold, which could be attributed to the transformation of a spirolactam ring to an acyclic form (Fig. 169). However, there was no change in emission spectra upon addition of competitive metal ions, which gave extraordinary selectivity towards Fe(III) ions. The detection limits and binding constant of **probe-114** were determined from the absorption spectra to be 6.94 μM and 1.13 × 10<sup>5</sup> M<sup>-1</sup>. Job's plot demonstrated the 1:1 ratio of **probe-114** and Fe(III) ions and was confirmed by UV-vis, FTIR and ESI-MS studies. The reversibility of **probe-114** was established upon addition of EDTA to the Fe-complex of **probe-114** that was

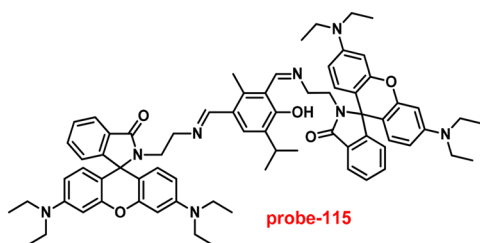


Fig. 170 Chemical structure of probe-115 (redrawn the ChemDraw structure from ref. 257).

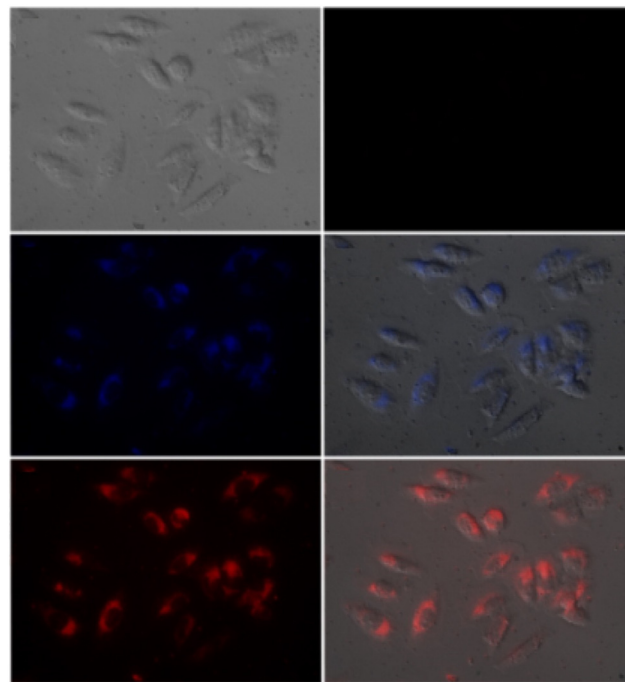


Fig. 171 Fluorescence microscopic images of HeLa cells treated with probe-115 and in the presence of Fe(III) ions (reprinted with permission from ref. 257, Copyright 2017 Elsevier).

found to exhibit a change from red to colorless as well as weak fluorescence emission. Though, re-addition of Fe(III) ions subsequently resulted in the retrieval of absorbance band and very bright luminescence. Thus, **probe-114** was found to have very promising photophysical properties and applied for the recognition of Fe(III) ions in biological and environmental samples.

Following the above-mentioned report, Adhikari *et al.* aimed to synthesise rhodamine B containing a Schiff base and conducted sensing studies by UV-vis and fluorescence spectroscopic methods, based on the suppression of PET and increase in the process of CHEF and FRET in 2017. Target **probe-115** (Fig. 170) was obtained from the amino group of rhodamine and aldehyde derivatives in ethanol under reflux conditions.<sup>257</sup> In the absorption titration, on adding Fe(III) ions there was an intensification in the absorbance with a

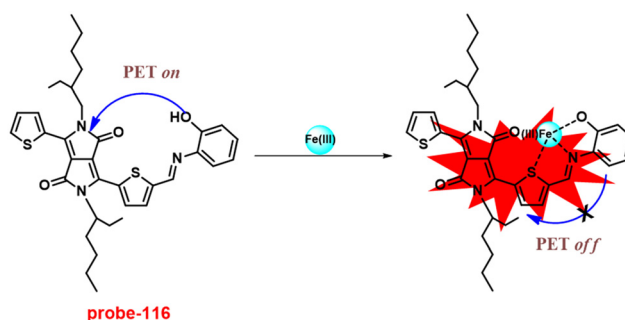


Fig. 172 Chemical structure and proposed sensing mechanism of probe-116 with Fe(III) (redrawn the ChemDraw structure from ref. 258).

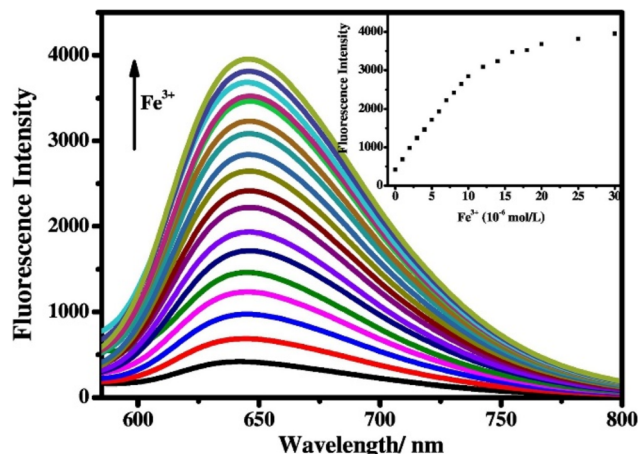


Fig. 173 Change in emission spectra of **probe-116** on increasing the concentration of  $\text{Fe(III)}$  ions (left) and with other ions (right) (reprinted with permission from ref. 258, Copyright 2018 Elsevier).

simultaneous color change of the solution from colorless to pink color. The color of emission changes from blue to orange color with the 95-fold fluorescence intensity enhancement on titrating with  $\text{Fe(III)}$  ions and very low detection limit as low as 20 nM. However, in the presence of other competitive metal ions, there was no change in emission spectra and the results strongly suggested that **probe-115** showed very sensitive and selective fluorescence turn-on response towards  $\text{Fe(III)}$  ions. **Probe-115** was found to show a ratiometric response and resulted in two iso-emissive points at 481 and 542 nm, which was designated as the molecular transfer from non-bound to metal bounded complexes. The association constant was estimated for **probe-115** with  $\text{Fe(III)}$  ions to be  $3.7025 \times 10^6 \text{ M}^{-1}$  from emission titration data using the Hill equation. The binding stoichiometry between **probe-115** with  $\text{Fe(III)}$  was estimated from Job's plot as 1:1 and was supported by the ESI-MS spectrum. Finally, authors demonstrated that **probe-115** show ability to detect  $\text{Fe(III)}$  ions in biological media and was found to be very efficient for intracellular  $\text{Fe(III)}$  ions in HeLa cells and established by fluorescence microscopic images. Further, the above finding was strongly verified by the DFT studies (Fig. 171).

Niu *et al.* obtained a diketopyrrolopyrrole-conjugated Schiff base derivative for the dual response such as colorimetric and fluorescence turn-on towards  $\text{Fe(III)}$  ions in 2018.<sup>258</sup> **Probe-116** was obtained from the reaction between the aldehyde of diketopyrrolopyrrole and *o*-aminophenol in anhydrous ethanol under reflux conditions for 12 h. While

other interfering metal ions do not cause any color changes, the absorption titration data of **probe-116** showed significant selectivity towards  $\text{Fe(III)}$  ions and color shifted from purple to red, which could be seen with the naked eye. In the case of emission spectra, upon addition of  $\text{Fe(III)}$  ions, remarkable fluorescence emission intensity enhancement by  $\sim 9.5$  fold at 645 nm was observed (Fig. 173) and the quantum yield was increased from 0.012 to 0.54, although there was no change or very slight alteration in the emission with other metal ions. The fluorescence enhancement could be attributed to the suppression of PET and CHEF effects (Fig. 172). The detection limits and association constants were calculated for **probe-116** with  $\text{Fe(III)}$  to be  $2.4 \times 10^4 \text{ M}^{-1}$  and 14.3 nM respectively. Further, the binding mode of **probe-116** and  $\text{Fe(III)}$  ions was validated by Job's plot analysis,  $^1\text{H}$  NMR and FTIR spectra. The reversibility of **probe-116** was obtained upon treatment with  $\text{S}^{2-}$  or  $\text{CN}^-$ . **Probe-116** possesses great stability, detection limit, quick response in a range of pH values, as well as good reversibility and it became a potential candidate for the recognition of  $\text{Fe(III)}$  ions in environmental and biological samples.

Following the above-mentioned report, Niu *et al.* aimed to synthesise a biphenyl-based Schiff base conjugate exhibiting chromogenic and fluorescence turn-on dual responses towards  $\text{Fe(III)}$  ions in 2019. The synthesis of a target compound (**probe-117**)<sup>259</sup> was obtained from 3,3'-dihydroxybenzidine and 1-naphthaldehyde in ethanol under reflux conditions for 6 h and a yellow solid was obtained as a product, which was verified by NMR and various spectroscopic analysis. The absorption titration data of **probe-117** showed selective response towards  $\text{Fe(III)}$  ions and color variations from yellow to colorless in DMSO/ $\text{H}_2\text{O}$  (1:1, v/v) solutions, whereas no change in the absorption spectra with other metal ions. On titrating with  $\text{Fe(III)}$  ions to **probe-117**, the emission intensity was enhanced with a gradual increment in quantum yields, due to the suppression of C=N isomerisation and PET (Fig. 174). However, on adding other competitive metal ions, there was no alteration in the emission spectra, which established the very high selectivity of **probe-117** towards  $\text{Fe(III)}$  ions. The complexation ratio of **probe-117** with  $\text{Fe(III)}$  ions was found to be 1:2 and confirmed by Job's plot,  $^1\text{H}$  NMR, HRMS analysis and theoretical studies. The LOD value of the complex with  $\text{Fe(III)}$  ions was estimated from the fluorescence titration spectra as low as 0.178  $\mu\text{M}$ . For the practical purpose, **probe-117** was utilized for the detection of  $\text{Fe(III)}$  ions in drinking water and food samples with good precision.

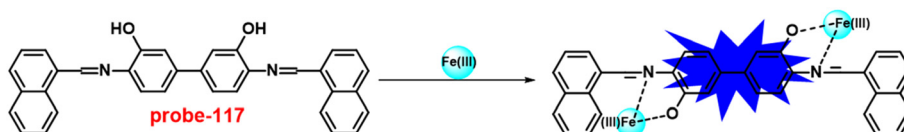


Fig. 174 Chemical structure and proposed sensing mechanism of **probe-117** with  $\text{Fe(III)}$  (redrawn the ChemDraw structure from ref. 259).





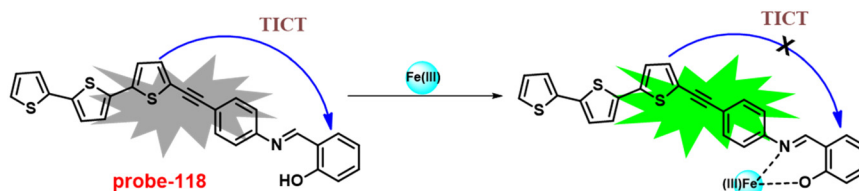


Fig. 175 Chemical structure and proposed sensing mechanism of **probe-118** with Fe(III) ions (redrawn the ChemDraw structure from ref. 260).

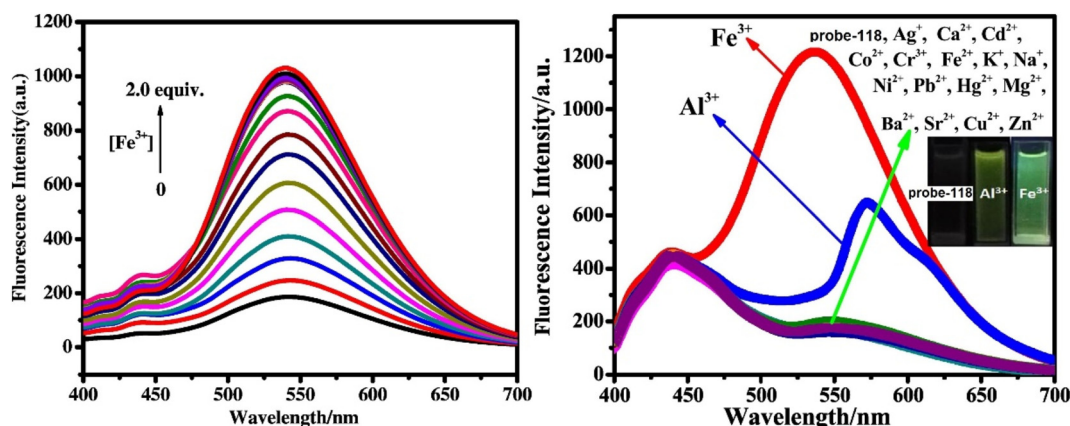


Fig. 176 Change in the emission spectra of **probe-118** on increasing the concentration of Fe(III) ions (left) and with other ions (right) (reprinted with permission from ref. 260, Copyright 2018 Elsevier).

A dual functional sensor based on oligothiophene-phenylamine for Al(III) and Fe(III) ions was obtained by Niu *et al.* in 2018.<sup>260</sup> **Probe-118** gave a very quick and selective fluorescence turn-on response towards Al(III) and Fe(III) ions without causing any intervening effect from competitive metal ions; however, Fe(III) ions were found to show better response than Al(III) ions. UV-vis studies were carried out in the presence of various metal ions with Fe(III) ions with **probe-118**. Upon addition of 2.0 eq. of Al(III) and Fe(III) ions, **probe-118** showed outstanding enhancement in the absorbance, which could be due to the construction of the metal complex of **probe-118**. Nonetheless, with other competitive metal ions, there was no change in the absorption and emission spectra (Fig. 176). The fluorescence emission studies demonstrated that the addition of Al(III) and Fe(III) ions induced a fluorescence turn-on (Fig. 175) behavior accompanied by a color transformation from colorless to green and emission bands at 536 and 572 nm. The LOD value of **probe-118** with Fe(III) ions was determined to be 0.172  $\mu\text{M}$  with a binding constant of  $1.04 \times 10^4 \text{ M}^{-1}$ . Job's plot revealed the stoichiometry of **probe-118** with Fe(III) ions as 1:1, which was further validated by ESI-MS,  $^1\text{H}$  NMR and FT-IR. The practical application of **probe-118** was established by the recognition of Fe(III) ions *via* a paper strip as well as in environmental and food samples.

In 2021, Tabassum *et al.* obtained a diaminobenzophenone-based Schiff base derivative (**probe-119**), which was structurally confirmed by  $^1\text{H}$  &  $^{13}\text{C}$  NMR, UV-

vis, FT-IR and ESI-MS analysis.<sup>261</sup> The titration studies were conducted by UV-vis and fluorescence spectroscopic analyses. In the absorption titration of **probe-119**, titration with Fe(II) ions caused colorimetric responses, showing color alteration from light yellow to brown, which can be identified through naked eyes. The fluorescence titration data demonstrated a significant fluorescence turn-on response towards Fe(II) ions, whereas with other competitive metal ions there was no change observed in the emission spectra. The emission turn-on behavior could be attributed to the suppression of PET, C=N isomerization and CHEF, which rose after the formation of metal coordination (Fig. 177). The binding constant of **probe-119** was estimated from the change in absorption spectra upon addition of Fe(II) ions as  $6.173 \times 10^7$

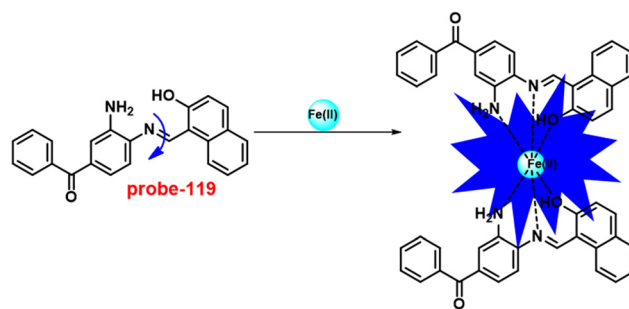


Fig. 177 Chemical structure and proposed sensing mechanism of **probe-119** with Fe(II) (redrawn the ChemDraw structure from ref. 261).



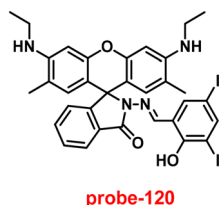


Fig. 178 Chemical structure of **probe-120** (redrawn the ChemDraw structure from ref. 262).

$M^{-2}$ . The association stoichiometry of **probe-119** with  $Fe(II)$  ions was estimated from Job's plot to be 2:1, which was supported by  $^1H$  NMR and theoretical calculations. The LOD value was appraised from the fluorescence titration data and exhibited to be  $0.0363\ \mu M$ , which is much lesser than the WHO suggested value ( $5\ \mu M$ ) for  $Fe(II)$  in the drinking water. As **probe-119** possesses a good binding constant and low detection limits, it was further applied for monitoring  $Fe(II)$  ions in diverse samples such as lake, well and river water.

Recently, Annaraj *et al.* have designed a rhodamine-containing Schiff base derivative for the selective recognition of  $Fe(III)$  ions and the tracking of  $Fe(III)$  ions in cellular media in 2020.<sup>262</sup> The absorption titration data showed that adding  $Fe(III)$  and  $Cu(II)$  ions to **probe-120** (Fig. 178) resulted in spectral changes accompanied by a color variation of solution from colorless to red color, which could originate from the cleavage of spirolactam, whereas there was no change in the presence of other competitive metal ions. The fluorescence titration data exhibited bright emission upon addition of  $Fe(III)$  ions to **probe-120** at 554 nm, which could be due to the presence of a new ICT process, whereas very minor enrichment was noticed in the presence of  $Fe(II)$  ions. However, with other competitive metal ions, no significant change was observed in the emission spectra that strongly supported the selectivity towards  $Fe(III)$  ions. The detection limits of **probe-120** towards  $Cu(II)$  and  $Fe(III)$  ions were calculated to be 263 pM and 3.1 nM respectively. The association constant of **probe-120** for  $Cu(II)$  and  $Fe(III)$  was determined by the B-H equation as  $5.2 \times 10^{-2}\ M^{-1}$  and  $1.1 \times 10^{-2}\ M^{-1}$  correspondingly and the binding ratio was calculated from Job's plot to be 1:1, which was strongly validated by  $^1H$  NMR, ESI-MS and DFT calculations. Further, with the ability of **probe-120** towards the detection of  $Fe(III)$  ions in cellular media, the fluorescence bio-imaging demonstrated its insignificant toxicity for the sensing of  $Fe(III)$  ions in zebrafish embryos. Thus, the results strongly

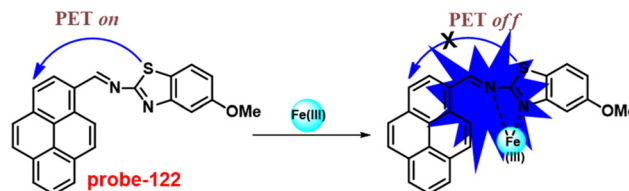


Fig. 180 Chemical structure and proposed sensing mechanism of **probe-122** with  $Fe(III)$  ions (redrawn the ChemDraw structure from ref. 264).

indicate that **probe-120** is a potential candidate for the recognition of  $Fe(III)$  ions in zebrafish embryos.

In 2018, Selvakumar and co-workers<sup>263</sup> designed and synthesized a naphthalene diamine-based  $\beta$ -diketone conjugate, which could exhibit a selective fluorescence turn-on response towards  $Fe(II)$  and a colorimetric response towards  $Fe(II)$  and  $Cu(II)$  ions. **Probe-121** was obtained by the Schiff base condensation reaction of naphthalene-1,5-diamine and acetylacetone in ethanol, and the target compound synthesis was confirmed *via* various spectroscopic analysis. The sensing studies of **probe-121** were conducted *via* UV-vis and fluorescence spectroscopic techniques. The absorption titration data demonstrated that upon addition of  $Fe(II)$  and  $Cu(II)$  ions to **probe-121**, absorbance was increased and competitive metal ions did not prompt any response. The fluorescence titration results of **probe-121** with  $Fe(II)$  ions show that the emission intensity was gradually increased due to the suppression of the PET process (Fig. 179), whereas other competitive metal ions do not show any response with **probe-121**, which suggests a greater selectivity towards  $Fe(II)$ . The complexometric ratio of **probe-121** with  $Cu(II)$  and  $Fe(II)$  ions was found to be 1:2 *via* Job's plot and supported by DFT studies, and the association constants were estimated as  $1.66 \times 10^{10}$  and  $9.22 \times 10^8\ M^{-1}$ , correspondingly. The LOD values were estimated from the emission titration data and was estimated as  $0.5\ \mu M$  for  $Fe(II)$  ions. Further, **probe-121** was found to show a binding interface with bovine serum albumin, which was detected by fluorescence quenching and FRET. Finally, the authors claimed that **probe-121** possesses potential ability for the instantaneous recognition of  $Fe(II)$  and  $Cu(II)$  metal ions.

Bhosale and co-worker aimed to synthesise benzothiazole and pyrene Schiff base derivatives for selective fluorescence turn-on behavior towards  $Fe(III)$  ions in 2017. The target molecule (**probe-122**)<sup>264</sup> was synthesised by a condensation

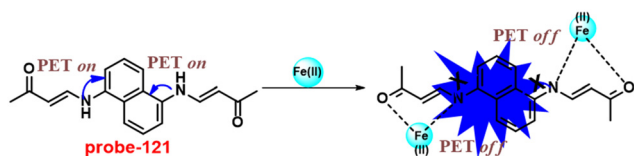


Fig. 179 Chemical structure and proposed sensing mechanism of **probe-121** with  $Fe(II)$  (redrawn the ChemDraw structure from ref. 263).

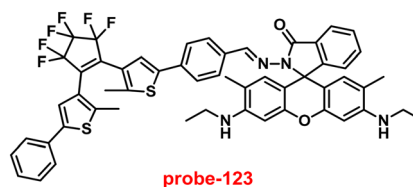


Fig. 181 Chemical structure of **probe-123** (redrawn the ChemDraw structure from ref. 265).



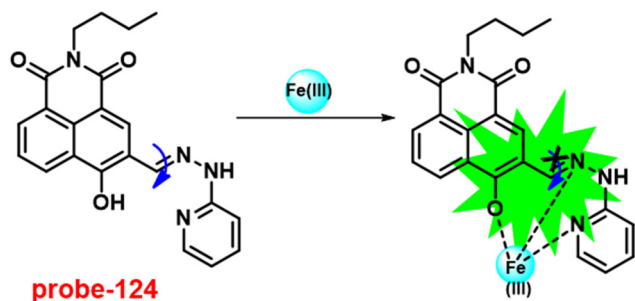


Fig. 182 Chemical structure and proposed sensing mechanism of **probe-124** with Fe(III) (redrawn the ChemDraw structure from ref. 266).

reaction between 2-amino-6-methoxy benzothiazole and pyrene aldehyde in ethanol under reflux conditions and the product was established by NMR and other analytical analyses. The sensing studies were conducted by using absorption and fluorescence spectroscopic techniques in CH<sub>3</sub>CN:H<sub>2</sub>O (1:1, v/v) solvent combinations. From the UV-vis absorption data, on adding Fe(II) and Fe(III) ions, **probe-122** exhibited a drastic change in absorption bands with colorimetric responses and the color variations from yellow to colorless and, no interference was observed with other metal ions. **Probe-122** exhibits very weak emission due to the PET process (Fig. 180) and on titrating with Fe(II) and Fe(III) ions, the bright emission was observed with 189- and 141-fold enhancement respectively at 456 nm, which could be contributed to the suppression of the PET process. Upon addition of other competitive metal ions, there was no alteration in the emission spectra, which strongly suggested the selectivity of **probe-122** towards Fe(II) and Fe(III) ions. The LOD values of **probe-122** with Fe(II) and Fe(III) ions was calculated from the fluorescence titration data to be 2.61 μM and 2.06 μM, correspondingly. The association constant was calculated from the B-H equation and displayed for Fe(III) as  $2.59 \times 10^4 \text{ M}^{-1}$  and the binding stoichiometry was obtained from Job's plot as 1:1 for **probe-122** and Fe(III) ions. The reversible nature of **probe-122** with Fe(III) ions was obtained upon addition of an EDTA solution. Thus, the authors claimed that **probe-122** possesses a good association

constant, and the detection limits make it a promising candidate for monitoring Fe(III) ions.

A novel rhodamine-based Schiff base derivative for selective fluorescence turn-on for Fe(III) ions was obtained by Xu *et al.* in 2017.<sup>265</sup> **Probe-123** was synthesized by a simple condensation reaction of rhodamine amine with aldehyde of a photochromic unit in ethanol under reflux conditions. The incorporation of photochromic units was found to have different color changes from blue to colorless under UV conditions and *vice versa* under visible light. The sensing studies of **probe-123** (Fig. 181) demonstrated that upon titration of **probe-123** with Fe(III) ions, the absorption bands at 360 and 530 nm were gradually increased and the color of solution was transformed from colorless to pink and very slight spectral changes were observed with the addition of Al(III) and Cr(III), whereas in the case of other competitive metal ions, no changes in the absorption spectra were observed. The fluorescence spectra of **probe-123** were found to exhibit very weak emission and after addition of Fe(III) ions, the bright emission was generated at 585 nm with 168-fold. Conversely, no alteration in emission spectra was noticed for other competitive metal ions but a very slight enhancement for Al(III) and Cr(III) ions. These results strongly suggested that **probe-123** shows very high selectivity towards Fe(III) ions. The binding stoichiometry of **probe-123** with Fe(III) ions was calculated from Job's plot as 1:1 and the LOD value of **probe-123** with Fe(III) ions was estimated from the emission titration spectra to be 65 nM. The binding constant was estimated from the B-H equation as  $5.97 \times 10^4 \text{ M}^{-1}$ . The reversibility of **probe-123** + Fe(III) ions was established upon addition of an EDTA solution.

Liang and team developed highly selective **probe-124** (ref. 266) for monitoring Fe(III) ions in living cells as well as aqueous solutions in 2020. Target fluorescent **probe-124** was synthesised *via* a condensation reaction between naphthalimide-monoaldehyde and 2-hydrazine pyridine. The emission profile of **probe-124** exhibited very weak fluorescence, while upon complexation with Fe(III) ions, the turn-on fluorescence response was observed due to the rigidity and planarity with inhibition of C=N isomerization

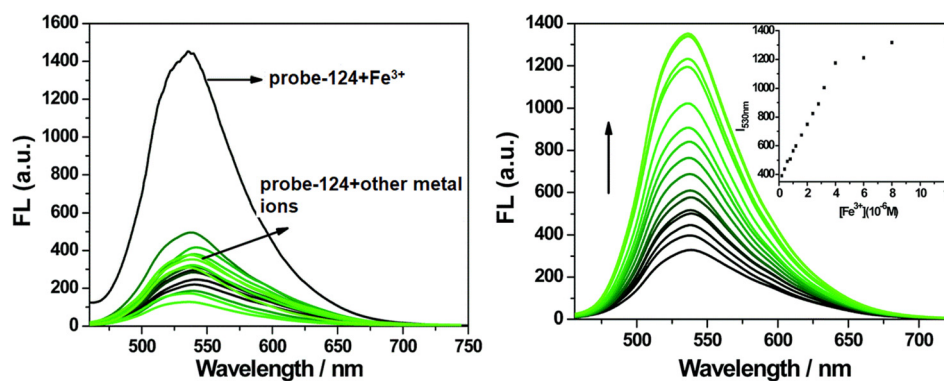


Fig. 183 Change in the emission spectra of **probe-124** on increasing the concentration of Fe(III) ions (left) and with other ions (right) (reprinted with permission from ref. 266, Copyright 2020 Royal Society of Chemistry).





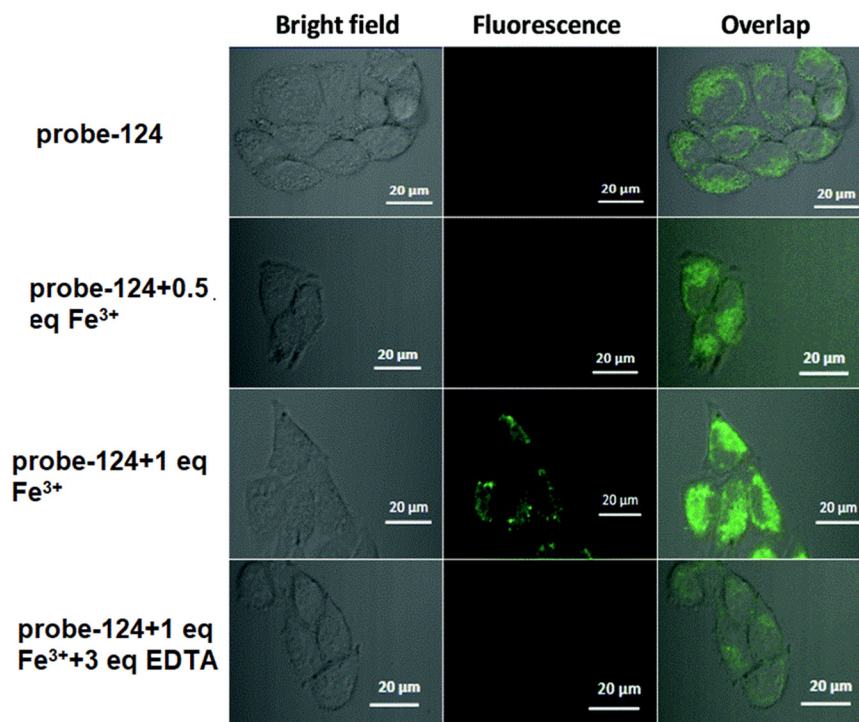


Fig. 184 Fluorescence microscopic images of bel-7420 cells treated with **probe-124** and in the presence of  $\text{Fe(III)}$  ions (reprinted with permission from ref. 266, Copyright 2020 Royal Society of Chemistry).

(Fig. 182). The selectivity of **probe-124** was determined with other metal ions, nonetheless no remarkable emission changes were observed for other metal ions apart from  $\text{Fe(III)}$  ions, which reveals the selectivity and recognition of **probe-124** even in the presence of other competitive metal ions (Fig. 183). The pH studies were carried out to identify the range over which the sensing was efficient and the results revealed that **probe-124** exhibited extreme high emission intensity in the array of 3.2 to 6.4. Absorbance studies demonstrated that titration with  $\text{Fe(III)}$  ions induced significant changes in the spectra with the generation of a new band at 426 nm, which indicates the successful complexation of the metal ion with the ligand and color alteration from orange to light yellow, which was detectable by the naked eye. The LOD value was estimated based on the  $3\sigma/\text{slope}$  method to be 38.3 nM with a binding constant of  $1.77 \times 10^6 \text{ M}^{-1}$ . **Probe-124** offers good water solubility with its non-toxic nature and better cell membrane penetrability and was applied for the sensing of  $\text{Fe(III)}$  ions in biological media.

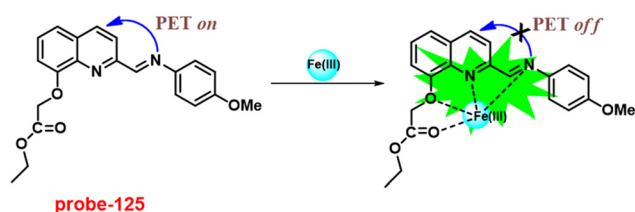


Fig. 185 Chemical structure and proposed sensing mechanism of **probe-125** with  $\text{Fe(III)}$  (redrawn the ChemDraw structure from ref. 267).

In short, **probe-124** could be considered as a promising candidate for the recognition of exogenous and endogenous detection of  $\text{Fe(III)}$  ions in biological samples and makes its practical applications very significant (Fig. 184).

A quinoline-based Schiff base conjugate showing selective fluorescence turn-on and colorimetric responses towards  $\text{Fe(III)}$  ions was designed by Tian and co-workers in 2017.<sup>267</sup> Target **probe-125** was synthesized by a reaction between quinone aldehyde and 4-methoxyaniline. The UV-vis titration data of **probe-125** demonstrated that on titrating with  $\text{Fe(III)}$  ions, **probe-125** resulted in an increase in absorbance with a color alteration from colorless to red color, while after addition of other competitive metal ions, there was no such significant change. The fluorescence spectra of **probe-125** showed very weak emission, while in the presence of  $\text{Fe(III)}$  ions, the emission intensity progressively increased by 44-fold due to the suppression of PET as well as  $\text{C=N}$  isomerization (Fig. 185). However, no other metal ions were found to have similar observations, which indicate that **probe-125** was very selective towards  $\text{Fe(III)}$  ions. The association constant of **probe-125** towards  $\text{Fe(III)}$  ions was found to be  $7.22 \times 10^4 \text{ M}^{-1}$  using the B-H equation. Further, the complexation ratio was estimated from Job's plot as 1:1, which was strongly supported by ESI-MS and  $^1\text{H}$  NMR. The LOD value was calculated from the fluorescence titration for **probe-125** with  $\text{Fe(III)}$  ions to be 0.048  $\mu\text{M}$ . Thus, due to the abnormal photophysical properties of **probe-125**, it was applied for the recognition of  $\text{Fe(III)}$  ions in environmental as well as biological samples.



## 11. Conclusion and future perspectives

The primary focus of this article is to review the recent design and synthesis of several novel Schiff base conjugates with fluorescent moieties for the sensitive and selective recognition of biological metal ions, especially transition metal ions. Transition metal ions play an important role in biological systems; hence recognition and monitoring are very mandatory. In this concern, bio-imaging can give more information regarding the accumulation of metal ions in particular organelles. There are several probes reported previously for the detection of transition metals, among which Schiff base-based chemosensors have attracted special attention due to their easy way of synthesis, stability towards heat and light and interesting optical properties such as poor emission in the absence of metal, whereas in the presence of specific metal ions (cavity size of Schiff bases), they show very bright luminescence. Here the sensing mechanism of Schiff bases with various metal ions is mainly based on the PET, RET, FRET, CHEF and ICT processes. Interestingly, after the incorporation of fluorescent moieties (signaling unit) in conjugation with Schiff bases, very high fluorescence was observed upon their binding to specific metal ions, which is utilized for the sensing of metal ions in cellular media *via* confocal fluorescence microscopic images. According to the recent literature reports, Schiff base-based fluorescent probes have very low cytotoxicity, and hence, they could be used to detect metal ions in biological media *via* cellular imaging with very good reversibility. Furthermore, their derivatives demonstrated a very efficient luminous response in biological media, allowing them to easily pass through the cells without interfering with or compromising cellular functions. Aside from the fluorescence turn-on response to metal ions, there are numerous Schiff base-based probes that can perform detection *via* colorimetric ability, in which the response can be seen with the naked eye and was used to detect metal ions in polluted ecological systems. Moreover, synthesizing materials by inclusion of Schiff bases in nanoparticles *via* self-assembly is also considered promising in the realm of supramolecular chemistry, and these materials are used as potential candidates for use in the fields of medicine, biotechnology, and biochemistry. However, a close examination of the recent literature reveals that the researchers are focusing mainly on the numerous design strategies based on Schiff base units for the selective and sensitive sensing of transition metal ions; however, the probes have innumerable restrictions in order to respond to metal ions in individual cell lines as well as specific organelles. There are few known Schiff base conjugates showing very low selectivity as well as poor permeability, and only few Schiff base-based probes for selective and sensitive detection of paramagnetic metal ions such as Fe(II), Cr(III), Fe(III), Cu(II), Ni(II), Co(II), and Mn(II) ions in biological media with moderately excellent quantum yields are known in the literature. In addition, many synthetic probes do not have the

potential to remove hazardous metal ions from ecological systems due to the lack of selectivity, which is a key issue in water research. As a result, this gap in work continues to motivate researchers to strive on enhanced probes.

In sensing chemistry, designing probes by focusing on the incorporation of several artificial fluorescent dyes such as quinoline, anthracene, coumarin, fluorescein, rhodamine, and bipyridine on Schiff bases *via* synthetic and structural modifications shows the potential detection of various metal ions *via* the fluorescence turn-on mechanism with interesting applications. For instance, such probes work with fast response to specific metal ions, with exceptionally low detection limits showing strong luminescence characteristics in the biological media. Moreover, these molecular systems can absorb and emit in the red or near-infrared range and be utilized for biological applications because of their ease of penetration *via* cellular media and the blood-brain barrier, which will provide a better picture about the accumulation of metal ions. Here, we have discussed some of the intriguing Schiff base-based probes for the detection of metal ions focusing on biological media as well as their imaging applications (Table 1). For example, the incorporation of a rhodamine moiety on the Schiff base unit, which exhibits red or NIR emission, can be effectively implemented for the tracking of metal ions in human organelles and will give the dye the exceptional feature to make it ideal for sensing and identifying early-stage diseases such as Alzheimer's and Parkinson's. Moreover, the monitoring of other biologically important paramagnetic metal ions is also possible with the help of other Schiff base-incorporated fluorescent dyes, which showed highly fluorescence turn-on.

The designing of receptor conjugates for the detection and monitoring of metal ions in biological systems needs to consider several parameters, and it should be stable in physiological media and meet the requirements of clinical diagnostics for the development of customized medicines in the future. Further, the design and synthesis of effective probes for the detection of analytes (especially biologically important metal ions) in complex biological fluids such as blood, serum, and urine is another hurdle in this field. Moreover, effective disease indicator recognition frequently necessitates multiplex exploration, which loads a significant number of relevant individual element detections. Regarding these, the design of particular fluorophores on Schiff bases as well as structural modification of Schiff bases needs to be reconsidered to show better photophysical properties and selective detection. Further, the incorporation of ammonium, phosphonium, and morpholine on Schiff bases can be utilized for the detection of metal ions in particular organelles.

Overall, in recent years, the development of Schiff base-based probes in the field of metal sensing chemistry has substantially favored the accurate monitoring of hazardous metal ions and health-related biomolecules, which is critical for safeguarding human health and the environment. Because of the functionalization of the Schiff base with fluorescent molecules, which works as a signaling agent and generates an exponential increase in its usage in sensing, the



**Table 1** Chart comparing the key characteristics of the reported Schiff base-based fluorescent turn-on probes for the above-mentioned biologically important metal ions

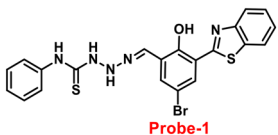
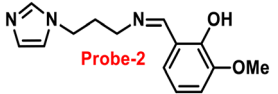
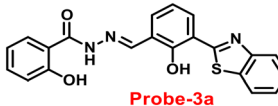
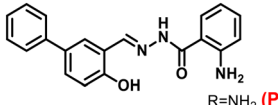
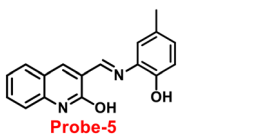
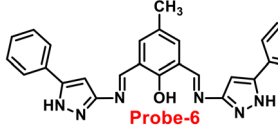
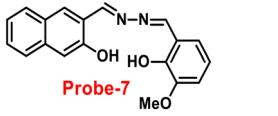
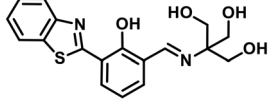
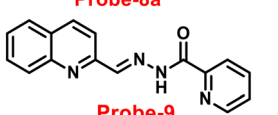
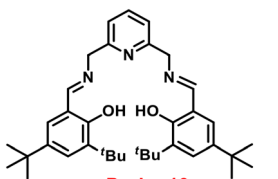
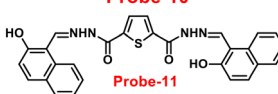
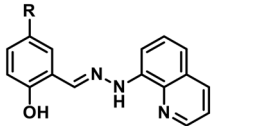
Sl. no.	Probe	Target metal ions	Association constant	Mechanism	Detection limit	Live cell imaging	Ref.
1	 <b>Probe-1</b>	Zn(II)	$4.155 \times 10^4 \text{ M}^{-1}$	CHEF on	37.7 nM	HeLa cells and live SH-SY5Y neuroblastoma cells	61
2	 <b>Probe-2</b>	Zn(II)	NA	Restriction of C=N isomerization	31.044 nM	HeLa and DU-145 cancer cell lines	62
3	 <b>Probe-3a</b>	Zn(II)	$1.6 \times 10^5 \text{ M}^{-1}$	Suppression of ESIPT	0.16 $\mu\text{M}$	Human breast cancer cell lines (MCF-7)	63
4	 <b>R = NH<sub>2</sub> (Probe-4)</b>	Zn(II)	NA	ICT and CHEF	72 nM	HeLa cells and zebrafish models	64
5	 <b>Probe-5</b>	Zn(II)	$3.7 \times 10^2 \text{ M}^{-1}$	PET off and CHEF	72 nM	A549 cells and zebrafish embryos	65
6	 <b>Probe-6</b>	Zn(II)	NA	CHEF	27.80 nM	NA	66
7	 <b>Probe-7</b>	Zn(II)	NA	CHEF	0.11 $\mu\text{M}$	NA	67
8	 <b>Probe-8a</b>	Zn(II)	$4.53 \times 10^4 \text{ M}^{-1}$	CHEF	7 nM	HeLa cells	68
9	 <b>Probe-9</b>	Zn(II)	$6.65 \times 10^3 \text{ M}^{-1}$	CHEF	72 nM	NA	69
10	 <b>Probe-10</b>	Zn(II)	$1.8 \times 10^1 \text{ M}^{-1}$	NA	7.2 $\mu\text{M}$	NA	70
11	 <b>Probe-11</b>	Zn(II)	$1.15 \times 10^4 \text{ M}^{-1}$	CHEF	0.15 $\mu\text{M}$	NA	71
12	 <b>R = H, Probe-12a</b> <b>R = CH<sub>3</sub>, Probe-12b</b>	Zn(II)	$5.90 \times 10^4 \text{ M}^{-1}$	PET	220.6 nM	C6 cells	72





Table 1 (continued)

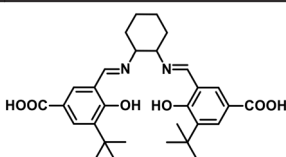
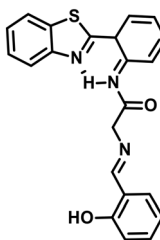
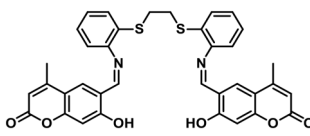
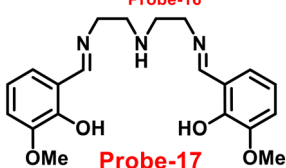
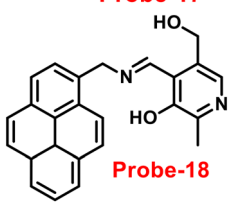
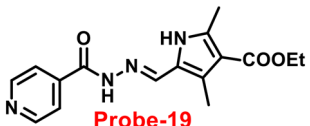
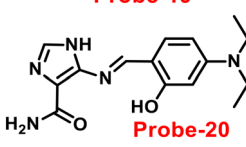
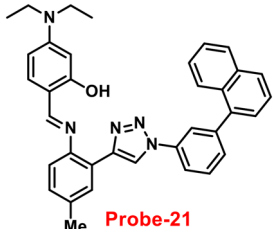
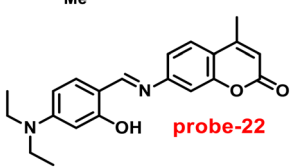
Sl. no.	Probe	Target metal ions	Association constant	Mechanism	Detection limit	Live cell imaging	Ref.
13	 <b>Probe-13</b>	Zn(II)	6.05 $\mu\text{M}$	ICT-off C=N isomerisation ESIPT	56 nM	Live cells, larval zebrafish, and plants	73
14	 <b>Probe-15</b>	Zn(II)	$2.4 \times 10^4 \text{ M}^{-1}$	C=N isomerisation ESIPT	4.5 nM	NA	75
15	 <b>Probe-16</b>	Zn(II)	$6.49 \times 10^4 \text{ M}^{-1}$	ESIPT and CHEF	0.068 $\mu\text{M}$	SCC084 (human oral carcinoma) cells	76
16	 <b>Probe-17</b>	Zn(II)	$31.647 \times 10^4 \text{ M}^{-1}$	CHEF and ESIPT	6.72 nM	HCT 116 cells	77
17	 <b>Probe-18</b>	Zn(II)	$\log \beta = 10.03(1)$	PET	2.34 $\mu\text{M}$	HeLa cells	78
18	 <b>Probe-19</b>	Zn(II)	$1.25 \times 10^4 \text{ M}^{-1}$	CHEF	0.18 $\mu\text{M}$	U251 cells	79
19	 <b>Probe-20</b>	Zn(II)	$2.0 \times 10^3 \text{ M}^{-1}$	PET off and CHEF	1.59 $\mu\text{M}$	HeLa cells	80
20	 <b>Probe-21</b>	Zn(II)	$9.06 \times 10^4 \text{ M}^{-1}$	CHEF	1.8 $\mu\text{M}$	NA	81
21	 <b>probe-22</b>	Zn(II)	$\log K = 6.04$	C=N isomerisation and PET	2.59 $\mu\text{M}$	NA	82



Table 1 (continued)

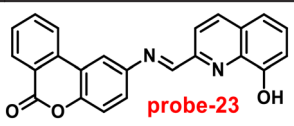
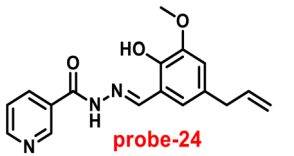
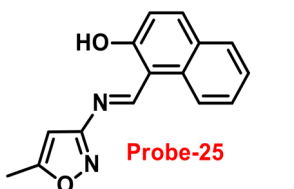
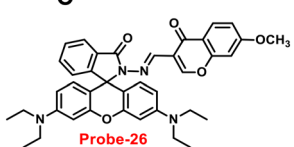
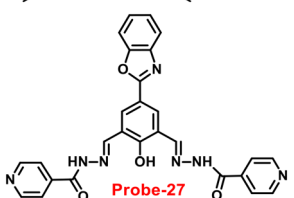
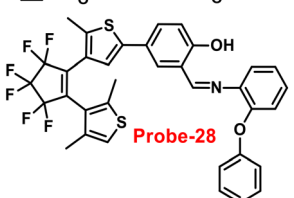
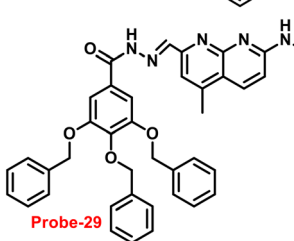
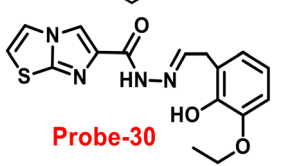
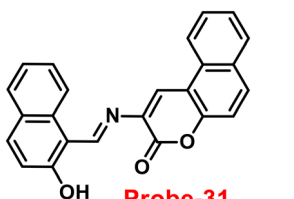
Sl. no.	Probe	Target metal ions	Association constant	Mechanism	Detection limit	Live cell imaging	Ref.
22	 <b>probe-23</b>	Zn(II)	$3.8 \times 10^3 \text{ M}^{-1}$	C=N isomerisation and PET	10 $\mu\text{M}$	NA	83
23	 <b>probe-24</b>	Zn(II)	$\log K = 5.63(0.15)$	CHEF and PET off	4.35 nM	A549 cells	84
24	 <b>Probe-25</b>	Zn(II)	$7.9 \times 10^4 \text{ M}^{-1}$	CHEF	1.29 $\mu\text{M}$	Zebrafish	85
25	 <b>Probe-26</b>	Zn(II)	$9.98 \times 10^4 \text{ M}^{-1}$	PET	0.33 $\mu\text{M}$	NA	86
26	 <b>Probe-27</b>	Zn(II)	$4.53 \times 10^4 \text{ M}^{-1}$	ICT	0.52 $\mu\text{M}$	HeLa cells	87
27	 <b>Probe-28</b>	Zn(II)	$3.49 \times 10^4 \text{ M}^{-1}$	Suppression of C=N isomerisation and CHEF on	13.4 nM	NA	88
28	 <b>Probe-29</b>	Zn(II)	$1.14 \times 10^5 \text{ M}^{-1}$	Suppression of PET and CHEF on	7.52 nM	NA	89
29	 <b>Probe-30</b>	Zn(II)	$2.2 \times 10^5 \text{ M}^{-1}$	Suppression of PET and CHEF on	1.2 nM	NA	90
30	 <b>Probe-31</b>	Zn(II)	$3.21 \times 10^4 \text{ M}^{-1}$	Suppression of C=N isomerisation and PET	3.6 $\mu\text{M}$	NA	91



Table 1 (continued)

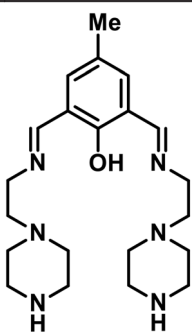
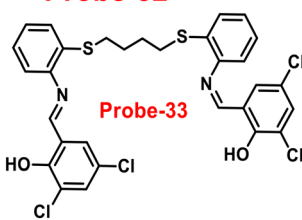
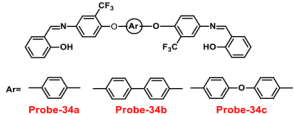
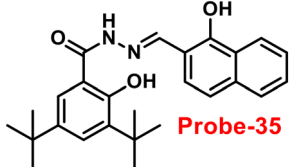
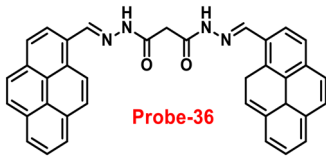
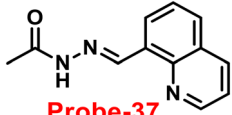
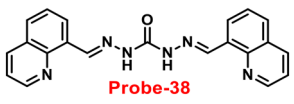
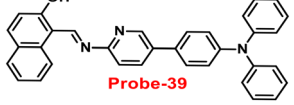
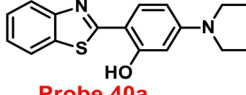
Sl. no.	Probe	Target metal ions	Association constant	Mechanism	Detection limit	Live cell imaging	Ref.
31	 <b>Probe-32</b>	Zn(II)	$7.14 \times 10^4 \text{ M}^{-1}$	CHEF	1.059 nM	MDA-MB-468 cells	92
32	 <b>Probe-33</b>	Zn(II)	$6.91 \times 10^4 \text{ M}^{-1}$	CHEF and suppression of ESIPT	1.73 nM	MCF-7 cells	93
33	 <b>Probe-34a</b>	Zn(II)	$1.42 \times 10^6 \text{ M}^{-1}$	CHEF and restriction of C=N isomerisation	67.2 nM	SW620 cancer cells	94
34	 <b>Probe-35</b>	Zn(II)	$7.79 \times 10^6 \text{ M}^{-1}$	ESIPT and ICT	0.31 $\mu\text{M}$	HeLa cells	95
35	 <b>Probe-36</b>	Zn(II)	$3 \times 10^5 \text{ M}^{-1}$	PET	5.1 nM	HeLa cells	96
36	 <b>Probe-37</b>	Zn(II)	NA	C=N isomerisation	89.3 nM	HeLa cells	97
37	 <b>Probe-38</b>	Zn(II)	$1.03 \times 10^4 \text{ M}^{-1}$	CHEF	0.66 $\mu\text{M}$	HeLa cells	98
38	 <b>Probe-39</b>	Zn(II)	$3.24 \times 10^4 \text{ M}^{-1}$	PET and CHEF	19.134 nM	HeLa cells	99
39	 <b>Probe 40a</b>	Zn(II)	$4.9 \times 10^4 \text{ M}^{-1}$	ESIPT and CHEF	67 nM	NA	100





Table 1 (continued)

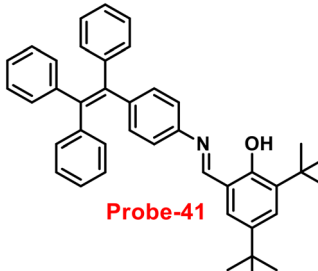
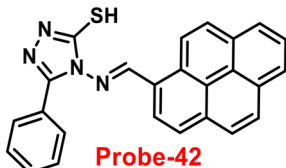
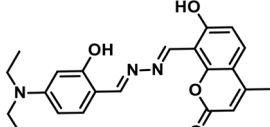
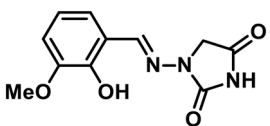
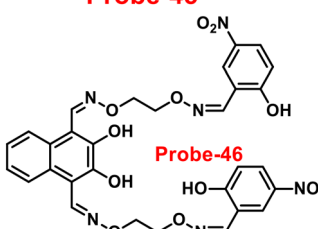
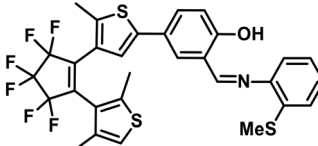
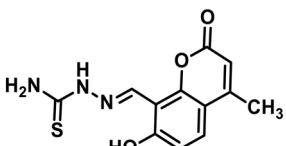
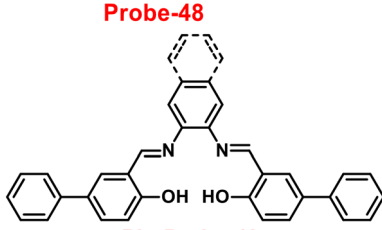
Sl. no.	Probe	Target metal ions	Association constant	Mechanism	Detection limit	Live cell imaging	Ref.
40	 <b>Probe-41</b>	Zn(II)	NA	PET	80.5 nM	NA	101
41	 <b>Probe-42</b>	Zn(II)	$4.205 \times 10^{-7} \text{ M}^{-2}$	PET	0.79 nM	B16F10 cell lines and in zebrafish	102
42	 <b>Probe-43</b>	Zn(II)	NA	Reduction of $\pi$ - $\pi$ interactions and PET	30.3 nM	SiHa cells	103
43	 <b>Probe-45</b>	Zn(II)	$4.5 \times 10^3 \text{ M}^{-1}$	CHEF	11.9 $\mu\text{M}$	HeLa cells	105
44	 <b>Probe-46</b>	Zn(II)	$2.71 \times 10^4 \text{ M}^{-1}$	PET off	0.52 $\mu\text{M}$	NA	106
45	 <b>Probe-47</b>	Zn(II)	$4.692 \times 10^5 \text{ M}^{-1}$	NA	38.6 nM	NA	107
46	 <b>Probe-48</b>	Zn(II)	$2.847 \times 10^3 \text{ M}^{-1}$	ESIPT	6 nM	Cancer cells	108
47	 <b>Ph: Probe-49a</b> <b>Naph: Probe-49b</b>	Zn(II)	NA	C=N isomerisation, PET and ESIPT	7.69 and 5.35 nM	HeLa cells	109



Table 1 (continued)

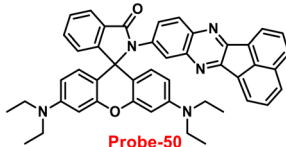
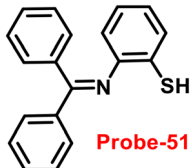
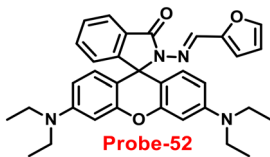
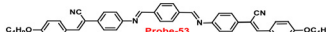
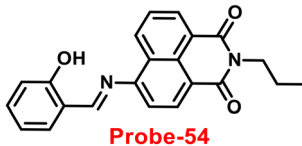
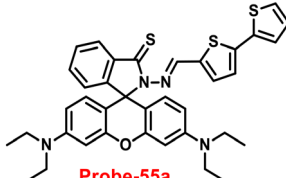
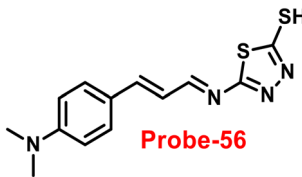
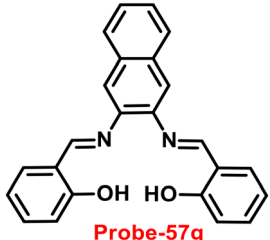
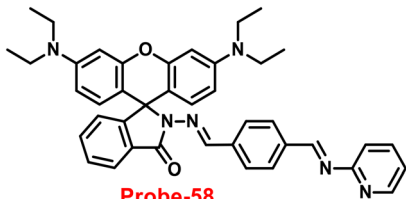
Sl. no.	Probe	Target metal ions	Association constant	Mechanism	Detection limit	Live cell imaging	Ref.
48	 <b>Probe-50</b>	Hg(II)	NA	Ring opening of spirolactum	10 nM	HeLa cells and zebra fish	120
49	 <b>Probe-51</b>	Hg(II)	$4.484 \times 10^5 \text{ M}^{-1}$	C=N isomerisation and ESIPT	22 nM	NA	121
50	 <b>Probe-52</b>	Hg(II)	$1.01 \times 10^{4.94} \text{ M}^{-1}$	Ring opening of spirolactum	0.09 $\mu\text{M}$	SW480 cells	122
51	 <b>Probe-53</b>	Hg(II)	NA	Suppression of RIR and C=N isomerisation	3.4 nM	HeLa cells	123
52	 <b>Probe-54</b>	Hg(II)	$6.89 \times 10^6 \text{ M}^{-1}$	Hydrolysis	0.5 nM	NA	124
53	 <b>Probe-55a</b>	Hg(II)	$3.94 \times 10^5 \text{ M}^{-1}$	Ring opening	0.62 ppb	HeLa cells	125
54	 <b>Probe-56</b>	Hg(II)	$2.5 \times 10^4 \text{ M}^{-1}$	CHEF	2 $\mu\text{M}$	NA	126
55	 <b>Probe-57g</b>	Hg(II)	NA	ESIPT	12.5 ppb	NA	127
56	 <b>Probe-58</b>	Hg(II)	$4.149 \times 10^3 \text{ M}^{-1}$	CHEF caused by ring opening	1.729 ng mL <sup>-1</sup>	A375 cells	128



Table 1 (continued)

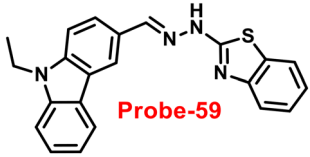
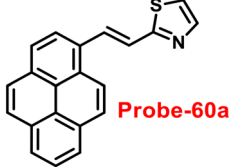
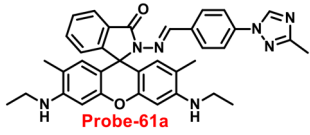
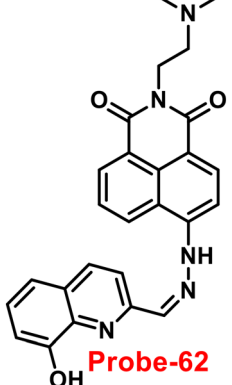
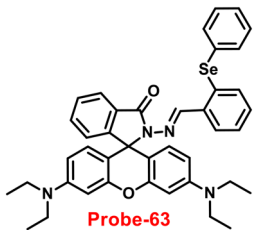
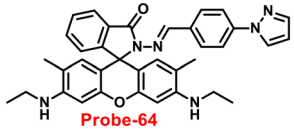
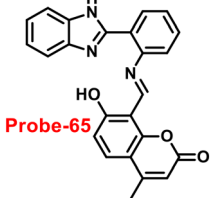
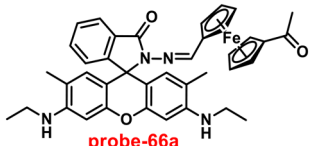
Sl. no.	Probe	Target metal ions	Association constant	Mechanism	Detection limit	Live cell imaging	Ref.
57	 <b>Probe-59</b>	Hg(II)	$1.88 \times 10^5 \text{ M}^{-1}$	ICT on	0.14 $\mu\text{M}$	NA	129
58	 <b>Probe-60a</b>	Hg(II)	$5.8 \times 10^5 \text{ M}^{-2}$	Schiff base hydrolysis	0.270 $\mu\text{M}$	NA	130
59	 <b>Probe-61a</b>	Hg(II)	NA	PET and C=N isomerisation	13.4 nM	Live breast cancer cells and MCF-7 cells	131
60	 <b>Probe-62</b>	Hg(II)	$4.12 \times 10^5 \text{ M}^{-1}$	PET	0.24 $\mu\text{M}$	NA	132
61	 <b>Probe-63</b>	Hg(II)	$7.44 \times 10^4 \text{ M}^{-1}$	Ring opening	12 nM	HeLa cells and zebrafish	133
62	 <b>Probe-64</b>	Hg(II)	NA	PET and CHEF	0.2 nM	NA	134
63	 <b>Probe-65</b>	Hg(II)	$8.75 \times 10^4 \text{ M}^{-1}$	Hydrolysis	70 nM	HeLa cells	135
64	 <b>probe-66a</b>	Hg(II)	NA	Ring opening	NA	THP-1 cells	136





Table 1 (continued)

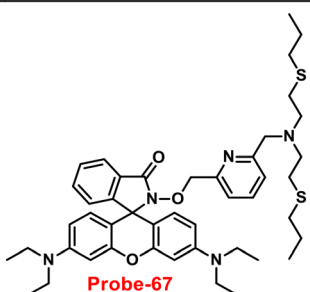
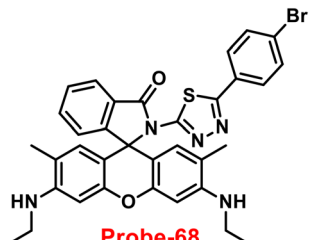
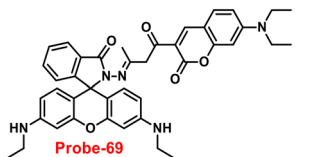
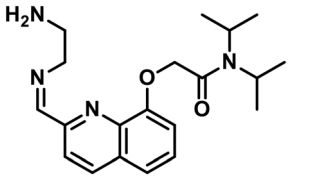
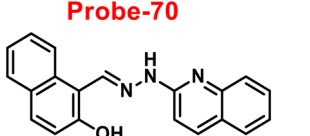
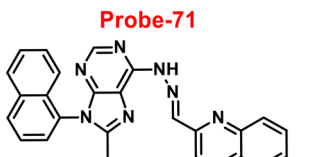
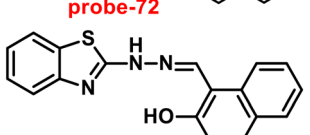
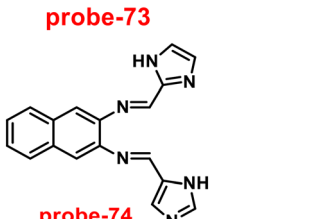
Sl. no.	Probe	Target metal ions	Association constant	Mechanism	Detection limit	Live cell imaging	Ref.
65	 <b>Probe-67</b>	Hg(II)	$3.28 \times 10^5 \text{ M}^{-1}$	Ring opening	2.36 $\mu\text{M}$	PC3 cells	137
66	 <b>Probe-68</b>	Hg(II)	$6 \times 10^4 \text{ M}^{-1}$	Ring opening	30.37 nM	MDA-MB-231 and A375 breast cancer cells	138
67	 <b>Probe-69</b>	Hg(II)	$3.34 \times 10^4 \text{ M}^{-1}$	Ring opening	2.96 $\mu\text{M}$	HeLa cells	139
68	 <b>Probe-70</b>	Cd(II)	NA	NA	2.4 nM	NA	150
69	 <b>Probe-71</b>	Cd(II)	$1.77 \times 10^5 \text{ M}^{-1}$	CHEF and C=N isomerisation	0.14 nM	NA	151
70	 <b>probe-72</b>	Cd(II)	$0.862 \times 10^5 \text{ M}^{-1}$	PET and C=N isomerisation	41 nM	HeLa cells	152
71	 <b>probe-73</b>	Cd(II)	$1.17 \times 10^4 \text{ M}^{-1}$	ICT on and CHEF	$\mu\text{M}$ level	HeLa cells	153
72	 <b>probe-74</b>	Cd(II)	$1.628 \times 10^4 \text{ M}^{-1}$	ICT off	0.38 $\mu\text{M}$	Human liver cancer cells (SMMC-7721), zebrafish, and live tissues of <i>Arabidopsis thaliana</i>	154



Table 1 (continued)

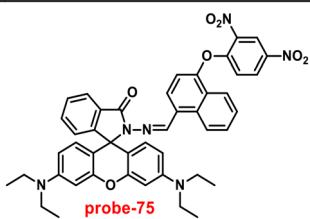
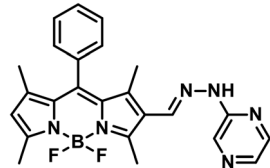
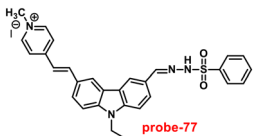
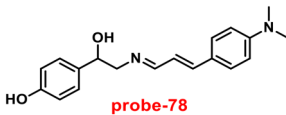
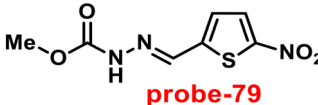
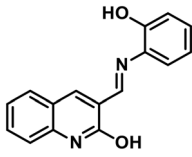
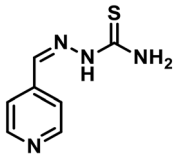
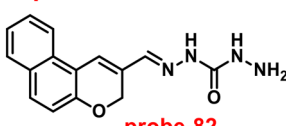
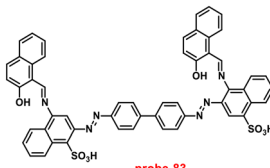
Sl. no.	Probe	Target metal ions	Association constant	Mechanism	Detection limit	Live cell imaging	Ref.
73	 probe-75	Au(III)	NA	Ring opening and suppression of PET	1.51 $\mu\text{M}$	MC3T3 cells	165
74	 probe-76a	Au(III)	NA	Hydrolysis	60 nM	PC12 cells and zebrafish	166
75	 probe-77	Au(III)	NA	Schiff base hydrolysis	22 nM	MCF-7 and HeLa cells	167
76	 probe-78	Ag(I)	$7.00 \times 10^4 \text{ M}^{-1}$	NA	1.49 $\mu\text{M}$	NA	180
77	 probe-79	Ag(I)	$1.58 \times 10^6 \text{ M}^{-1}$	ICT off	0.12 $\mu\text{M}$	<i>E. coli</i> cells	181
78	 probe-80	Ag(I)	$2.41 \times 10^4 \text{ M}^{-2}$	PET off and ICT on	14 $\mu\text{M}$	<i>E. coli</i> cells	182
79	 probe-81	Ag(I)	$2.8 \times 10^9 \text{ M}^{-2}$	PET off	1.6 $\mu\text{M}$	NA	183
80	 probe-82	Cu(II)	NA	ICT on	10.4 nM	HeLa cells	195
81	 probe-83	Cu(II)	$1.03 \times 10^6 \text{ M}^{-1}$	CHEF	0.1 nM	HepG2 cells	196



Table 1 (continued)

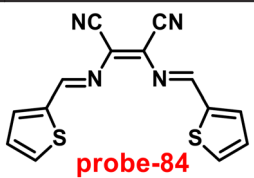
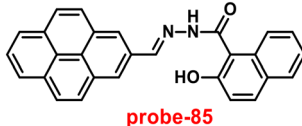
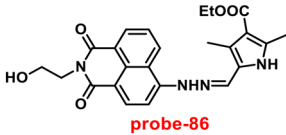
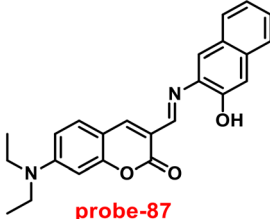
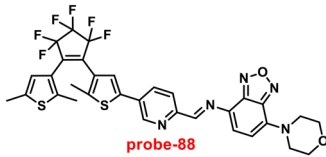
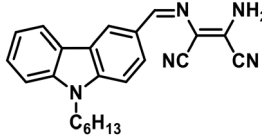
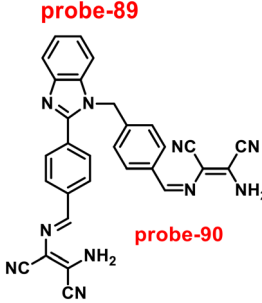
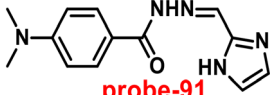
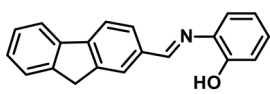
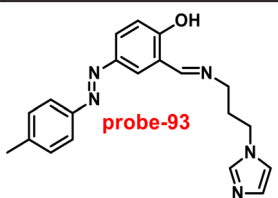
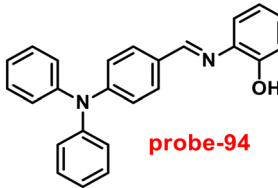
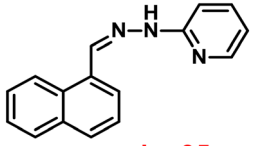
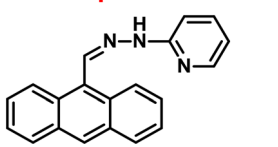
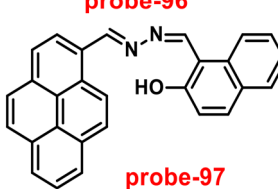
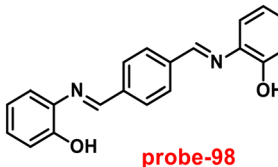
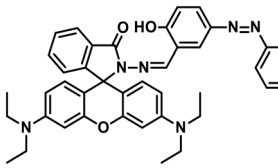
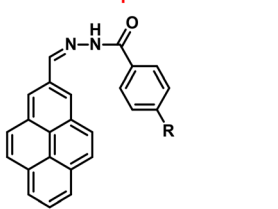
Sl. no.	Probe	Target metal ions	Association constant	Mechanism	Detection limit	Live cell imaging	Ref.
82	 <b>probe-84</b>	Cu(II)	$7.31 \times 10^4 \text{ M}^{-1}$	CHEF	14.5 nM	NA	197
83	 <b>probe-85</b>	Cu(II)	$1.16 \times 10^4 \text{ M}^{-1}$	PET off	0.26 $\mu\text{M}$	RAW 264.7 cells	198
84	 <b>probe-86</b>	Cu(II)	NA	Hydrolysis	1.50 $\mu\text{M}$	HeLa cells	199
85	 <b>probe-87</b>	Cu(II)	$1.74 \times 10^5 \text{ M}^{-1}$	Decomposition of imine bond	12.7 nM	HepG2 cells	200
86	 <b>probe-88</b>	Cu(II)	$4 \times 10^4 \text{ M}^{-1}$	CHEF and restriction of C=N isomerisation	1.49 $\mu\text{M}$	NA	201
87	 <b>probe-89</b>	Cu(II)	$1.26 \times 10^{-6} \text{ M}^{-1}$	ICT	27.4 nM	NA	202
88	 <b>probe-90</b>	Cu(II)	$2.5 \times 10^8 \text{ M}^{-2}$	Suppression of C=N isomerisation	0.49 $\mu\text{M}$	HepG2 cells	203
89	 <b>probe-91</b>	Cu(II)	$4.3 \times 10^7 \text{ M}^{-1}$	Suppression of PET	15 nM	NA	204
90	 <b>probe-92</b>	Cu(II)	$2.84 \times 10^5 \text{ M}^{-1}$	ICT quenching	1.54 nM	NA	205





Table 1 (continued)

Sl. no.	Probe	Target metal ions	Association constant	Mechanism	Detection limit	Live cell imaging	Ref.
91	 <b>probe-93</b>	Cu(II)	NA	CHEF and restriction of C=N isomerisation	1.8 μM	NA	206
92	 <b>probe-94</b>	Cu(II)	$1.96 \times 10^7 \text{ M}^{-1}$	Restriction of C=N isomerisation	0.18 μM	NA	207
93	 <b>probe-95</b>	Cu(II)	$1.38 \times 10^5 \text{ M}^{-2}$	Suppression of PET	3.90 nM	NA	208
94	 <b>probe-96</b>	Cu(II)	$2.12 \times 10^6 \text{ M}^{-1}$	Suppression of PET	0.1 nM	Raw 264.7 cells	209
95	 <b>probe-97</b>	Cu(II)	$4.8 \times 10^6 \text{ M}^{-1}$	Break down the excimer formation	0.1 μM	HEK 293 cells	210
96	 <b>probe-98</b>	Cu(II)	$6.67 \times 10^4 \text{ M}^{-1}$	Suppression of PET and C=N isomerisation	0.62 μM	L929 cells	211
97	 <b>probe-99</b>	Cu(II)	NA	Spirolactone ring opening	NA	HepG2 cells	212
98	 <b>probe-100a</b> <b>probe-100b</b>	Cu(II)	$1.29 \times 10^5 \text{ M}^{-1}$ for <b>100a</b> ; $1.55 \times 10^4 \text{ M}^{-1}$ for <b>100b</b>	PET	88 nM for <b>100a</b> ; 0.49 μM for <b>100b</b>	NA	213

R = OMe

R = OCH<sub>2</sub>CON(CH<sub>2</sub>CH<sub>3</sub>)<sub>2</sub>**probe-100a****probe-100b**

Table 1 (continued)

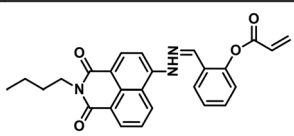
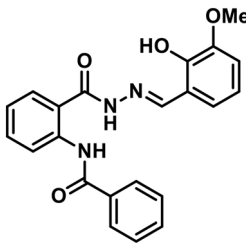
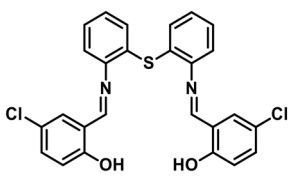
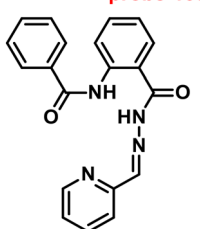
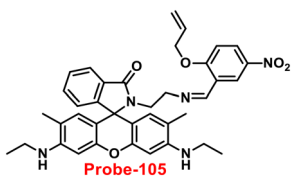
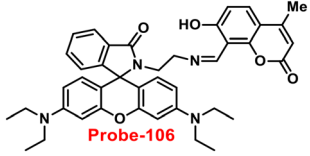
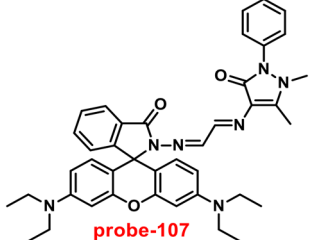
Sl. no.	Probe	Target metal ions	Association constant	Mechanism	Detection limit	Live cell imaging	Ref.
99	 <b>probe-101</b>	Cu(II)	NA	NA	25 nM	HeLa cells	214
100	 <b>probe-102</b>	Ni(II)	$1.1 \times 10^4 \text{ M}^{-1}$	PET, ESIPT and C=N isomerisation	1.71 $\mu\text{M}$	HeLa cells	225
101	 <b>probe-103</b>	Ni(II)	$4.18 \times 10^5 \text{ M}^{-1}$	CHEF	8.67 nM	HeLa cells	226
102	 <b>probe-104</b>	Ni(II)	$1.45 \times 10^3 \text{ M}^{-1/2}$	PET off	1.18 $\mu\text{M}$	HeLa cells	227
103	 <b>Probe-105</b>	Pd(II)	NA	Ring opening of spirolactum	50 nM	HCT 116 cells	237
104	 <b>Probe-106</b>	Pd(II)	$9.1 \times 10^4 \text{ M}^{-1}$	Ring opening of spirolactum	18.8 nM	MCF7 cells	238
105	 <b>probe-107</b>	Pd(II)	$8.36 \times 10^3 \text{ M}^{-1}$	Ring opening of spirolactum	11.9 $\mu\text{M}$	MDA-MB-468 cells	239



Table 1 (continued)

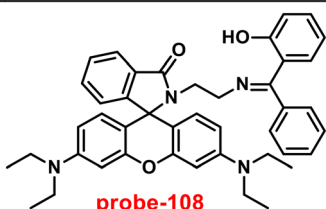
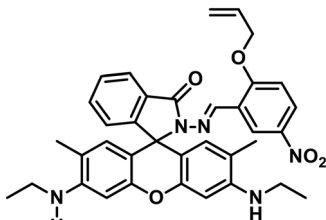
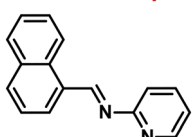
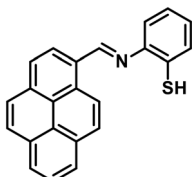
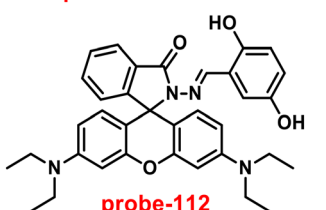
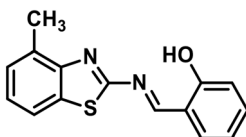
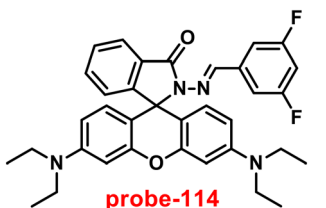
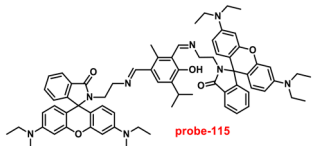
Sl. no.	Probe	Target metal ions	Association constant	Mechanism	Detection limit	Live cell imaging	Ref.
106	 <b>probe-108</b>	Pd(II)	$1.99 \times 10^4 \text{ M}^{-1}$	Ring opening of spirolactone	34 nM	MDA-MB-231 cells	240
107	 <b>probe-109</b>	Pd(II)	NA	Ring opening of spirolactone	95 nM	RAW 264.7 cells	241
108	 <b>probe-110</b>	Fe(II)	$5.02 \times 10^4 \text{ M}^{-2}$	ICT	0.15 $\mu\text{M}$	NA	252
109	 <b>probe-111</b>	Fe(II)	$3.04 \times 10^9 \text{ M}^{-1}$	CHEF	0.3 ppm	NA	253
110	 <b>probe-112</b>	Fe(III)	$5 \times 10^4 \text{ M}^{-1}$	Ring opening of spirolactone	19 nM	NA	254
111	 <b>probe-113</b>	Fe(III)	$3.6 \times 10^6 \text{ M}^{-1}$	ICT	0.89 nM	HeLa cells	255
112	 <b>probe-114</b>	Fe(III)	$1.13 \times 10^5 \text{ M}^{-1}$	Ring opening of spirolactone	6.94 $\mu\text{M}$	NA	256
113	 <b>probe-115</b>	Fe(III)	$3.7025 \times 10^6 \text{ M}^{-1}$	PET suppression and CHEF, FRET on	20 nM	HeLa cells	257





Table 1 (continued)

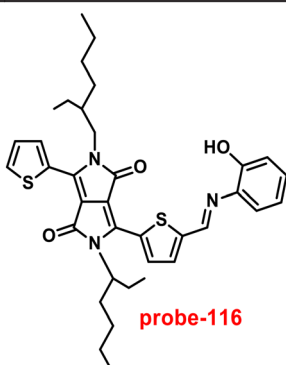
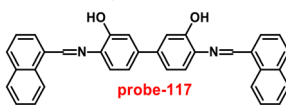
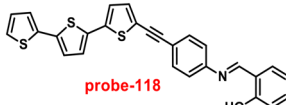
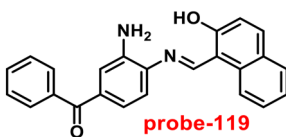
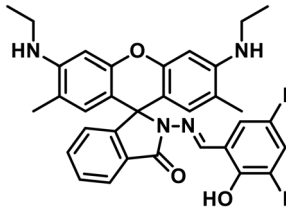
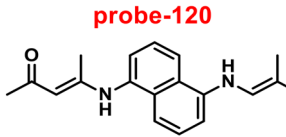
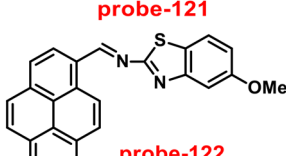
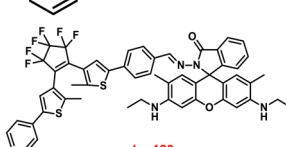
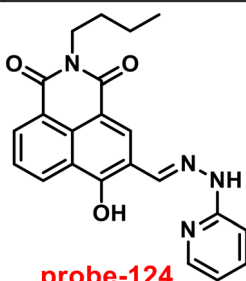
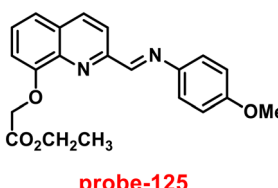
Sl. no.	Probe	Target metal ions	Association constant	Mechanism	Detection limit	Live cell imaging	Ref.
114	 probe-116	Fe(III)	$2.4 \times 10^4 \text{ M}^{-1}$	Suppression of PET and CHEF	14.3 nM	NA	258
115	 probe-117	Fe(III)	$3.099 \times 10^4 \text{ M}^{-2}$	C=N isomerisation and PET	0.178 $\mu\text{M}$	NA	259
116	 probe-118	Fe(III)	$1.04 \times 10^4 \text{ M}^{-1}$	TICT	0.172 $\mu\text{M}$	NA	260
117	 probe-119	Fe(II)	$6.173 \times 10^7 \text{ M}^{-2}$	PET, C=N isomerisation, CHEF	0.0363 $\mu\text{M}$	NA	261
118	 probe-120	Fe(III)	$1.1 \times 10^{-2} \text{ M}^{-1}$	ICT	3.1 nM	Zebrafish	262
119	 probe-121	Fe(II)	$9.22 \times 10^8 \text{ M}^{-1}$	PET off	0.5 $\mu\text{M}$	NA	263
120	 probe-122	Fe(III)	$2.59 \times 10^4 \text{ M}^{-1}$	PET off	2.06 $\mu\text{M}$	NA	264
121	 probe-123	Fe(III)	$5.97 \times 10^4 \text{ M}^{-1}$	Ring opening	65 nM	NA	265



Table 1 (continued)

Sl. no.	Probe	Target metal ions	Association constant	Mechanism	Detection limit	Live cell imaging	Ref.
122		Fe(III)	$1.77 \times 10^6 \text{ M}^{-1}$	Inhibition of C=N isomerisation	38 nM	bel-7420 cells	266
123		Fe(III)	$7.22 \times 10^4 \text{ M}^{-1}$	PET and C=N isomerisation	0.048 $\mu\text{M}$	NA	267

domains of advanced functional materials, environmental protection, and healthcare can continue to improve for years to come.

## Abbreviations

ICP-MS	Inductively coupled plasma mass spectroscopy
ICP-AES	Inductively coupled plasma atomic emission spectroscopy
AAS/AES	Atomic absorption/emission spectroscopy
AIE	Aggregation-induced emission
ESIPT	Excited-state intramolecular proton transfer
PET	Photoinduced electron transfer
ICT	Intramolecular charge transfer
CHEF	Chelation induced enhanced fluorescence
FRET	Fluorescence resonance energy transfer
nm	Nanometer
nM	Nanomolar
$\mu\text{M}$	Micromolar
NMR	Nuclear magnetic resonance
HRMS	High-resolution mass spectrometry
FT-IR	Fourier transform infrared
ATR-FTIR	Attenuated total reflectance-Fourier transform infrared spectroscopy
XRD	X-ray diffraction
LOD	Limit of detection
B-H	Benesi-Hildebrand
DFT	Density functional theory
TD-DFT	Time-dependent density-functional theory
ESI-MS	Electrospray ionisation mass spectrometry
WHO	World Health Organisation
EDTA	Ethylene diamine tetraacetate
AIEE	Aggregation-induced emission enhancement
DMF	Dimethylformamide

PPI	Pyrophosphate
PA	Picric acid
UV/PL	UV-vis absorption/photoluminescence
PXRD	Powder X-ray diffraction
SEM	Scanning electron microscope
TEM	Transmission electron microscopy
AFM	Atomic force microscopy
DLS	Dynamic light scattering
US-EPA	U.S. Environmental Protection Agency
EA	Elemental analysis
Cys	Cysteine
THF	Tetrahydrofuran
ppb	Parts per billion
ppm	Parts per million
ns	Nanoseconds
CV	Cyclic voltammogram
LC-MS	Liquid chromatography with tandem mass spectrometry
DMSO	Dimethylsulfoxide
BODIPY	Boron-dipyrromethene
MALDI-TOF	Matrix-assisted laser desorption ionization-time of flight mass spectrometry
ACN	Acetonitrile
LMCT	Ligand to metal charge transfer
MFC	Mechanofluorochromism
RIR	Restricted the intramolecular rotations
TEA	Triethylamine

## Author contributions

A. A. contributed to the conceptualization, planning, execution and drafting of the article. A. J. contributed to investigating standard detection techniques and future perspectives. C. A. S. P. contributed with proposed the



conception, supervision, resources, review and editing of the article. All the authors thoroughly read the final manuscript draft and gave permission for its submission.

## Conflicts of interest

The authors declare no competing financial interest.

## Acknowledgements

C. A. S. P. thanks, SERB/SRG/2021/002112 for funding and National Institute of Technology for support. Ms. A. J. thanks National Institute of Technology, Calicut for institute fellowship and Ms. A. A. thanks for SERB/EEQ/2021/000180.

## References

- 1 Y. Hang, J. Boryczka and N. Wu, *Chem. Soc. Rev.*, 2022, **51**, 329.
- 2 X. Zheng, W. Cheng, C. Ji, J. Zhang and M. Yin, *Rev. Anal. Chem.*, 2020, **39**, 231.
- 3 S. A. A. Razavi and A. Morsali, *Coord. Chem. Rev.*, 2020, **415**, 213299.
- 4 R. A. Bisergaevam and Y. N. Sirieva, *J. Phys.: Conf. Ser.*, 2020, **1691**, 012055.
- 5 T. Xu, J. Hu and H. Chen, *Microchem. J.*, 2019, **149**, 103972.
- 6 Y. Qing, Y. Hang, R. Wanjaul, Z. Jiang and B. Hu, *Anal. Sci.*, 2003, **19**, 1417.
- 7 L. Cui, J. Wu and H. Ju, *Biosens. Bioelectron.*, 2015, **63**, 276.
- 8 J. F. Zhang, Y. Zhou, J. Yoon and J. S. Kim, *Chem. Soc. Rev.*, 2011, **40**, 3416.
- 9 L. Prodi, F. Bolletta, M. Montalti and N. Zaccheroni, *Coord. Chem. Rev.*, 2000, **205**, 59.
- 10 J. S. Wu, W. M. Liu, J. C. Ge, H. Y. Zhang and P. F. Wang, *Chem. Soc. Rev.*, 2011, **40**, 3483.
- 11 D. Udhayakumari and V. Inbaraj, *J. Fluoresc.*, 2020, **30**, 1203.
- 12 K. P. Carter, A. M. Young and A. E. Palmer, *Chem. Rev.*, 2013, **114**, 4564.
- 13 M. Formica, V. Fusi, L. Giorgi and M. Micheloni, *Coord. Chem. Rev.*, 2012, **256**, 170.
- 14 D. Wu, A. C. Sedgwick, T. Gunnlaugsson, E. U. Akkaya, J. Yoon and T. D. James, *Chem. Soc. Rev.*, 2017, **46**, 7105.
- 15 S. Chowdhury, B. Rooj, A. Dutta and U. Mandal, *J. Fluoresc.*, 2018, **28**, 999.
- 16 P. Bhalla, K. Malhotra, N. Tomer and R. Malhotra, *Inorg. Chem. Commun.*, 2022, **146**, 110026.
- 17 P. A. Gale and C. Caltagirone, *Chem. Soc. Rev.*, 2015, **44**, 4212.
- 18 P. Jiang and Z. Guo, *Coord. Chem. Rev.*, 2004, **248**, 205.
- 19 G. Sivaraman, M. Iniya, T. Anand, N. G. Kotla, O. Sunnapu, S. Singaravadi, A. Gulyani and D. Chellappa, *Coord. Chem. Rev.*, 2018, **357**, 50.
- 20 J. Wu, W. Liu, J. Ge, H. Zhang and P. Wang, *Chem. Soc. Rev.*, 2011, **40**, 3483.
- 21 J. Liu, Y. Q. Xie, Q. Lin, B. B. Shi, P. Zhang, Y. M. Zhang and T. B. Wei, *Sens. Actuators, B*, 2013, **186**, 657.
- 22 S. A. Ingale and F. Seela, *J. Org. Chem.*, 2012, **77**, 9352.
- 23 I. Ravikumar and P. Ghosh, *Inorg. Chem.*, 2011, **50**, 4229.
- 24 M. Xiong, Z. Yang, R. J. Lake, J. Li, S. Hong, H. Fan, X.-B. Zhang and Y. Lu, *Angew. Chem., Int. Ed.*, 2022, **59**, 1891.
- 25 J. H. Wang, Y. M. Liu, J. B. Chao, H. Wang, Y. Wang and S. Shuang, *Sens. Actuators, B*, 2020, **303**, 127216.
- 26 L. Chen, D. Liu, J. Peng, Q. Du and H. He, *Coord. Chem. Rev.*, 2020, **404**, 213113.
- 27 P. Chen, W. Bai and Y. Bao, *J. Mater. Chem.*, 2019, **7**, 11731.
- 28 S. Xu, K. Chen and H. Tian, *J. Mater. Chem.*, 2005, **15**, 2676.
- 29 S. Subedi, L. N. Neupane, H. Yu and K. H. Lee, *Sens. Actuators, B*, 2021, **338**, 129814.
- 30 L. Fu, F. L. Jiang, D. Fortin, P. D. Harvey and Y. Liu, *Chem. Commun.*, 2011, **47**, 5503.
- 31 D. Maity, A. Mukherjee, S. K. Mandal and P. Roy, *J. Lumin.*, 2019, **210**, 508.
- 32 J. H. Kim, J. Y. Noh, I. H. Hwang, J. Kang, J. Kim and C. Kim, *Tetrahedron Lett.*, 2013, **54**, 2415.
- 33 H. Li, L. Cai and Z. Chen, *Adv. Chem. Sens.*, 2021, **1**, 121.
- 34 C. Liu, S. Huang, H. Yao, S. He, Y. Lu, L. Zhao and X. Zeng, *RSC Adv.*, 2014, **4**, 16109.
- 35 H. N. Kim, M. H. Lee, H. J. Kim, J. S. Kim and J. Yoon, *Chem. Soc. Rev.*, 2008, **37**, 1465.
- 36 K. T. A. Priyanga, Y. S. Kurniawan, K. Ohto and J. Jumina, *J. Multidiscip. Appl. Nat. Sci.*, 2022, **2**, 23.
- 37 J. L. Segura, M. J. Mancheno and F. Zamora, *Chem. Soc. Rev.*, 2016, **45**, 5635.
- 38 J. Wang, Q. Meng, Y. Yang, S. Zhong, R. Zhang, Y. Fang, Y. Gao and X. Cui, *ACS Sens.*, 2022, **7**, 2521.
- 39 C. M. Da Silva, L. V. Modolo, R. B. Alves, M. A. de Resende, C. V. Martins and A. de Fátima, *J. Adv. Res.*, 2011, **2**, 1.
- 40 J. Cheng, K. Wei, X. Ma, X. Zhou and H. Xiang, *J. Phys. Chem. C*, 2013, **117**, 16552.
- 41 P. G. Cozzi, *Chem. Soc. Rev.*, 2004, **33**, 410.
- 42 S. Khan, X. Chen, A. Almahri, E. S. Allehyani, F. A. Alhumaydhi, M. M. Ibrahim and S. Ali, *J. Environ. Chem. Eng.*, 2021, **9**, 106381.
- 43 V. K. Gupta, A. K. Singh and L. K. Kumawat, *Sens. Actuators, B*, 2014, **195**, 98.
- 44 J. Berrones-Reyes, B. M. Munoz-Flores, A. Gomez-Trevino, M. A. Treto-Suarez, D. Paez-Hernandez, E. Schott, X. Zarate and V. M. Jimenez-Perez, *Mater. Chem. Phys.*, 2019, **233**, 89.
- 45 Y. Wang, Z. Y. Ma, D. L. Zhang, J. L. Deng, X. Chen, C. Z. Xie, X. Qiao, Q. Z. Li and J. Y. Xu, *Spectrochim. Acta, Part A*, 2018, **195**, 57.
- 46 H. Tian, X. Qiao, Z. L. Zhang, C. Z. Xie, Q. Z. Li and J. Y. Xu, *Spectrochim. Acta, Part A*, 2019, **207**, 31.
- 47 A. Jayaraj, M. S. Gayathri, G. Sivaraman and P. C. A. Swamy, *J. Photochem. Photobiol., B*, 2022, **226**, 112371.
- 48 P. Middya, A. Saha and S. Chattopadhyay, *Inorg. Chim. Acta*, 2022, **545**, 121246.
- 49 A. Kumar, M. Saini, B. Mohan and M. Kamboj, *Microchem. J.*, 2022, **181**, 107798.
- 50 M. Kaur, S. Kumar, M. Yusuf, J. Lee, R. J. Brown, K. H. Kim and A. K. Malik, *Coord. Chem. Rev.*, 2021, **449**, 214235.
- 51 J. M. Berg and Y. Shi, *Science*, 1996, **271**, 1081.
- 52 X. Xie and T. G. Smart, *Nature*, 1991, **349**, 521.





- 53 Q. Ai, *BioMetals*, 2001, **14**, 315.
- 54 B. L. Vallee and K. H. Falchuk, *Physiol. Rev.*, 1993, **73**, 79.
- 55 (a) A. Helal and H. S. Kim, *Tetrahedron Lett.*, 2009, **50**, 5510; (b) J. H. Weiss, S. L. Sensi and J. Y. Koh, *Trends Pharmacol. Sci.*, 2000, **21**, 395.
- 56 (a) A. Azam, H. M. Chawla and S. Pandey, *Tetrahedron Lett.*, 2010, **51**, 4710; (b) S. H. Mashraqui, T. Khan, S. Sundaram, R. Betkar and M. Chandiramani, *Tetrahedron Lett.*, 2007, **48**, 8487.
- 57 (a) A. Voegelin, S. Pfister, A. C. Scheinost, M. A. Marcus and R. Kretzschmar, *Environ. Sci. Technol.*, 2005, **39**, 6616; (b) E. Callender and K. C. Rice, *Environ. Sci. Technol.*, 2000, **34**, 232.
- 58 Z. Xu, J. Yoon and D. R. Spring, *Chem. Soc. Rev.*, 2010, **39**, 1996.
- 59 E. Tomat and S. J. Lippard, *Curr. Opin. Chem. Biol.*, 2010, **14**, 225.
- 60 (a) D. Buccella, J. A. Horowitz and S. J. Lippard, *J. Am. Chem. Soc.*, 2011, **133**, 4101; (b) S. K. Rastogi, P. Pal, D. E. Aston, T. E. Bitterwolf and A. L. Brannen, *ACS Appl. Mater. Interfaces*, 2011, **3**, 1731; (c) A. Krezel, J. Wojcik, M. Maciejczyk and W. Bal, *Inorg. Chem.*, 2011, **50**, 72; (d) E. Tomat and S. J. Lippard, *Inorg. Chem.*, 2010, **49**, 9113; (e) S. Y. Kim and J. I. Hong, *Tetrahedron Lett.*, 2009, **50**, 2822; (f) L. Xue, H. H. Wang and H. Jiang, *Inorg. Chem.*, 2008, **47**, 4310; (g) B. Mohan, P. Balakrishnan, D. Umadevi and S. Shanmugaraju, *Inorg. Chim. Acta*, 2022, **533**, 120798.
- 61 Q. Wu, L. Feng, J. B. Chao, Y. Wang and S. Shuang, *Analyst*, 2021, **146**, 4348.
- 62 S. N. Ansari, A. K. Saini, B. P. Kumari and S. M. Mobin, *Inorg. Chem. Front.*, 2019, **6**, 736.
- 63 S. Gharami, K. Aich, D. Sarkar, P. Ghosh, N. Murmu and T. K. Mondal, *New J. Chem.*, 2019, **43**, 1857.
- 64 Z. Lu, W. Fan, Y. Lu, C. Fan, H. Zhao, K. Guo, W. Chua and Y. Lu, *New J. Chem.*, 2018, **42**, 12198.
- 65 A. S. Murugan, N. Vidhyalakshmi, U. Ramesh and J. Annaraj, *J. Mater. Chem. B*, 2017, **5**, 3195.
- 66 S. Lohar, S. Pal, M. Mukherjee, A. Maji, N. Demitri and P. Chattopadhyay, *RSC Adv.*, 2017, **7**, 25528.
- 67 M. Shyamal, P. Mazumdar, S. Maity, S. Samanta, G. P. Sahoo and A. Misra, *ACS Sens.*, 2016, **1**, 739.
- 68 C. Chang, F. Wang, T. Wei and X. Chen, *Ind. Eng. Chem. Res.*, 2017, **56**, 8797.
- 69 J.-T. Wang, Y.-Y. Pei, M.-Y. Yan, Y. G. Li, G.-G. Yang, C.-H. Qu, W. Luo, J. Wang and Q.-F. Li, *Microchem. J.*, 2021, **160**, 105776.
- 70 K. M. Wyss, E. E. Hardy and A. E. V. Gorden, *Inorg. Chim. Acta*, 2019, **492**, 156.
- 71 M. M. Mathew and A. Sreekanth, *Inorg. Chim. Acta*, 2021, **516**, 120149.
- 72 D. Maity, A. Mukherjee, S. K. Mandal and P. Roy, *J. Lumin.*, 2019, **210**, 508.
- 73 X. He, F. Ding, X. Sun, Y. Zheng, W. Xu, L. Ye, H. Chen and J. Shen, *Inorg. Chem.*, 2021, **60**, 5563.
- 74 S. J. Malthus, S. A. Cameron and S. Brooker, *Inorg. Chem.*, 2018, **57**, 2480.
- 75 S. Janakipriya, S. Tamilmani and S. Thennarasu, *RSC Adv.*, 2016, **6**, 71496.
- 76 C. Patra, A. K. Bhanja, A. Mahapatra, S. Mishra, K. D. Sahab and C. Sinha, *RSC Adv.*, 2016, **6**, 76505.
- 77 B. Naskar, R. Modak, D. K. Maiti, M. G. B. Drew, A. Bauza, A. Frontera, C. D. Mukhopadhyay, S. Mishra, K. D. Sahae and S. Goswami, *Dalton Trans.*, 2017, **46**, 9498.
- 78 Y. Upadhyay, T. Anand, L. T. Babu, P. Paira, G. Crisponi, S. K. A. Kumar, R. Kumar and S. K. Sahoo, *Dalton Trans.*, 2018, **47**, 742.
- 79 Y. Wang, X. Hou, Z. Li, Q. Zhou, M. Lei, S. Hu, X. Wu, C. Li, Z. Xu and Y. Wang, *Anal. Methods*, 2018, **10**, 5790.
- 80 J. Y. Yun, J. B. Chae, M. Kim, M. H. Lim and C. Kim, *Photochem. Photobiol. Sci.*, 2019, **18**, 166.
- 81 S. Ghosh, N. Baildya and K. Ghosh, *New J. Chem.*, 2021, **45**, 10923.
- 82 J.-C. Qin, L. Fan and Z.-Y. Yang, *Sens. Actuators, B*, 2016, **228**, 156.
- 83 N. Roy, A. Dutta, P. Mondal, P. C. Paul and T. S. Singh, *Sens. Actuators, B*, 2016, **236**, 719.
- 84 M. Patil, S. Bothra, S. K. Sahoo, H. A. Rather, R. Vasita, R. Bendre and A. Kuwar, *Sens. Actuators, B*, 2018, **270**, 200.
- 85 J. M. Jung, D. Yun, H. Lee, K.-T. Kim and C. Kim, *Sens. Actuators, B*, 2019, **297**, 126814.
- 86 L.-M. Liu and Z.-Y. Yang, *J. Photochem. Photobiol., A*, 2018, **364**, 558.
- 87 A. Gomathi, P. Viswanathamurthi and K. Natarajan, *J. Photochem. Photobiol., A*, 2019, **370**, 75.
- 88 F. Liu, C. Fan and S. Pu, *J. Photochem. Photobiol., A*, 2019, **371**, 248.
- 89 C.-R. Li, G.-Q. Wang, L. Fan, S. L. Li, J.-C. Qin and Z.-Y. Yang, *J. Photochem. Photobiol., A*, 2019, **375**, 231.
- 90 Y. Xu, H. Wang, J. Zhao, X. Yang, M. Pei, G. Zhang, Y. Zhang and L. Lin, *J. Photochem. Photobiol., A*, 2019, **383**, 112026.
- 91 C. Liu, J.-C. Qin, J. Xue, L.-M. Tian, T.-R. Li and Z.-Y. Yang, *J. Photochem. Photobiol., A*, 2019, **385**, 112091.
- 92 J. Mandal, P. Ghorai, K. Pal, P. Karmakar and A. Saha, *J. Lumin.*, 2019, **205**, 14.
- 93 S. Acharyya, S. Gharami, D. Sarkar, P. Ghosh, N. Murmu and T. K. Mondal, *J. Mol. Struct.*, 2021, **1224**, 129179.
- 94 X. Wang, G. Ding, Y. Duan, M. Wang, G. Zhu, X. Li, Y. Zhang and X. Qin, *Tetrahedron*, 2020, **76**, 131108.
- 95 M. Budri, G. Naik, S. Patil, P. Kadolkar, K. Gudasi and S. Inamdar, *J. Photochem. Photobiol., A*, 2020, **390**, 112298.
- 96 B. K. Rani and S. A. John, *J. Photochem. Photobiol., A*, 2021, **418**, 113372.
- 97 W.-N. Wu, P.-D. Mao, Y. Wang, X.-L. Zhao, Z.-Q. Xu, Z.-H. Xu and Y. Xue, *Spectrochim. Acta, Part A*, 2018, **188**, 324.
- 98 L.-L. Gao, S.-P. Li, Y. Wang, W.-N. Wu, X.-L. Zhao, H.-J. Li and Z.-H. Xu, *Spectrochim. Acta, Part A*, 2020, **230**, 118025.
- 99 D. Wang, Q. Yin, M. Zheng, Y. Xie, W. He, Z. Li, S. Hou and H. Wang, *Spectrochim. Acta, Part A*, 2021, **251**, 119480.
- 100 V. Venkatesan, R. S. Kumar, S. K. A. Kumar and S. K. Sahoo, *Inorg. Chem. Commun.*, 2019, **102**, 171.
- 101 J. Jia and H. Zhao, *Org. Electron.*, 2019, **73**, 55.



- 102 M. Shellaiah, Y.-T. Chen, N. Thirumalaivasan, B. Azaad, K. Awasthi, K. W. Sun, S.-P. Wu, M.-C. Lin and N. Ohta, *ACS Appl. Mater. Interfaces*, 2021, **13**, 28610.
- 103 A. Pandey, S. K. Asthana, A. Prakash, J. K. Roy, I. Tiwaria and K. K. Upadhyay, *Dalton Trans.*, 2019, **48**, 2068.
- 104 S. Das, J. Adhikary, P. Chakraborty, T. Chakraborty and D. Das, *RSC Adv.*, 2016, **6**, 98620.
- 105 M. S. Kim, T. G. Jo, M. Yang, J. Han, M. H. Lim and C. Kim, *Spectrochim. Acta, Part A*, 2019, **211**, 34.
- 106 L.-Z. Liu, L. Wang, M. Yu, Q. Zhao, Y. Zhang, Y.-X. Sun and W.-K. Dong, *Spectrochim. Acta, Part A*, 2019, **222**, 117209.
- 107 S. Guo, G. Liu, C. Fan and S. Pu, *Sens. Actuators, B*, 2018, **266**, 603.
- 108 L. Wang, W. Li, W. Zhi, Y. Huang, J. Han, Y. Wang, Y. Ren and L. Ni, *Sens. Actuators, B*, 2018, **260**, 243.
- 109 M. Berlin, R. K. Zalups and B. A. Fowler, "Mercury", in *Handbook on the Toxicology of Metals*, ed. G. F. Nordberg, B. A. Fowler, M. Nordberg and L. T. Friberg, Elsevier, New York, NY, USA, 3rd edn, 2007, ch. 33.
- 110 S. Bose-O'Reilly, L. Beate, R. M. Gothe, C. Beinhoff, U. Siebert and G. Drasch, *Environ. Res.*, 2008, **107**, 89.
- 111 T. W. Clarkson, L. Magos and G. J. Myers, *N. Engl. J. Med.*, 2003, **349**, 1731.
- 112 T. W. Clarkson and L. Magos, *Crit. Rev. Toxicol.*, 2006, **36**, 609.
- 113 M. R. Knecht and M. Sethi, *Anal. Bioanal. Chem.*, 2009, **394**, 33.
- 114 Y. M. Yang, Q. Zhao, W. Feng and F. Y. Li, *Chem. Rev.*, 2013, **113**, 192.
- 115 (a) N. Kumari, N. Dey and S. Bhattacharya, *Analyst*, 2014, **139**, 2370; (b) N. Kumari, N. Dey and S. Bhattacharya, *RSC Adv.*, 2014, **4**, 4230.
- 116 (a) S. Saha, H. Agarwalla, H. Gupta, M. Baidya, E. Suresh, S. K. Ghosh and A. Das, *Dalton Trans.*, 2013, **42**, 15097; (b) P. Mahato, S. Saha, P. Das, H. Agarwalla and A. Das, *RSC Adv.*, 2014, **4**, 36140.
- 117 U. G. Reddy, V. Ramu, S. Roy, N. Taye, S. Chattopadhyay and A. Das, *Chem. Commun.*, 2014, **50**, 14421.
- 118 N. Kumari, N. Dey, S. Jha and S. Bhattacharya, *ACS Appl. Mater. Interfaces*, 2013, **5**, 2438.
- 119 S. Saha, P. Mahato, U. G. Reddy, E. Suresh, A. Chakrabarty, M. Baidya, S. K. Ghosh and A. Das, *Inorg. Chem.*, 2012, **51**, 336.
- 120 C. Cui, X. Gao, X. Jia, Y. Jiao and C. Duan, *Inorg. Chim. Acta*, 2021, **520**, 120285.
- 121 Q. Su, Q. Niu, T. Sun and T. Li, *Tetrahedron Lett.*, 2016, **57**, 4297.
- 122 B. Liu, X. Hu, J. Chai and B. Yang, *Sens. Actuators, B*, 2016, **228**, 94.
- 123 W. Fang, G. Zhang, J. Chen, L. Kong, L. Yang, H. Bi and J. Yang, *Sens. Actuators, B*, 2016, **229**, 338.
- 124 R. Goel, S. Sharma, K. Paul and V. Luxami, *Sens. Actuators, B*, 2017, **246**, 776.
- 125 Y. Fang, X. Li, J.-Y. Li, G.-Y. Wang, Y. Zhou, N.-Z. Xu, Y. Hu and C. Yao, *Sens. Actuators, B*, 2018, **255**, 1182.
- 126 R. Singh and G. Das, *Sens. Actuators, B*, 2018, **258**, 478.
- 127 Z.-L. Wu, D. Shi, L. Huang, W.-Y. He, X.-Y. Sun, B. Liu and J.-S. Shen, *Sens. Actuators, B*, 2019, **281**, 311.
- 128 P. G. Mahajan, J. S. Shin, N. C. Dige, B. D. Vanjare, Y. Han, N. G. Choi, S. J. Kim, S. Y. Seo and K. H. Lee, *J. Photochem. Photobiol., A*, 2020, **397**, 112579.
- 129 D. B. C. Leslee, K. Sekar and M. M. Kothottil, *J. Photochem. Photobiol., A*, 2021, **415**, 113303.
- 130 V. Tekuri, S. K. Sahoo and D. R. Trivedi, *Spectrochim. Acta, Part A*, 2019, **218**, 19.
- 131 W. Zhong, L. Wang, D. Qin, J. Zhou and H. Duan, *ACS Omega*, 2020, **5**, 24285.
- 132 Y.-K. La, J.-A. Hong, Y.-J. Jeong and J. Lee, *RSC Adv.*, 2016, **6**, 84098.
- 133 P. Venkatesan, N. Thirumalivasan and S.-P. Wu, *RSC Adv.*, 2017, **7**, 21733.
- 134 G. Yang, X. Meng, S. Fang, H. Duan, L. Wang and Z. Wang, *RSC Adv.*, 2019, **9**, 8529.
- 135 Y. Gao, C. Zhang, S. Peng and H. Chen, *Sens. Actuators, B*, 2017, **238**, 455.
- 136 S. Dewangan, T. Barik, B. Halder, A. Mishra, R. Dhiman, T. Sasamori and S. Chatterjee, *J. Organomet. Chem.*, 2021, **948**, 121922.
- 137 M. Li, Y. Sun, L. Dong, Q.-C. Feng, H. Xu, S.-Q. Zang and T. C. W. Mak, *Sens. Actuators, B*, 2016, **226**, 332.
- 138 B. D. Vanjare, P. G. Mahajan, H.-I. Ryoo, N. C. Dige, N. G. Choi, Y. Han, S. J. Kim, C.-H. Kim and K. H. Lee, *Sens. Actuators, B*, 2021, **330**, 129308.
- 139 Z.-Q. Xu, X.-J. Mao, Y. Wang, W.-N. Wu, P.-D. Mao, X.-L. Zhao, Y.-C. Fan and H.-J. Li, *RSC Adv.*, 2017, **7**, 42312.
- 140 P. Wang, D. Zhou and B. Chen, *Spectrochim. Acta, Part A*, 2019, **207**, 276.
- 141 N. Shaily, A. Kumar and N. Ahmed, *New J. Chem.*, 2017, **41**, 14746.
- 142 M. Huang, C. Lv, Q. Huang, J. Lai and H. Sun, *RSC Adv.*, 2019, **9**, 36011.
- 143 B. Makwanal, D. Vyas, K. Bhatt, S. Darji and V. Jain, *Appl. Nanosci.*, 2016, **6**, 555.
- 144 Z. Liu, C. Zhang, W. He, Z. Yang, X. Gao and Z. Guo, *Chem. Commun.*, 2010, **46**, 6138.
- 145 A. Maity, U. Ghosh, D. Giri, D. Mukherjee, T. Maiti and S. Patra, *Dalton Trans.*, 2019, **48**, 2108.
- 146 B. R. Singh, *Cadmium in Soils and Plants*, ed. M. J. McLaughlin and B. R. Singh, 1999, vol. 257.
- 147 L. Xue, G. Li, Q. Liu, H. Wang, C. Liu, X. Ding, S. He and H. Jiang, *Inorg. Chem.*, 2011, **50**, 3680.
- 148 C. Lu, Z. Xu, J. Cui, R. Zhang and X. Qian, *J. Organomet. Chem.*, 2007, **72**, 3554.
- 149 L. Xu, M.-L. He, H.-B. Yang and X. Qian, *Dalton Trans.*, 2013, **42**, 8218.
- 150 X. Wan, H. Ke, J. Tang and G. Yang, *Talanta*, 2019, **199**, 8.
- 151 D. Mohanasundaram, R. Bhaskar, G. G. V. Kumar, J. Rajesh and G. Rajagopal, *Microchem. J.*, 2021, **164**, 106030.
- 152 W. Chen, H. Xu, L. Ju and H. Lu, *Tetrahedron*, 2021, **88**, 132123.
- 153 S. A. Khan, Q. Ullah, A. S. A. Almalki, S. Kumar, R. J. Obaid, M. A. Alsharif, S. Y. Alfaifi and A. A. Hashmi, *J. Mol. Liq.*, 2021, **328**, 115407.



- 154 J. H. Wang, Y. M. Liu, J. B. Chao, H. Wang, Y. Wang and S. M. Shuang, *Sens. Actuators, B*, 2020, **303**, 127216.
- 155 *Gold: Progress in Chemistry, Biochemistry and Technology*, ed. H. Schmidbaur, Wiley, Chichester, 1999.
- 156 *Gold Chemistry Applications and Future Directions in the Life Sciences*, ed. F. Mohr, Wiley-VCH, Weinheim, 2009.
- 157 S. Singha, D. Kim, H. Seo, S. W. Cho and K. H. Ahn, *Chem. Soc. Rev.*, 2015, **44**, 4367.
- 158 J. F. Zhang, Y. Zhou, J. Yoon and J. S. Kim, *Chem. Soc. Rev.*, 2011, **40**, 3416–3429.
- 159 N. Duman, S. E. Evans, O. Karadag, S. As-çioğlu, B. S. Ener, S. Kiraz and S. S. Ahin, *Int. J. Dermatol.*, 2014, **53**, 1286.
- 160 I. Ott, *Coord. Chem. Rev.*, 2009, **253**, 1670.
- 161 M. Navarro, *Coord. Chem. Rev.*, 2009, **253**, 1619.
- 162 L. Messori and G. Marcon, *Gold Complexes in the Treatment of Rheumatoid Arthritis, Metal Ions and their Complexes in Medication*, CRC Press, 2004.
- 163 C. F. Shaw, *Chem. Rev.*, 1999, **99**, 2589.
- 164 A. Locke and E. R. Main, *JAMA, J. Am. Med. Assoc.*, 1928, **90**, 259.
- 165 S. Mondal, S. K. Manna, S. Pathak, A. Ghosh, P. Datta, D. Mandal and S. Mukhopadhyay, *New J. Chem.*, 2020, **44**, 7954.
- 166 E. Wang, L. Pang, Y. Zhou, J. Zhang, F. Yu, H. Qiao and X. Pang, *Biosens. Bioelectron.*, 2016, **77**, 812.
- 167 W. Wang, Y. Huang, S. Wang, Y. Zhou, W. Huang, Y. Feng, W. Zhang, W. Yu, Q. Zhou, M. Chen and M. Fang, *Spectrochim. Acta, Part A*, 2017, **187**, 110.
- 168 T. W. Purcell and J. J. Peters, *Environ. Toxicol. Chem.*, 1998, **17**, 539.
- 169 M. Á. Corral, M. M. Dorado and I. R. Garcia, *Chem. Rev.*, 2008, **108**, 3174.
- 170 J. F. Zhang, Y. Zhou, J. Yoon and J. S. Kim, *Chem. Soc. Rev.*, 2011, **40**, 3416.
- 171 (a) G. Chakrapani, P. L. Mahanta, D. S. R. Murty and B. Gomathy, *Talanta*, 2001, **53**, 1139; (b) S. Dadfarnia, A. M. Haji Shabani and M. Gohari, *Talanta*, 2004, **64**, 682; (c) G. S. Pomales, T. K. Mudalige, J. H. Lim and S. W. Linder, *J. Agric. Food Chem.*, 2013, **61**, 7250.
- 172 E. Tan, P. Yin, X. Lang, X. Wang, T. You and L. Guo, *Analyst*, 2012, **137**, 3925.
- 173 K. Wygladacz, A. Radu, C. Xu, Y. Qin and E. Bakker, *Anal. Chem.*, 2005, **77**, 4706.
- 174 R. K. Shervedani and M. K. Babadi, *Talanta*, 2006, **69**, 741.
- 175 Y. H. Li, H. Q. Xie and F. Q. Zhou, *Talanta*, 2005, **67**, 28.
- 176 A. Mohadesi and M. A. Taher, *Talanta*, 2007, **71**, 615.
- 177 R. P. Singh and E. R. Pambid, *Analyst*, 1990, **115**, 301.
- 178 (a) K. Ndung, M. A. Ranville, R. P. Franks and A. R. Flegel, *Mar. Chem.*, 2006, **98**, 109; (b) L. Yang and R. E. R. Sturgeon, *J. Anal. At. Spectrom.*, 2002, **7**, 88; (c) R. K. Katarina, T. Takayanagi, M. Oshima and S. Motomizu, *Anal. Chim. Acta*, 2006, **558**, 246.
- 179 M. Shamsipur, M. Javanbakht, V. Lippolis, A. Garau, G. D. Filippio, M. R. Ganjali and A. Yari, *Anal. Chim. Acta*, 2002, **462**, 225.
- 180 J. H. Kang, J. B. Chae and C. Kim, *R. Soc. Open Sci.*, 2018, **5**, 180293.
- 181 N. Bhuvanesh, S. Suresh, P. R. Kumar, E. M. Mothi, K. Kannan, V. R. Kannan and R. Nandhakumar, *J. Photochem. Photobiol., A*, 2018, **360**, 6.
- 182 N. Bhuvanesh, S. Suresh, J. Prabhu, K. Kannan, V. R. Kannan and R. Nandhakumar, *Opt. Mater.*, 2018, **82**, 123.
- 183 M. Sahu, A. K. Manna, K. Rout, J. Mondal and G. K. Patra, *Inorg. Chim. Acta*, 2020, **508**, 119633.
- 184 Y. K. Jang, U. C. Nam, H. L. Kwon, I. H. Hwang and C. Kim, *Dyes Pigm.*, 2013, **99**, 6.
- 185 X. Chen, M. J. Jou, H. Lee, S. Kou, J. Lim, S.-W. Nam, S. Park, K.-M. Kim and J. Yoon, *Sens. Actuators, B*, 2009, **137**, 597.
- 186 J. A. Cotruvo, A. T. Aron, K. M. Ramos-Torres and C. J. Chang, *Chem. Soc. Rev.*, 2015, **44**, 4400.
- 187 C. J. Chang, *Nat. Chem. Biol.*, 2015, **11**, 744.
- 188 A. T. Aron, K. M. Ramos-Torres, J. A. Cotruvo and C. J. Chang, *Acc. Chem. Res.*, 2015, **48**, 2434.
- 189 L. Krishnamoorthy, J. A. Cotruvo, J. Chan, H. Kaluarachchi, A. Muchenditsi, V. S. Pendyala, S. Jia, A. T. Aron, C. M. Ackerman, M. N. V. Wal, T. Guan, L. P. Smaga, S. L. Farhi, E. J. New, S. Lutsenko and C. J. Chang, *Nat. Chem. Biol.*, 2016, **12**, 586.
- 190 Y. J. Na, Y. W. Choi, J. Y. Yun, K.-M. Park, P.-S. Chang and C. Kim, *Spectrochim. Acta, Part A*, 2015, **136**, 1649.
- 191 E. Madsen and J. D. Gitlin, *Annu. Rev. Neurosci.*, 2007, **30**, 317.
- 192 K. J. Barnham, C. L. Masters and A. I. Bush, *Nat. Rev. Drug Discovery*, 2004, **3**, 205.
- 193 P. G. Georgopoulos, A. Roy, M. J. Yonone-Lioy, R. E. Opiekun and P. J. Lioy, *J. Toxicol. Environ. Health, Part B*, 2001, **4**, 341.
- 194 (a) Y.-F. Tan, N. O'Toole, N. L. Taylor and A. H. Millar, *Plant Physiol.*, 2010, **152**, 747; (b) R. Uauy, M. Araya and B. Lonnerdal, Preface, *Am. J. Clin. Nutr.*, 2008, **88**, 819S; (c) A. Malik, *Environ. Int.*, 2004, **30**, 261.
- 195 Y. Wang, H. Wu, W.-N. Wu, Y.-P. Yu, X.-L. Zhao, Z.-H. Xu, Z.-Q. Xu and Y.-C. Fan, *J. Lumin.*, 2018, **204**, 289.
- 196 H. Ni, Q. Wang, L. Jin, W. Wang, L. Dai and C. Zhao, *J. Lumin.*, 2019, **206**, 125–131.
- 197 V. Venkatesan, R. S. Kumar, S. K. A. Kumar and S. K. Sahoo, *J. Mol. Struct.*, 2019, **1198**, 126906.
- 198 A. Saravanan, G. Subashini, S. Shyamsivappan, T. Suresh, K. Kadirvelu, N. Bhuvanesh, R. Nandhakumar and P. S. Mohan, *J. Photochem. Photobiol., A*, 2018, **364**, 424.
- 199 Y. Wang, P.-D. Mao, W.-N. Wu, X.-J. Mao, X.-L. Zhao, Z.-Q. Xu, Y.-C. Fan and Z.-H. Xu, *Sens. Actuators, B*, 2017, **251**, 813.
- 200 S. Wang, Z. Wang, Y. Yin, J. Luo and L. Kong, *J. Photochem. Photobiol., A*, 2017, **333**, 213.
- 201 W. Gao, H. Li and S. Pu, *J. Photochem. Photobiol., A*, 2018, **364**, 208.
- 202 J. Yin, Q. Bing, L. Wang and G. Wang, *Spectrochim. Acta, Part A*, 2018, **189**, 495.
- 203 Q. Bing, L. Wang, D. Li and G. Wang, *Spectrochim. Acta, Part A*, 2018, **202**, 305.
- 204 H. Fang, P.-C. Huang and F.-Y. Wu, *Spectrochim. Acta, Part A*, 2018, **204**, 568.





- 205 F. N. Moghadam, M. Amirnasr, S. Meghdadi, K. Eskandari, A. Buchholz and W. Plass, *Spectrochim. Acta, Part A*, 2019, **207**, 6.
- 206 S. Slassi, M. Aarjane, A. El-Ghayoury and A. Amine, *Spectrochim. Acta, Part A*, 2019, **215**, 348.
- 207 X. Wang, W. Shi, L. Feng, J. Ma, Y. Li, X. Kong, Y. Chen, Y. Hui and Z. Xie, *Inorg. Chem. Commun.*, 2017, **79**, 50.
- 208 N. Xiao and C. Zhang, *Inorg. Chem. Commun.*, 2019, **107**, 107467.
- 209 T. Simon, M. Shellaiah, V. Srinivasadesikan, C.-C. Lin, F.-H. Ko, K. W. Sun and M.-C. Lin, *New J. Chem.*, 2016, **40**, 6101.
- 210 S. Ghosh, A. Ganguly, Md. R. Uddin, S. Mandal, Md. A. Alam and N. Guchhait, *Dalton Trans.*, 2016, **45**, 11042.
- 211 P. Torawane, K. Keshav, M. K. Kumawat, R. Srivastava, T. Anand, S. Sahoo, A. Borse and A. Kuwar, *Photochem. Photobiol. Sci.*, 2017, **16**, 1464.
- 212 M. Yang, L. Ma, J. Li and L. Kang, *RSC Adv.*, 2019, **9**, 16812.
- 213 Z. Kowser, C.-C. Jin, X. Jiang, S. Rahman, P. E. Georgiou, X.-L. Ni, X. Zeng, C. Redshaw and T. Yamato, *Tetrahedron*, 2016, **72**, 4575.
- 214 R. Shen, J. J. Yang, H. Luo, B. Wang and Y. Jiang, *Tetrahedron*, 2017, **73**, 373.
- 215 B. Zambelli, F. Musiani, S. Benini and S. Ciurli, *Acc. Chem. Res.*, 2011, **44**, 520.
- 216 S. W. Ragsdale, *J. Biol. Chem.*, 2009, **284**, 18571.
- 217 R. J. Maier, *Biochem. Soc. Trans.*, 2005, **33**, 83.
- 218 Y. Lee, H. Liu, J. Lee, S. Kim, J. Sessler and Y. Kim, *Chem. – Eur. J.*, 2010, **16**, 5895.
- 219 P. Bandyopadhyay and A. K. Ghosh, *J. Phys. Chem. B*, 2010, **114**, 11462.
- 220 K. S. Kasprzak, F. W. Sunderman and K. Salnikowa, *Mutat. Res.*, 2003, **533**, 67.
- 221 P. H. Kuck, *Mineral Commodity Summaries: Nickel*, United States Geological Survey, 2006.
- 222 (a) E. Denkhaus and K. Salnikow, *Crit. Rev. Oncol. Hematol.*, 2002, **42**, 35; (b) *Nickel and Its Surprising Impact in Nature*, ed. H. Sigal, A. Sigal and R. O. K. Sigal, John Wiley and Sons Ltd, UK, 2007.
- 223 W. Lee, K. A. Davis, R. L. Rettmer and R. F. Labbe, *Am. J. Clin. Nutr.*, 1988, **48**, 286.
- 224 (a) X. Q. Liu, X. Zhou, X. Shu and J. Zhu, *Macromolecules*, 2009, **42**, 7634; (b) S. C. Dodani, Q. He and C. J. Chang, *J. Am. Chem. Soc.*, 2009, **131**, 18020.
- 225 A. K. Manna, K. Rout, S. Chowdhury and G. K. Patra, *Photochem. Photobiol. Sci.*, 2019, **18**, 1512.
- 226 G. G. V. Kumar, M. P. Kesavan, M. Sankarganesh, K. Sakthipandi, J. Rajesh and G. Sivaraman, *New J. Chem.*, 2018, **42**, 2865.
- 227 A. K. Manna, S. Chowdhury and G. K. Patra, *Dalton Trans.*, 2019, **48**, 12336.
- 228 S. J. Lippard and J. M. Berg, *Principles of Bioinorganic Chemistry*, University Science Books, 1994.
- 229 C. Melber, D. Keller and I. Mangelsdorf, *Environmental Health Criteria* 226, Palladium, World Health Organization, Geneva, 2002, p. 1.
- 230 Z. Berner, C. Menzel, A. Zeller, J. D. Eckhardt, D. Stüben and A. Hartwig, *Analytical Procedure for the Quantification of in vitro Induced Pt- and Pd-DNA Adducts in Human Lung Cells*, in *Palladium Emissions in the Environment*, ed. F. Zereini and F. Alt, Springer, Berlin, Heidelberg, 2006, DOI: [10.1007/3-540-29220-9\\_16](https://doi.org/10.1007/3-540-29220-9_16).
- 231 International Programme on Chemical Safety, *Palladium; Environmental Health Criteria Series* 226, World Health Organization, Geneva, 2002.
- 232 T. Gebel, H. Lantzsch, K. Plebow and H. Dunkelberg, *Mutat. Res., Genet. Toxicol. Environ. Mutagen.*, 1997, **389**, 183.
- 233 (a) J. Kielhorn, C. Melber, D. Keller and I. Mangelsdorf, *Int. J. Hyg. Environ. Health*, 2002, **205**, 417; (b) J. C. Wataha and C. T. Hanks, *J. Oral Rehabil.*, 1996, **23**, 309.
- 234 (a) C. L. S. Wiseman and F. Zereini, *Sci. Total Environ.*, 2009, **407**, 2493; (b) T. Z. Liu, S. D. Lee and R. S. Bhatnagar, *Toxicol. Lett.*, 1979, **60**, 469.
- 235 C. Melber, D. Keller and I. Mangelsdorf, *Environmental Health Criteria for Palladium*, World Health Organization, Geneva, 2002.
- 236 *Palladium Emissions in the Environment Analytical Methods, Environmental Assessment and Health Effects*, ed. F. Alt and F. Zereini, Springer-Verlag, Berlin, 2006.
- 237 A. K. Bhanja, S. Mishra, K. D. Sahab and C. Sinha, *Dalton Trans.*, 2017, **46**, 9245.
- 238 A. K. Adak, R. Purkait, S. K. Manna, B. C. Ghosh, S. Pathak and C. Sinha, *New J. Chem.*, 2019, **43**, 3899.
- 239 S. Mondal, S. K. Manna, S. Pathak, A. A. Masum and S. Mukhopadhyay, *New J. Chem.*, 2019, **49**, 3513.
- 240 A. K. Adak, B. Dutta, S. K. Manna and C. Sinha, *ACS Omega*, 2019, **4**, 18987.
- 241 A. K. Bhanja, S. Mishra, K. Kar, K. Naskar, S. Maity, K. D. Sahab and C. Sinha, *New J. Chem.*, 2018, **42**, 17351.
- 242 J.-W. Lee and J. D. Helmann, *Nature*, 2006, **440**, 363.
- 243 B. He, A. B. Pun, D. Zherebetsky, Y. Liu, F. Liu, L. M. Klivansky, A. M. McGough, B. Zhang, K. Lo, T. P. Russell, L. N. Wang and Y. Liu, *J. Am. Chem. Soc.*, 2014, **136**, 15093.
- 244 J. P. Sumner and R. Kopelman, *Analyst*, 2005, **130**, 528.
- 245 (a) R. S. Eisenstein, *Annu. Rev. Nutr.*, 2000, **20**, 627; (b) T. A. Rouault, *Nat. Chem. Biol.*, 2006, **2**, 406.
- 246 (a) C. Brugnara, *Clin. Chem.*, 2003, **49**, 1573; (b) N. R. Chereddy, K. Suman, P. S. Korrapati, S. A. Thennarasu and B. Manda, *Dyes Pigm.*, 2012, **95**, 606.
- 247 D. A. Weinstein, C. N. Roy, M. D. Fleming, M. F. Loda, J. I. Wolfsdorf and N. C. Andrews, *Blood*, 2002, **100**, 3776.
- 248 X. Huang, *Mutat. Res., Fundam. Mol. Mech. Mutagen.*, 2003, **533**, 153.
- 249 R. Agarwal, N. Vasavada, N. G. Sachs and S. Chase, *Kidney Int.*, 2004, **65**, 82279.
- 250 W. H. Hoerl, *J. Am. Soc. Nephrol.*, 2007, **18**, 382.
- 251 S. Epsztejn, H. Glickstein, V. Picard, I. N. Slotki, W. Breuer, C. Beaumont and Z. I. Cabantchik, *Blood*, 1999, **94**, 3593.
- 252 S. Santhoshkumar, K. Velmurugan, J. Prabhu, G. Radhakrishnan and R. Nandhakumar, *Inorg. Chim. Acta*, 2016, **439**, 1.
- 253 C.-F. Wan, Y.-J. Chang, C.-Y. Chien, Y.-W. Sie, C.-H. Hu and A.-T. Wu, *J. Lumin.*, 2016, **178**, 115.





- 254 V. K. Gupta, N. Mergu and L. K. Kumawat, *Sens. Actuators, B*, 2016, **223**, 101.
- 255 T. Nandhini, P. Kaleeswaran and K. Pitchumani, *Sens. Actuators, B*, 2016, **230**, 199.
- 256 P. S. Nayab and M. Shkir, *Sens. Actuators, B*, 2017, **245**, 395.
- 257 S. Adhikari, A. Ghosh, M. Ghosh, S. Guria and D. Das, *Sens. Actuators, B*, 2017, **251**, 942.
- 258 S. Zhang, T. Sun, D. Xiao, F. Yuan, T. Li, E. Wang, H. Liu and Q. Niu, *Spectrochim. Acta, Part A*, 2018, **189**, 594.
- 259 Z. Zuo, X. Song, D. Guo, Z. Guo and Q. Niu, *J. Photochem. Photobiol., A*, 2019, **382**, 111876.
- 260 Z. Guo, Q. Niu and T. Li, *Spectrochim. Acta, Part A*, 2018, **200**, 76.
- 261 R. Kouser, S. Zehra, R. A. Khan, A. Alsalme, F. Arjmand and S. Tabassum, *Spectrochim. Acta, Part A*, 2021, **247**, 119156.
- 262 A. S. Murugan, M. Kiruthika, E. R. A. Noelson, P. Yogapandi, G. G. Kumar and J. Annaraj, *Arabian J. Chem.*, 2021, **14**, 102910.
- 263 G. T. Selvan, C. Varadaraju, R. T. Selvan, Israel V. M. V. Enoch and P. M. Selvakumar, *ACS Omega*, 2018, **3**, 7985.
- 264 S. D. Padghan, A. L. Puyad, R. S. Bhosale, S. V. Bhosale and S. V. Bhosale, *Photochem. Photobiol. Sci.*, 2017, **16**, 1591.
- 265 H. Xu, H. Ding, G. Li, C. Fan, G. Liu and S. Pu, *RSC Adv.*, 2017, **7**, 29827.
- 266 L. Hou, T. Liu, Y. Gong, J. Li, C. Deng, C. Zhang, Y. Wang, S. Shuang and W. Liang, *New J. Chem.*, 2020, **44**, 19642.
- 267 B. Li, J. Tian, D. Zhang and F. Tian, *Luminescence*, 2017, **8**, 1.

